



**HAL**  
open science

# Manipulation and detection of spin waves using spin-orbit interaction in ultrathin perpendicular anisotropy Ta/FeCoB/MgO waveguides

Mathieu-Bhayu Fabre

► **To cite this version:**

Mathieu-Bhayu Fabre. Manipulation and detection of spin waves using spin-orbit interaction in ultrathin perpendicular anisotropy Ta/FeCoB/MgO waveguides. Condensed Matter [cond-mat]. Université Grenoble Alpes, 2019. English. NNT : 2019GREAY028 . tel-02461334

**HAL Id: tel-02461334**

**<https://theses.hal.science/tel-02461334v1>**

Submitted on 30 Jan 2020

**HAL** is a multi-disciplinary open access archive for the deposit and dissemination of scientific research documents, whether they are published or not. The documents may come from teaching and research institutions in France or abroad, or from public or private research centers.

L'archive ouverte pluridisciplinaire **HAL**, est destinée au dépôt et à la diffusion de documents scientifiques de niveau recherche, publiés ou non, émanant des établissements d'enseignement et de recherche français ou étrangers, des laboratoires publics ou privés.



## **THÈSE**

Pour obtenir le grade de

### **DOCTEUR DE LA COMMUNAUTÉ UNIVERSITÉ GRENOBLE ALPES**

Spécialité : NANOPHYSIQUE

Arrêté ministériel : 25 mai 2016

Présentée par

**Mathieu-Bhayu FABRE**

Thèse dirigée par **Ursula EBELS**  
et codirigée par **Gilles GAUDIN**, CNRS

préparée au sein du **Laboratoire Spintronique et Technologie  
des Composants**  
dans l'**École Doctorale Physique**

**Manipulation et détection d'ondes de spin  
via l'interaction spin-orbite dans des guides  
d'ondes ultraminces Ta/FeCoB/MgO à  
anisotropie perpendiculaire**

**Manipulation and detection of spin waves  
using spin-orbit interaction in ultrathin  
perpendicular anisotropy Ta/FeCoB/MgO  
waveguides**

Thèse soutenue publiquement le **10 juillet 2019**,  
devant le jury composé de :

**Monsieur JOO-VON KIM**

CHARGE DE RECHERCHE, CNRS ILE-DE-FRANCE-GIF-SUR-  
YVETTE, Rapporteur

**Monsieur GREGOIRE DE LOUBENS**

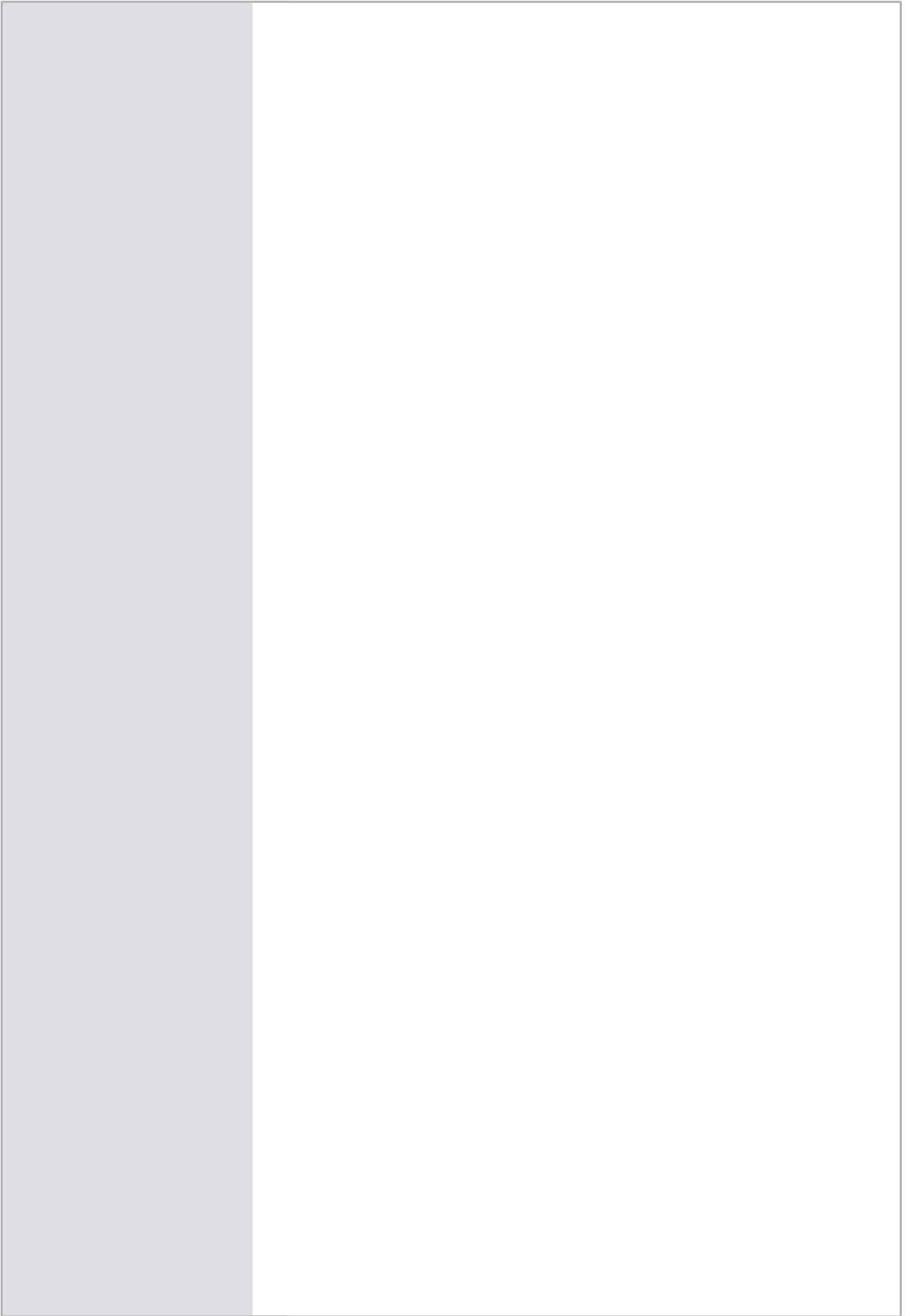
INGENIEUR DE RECHERCHE, CEA DE SACLAY, Rapporteur

**Monsieur DIRK GRUNDLER**

PROFESSEUR ASSOCIE, ECOLE POLYTECH FEDERALE LAUSANNE  
-SUISSE, Examineur

**Monsieur OLIVIER FRUCHART**

DIRECTEUR DE RECHERCHE, CNRS DELEGATION ALPES, Président



# Contents

<b>Introduction</b>	<b>1</b>
<b>1 Theoretical Background</b>	<b>7</b>
1.1 Energy contributions in a thin film ferromagnetic system . . . . .	7
1.1.1 The exchange energy . . . . .	8
1.1.2 The dipolar energy . . . . .	9
1.1.3 Magnetocrystalline anisotropy energy . . . . .	10
1.1.4 The Zeeman energy . . . . .	11
1.1.5 Energy minimization . . . . .	12
1.1.6 The effective field . . . . .	12
1.2 Uniform magnetization dynamics . . . . .	13
1.2.1 Equations of motion of the magnetization . . . . .	13
1.2.2 Polder susceptibility tensor . . . . .	15
1.2.3 Susceptibility for an infinite ferromagnetic medium . . . . .	15
1.2.4 Susceptibility for a ferromagnetic thin film . . . . .	17
1.2.5 Lineshape of the susceptibilities . . . . .	19
1.3 Magnetostatic spin-waves . . . . .	21
1.3.1 Spin-waves in the magnetostatic approximation . . . . .	21
1.3.2 Exchange spin-waves in an infinite ferromagnetic medium . . . . .	23
1.3.3 Exchange spin-waves in a ferromagnetic thin film . . . . .	24
1.3.4 Relaxation rate . . . . .	27
1.4 Spintronics phenomena . . . . .	27
1.4.1 The Rashba effect . . . . .	28
1.4.2 Spin Hall effects . . . . .	30
1.4.3 Detection of magnetization dynamics via spin pumping and inverse spin Hall effect . . . . .	32
1.4.4 Modification of the LLG including the field-like torque and the damping-like torque . . . . .	34
1.4.5 Anisotropic magnetoresistance . . . . .	35
<b>2 Device fabrication</b>	<b>37</b>
2.1 Wafer deposition and annealing . . . . .	37
2.2 Device fabrication . . . . .	38

2.3	Device description . . . . .	39
2.4	Measured samples . . . . .	41
<b>3</b>	<b>Spin-orbit torques</b>	<b>43</b>
3.1	Spin-torque resonance technique . . . . .	43
3.2	RF Excitation mechanisms . . . . .	46
3.2.1	Excitation by RF Ørsted field or RF field-like torque . . . . .	47
3.2.2	Excitation by RF damping-like torque . . . . .	47
3.2.3	Influence of a DC current on resonance conditions . . . . .	49
3.2.4	Influence of the DC damping-like torque on resonance conditions . . . . .	49
3.3	Electrical detection of magnetization dynamics . . . . .	52
3.3.1	DC signal via to anisotropic magnetoresistance . . . . .	52
3.3.2	DC signal via spin pumping and inverse spin Hall rectification . . . . .	56
3.3.3	Conclusion: AMR vs iSHE . . . . .	59
3.4	ST-FMR characterization at zero DC current . . . . .	61
3.4.1	Measurement protocol . . . . .	61
3.4.2	Angle dependence . . . . .	64
3.4.3	Saturation magnetization and interfacial anisotropy . . . . .	64
3.4.4	Linewidth and damping in the absence of DC current . . . . .	69
3.5	ST-FMR characterization with DC current . . . . .	78
3.5.1	Shifting of the resonance field via DC current . . . . .	80
3.5.2	Control of the damping via DC current . . . . .	86
3.6	Conclusion . . . . .	92
<b>4</b>	<b>Spin-wave excitation and detection</b>	<b>95</b>
4.1	Material and device characterization . . . . .	95
4.2	Verification of the dispersion relation . . . . .	97
4.3	Excitation of spin-waves via coplanar waveguides . . . . .	98
4.3.1	Magnetic field generated by a coplanar waveguide . . . . .	99
4.3.2	Spatial profile of spin-waves in a spin-wave waveguide in the Damon-Eshbach configuration . . . . .	103
4.3.3	Excitation efficiency . . . . .	104
4.3.4	Non-zero linewidth model . . . . .	106
4.4	Spin-wave rectification experiments . . . . .	108
4.4.1	Experimental setup . . . . .	108
4.4.2	Measurement protocol . . . . .	109
4.4.3	Angle dependence of spin-wave rectification . . . . .	110
4.4.4	Experimental results . . . . .	111
4.5	Brillouin light scattering experiments . . . . .	117
4.5.1	Working principle . . . . .	118
4.5.2	Description of the microscope . . . . .	118
4.5.3	BLS measurements . . . . .	119
4.5.4	Spin-wave decay length . . . . .	121
4.6	Comparison of spin-wave detection methods . . . . .	126

<i>CONTENTS</i>	iii
4.7 Conclusion . . . . .	127
<b>Conclusion and perspectives</b>	<b>129</b>
<b>A Linewidth under a DC damping-like torque</b>	<b>133</b>
<b>Bibliography</b>	<b>133</b>



# Introduction

The development of complementary metal-oxide-semiconductor (CMOS) transistors have long followed Gordon Moore's projection, namely that the density of transistors on a chip doubles every 18 months. However, this sustained exponential growth has met serious obstacles. Microelectronics require a variety of memory types that form a hierarchy: the closer the memory is to the processing unit (CPU), the faster it must be to deal with the rapid flux of information. The memory closest to the processor is called CPU cache and is typically static random-access memory (SRAM). SRAM has access times in the nanosecond range, requires constant voltage to retain information and is typically made up of 6 transistors, which represents a high cost in terms of space. With transistor density in modern processors reaching dozens of millions of transistors per squared millimeter, the power consumption and the low density of SRAM represents a significant technological hurdle, one that is amplified by the current leakage experienced by nm-sized transistors, leading to heat management issues. One possible solution is the use of non-volatile, memory to reduce the static power consumption of the CPU cache. A candidate to fulfill the requirements of CPU cache is magnetic random-access memory (MRAM), a technology that is at the forefront of a field of research called spintronics.

Spintronics, a portmanteau of spin electronics, concerns the study of solid state devices in which the spin of an electron, in addition to its charge, plays a pivotal role. Historically, the first development in spintronics was the discovery of tunnel magnetoresistance (TMR) by Jullière in 1975 [Jul75], where the resistance of two ferromagnetic layers separated by an insulator depends on the relative orientation of each ferromagnet's magnetization. Nowadays, the magnetoresistance of so-called magnetic tunnel junctions based on CoFeB/MgO/CoFeB pillars can change by up to several hundreds of % based on the magnetization state of the two CoFeB layers. However, Jullière's discovery did not attract too much attention initially, and instead the development of spintronics was arguably sparked by the discovery of a similar phenomenon called giant magnetoresistance (GMR) by Fert and Grunberg in 1986 [Bai88; Bin89] which proved more readily exploitable using the material deposition techniques available at the time.

Only 11 years after their seminal discovery, IBM commercialized the first hard disk drives with giant magnetoresistance read heads. Due to the radical increases in hard drive density made possible by their breakthrough, they were awarded the Nobel prize in physics in 2007. Today, much of the current interest on spintronics lies in the potential for scalable, non-volatile memory that can be integrated in CMOS chips. This

pursuit was bolstered by the prediction of spin-transfer torque (STT) [Slo96; Ber96] and its subsequent observation [Tso98], where electrons flowing in a ferromagnetic layer become spin-polarized in the direction of the magnetization, i.e., the proportion of up and down spins are not equal. When passing through a second ferromagnetic layer, the electrons are re-polarized in the direction of the second layer's magnetization. In effect, the coupled spin-charge current allows the transfer of angular momentum between the two ferromagnetic layers, meaning that one can control the magnetization state of the system by injecting a current through the device. Combining spin-transfer torque with tunnel magnetoresistance, one has the ingredients for an MRAM cell where the information is stored in the magnetization state, and a current is used either to read its state or to switch it. Such STT-MRAM modules are already commercialized today by Everspin [Mer19], serving as dynamic random-access memory. Modern magnetic tunnel junctions based on CoFeB/MgO/CoFeB are CMOS compatible due to the fact that the materials can be deposited on a Si wafer by magnetron sputtering, with Ta serving as a growth layer [Teh99; Gal06; Lin09]. Thus, STT-MRAM can be integrated on top of the processing elements [Pre09], instead of adjacent to it, which is the case for SRAM, thus saving space on the integrated circuit and potentially reducing access time. STT-MRAM uses power while reading or writing information but has no static power consumption, in fact memory is retained even when powered off. Sub-nanosecond switching has been demonstrated [Zha11], fulfilling the most important requirement of CPU cache: speed. Furthermore, its footprint is small as it requires only a single transistor and the magnetic tunnel junction itself, which can scale down to diameters in the nm range [Sai17]. In addition, STT-MRAM has the potential to be tailored to compete with other memory types: dynamic RAM by being non-volatile, and flash memory by being faster. However the high current required to switch the magnetic state can eventually lead to the breakdown of the junction, which presents an important hurdle, especially for CPU cache applications as writing speeds need to be high, implying high switching currents, and the endurance virtually unlimited.

Developments in spintronics in the last decade have led to the resurgence of two phenomena discovered in the 1970s which have helped overcome this obstacle: the Rashba effect [Ohk74; Byc84] and the spin Hall effect [Dya71b; Dya71a], both of which were first predicted for semiconductors or 2D electron gases. When they were discovered to be present in normal metals [Mir10; Mir11], it opened a new research field called spin-orbitronics. The aforementioned phenomena allow the creation of so-called spin-orbit torques (SOT) that are generated by a charge current in a normal metal, leading to new approaches for exciting the magnetization of an adjacent ferromagnet. The materials used to generate these effects include heavy metals such as Pt, Ta or W, owing to their large atomic number and thus large spin-orbit coupling. Ta and W have the advantage of being compatible with CoFeB/MgO/CoFeB magnetic tunnel junctions, retaining their compatibility with CMOS chips. Thus, a new class of devices emerged, called SOT-MRAM, which has the benefit of separating the reading current from the writing current, resulting in increased reliability and endurance [Pre16; Gar18], while still demonstrating sub-nanosecond switching times [Cub18].

Spintronics show the potential to disrupt conventional electronics in even more radical ways. The reduction of the transistor gate size has led to the static power dissipated by leakage has reached the same order of magnitude as the active power consumption [Jeo10]. This is due to the fact that energy, or information, in conventional electronics is physically manifested by currents and voltages, which, in nm-sized transistor gates inevitably leads to losses via switching or leakage by electron tunneling. In spintronics, information is mediated by spin moments, which can propagate without a net flow of charges. This propagation of spin currents can occur via spin-waves, the collective motion of local magnetic moments in a ferromagnetic or antiferromagnetic medium. Additionally, their wave-like nature allows wave-based logic in which information is encoded in the amplitude or the phase of the spin-wave. Proof-of-concept devices include a variety of logic gates (AND gate, XOR gate, etc.) [Sch08; Khi11; Nik15], majority gates [Kli14], magnon transistors [Chu14], spin-wave multiplexer [Vog14], spin-wave couplers [Sad15a] and beam splitter [Sad15b].<sup>1</sup> Some of these devices require less components than their semiconductor equivalents and thus, if they can be miniaturized successfully, they could have smaller footprints or consume less power. Thus, the study of spin-waves, a field called magnonics,<sup>2</sup> shows potential for the propagation as well as the processing of information with small footprints and low power consumption. Combined with MRAM cache, memory and storage, one can even envision all-magnetic processors.

One of the most ubiquitous materials studied for magnonics is the yttrium iron garnet (YIG), a ferrimagnetic insulator in which spin-waves can propagate distances on the order of cm thanks to its damping parameter in the  $10^{-5}$  range, which is the lowest of all known materials [Che93]. Even though there is much research activity on growing YIG thin films and creating YIG microstructures [Ham14], including all of the proof-of-concepts cited earlier, a significant problem lies in its inherent incompatibility with CMOS, due to the fact that YIG is grown via liquid phase epitaxy [Gla76; Sho85] or pulsed laser deposition [Dor93; Sun12], on a specific substrate: gadolinium gallium garnet. Thus, there is also significant interest in CMOS-compatible material systems such as metallic NiFe alloys<sup>3</sup> [Bai03; Sch08; Dem09] and CoFeB alloys<sup>4</sup> [Con13; Ran17] as well as half-metallic Co-based Heusler compounds [Seb12; Pir14]. However these materials have larger damping parameters in the  $10^{-3}$  range and thus the spin-wave propagation distances are only on the order of  $\mu\text{m}$ .

For magnonic devices to compete with conventional electronics, they must be CMOS-compatible, scalable into the nanometer range and accordingly use spin-waves with wavelengths in the same range. This requires the development of materials and microstructures in which such spin-waves can propagate far enough to be of use, as well as integrated

---

<sup>1</sup>For a review on magnonic devices, see [Chu17].

<sup>2</sup>From the wave-particle equivalence picture, a quantized spin-wave is a quasiparticle called a magnon, leading to the name of the field of research.

<sup>3</sup>NiFe alloys studied in spintronics and magnonics usually have one of the following compositions:  $\text{Ni}_{80}\text{Fe}_{20}$  or  $\text{Ni}_{81}\text{Fe}_{19}$ . These alloys are often called permalloy, abbreviated as Py.

<sup>4</sup>There are many different studied CoFeB alloys including  $\text{Co}_{60}\text{Fe}_{20}\text{B}_{20}$ ,  $\text{Co}_{20}\text{Fe}_{40}\text{B}_{20}$ ,  $\text{Co}_{20}\text{Fe}_{60}\text{B}_{20}$ . The Fe-rich alloy used in this work is rather specific to the Spintec laboratory and is referred to as either  $\text{Fe}_{72}\text{Co}_{8}\text{B}_{20}$  or FeCoB here.

methods to generate, interact with, and detect these spin-waves on-chip. Moreover, due to the need for nm-sized devices, the disadvantage of metallic systems with high damping and low propagation length is less important.

Much like phonons, non-coherent magnons spontaneously appear in ferromagnetic materials at non-zero temperature. However, magnonics often involves the study of coherent, non-thermal spin-waves, thus requiring methods for exciting spin-waves with higher energy. The simplest method involves driving an RF current in the GHz range into an antenna near the ferromagnetic material, thereby exciting via the Ørsted field a range of spin-waves dictated by the conductor's geometry [Ols67]. The technique was further refined by using microstructured antennae such as microstrips [Gan75] and coplanar waveguides [Bai03]. Spin torques can also be used to excite spin-waves, though they are not wavevector selective, meaning that they excite a broad range of spin-waves including thermal spin-waves [Dem11]. Coherent spin-wave excitation can be obtained by using a point contact geometry, through which a spin-polarized current is injected into a ferromagnetic layer to generate localized spin-waves [Ji03; Sla05]. Alternatively, by patterning a FM/NM layer (ferromagnetic/normal metal with spin-orbit interaction such as NiFe/Pt) into a nanoconstriction [Dem14; Che16] or other restrictive shapes [Dua14], thereby modifying the local demagnetizing field, SOTs can excite a single spin-wave mode, the so-called localized spin-wave bullet. These are non-propagating spin-waves, and thus of limited interest for spin-wave based logic, though Madami *et al.* observed out-of-plane spin-waves excited locally by STT propagate into the ferromagnetic medium [Mad11]. Novel techniques include femto-second lasers [Iih16] or the use of an RF localized electric field to modify the perpendicular magnetic anisotropy of the CoFeB/MgO interface [Ran17].

Another obstacle for the integration of spin-wave based devices onto CMOS integrated circuits is the detection of the spin-waves themselves. Detection methods include large and expensive *ex situ* equipment such as Brillouin light scattering spectroscopy [Seb15; Dem15] and magneto-optical Kerr effect microscopy [Par02], as well as propagating spin-wave spectroscopy [Bai03]. The first two are laboratory equipments and in no way integrable onto a chip. The last is based on waveguides for the inductive detection of spin-waves, which has its own drawbacks, owing to the fact that the inductive coupling is wavevector-dependent. The reciprocal of the spin Hall effect, called the inverse spin Hall effect (iSHE), has been shown to be able to detect spin-wave dynamics in Pt/NiFe systems [And09] and YIG/Pt [Hah13], and only requires that a metal with high spin-orbit coupling be adjacent to the material in which the spin-waves propagate, making the inverse spin Hall effect a promising detection method for scalable integration.

This thesis addresses the development of scalable CMOS-compatible spin-wave devices by investigating the properties of a spin-wave waveguide based on an ultrathin Ta/FeCoB/MgO wire. The material system was chosen for its compatibility with CMOS processes, the perpendicular anisotropy arising from the FeCoB/MgO interface [Cuc15] and strong spin-orbit interactions in the Ta and at the Ta/FeCoB interface [Cub18]. The purpose of the spin-orbit interactions is twofold: firstly, to allow the manipulation of spin-waves via spin-orbit torques [Dem11], secondly, to allow the detection of magneti-

zation dynamics via the combined effects of spin-pumping and the iSHE [And09]. For the excitation of spin-waves, we designed nanometric coplanar waveguides on top of the SWWs capable of exciting a large range of non-zero wavevectors. This thesis is organized as follows:

The first chapter gives an overview of the theory needed to understand the experiments described in this thesis. The different energy contributions present in a magnetic system are introduced, and the Landau-Lifshitz equation, which governs magnetization dynamics, is given. Subsequently, we calculate the susceptibility tensor for a variety of systems, successively adding terms such as the shape anisotropy, perpendicular magnetic anisotropy, and damping. Similarly, we introduce spin-waves and give the frequency-wavevector dispersion relation for several systems. The last section concerns spin-orbit interactions such as the Rashba effect and the spin Hall effect, which can interact with the magnetization dynamics via the field-like torque and the damping-like torque; as well as the inverse spin Hall effect and anisotropic magnetoresistance, which can be used to detect magnetization dynamics.

In the second chapter we briefly describe the cleanroom fabrication process of the spin-wave waveguides and the coplanar waveguides, and give a detailed description of the devices.

The third chapter concerns ST-FMR experiments. We derive the rectified voltages that may arise from the different potential sources of rectification and then determine magnetic properties of Ta/FeCoB/MgO as a function of the FeCoB thickness. Doing so, we identify the ferromagnetic layer thickness for which the magnetization transitions from in-plane to out-of-plane, and focus on devices with a thickness around and at the transition. Subsequently, by performing a DC current-dependent study, we characterize the field-like and damping-like torques as a function of the ferromagnetic thickness as well.

The fourth chapter deals with the excitation of spin-waves and their detection via the inverse spin Hall effect. First we give the expected spin-wave spectrum excited by an RF current injected in nanometric coplanar waveguides, taking into account the perpendicular magnetic anisotropy and the non-zero linewidth of the spin-waves. We then perform SWR spectroscopy. Similarly to ST-FMR, the spin-wave dynamics leads to a rectified signal that can be detected electrically via the iSHE. Afterwards we compare these results to Brillouin light scattering microscopy performed on the same type of devices. The BLS experiments also allow us to characterize the spin-wave decay length and lifetime in systems with perpendicular magnetic anisotropy.

Finally, a brief summary of the findings is presented at the end of this thesis, and a perspective for scalable, integrated magnonics-spin-orbitronics is given.



# Chapter 1

## Theoretical Background

This chapter gives an overview of the theoretical background necessary to understand the experimental studies presented in this thesis. In order to characterize the spin-orbit torques' effects in Ta/FeCoB/MgO structures, we excite ferromagnetic resonance and spin-waves via a high frequency Ørsted field or spin-orbit torque, and we detect the magnetization dynamics by the combined effects of spin-pumping and the inverse spin Hall effect.

Therefore, in this chapter we introduce the underlying physical phenomena of magnetization dynamics, spin-orbit torques, spin-pumping, and the inverse spin Hall effect. For the magnetization dynamics, we present the different energies that arise in a ferromagnetic system, and how they contribute to the equilibrium magnetization. Next, we provide the equation that governs the dynamics of the magnetization, and from it, derive the Polder susceptibility tensor, which gives the uniform magnetization's response to a high frequency excitation. This is done for several cases, from the infinite ferromagnet to the thin film with perpendicular anisotropy. We then address the formalism for non-uniform magnetization dynamics, known as spin-waves, and derive the linear spin-wave dispersion relation for several ferromagnetic systems. Next, we present the spin-orbit phenomena that allow the control of the magnetization dynamics, specifically the Rashba effect and the spin Hall effect, and the two torques that arise: the field-like torque and the damping-like torque. We also discuss the inverse spin Hall effect, which, coupled with spin-pumping, is used for the detection of magnetization dynamics in the devices studied in my thesis. The final subsection deals with anisotropic magnetoresistance, a further spin-orbit effect present in ferromagnetic materials that can also be used for probing the magnetization's state.

### 1.1 Energy contributions in a thin film ferromagnetic system

The internal energy of a ferromagnetic system such as the Ta/FeCoB/MgO system considered in this work is, among others, the sum of the exchange energy, the Zeeman

energy, the magnetocrystalline anisotropy energy and the dipolar energy of the ferromagnetic material. In this section we describe each energy involved and their origin for a ferromagnetic material. The case of the ferromagnetic thin film, where the thickness is in the nanometer range and the lateral dimensions are several orders of magnitude larger, will be considered.

### 1.1.1 The exchange energy

The exchange interaction is a purely quantum mechanical effect which arises as a consequence of the Pauli exclusion principle and the fact that electrons are indistinguishable in a solid. It is responsible for the spontaneous ordering of spins within ferromagnetic and antiferromagnetic materials. The Heisenberg model [Hei28], a derivation of which can be found in English in [Stö06], describes the exchange energy between an atom  $j$  with spin  $\mathbf{S}_j$  and all other atoms  $i$  with spin  $\mathbf{S}_i$  in a crystal. A simplified form consists of considering only the nearest neighbors' interaction (symbolized by  $nn$  in the equation) in the summation [OHa99]:

$$E_{ex,j} = -2 \sum_{i < j}^{nn} J_{ij} \mathbf{S}_i \cdot \mathbf{S}_j \quad (1.1)$$

where  $J_{ij}$ , expressed in units of Joules, is the exchange constant for the considered spins. It is positive for ferromagnets (favoring parallel alignment of spins) and negative for antiferromagnets (favoring anti-parallel alignment). The exchange interaction is stronger than any other interaction considered in this section, but its range is very small, such that one can simply consider the interaction between an atom  $j$  and only its nearest neighbors. In the continuum approach, one can derive an expression of the energy for continuous media [OHa99], yielding an exchange energy for the local magnetization  $\mathbf{M}(\mathbf{r})$  at the coordinate  $\mathbf{r}$  that is written:

$$E_{ex} = \int_V \frac{A_{ex}}{M_s^2} \left( \left( \frac{\partial \mathbf{M}(\mathbf{r})}{\partial x} \right)^2 + \left( \frac{\partial \mathbf{M}(\mathbf{r})}{\partial y} \right)^2 + \left( \frac{\partial \mathbf{M}(\mathbf{r})}{\partial z} \right)^2 \right) d^3r \quad (1.2)$$

where  $M_s = |\mathbf{M}|$  is the saturation magnetization of the considered magnetic material (in  $\text{A m}^{-1}$ ) and  $A_{ex}$  is the exchange stiffness constant (in  $\text{J m}^{-1}$ ), which is a macroscopic measure of the stiffness of coupling of the spins. While the exchange energy is the dominant term for magnetic ordering at the atomic scale, it is too short-ranged to be responsible for the formation of magnetic domains or hysteretic behavior. For a uniform magnetization, the exchange energy is minimal and the exchange interaction doesn't appear in magnetostatics or magnetization dynamics. However, it can have a significant role in the boundary between two magnetic domains, called domain walls; and the propagation of perturbations in the magnetic ordering, called spin-waves; in both cases, the magnetization deviates from a uniform parallel alignment.

### 1.1.2 The dipolar energy

The dipolar energy, also called magnetostatic or demagnetizing energy, arises from the dipole-dipole interaction between magnetic moments. In contrast to the exchange interaction, the dipolar interaction is weak but long-ranged, such that for finite systems its analytical calculation is complex and its computation in micromagnetic simulations time-consuming. The magnetic field created by a magnetic dipole  $\boldsymbol{\mu}_j$  at a position  $\mathbf{r}$  is:

$$\mathbf{H}_j(\mathbf{r}) = \frac{1}{4\pi} \left( \frac{3\mathbf{r}(\mathbf{r} \cdot \boldsymbol{\mu}_j)}{r^5} - \frac{\boldsymbol{\mu}_j}{r^3} \right) \quad (1.3)$$

where  $r = |\mathbf{r}|$ . The dipolar energy is the sum of the energy arising from the dipolar interaction between all of the moments. For an infinite magnetic medium, these interactions cancel each other out if the magnetization is uniform. For finite solids, the magnetic moments do not compensate each other at the boundary surfaces, resulting in dipolar fields. Inside the ferromagnet, these are referred to as demagnetizing fields, while outside of it they are called stray fields.

Accounting for all the magnetic moments in a solid, the volumetric energy of the dipolar field  $\mathbf{H}_d$  is given by [Mor01]:

$$\frac{E_d}{V} = -\frac{\mu_0}{2V} \int_V \mathbf{H}_d(\mathbf{r}) \cdot \mathbf{M}(\mathbf{r}) d^3r = \frac{\mu_0}{2V} \int_\infty \mathbf{H}_d^2(\mathbf{r}) d^3r \quad (1.4)$$

where  $V$  is the volume of the ferromagnetic solid and  $\mu_0$  is the vacuum permeability.<sup>1</sup> The first expression indicates that the energy is localized in the magnetic volume. However the equivalent second expression is obtained by considering the energy of the dipolar field created by the ferromagnet, distributed throughout space [Mor01]. It shows that the dipolar energy is always positive and that the greater the stray fields, the greater the energy, which is unfavorable. As a consequence, in ferromagnets where the dipolar interaction is dominant, the magnetization at the edges of a solid will favor aligning parallel to the edges, minimizing the stray fields. In the case of a thin rectangular wire, the magnetization will tend to align with in-plane and parallel to the long axis of the rectangle. This behavior of the magnetization, which favors a particular direction in the solid to minimize the dipolar energy, is referred to as shape anisotropy, and can result in the hysteretic behavior of ferromagnets. On the other hand, for an infinite ferromagnetic medium, there is no shape and thus no shape anisotropy.

In the case of a uniform magnetization  $\mathbf{M}$ , the expression of the dipolar energy density can be simplified to:

$$e_d = \frac{\mu_0}{2} \mathbf{M}^T \cdot \overline{\overline{N}} \cdot \mathbf{M} \quad (1.5)$$

where  $\mathbf{M}^T$  is the transpose of the magnetization vector and  $\overline{\overline{N}}$  is the demagnetizing tensor, a set of parameters dependent on the geometry of the magnetic volume. Its expression can be found in [New93]. However its analytical calculation is non-trivial

---

<sup>1</sup> $\mu_0 = 4\pi \times 10^{-7} \text{ T m A}^{-1} \approx 1.2566 \times 10^{-6} \text{ T m A}^{-1}$ .

for many geometries, such that developing efficient and accurate approximations is a concern for micromagnetic simulations. The tensor can be diagonalized, and it can be shown that its trace is equal to one [New93]. For a thin film with a uniform magnetization and lateral dimensions much greater than the thickness, a sufficient approximation for the demagnetizing tensor is to consider only one non-zero coefficient,  $N_{xx} = 1$ , with  $\hat{\mathbf{x}}$  the growth direction of the thin film, perpendicular to the thin film plane (see Fig. 1.1). The demagnetization energy density becomes:

$$e_d = \frac{\mu_0}{2} (\mathbf{M} \cdot \hat{\mathbf{x}})^2 \quad (1.6)$$

Thus, the dipolar energy in thin films is minimized when the magnetization lies in the thin film plane. Formulas and tables for demagnetizing tensor components have been calculated for different geometries, such as ellipsoids [Os45], cylinders [Boz42] and slabs [Jos65].

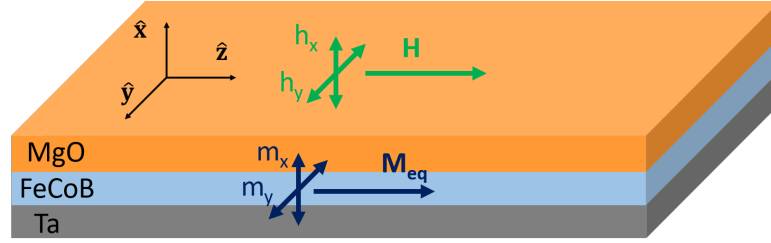


Figure 1.1: Coordinate system for describing resonance in a Ta/FeCoB/MgO spin-wave waveguide. The  $\hat{\mathbf{x}}$  axis is perpendicular to the film plane and the  $\hat{\mathbf{z}}$  axis is parallel to the external magnetic field  $\mathbf{H}$ . The magnetization is saturated by the field and its equilibrium magnetization  $\mathbf{M}_{\text{eq}}$  is also parallel to  $\hat{\mathbf{z}}$ .

### 1.1.3 Magnetocrystalline anisotropy energy

In crystalline ferromagnetic media, an energy contribution appears due to electron orbitals coupling with the lattice and with the spin moments, the magnetocrystalline anisotropy energy. This gives rise to preferential magnetization directions that are often along crystalline axes and contribute to the hysteretic behavior of ferromagnets. In materials such as hcp (0001) Co [Heh96], there is one preferential direction called the easy axis, and the anisotropy is called magnetocrystalline uniaxial anisotropy. The energy density for a magnetization  $\mathbf{M}$  is:

$$e_{mc} = K_u \left( 1 - \left( \frac{\mathbf{M}}{M_s} \cdot \hat{\mathbf{k}} \right)^2 \right) \quad (1.7)$$

where  $K_u$  is the uniaxial anisotropy constant (in  $\text{J m}^{-3}$ ), and  $\hat{\mathbf{k}}$  is the direction of the easy axis.

The material system used in this work is a thin film stack deposited on a silicon wafer by magnetron sputtering, starting from the silicon substrate: Ta, Fe<sub>72</sub>Co<sub>8</sub>B<sub>20</sub> (hereafter referred to as FeCoB) and Mg. The sample is then oxidized and annealed. As a result, the material is polycrystalline in nature, but the distribution of the crystalline orientations is not random, instead the grains show a preferential growth direction. Such a material is said to be textured [Tak07], but the resulting magnetocrystalline uniaxial anisotropy is negligible in such materials.

However another source of magnetocrystalline anisotropy can appear in such a material system. The electronic environment of the atoms at the interface of the ferromagnetic layer has reduced symmetry compared to those in the volume which modifies the atomic orbitals and can lead to a magnetic anisotropy perpendicular to the plane. In the presence of a metallic oxide such as MgO the perpendicular anisotropy is further increased, which is attributed to the hybridization of oxygen and transition metal orbitals [Yan11]. Experimentally, the anisotropy can be tuned by the oxidation and annealing conditions [Mon02; Rod09]. Both phenomena occur at the interface between FeCoB and MgO, giving rise to a magnetocrystalline anisotropy that favors a magnetization along the growth axis. It is called perpendicular magnetic anisotropy (PMA), surface anisotropy or interfacial anisotropy. For a ferromagnetic thin film with a uniform magnetization  $\mathbf{M}$ , the energy density of PMA for a ferromagnetic layer of thickness  $t_f$  is:

$$e_{mc} = \frac{K_i}{t_f} \left( 1 - \left( \frac{\mathbf{M}}{M_s} \cdot \hat{\mathbf{x}} \right)^2 \right) \quad (1.8)$$

where  $\hat{\mathbf{x}}$  is the growth axis and the normal to the interface and  $K_i$  is the interfacial anisotropy constant for the ferromagnet/oxide interface (in J m<sup>-2</sup>). The PMA energy is minimum when the magnetization is either parallel or anti-parallel to the growth axis. Due to the thickness dependence, the anisotropy can be extremely high for thin films in the nanometer range, such that it overcomes the demagnetization energy and reorients the magnetization perpendicular.

#### 1.1.4 The Zeeman energy

The Zeeman energy is the potential energy of a ferromagnetic solid subjected to an external magnetic field. The moments in the solid will tend to align with the field to minimize the energy. For a magnetization  $\mathbf{M}$  in a field  $\mathbf{H}$ , the energy density is:

$$e_Z = -\mu_0 \mathbf{M} \cdot \mathbf{H} \quad (1.9)$$

It is minimum when the magnetization is aligned parallel with the field. In contrast to the interactions in previous sections, the Zeeman energy favors a single direction for the magnetization for ferromagnetic materials. In the work presented here, the static external field is always in the plane of the thin film.

### 1.1.5 Energy minimization

The ferromagnetic system reaches an equilibrium state when the energy is minimized. The mechanisms of how this equilibrium is reached is described in Sec. 1.2.1. The total internal energy density  $e$  is the sum of the energy densities seen in the previous sections:

$$e = e_{ex} + e_d + e_{mc} + e_Z \quad (1.10)$$

As the interactions responsible for these energies compete with each other, the equilibrium state can be a state where none of the energies are individually minimized. It is represented by the magnetization  $\mathbf{M}$ , which can be uniform, split into domains, or present complex structures such as vortices.

For thin films, materials can be referred to as in-plane magnetized, i.e., the magnetization lies in the plane in the absence of an external field, or as out-of-plane, i.e., the equilibrium position is normal to the plane; there are also cases where the magnetization is oriented in an intermediate direction. When the magnetic system has PMA, there is a critical thickness  $t_c$ , defined further below, where the magnetization reorients from the in-plane to the out-of-plane direction

### 1.1.6 The effective field

To include the different interactions described in the previous section into an equation describing the dynamics of the magnetization, it is useful to express the interactions in the form of an effective field. For each energy density  $e_i$  defined above, where  $i = \{ex, d, mc, Z\}$ , one can define the corresponding effective field  $\mathbf{H}_{\text{eff}}^i$ :

$$\mathbf{H}_{\text{eff}}^i = -\frac{1}{\mu_0} \begin{pmatrix} \frac{\partial e_i}{\partial M_x} \\ \frac{\partial e_i}{\partial M_y} \\ \frac{\partial e_i}{\partial M_z} \end{pmatrix} = -\frac{1}{\mu_0} \frac{\partial e_i}{\partial \mathbf{M}} \quad (1.11)$$

$$\mathbf{H}_{\text{eff}} = \sum_i \mathbf{H}_{\text{eff}}^i = -\frac{1}{\mu_0} \frac{\partial e}{\partial \mathbf{M}}$$

The total effective field  $\mathbf{H}_{\text{eff}}$  is the local field felt by the magnetization, the field along which the magnetization will align if there is damping, through mechanisms detailed in the next section. The effective fields for the interactions described in the previous sections, assuming the presence of interfacial anisotropy, are:

$$\mathbf{H}_{\text{eff}} = \frac{2A_{ex}}{\mu_0 M_s^2} \nabla^2 \mathbf{M}(\mathbf{r}) + \mathbf{M}(\mathbf{r}) \cdot \hat{\mathbf{x}} \left( \frac{2K_i}{\mu_0 M_s^2 t_f} - 1 \right) \hat{\mathbf{x}} + \mathbf{H} \quad (1.12)$$

where  $\nabla^2$  is the vector Laplace operator, which, in Cartesian coordinates, is written for  $\mathbf{M}(\mathbf{r})$ :

$$\nabla^2 \mathbf{M}(\mathbf{r}) = \begin{pmatrix} \nabla^2 M_x(\mathbf{r}) \\ \nabla^2 M_y(\mathbf{r}) \\ \nabla^2 M_z(\mathbf{r}) \end{pmatrix} \quad (1.13)$$

The right side of Eq. (1.12) contains the exchange field, the anisotropy field, the demagnetizing field and the external field. In the case of a uniform magnetization, the exchange field is zero. The demagnetizing and interfacial anisotropy fields depend on the same component of the magnetization and directly compete with each other: the former brings the magnetization into the plane, while the latter tries to pull it out of the plane. It is often useful to define an effective magnetization that sums up their effect:

$$M_{eff} = M_s - \frac{2K_i}{\mu_0 M_s t_f} \quad (1.14)$$

Thus, the sign of the effective magnetization gives the defining behavior of the material in the absence of an external field: in-plane ferromagnetic thin films have  $M_{eff} > 0$  while out-of-plane ferromagnetic thin films have  $M_{eff} < 0$ , and  $M_{eff} = 0$  defines the critical thickness  $t_c$  of the reorientation from in- to out-of-plane, given by:

$$t_c = \frac{2K_i}{\mu_0 M_s^2} \quad (1.15)$$

## 1.2 Uniform magnetization dynamics

### 1.2.1 Equations of motion of the magnetization

Now that we have defined the effective field, we can describe the behavior of the magnetization when it experiences small perturbations. The equation of motion of the magnetization in response to a perturbation is given by the effective field  $\mathbf{H}_{eff}$ :

$$\frac{d\mathbf{M}}{dt} = -\gamma\mu_0\mathbf{M} \times \mathbf{H}_{eff} \quad (1.16)$$

where  $\gamma$  is the gyromagnetic ratio defined by:

$$\begin{aligned} \gamma &= \frac{|e|g}{2m_e} = 1.84 \times 10^{11} \text{ rad s}^{-1} \text{ T}^{-1} \\ \gamma' &= \frac{\gamma}{2\pi} = 29.25 \text{ GHz T}^{-1} \end{aligned} \quad (1.17)$$

where  $e$  and  $m_e$  are the electron's charge (in Coulomb) and its mass (in kg), and  $g$  is the unitless Landé g-factor.<sup>2</sup> Eq. (1.16), which is also called the lossless Landau-Lifshitz equation, describes the precessional motion of the magnetization around the effective field at an angular frequency  $\gamma\mu_0 H_{eff}$ . Additionally, since the effective field depends on the magnetization, the field's direction and magnitude can change as the magnetization precesses around it.

Eq. (1.16) does not accurately describe the magnetization dynamics because it describes only the precession of the magnetization around its equilibrium but not the losses

---

<sup>2</sup>The value used in this work is the value found for bulk Fe  $g = 2.09$  found in [Dev13].

that are needed to bring the magnetization back to its equilibrium parallel to the effective field. Experimentally, applying a magnetic field on a ferromagnet will result in the magnetization taking a damped, swirling trajectory around the field, until it is aligned parallel to it. Phenomenologically, this can be described by the ansatz used by Landau and Lifshitz [Lan35], in what is now referred to as the Landau-Lifshitz (LL) equation:

$$\frac{d\mathbf{M}}{dt} = -\gamma\mu_0\mathbf{M} \times \mathbf{H}_{\text{eff}} - \frac{\alpha'\gamma\mu_0}{M_s} (\mathbf{M} \times (\mathbf{M} \times \mathbf{H}_{\text{eff}})) \quad (1.18)$$

where the last term describes a dissipative torque that leads to the magnetization aligning parallel with the field, with  $\alpha'$  being a dimensionless damping parameter. The damped precessional motion is illustrated in Fig. 1.2.

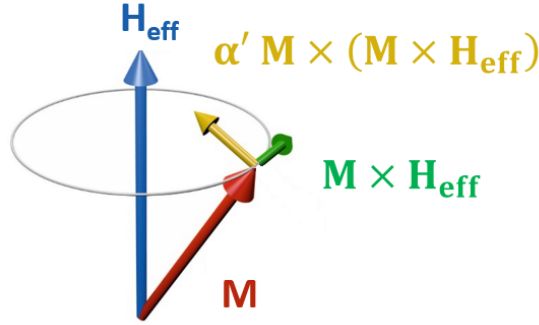


Figure 1.2: Motion of the magnetization  $\mathbf{M}$  due to an effective field  $\mathbf{H}_{\text{eff}}$  in the presence of damping. The precessional term (green) makes the magnetization turn around the effective field while the damping term (yellow) reduces the angle of the cone of precession until the magnetization is aligned with the effective field.

However later experiments by Gilbert and Kelly showed that the LL equation could not adequately predict the high damping factors or times scales of relaxation they measured. The Landau-Lifshitz-Gilbert (LLG) equation was then proposed in 1955 [Gil55] to accurately model materials with high damping:

$$\frac{d\mathbf{M}}{dt} = -\gamma\mu_0\mathbf{M} \times \mathbf{H}_{\text{eff}} + \frac{\alpha}{M_s} \left( \mathbf{M} \times \frac{d\mathbf{M}}{dt} \right) \quad (1.19)$$

It is possible to transform the LLG into an equation of the same form as the LL by injecting the expression of  $\frac{d\mathbf{M}}{dt}$  back into the LLG itself:

$$\frac{d\mathbf{M}}{dt} = -\frac{\gamma\mu_0}{1+\alpha^2}\mathbf{M} \times \mathbf{H}_{\text{eff}} - \frac{\alpha'\gamma\mu_0}{M_s(1+\alpha'^2)} (\mathbf{M} \times (\mathbf{M} \times \mathbf{H}_{\text{eff}})) \quad (1.20)$$

The subtle difference between the two equations and the two dampings is a long standing debate in the literature. However, even for rather large damping  $\alpha = 0.1$ , we only have  $1 + \alpha^2 \approx 1.01$ . Thus, in the analytical calculations described in this work, this factor

will be neglected and we will consider the LL and the LLG equations to be equivalent, and the damping parameters equal  $\alpha = \alpha'$ . In simulations, it is advantageous to use the LL equation or the LLG equation as written in Eq. (1.20) since the time derivative of the magnetization appears only on the left side of the equation, allowing for algorithms to solve the differential equation such as the predictor-corrector method used in the OOMMF micromagnetic simulation program.<sup>3</sup>

### Dissipation mechanisms

The dissipation of angular momentum in magnetization dynamics can have intrinsic [Hic09] and extrinsic origins. The latter includes impurities [Nem11], two-magnon scattering [Hei85; Lin03] and spin pumping [Tse02a]. It was initially assumed in this work that there are only damping processes of the viscous or Gilbert-type, such that it can be described by  $\alpha$  in the LL or LLG equations. However, in Sec. 3.4.4, we present signatures of non-Gilbert-type damping for the system studied here, Ta/FeCoB/MgO, related to inhomogeneities.

#### 1.2.2 Polder susceptibility tensor

The Polder susceptibility tensor  $\bar{\chi}$  describes the dynamic response of the magnetization of a ferromagnetic system to an external alternating field. The susceptibility is defined by the following relation:

$$\mathbf{M} = \bar{\chi} \mathbf{h} \quad (1.21)$$

where  $\mathbf{h}$  is the excitation RF magnetic field. In the following section, the susceptibility tensor will be calculated for different geometrical and material considerations.

#### 1.2.3 Susceptibility for an infinite ferromagnetic medium

Let us linearize the lossless equation of motion Eq. (1.16) by evaluating small-angle displacements of the magnetization  $\mathbf{M}$  of an unbounded ferromagnet under the effect of a static external magnetic field  $\mathbf{H}$  applied along  $\hat{\mathbf{z}}$ . Since the ferromagnet is infinite, and the magnetization is considered uniform, there is no demagnetizing field and no interfacial anisotropy. The magnetization at equilibrium  $\mathbf{M}_{\text{eq}}$  is saturated and is aligned with  $\mathbf{H}$ . If we now consider that the magnetization is slightly tilted out of equilibrium, and apply a time dependent magnetic field  $\mathbf{h}$  in the  $xy$  plane, then the magnetization will precess around the applied field and we can write:

$$\begin{aligned} \mathbf{M} &= \mathbf{M}_{\text{eq}} + \mathbf{m} \\ \mathbf{H}_{\text{eff}} &= \mathbf{H} + \mathbf{h} \end{aligned} \quad (1.22)$$

where  $h \ll H$  and  $m \ll M_{\text{eq}}$ , such that  $M_{\text{eq}} \approx M_s$ . The term  $\mathbf{m}$  is the dynamic component of the magnetization that rotates in the  $xy$  plane around the applied field  $\mathbf{H}$ ,

---

<sup>3</sup>The Object Oriented MicroMagnetic Framework (OOMMF) project at IITL/NIST. For more information, see: <https://math.nist.gov/oommf/>.

while  $\mathbf{M}_{\text{eq}}$  is constant. Similarly,  $\mathbf{H}_{\text{eff}}$  is split into the static field  $\mathbf{H}$  and the dynamic field  $\mathbf{h}$ . Substituting Eqs. (1.22) into Eq. (1.16), we obtain:

$$\frac{d\mathbf{M}}{dt} = -\gamma\mu_0 (\mathbf{M}_{\text{eq}} \times \mathbf{H} + \mathbf{M}_{\text{eq}} \times \mathbf{h} + \mathbf{m} \times \mathbf{H} + \mathbf{m} \times \mathbf{h}) \quad (1.23)$$

Since the magnetization at equilibrium is considered to be aligned with the static field, the first term on the right side is zero, and the last term is of second order and therefore neglected. We then obtain the linearized equation of motion for an undamped, infinite, ferromagnetic medium:

$$\frac{d\mathbf{m}}{dt} = -\gamma\mu_0 (\mathbf{M}_{\text{eq}} \times \mathbf{h} + \mathbf{m} \times \mathbf{H}) \quad (1.24)$$

Assuming that the time dependent field and the dynamic component of the magnetization have the same time dependence  $e^{i\omega t}$ , Eq. (1.24) can be rewritten:

$$i\omega\mathbf{m} = -\hat{\mathbf{z}} \times (\omega_M\mathbf{h} - \omega_H\mathbf{m}) \quad (1.25)$$

where the saturation magnetization and static field are written in terms of angular frequencies:

$$\begin{aligned} \omega_M &= \gamma\mu_0 M_s \\ \omega_H &= \gamma\mu_0 H \end{aligned} \quad (1.26)$$

Assuming that the dynamic components of the magnetization and field along the  $\hat{\mathbf{z}}$  axis are negligible, we solve Eq. (1.25) for  $\mathbf{h}$  in two dimensions:

$$\begin{pmatrix} h_x \\ h_y \end{pmatrix} = \frac{1}{\omega_M} \begin{pmatrix} \omega_H & -i\omega \\ i\omega & \omega_H \end{pmatrix} \begin{pmatrix} m_x \\ m_y \end{pmatrix} \quad (1.27)$$

where  $h_i$  and  $m_i$  are the components of  $\mathbf{h}$  and  $\mathbf{m}$  respectively. The inverse of the Polder susceptibility tensor defined by Eq. (1.21) can be recognized:

$$\mathbf{h} = \overline{\overline{\chi}}^{-1} \mathbf{m} \quad (1.28)$$

where  $\mathbf{M}$  can be substituted by  $\mathbf{m}$  since we are only interested in the dynamic component. Inverting the matrix, we obtain the Polder susceptibility tensor and its components:

$$\overline{\overline{\chi}} = \begin{pmatrix} \chi_{\parallel} & i\chi_{\perp} \\ -i\chi_{\perp} & \chi_{\parallel} \end{pmatrix} \quad \begin{aligned} \chi_{\parallel} &= \frac{\omega_H\omega_M}{\omega_H^2 - \omega^2} \\ \chi_{\perp} &= \frac{\omega\omega_M}{\omega_H^2 - \omega^2} \end{aligned} \quad (1.29)$$

As  $\omega \rightarrow \omega_H$ , the magnetization enters resonance, which is translated by the elements of  $\overline{\overline{\chi}}$  diverging. This frequency is called the ferromagnetic resonance frequency (FMR). In the next sections, the LL equation and the effective field will be modified to take into account additional interactions, yielding different expressions for the components of the susceptibility tensor.

### 1.2.4 Susceptibility for a ferromagnetic thin film

For bounded systems, the dipolar energy is non-zero and adds a term in the effective field that is dependent on the magnetization. For in-plane magnetized thin films with  $\hat{\mathbf{x}}$  normal to the film plane, the total effective field becomes:

$$\mathbf{H}_{\text{eff}} = \mathbf{H} + \mathbf{h} - (\mathbf{m} \cdot \hat{\mathbf{x}}) \hat{\mathbf{x}} \quad (1.30)$$

where the last term is the demagnetization field, and where the static field  $\mathbf{H}$  is still applied along the  $\hat{\mathbf{z}}$  axis and the dynamic field  $\mathbf{h}$  is in the  $xy$  plane. For the demagnetization term, only  $\mathbf{m}$  remains since the magnetization is still saturated and  $\mathbf{M}$  is parallel to  $\hat{\mathbf{z}}$ . Injecting the above into Eq. (1.16) and once again neglecting the products of second order, we obtain:

$$\begin{pmatrix} h_x \\ h_y \end{pmatrix} = \frac{1}{\omega_M} \begin{pmatrix} \omega_H + \omega_M & -i\omega \\ i\omega & \omega_H \end{pmatrix} \begin{pmatrix} m_x \\ m_y \end{pmatrix} \quad (1.31)$$

Inverting Eq. (1.31) yields the susceptibility components:

$$\bar{\chi} = \begin{pmatrix} \chi_{xx} & i\chi_{xy} \\ -i\chi_{xy} & \chi_{yy} \end{pmatrix} \quad \begin{aligned} \chi_{xx} &= \frac{\omega_H \omega_M}{\omega_0^2 - \omega^2} \\ \chi_{xy} &= \frac{\omega \omega_M}{\omega_0^2 - \omega^2} \\ \chi_{yy} &= \frac{\omega_M (\omega_H + \omega_M)}{\omega_0^2 - \omega^2} \end{aligned} \quad (1.32)$$

where:

$$\omega_0^2 = \omega_H (\omega_H + \omega_M) \quad (1.33)$$

is the square of the ferromagnetic resonance angular frequency for the thin film. The equation for the FMR frequency  $\omega_0$  of a ferromagnet is known as the Kittel formula; a number of geometric configurations can be found in [Kit48]. Compared to the bulk, the thin film reduces the symmetry of the system, which results in the diagonal components of the tensor being no longer equal.

#### With interfacial anisotropy

As seen in Sec. 1.1.6, interfacial anisotropy directly competes with the dipolar interaction in thin film stacks. The effective field becomes:

$$\mathbf{H}_{\text{eff}} = \mathbf{H} + \mathbf{h} + (\mathbf{m} \cdot \hat{\mathbf{x}}) \left( \frac{2K_i}{\mu_0 M_s^2 t_f} - 1 \right) \hat{\mathbf{x}} \quad (1.34)$$

In the case of in-plane magnetized samples, the equilibrium magnetization will align with the static field. However for out-of-plane magnetized samples, the static field must be strong enough so that  $\mathbf{M}_{\text{eq}}$  becomes aligned with  $\mathbf{H}$  in the plane, so that the derivation of the susceptibility in the previous sections is still valid. Injecting the equation above into Eq. (1.16) and solving for  $\mathbf{h}$  yields:

$$\begin{pmatrix} h_x \\ h_y \end{pmatrix} = \frac{1}{\omega_M} \begin{pmatrix} \omega_H + \omega_M - \omega_K & -i\omega \\ i\omega & \omega_H \end{pmatrix} \begin{pmatrix} m_x \\ m_y \end{pmatrix} \quad (1.35)$$

The components of the Polder tensor are then:

$$\begin{aligned}\chi_{xx} &= \frac{\omega_H \omega_M}{\omega_0^2 - \omega^2} \\ \chi_{xy} &= \frac{\omega \omega_M}{\omega_0^2 - \omega^2} \\ \chi_{yy} &= \frac{\omega_M (\omega_H + \omega_M - \omega_K)}{\omega_0^2 - \omega^2}\end{aligned}\tag{1.36}$$

where the anisotropy field is expressed in terms of angular frequency:

$$\omega_K = \gamma \frac{2K_i}{M_s t_f}\tag{1.37}$$

and the resonance frequency is defined by:

$$\omega_0^2 = \omega_H (\omega_H + \omega_M - \omega_K)\tag{1.38}$$

Thus the interfacial anisotropy introduces a thickness dependence, and for a given applied field, reduces the resonance frequency. The dependence of the resonance frequency on  $\omega_M - \omega_K = \mu_0 \gamma M_{eff}$  makes it impossible to disentangle the contribution of the demagnetizing field and of the anisotropy field from a single FMR experiment for a fixed ferromagnetic layer thickness. Only the effective magnetization  $M_{eff}$  can be obtained from a single measurement. To disentangle  $K_i$  and  $M_s$  it is necessary to do a thickness dependent study as will be shown in Chap. 3.

### With damping

The equation of motion used so far in this section to describe the magnetization dynamics does not take into account the dissipation of angular momentum. The LLG equation provides a convenient way of deriving the susceptibility in lossy ferromagnetic media. Rewriting Eq. (1.19) using the same separation of static and dynamic components as in Eq. (1.23), and neglecting products of second order, we obtain:

$$\frac{d\mathbf{m}}{dt} = -\gamma \mu_0 (\mathbf{M}_{\mathbf{eq}} \times \mathbf{h} + \mathbf{m} \times \mathbf{H}) + \frac{\alpha}{M_s} \left( (\mathbf{M}_{\mathbf{eq}} + \mathbf{m}) \times \frac{d\mathbf{m}}{dt} \right)\tag{1.39}$$

Assuming the same time dependence  $e^{i\omega t}$  for the applied dynamic field and the dynamic magnetizations, we can write:

$$\begin{aligned}i\omega \mathbf{m} &= -\hat{\mathbf{z}} \times (\omega_M \mathbf{h} - \omega_H \mathbf{m}) + \frac{\alpha}{M_s} ((\mathbf{M}_{\mathbf{eq}} + \mathbf{m}) \times i\omega \mathbf{m}) \\ &\approx -\hat{\mathbf{z}} \times (\omega_M \mathbf{h} - (\omega_H + i\alpha\omega) \mathbf{m})\end{aligned}\tag{1.40}$$

Thus, including the damping term is equivalent to making the substitution  $\omega_H \rightarrow \omega_H + i\alpha\omega$ . For a thin film including a demagnetizing field, without interfacial anisotropy, the

Polder susceptibility tensor's components are:

$$\begin{aligned}\chi_{xx} &= \frac{\omega_M \omega_H}{\omega_0^2 - \omega^2 + i\alpha\omega(\omega_M + 2\omega_H)} \\ \chi_{xy} &= \frac{\omega\omega_M}{\omega_0^2 - \omega^2 + i\alpha\omega(\omega_M + 2\omega_H)} \\ \chi_{yy} &= \frac{\omega_M(\omega_M + \omega_H)}{\omega_0^2 - \omega^2 + i\alpha\omega(\omega_M + 2\omega_H)}\end{aligned}\quad (1.41)$$

where the resonance frequency is defined by:

$$\omega_0^2 = \omega_H(\omega_H + \omega_M) \quad (1.42)$$

The term  $i\alpha\omega$  in the numerators of  $\chi_{xx}$  and  $\chi_{yy}$  in Eq. (1.41) and the term  $\alpha^2\omega^2$  in the denominators are neglected. Indeed, the inclusion of these terms in the susceptibilities changes the resonance frequency, amplitude and linewidth by less than 1%.<sup>4</sup> The term in  $i\alpha\omega$  in the denominators removes the singularity, resulting in finite amplitude and a non-zero linewidth of the resonance that is proportional to the damping constant  $\alpha$ .

### 1.2.5 Lineshape of the susceptibilities

The susceptibility components  $\chi_{kl}$  can be separated into their real and imaginary parts, as described in [Har16]:

$$\chi_{kl} = (D + iL)A_{kl} \quad (1.43)$$

where  $D$ ,  $L$  and  $A_{kl}$  are real.  $D$  represents the real, antisymmetric, dispersive line shape component of the susceptibility, whereas  $L$  represents the imaginary, symmetric, Lorentzian line shape. When detecting the magnetization dynamics during an FMR experiment using a current flowing through the device, the electrical signal of ferromagnetic resonance can have several origins [Jur60], such as anisotropic magnetoresistance [Liu11], anomalous Hall effect [Yam09] or spin pumping combined with the inverse spin Hall effect [And08]. Each mechanism couples differently with the components of the susceptibility. Thus separating the susceptibility into its real and imaginary components, or antisymmetric and symmetric components, can help understand where the FMR signal is coming from.

First let us express the susceptibility components for a lossy thin film with interfacial anisotropy by taking Eq. (1.36) and making the substitution  $\omega_H \rightarrow \omega_H + i\alpha\omega$  to introduce damping:

$$\begin{aligned}\chi_{xx} &= \frac{\omega_H \omega_M}{\omega_0^2 - \omega^2 + i\alpha\omega(\omega_M - \omega_K + 2\omega_H)} \\ \chi_{xy} &= \frac{\omega\omega_M}{\omega_0^2 - \omega^2 + i\alpha\omega(\omega_M - \omega_K + 2\omega_H)} \\ \chi_{yy} &= \frac{\omega_M(\omega_H + \omega_M - \omega_K)}{\omega_0^2 - \omega^2 + i\alpha\omega(\omega_M - \omega_K + 2\omega_H)}\end{aligned}\quad (1.44)$$

---

<sup>4</sup>Numerical verification using  $M_s = 1.256 \text{ MA m}^{-1}$ ,  $\alpha = 0.02$  and  $H = 7.18 \text{ kA m}^{-1}$ .

where the resonance frequency  $\omega_0$  is still defined by Eq. (1.38). As mentioned in the previous section, we neglect the  $i\alpha\omega$  term in the numerators and the  $\alpha^2\omega^2$  term in the denominators.

Eqs. (1.44) are written as functions of angular frequencies, and thus correspond to finding the resonance peak by sweeping the frequency. However, in many experiments, including most of the ones described in this work, the resonance peak, characterized by its resonance field  $H_r$ , is found by sweeping the applied field  $H$  for a fixed frequency  $\omega$ . Therefore it is more convenient to express the susceptibility components as functions of fields. This can be done by using Eq. (1.38) to replace  $\omega_0$ . Using the same equation, we can write  $\omega$  as a function of the resonance field  $H_r$  corresponding to it:

$$\left(\frac{\omega}{\gamma\mu_0}\right)^2 = H_r(H_r + M_{eff}) \quad (1.45)$$

Thus, using Eqs. (1.38) and (1.45) (as well as Eqs. (1.26) and (1.37)), we rewrite Eq. (1.44):

$$\begin{aligned} \chi_{xx} &= \frac{M_s H}{(H - H_r)(H + H_r + M_{eff}) + i\frac{\alpha\omega}{\gamma\mu_0}(M_{eff} + 2H)} \\ \chi_{xy} &= \frac{\frac{\omega}{\gamma\mu_0} M_s}{(H - H_r)(H + H_r + M_{eff}) + i\frac{\alpha\omega}{\gamma\mu_0}(M_{eff} + 2H)} \\ \chi_{yy} &= \frac{M_s(M_{eff} + H)}{(H - H_r)(H + H_r + M_{eff}) + i\frac{\alpha\omega}{\gamma\mu_0}(M_{eff} + 2H)} \end{aligned} \quad (1.46)$$

where  $M_{eff}$  is defined in Eq. (1.14). Then, we can separate the real and imaginary parts:

$$\begin{aligned} \chi_{xx} &= \frac{M_s H}{H + H_r + M_{eff}} \frac{(H - H_r) - i\frac{\alpha\omega}{\gamma\mu_0} \frac{M_{eff} + 2H}{H + H_r + M_{eff}}}{(H - H_r)^2 + \left(\frac{\alpha\omega}{\gamma\mu_0} \frac{M_{eff} + 2H}{H + H_r + M_{eff}}\right)^2} \\ \chi_{xy} &= \frac{\frac{\omega}{\gamma\mu_0} M_s}{H + H_r + M_{eff}} \frac{(H - H_r) - i\frac{\alpha\omega}{\gamma\mu_0} \frac{M_{eff} + 2H}{H + H_r + M_{eff}}}{(H - H_r)^2 + \left(\frac{\alpha\omega}{\gamma\mu_0} \frac{M_{eff} + 2H}{H + H_r + M_{eff}}\right)^2} \\ \chi_{yy} &= \frac{M_s(M_{eff} + H)}{H + H_r + M_{eff}} \frac{(H - H_r) - i\frac{\alpha\omega}{\gamma\mu_0} \frac{M_{eff} + 2H}{H + H_r + M_{eff}}}{(H - H_r)^2 + \left(\frac{\alpha\omega}{\gamma\mu_0} \frac{M_{eff} + 2H}{H + H_r + M_{eff}}\right)^2} \end{aligned} \quad (1.47)$$

Finally we can separate the susceptibility components into  $D$ ,  $L$  and  $A_{kl}$  via Eq. (1.43), as in [Har16]:

$$\begin{aligned} A_{xx} &= \frac{\gamma\mu_0 M_s H}{\alpha\omega(M_{eff} + 2H)} & L &= \frac{\frac{\Delta H_g^2}{4}}{(H_r - H)^2 + \frac{\Delta H_g^2}{4}} \\ A_{xy} &= \frac{M_s}{\alpha(M_{eff} + 2H)} & D &= \frac{\frac{\Delta H_g}{2}(H_r - H)}{(H_r - H)^2 + \frac{\Delta H_g^2}{4}} \\ A_{yy} &= \frac{\gamma\mu_0 M_s(M_{eff} + H)}{\alpha\omega(M_{eff} + 2H)} \end{aligned} \quad (1.48)$$

where the Lorentzian function  $L$  is defined such it is unitless and its maximum value is equal to 1. The dispersive function  $D$  is defined such that it is unitless.  $H_r$  is the resonance field, obtained by solving Eq. (1.45) for  $H_r > 0$ :

$$H_r = \frac{1}{2} \left( -M_{eff} + \sqrt{M_{eff}^2 + \left( \frac{2\omega}{\gamma\mu_0} \right)^2} \right) \quad (1.49)$$

$\Delta H_g$  is a generalized expression of the linewidth defined from the imaginary part of the nominator of the second quotient of the susceptibility components in Eq. (1.48):

$$\begin{aligned} \Delta H_g &= \frac{2\alpha\omega}{\gamma\mu_0} \left( \frac{M_{eff} + 2H}{H + H_r + M_{eff}} \right) \\ \lim_{H \rightarrow H_r} \Delta H_g &= \frac{2\alpha\omega}{\gamma\mu_0} = \Delta H_0 \end{aligned} \quad (1.50)$$

At resonance, this expression of the linewidth gives the full width at half maximum (FWHM) of the FMR peak. In the present case, only Gilbert-type damping is included, its contribution is written  $\Delta H_0$ .

### 1.3 Magnetostatic spin-waves

Magnetization dynamics have been treated so far in the case of a uniform magnetization using the Landau-Lifshitz equation. In this section, we will treat propagating excitations of the local magnetization in the magnetostatic regime. These collective excitations are called spin-waves, and from the equivalent quasiparticle point of view, they are known as magnons. An illustration of spin waves is shown in Fig. 1.3. To take into account their behavior as waves, it is natural to describe them using Maxwell's equations, and then, using the susceptibility obtained via the Landau-Lifshitz equation, to obtain their dispersion laws [Sta09].

#### 1.3.1 Spin-waves in the magnetostatic approximation

Let us consider the propagation of a uniform electromagnetic plane wave in the case of an unbounded ferromagnetic medium, in which the magnetization of the material is saturated by a magnetic field  $\mathbf{H}$  in the  $\hat{\mathbf{z}}$  direction. spin-waves are characterized by their angular frequency  $\omega$ , and their wavevector  $\mathbf{k}$  or the wavenumber  $k = |\mathbf{k}|$ . The group velocity of the wave:

$$\mathbf{v}_g = \frac{\partial \omega}{\partial \mathbf{k}} \quad (1.51)$$

gives the direction of propagation:  $\frac{\mathbf{v}_g}{|\mathbf{v}_g|}$ . For plane waves, the direction of propagation is always parallel to the wavevector.

Waves such that the wavenumber  $k \gg \frac{\omega}{c}$ ,  $c$  being the speed of light, are called magnetostatic waves. In other words, the wavenumber in the ferromagnetic media is much greater than the wavenumber in free space. In this regime, assuming there are no

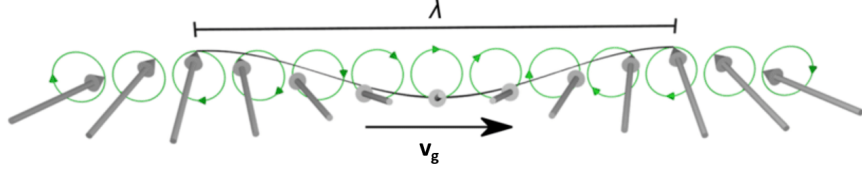


Figure 1.3: Illustration of a propagating spin wave with wavelength  $\lambda = \frac{2\pi}{k}$  and group velocity  $\mathbf{v}_g$ . Taken from [Die19].

charges or currents, we can use Maxwell's equations in the magnetostatic approximation, a derivation of which can be found in [Sta09]:

$$\begin{aligned}\nabla \times \mathbf{h} &= 0 \\ \nabla \cdot \mathbf{b} &= 0\end{aligned}\tag{1.52}$$

where  $\mathbf{h}$  is the time-varying magnetic field of the electromagnetic wave and  $\mathbf{b}$  the magnetic flux density, related by the constitutive relation  $\mathbf{b} = \bar{\mu} \cdot \mathbf{h}$ . The permeability tensor  $\bar{\mu}$  is defined by:

$$\bar{\mu} = \mu_0(I_3 + \bar{\chi})\tag{1.53}$$

where  $I_3$  is the identity matrix. Introducing the magnetic scalar potential  $\psi$ , defined by  $\mathbf{h} = -\nabla\psi$ , we can rewrite the second line of Eq. (1.52) using Eq. (1.53):

$$\nabla \cdot (\bar{\mu} \cdot \nabla\psi) = 0\tag{1.54}$$

Using the expression of  $\bar{\chi}$  in Eq. (1.29), we obtain Walker's equation [Wal58]:

$$(1 + \chi_{\parallel}) \left( \frac{\partial^2 \psi}{\partial x^2} + \frac{\partial^2 \psi}{\partial y^2} \right) + \frac{\partial^2 \psi}{\partial z^2} = 0\tag{1.55}$$

where  $\chi_{\parallel}$  is the diagonal element of the susceptibility tensor of an infinite ferromagnetic medium given in Eq. (1.29). The solutions to this equation constitute magnetostatic spin-waves. Assuming that the plane waves are propagating and are of the form  $\mathbf{m}(\mathbf{r}, t) \propto e^{-i\mathbf{k} \cdot \mathbf{r}} e^{i\omega t}$ , where  $\mathbf{m}$  is the magnetization of a volume element and  $\mathbf{r}$  its position, and  $\omega$  the frequency of the spin-wave; the magnetostatic scalar potential will have the same dependence, and Walker's equation becomes:

$$(1 + \chi_{\parallel}) (k_x^2 + k_y^2) + k_z^2 = 0\tag{1.56}$$

where  $k_i$  are the components of the wavevector. Let  $\theta_k$  be the polar angle between the direction of the propagation of the wave and the applied field, then:

$$\begin{aligned}k_x^2 + k_y^2 &= k^2 \sin^2 \theta_k \\ k_z^2 &= k^2 \cos^2 \theta_k\end{aligned}\tag{1.57}$$

where  $k = \sqrt{k_x^2 + k_y^2 + k_z^2}$  is the wavenumber. Substituting the above into Walker's equation yields:

$$\chi_{\parallel} \sin^2 \theta_k = -1\tag{1.58}$$

Substituting this result into Eq. (1.29), we obtain the dispersion law for magnetostatic spin-waves in an infinite ferromagnet:

$$\omega^2(\mathbf{k}) = \omega_H (\omega_H + \omega_M \sin^2 \theta_k) \quad (1.59)$$

Since the exchange interaction is not included in the expression of the susceptibility, these magnetostatic oscillations are called non-exchange spin-waves or dipole spin-waves. It is interesting to note that the dispersion law is only dependent on the direction of propagation and not on the wavenumber. Thus, the group velocity is zero and the non-exchange magnetostatic waves are non-propagative. In addition, they are degenerate: for a given frequency, a wave can have any wavenumber. The degeneracy is lifted when taking into account the exchange interaction or when introducing boundaries to the medium.

The magnetostatic approximation is valid only within a certain wavenumber range, the lower limit of which was given at the beginning of this section. The upper limit can be established when the frequency given by Eq. (1.59), in the magnetostatic approximation, no longer corresponds to the one found using the full Maxwell equations.

So far we have ignored the contribution of exchange fields even though a spin-wave is a propagating excitation of the local magnetization, which implies a non-zero contribution of the exchange interaction due to non-parallel spins. The dispersion law above is only correct for small enough wavenumbers such that the exchange field is negligible versus the dipolar field, leading to the terms dipole-dominated spin-waves or non-exchange spin-waves for the magnetic excitations described in this section.

### 1.3.2 Exchange spin-waves in an infinite ferromagnetic medium

For large enough wavenumbers,  $\lambda_{ex}k^2$  approaches unity, where  $\lambda_{ex}$  (in  $\text{m}^2$ ) is the the square of the exchange length  $l_{ex}$ :

$$\lambda_{ex} = l_{ex}^2 = \frac{2A_{ex}}{\mu_0 M_s^2} \quad (1.60)$$

where  $A_{ex}$  is the exchange stiffness constant of the ferromagnetic material. In such conditions, the expression of the susceptibility used previously is no longer valid, and the exchange interaction needs to be taken into account. In this regime, magnetic oscillations are called dipole-exchange spin-waves or exchange spin-waves. Assuming the plane wave is of the form  $\mathbf{m} \propto e^{-i\mathbf{k}\cdot\mathbf{r}}$ , the exchange field, defined in Eq. (1.12), can be rewritten:

$$\mathbf{h}_{ex} = -\lambda_{ex}k^2\mathbf{m} \quad (1.61)$$

It can be shown that including the exchange field in the susceptibility in Eq. (1.29) can be done by simply substituting the term:

$$\omega_H \rightarrow \omega_H + \omega_M \lambda_{ex}k^2 \quad (1.62)$$

A quantum-mechanical derivation of the dispersion relation in an unbounded medium can be found in [Hol40] or [Her51]. The diagonal susceptibility component in the presence

of exchange becomes:

$$\chi_{\parallel} = \frac{\omega_M (\omega_H + \omega_M \lambda_{ex} k^2)}{(\omega_H + \omega_M \lambda_{ex} k^2)^2 - \omega^2} \quad (1.63)$$

The susceptibility now depends on both the frequency and the wavevector. Substituting the above into Walker's equation (1.58), we obtain the dispersion law for dipole-exchange spin-waves in an unbounded ferromagnet:

$$\omega^2(\mathbf{k}) = (\omega_H + \omega_M \lambda_{ex} k^2) (\omega_H + \omega_M \lambda_{ex} k^2 + \omega_M \sin^2 \theta_k) \quad (1.64)$$

Thus, taking into account the exchange interaction lifts the degeneracy. In the present case, spin-waves propagating perpendicular to the applied field have higher frequencies relative to spin-waves propagating parallel.

### 1.3.3 Exchange spin-waves in a ferromagnetic thin film

The theory for dipole-exchange spin-waves in thin films was established by Kalinikos and Slavin [Kal86] by solving the undamped Landau-Lifshitz equation for plane waves in a ferromagnetic thin film, based on previous work by Kalinikos [Kal81]. Another approach, the Hamiltonian formulation of spin-wave dynamics, can be found in [Kri10]. In the context of this work, only some results of these calculations will be given, restricted to the case where the thin film is homogeneously magnetized across its thickness and the applied field is in the plane of the thin film. For an infinite ferromagnetic thin film the dispersion law is given by [Kal86]:

$$\omega^2(\mathbf{k}) = (\omega_H + \omega_M \lambda_{ex} k^2) (\omega_H + \omega_M \lambda_{ex} k^2 + \omega_M F_{00}) \quad (1.65)$$

where  $F_{00}$  is a function that represents the effective demagnetization factor of a non-uniform magnetization distribution, i.e., it scales  $M_s$  down since the non-uniform distribution leads to a partial cancellation of demagnetizing fields.  $F_{00}$  is defined by:

$$F_{00} = 1 + g_k (\sin^2 \theta_k - 1) + \frac{\omega_M g_k (1 - g_k) \sin^2 \theta_k}{\omega_H + \omega_M \lambda_{ex} k^2} \quad (1.66)$$

and where  $g_k$  is a function that allows the demagnetizing field to be taken into account in the thin film approximation [Har68], such that  $kt_f \ll 1$ ,  $t_f$  being the thickness of the ferromagnet:

$$g_k = 1 - \frac{1 - e^{-kt_f}}{kt_f} \quad (1.67)$$

In thin films, the small ferromagnetic layer thickness  $t_f$  leads to a standing wave across the thickness and a quantization of the wavevector component perpendicular to the thin film plane:

$$k_x = k_p = \frac{p\pi}{t_f} \quad (1.68)$$

where  $p$  is the order of the  $p$ -th perpendicular standing spin-wave mode (PSSW). Due to the nanometer thickness of the FeCoB layers used, the experiments presented in this

manuscript can be adequately described by only considering the lowest thickness mode  $p = 0$ , which features a quasi-uniform magnetization distribution across the thickness of the film. Higher order modes, which present a non-uniform magnetization across the thickness, possess a large amount of exchange energy according to Eq. (1.2). As a result, observing these modes requires an excitation at a much higher frequency than the range explored in this work. An expression for all PSSW modes can be found in [Kal86].

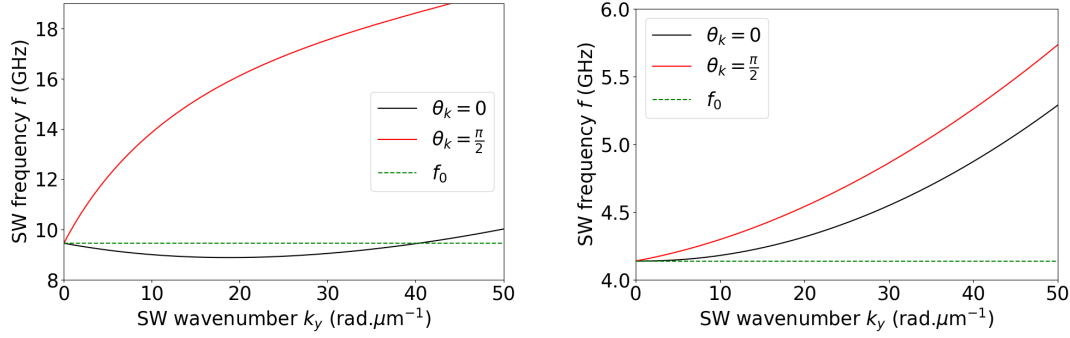
(a) NiFe with  $d = 30$  nm without PMA.(b) FeCoB with  $d = 1.3$  nm with PMA.

Figure 1.4: Dipole-exchange spin-wave dispersion relations for different material systems, for  $\theta_k = 0$  (solid black) and  $\theta_k = \frac{\pi}{2}$  (solid red), for an applied field  $\mu_0 H = 100$  mT. The dispersion relation continuously shifts from one curve to the other as a function of  $\theta_k$ .  $f_0$  (dashed green line) shows the FMR frequency of the corresponding material system. (a) Dispersion relation for a  $t_f = 30$  nm thick NiFe thin film without PMA. (b) Dispersion relation for a  $t_f = 1.3$  nm thick FeCoB thin film with an adjacent MgO layer that induces PMA.

### Spin-waves in NiFe and FeCoB

To summarize this section, the spin-wave dispersion relation according to Eq. (1.65) is shown in Fig. 1.4 for two material systems, the first, based on  $\text{Ni}_{81}\text{Fe}_{19}$  (hereafter referred to as NiFe) and the second on FeCoB. Only the two extreme angles are plotted for each system:  $\theta_k = 0$  where the applied field is parallel to the direction of propagation, and  $\theta_k = \frac{\pi}{2}$  where the applied field is perpendicular to the direction of propagation. However the spin-wave dispersion relation describes a spin-wave manifold for all  $\theta_k$ . Therefore solutions for the intermediate angles lie between the curve for  $\theta_k = 0$  and the curve for  $\theta_k = \frac{\pi}{2}$ .

The first example, shown in Fig. 1.4(a), is a  $d = 30$  nm thick NiFe thin film with  $\mu_0 M_s = 1.04$  T and  $A_{ex} = 13$  pJ m $^{-1}$ , under an applied field  $\mu_0 H = 100$  mT. The second example considers a system similar to the one investigated in my thesis and is a  $d = 1.3$  nm thick FeCoB thin film with  $\mu_0 M_s = 1.57$  T and  $A_{ex} = 10$  pJ m $^{-1}$ , under an applied field  $\mu_0 H = 100$  mT. An MgO/FeCoB interface inducing interfacial anisotropy is included using a PMA constant of  $K_i = 1.18$  mJ m $^{-2}$ .

The spin-wave frequency for both angles (and all angles in-between) coincides at  $k = 0$  with the ferromagnetic resonance frequency and splits for  $|k| > 0$ . In fact, for  $k \rightarrow 0$ ,  $\lim_{k \rightarrow 0} F_{00} = 1$  and Eq. (1.65) gives the ferromagnetic resonance frequency expected from the Kittel formula in Eq. (1.42).

On the  $\theta_k = 0$  branch, the spin-wave frequency initially decreases for small wave-numbers. This is a consequence of the dipolar interaction, and as a result, for low  $k$ , the spin-wave group velocity (in the 1D case):

$$v_g = \frac{\partial \omega(k)}{\partial k} \quad (1.69)$$

is negative for small positive  $k$  (the phase velocity  $v_p = \frac{k}{\omega}$  being positive). This property of the  $\theta_k = 0$  branch has led to it being named the backward volume magnetostatic configuration. More importantly, in NiFe for  $\mu_0 H = 100$  mT the group velocity  $v_g$  is close to 0 up to  $k = 40$  rad  $\mu\text{m}^{-1}$  meaning that for  $\theta_k = 0$ , the spin-waves propagate slowly. In FeCoB, the anisotropy field opposes the dipolar field, resulting in the group velocity quickly increasing with  $k$ .

Historically, the spin-waves mode excited in the  $\theta_k = \frac{\pi}{2}$  configuration were identified in ferromagnetic films as propagating on both interfaces of the thin film. This geometry is called the Damon-Eshbach configuration, after the scientists who predicted surface magnetostatic spin-waves [Dam61]. It is shown in [Esh60] that the amplitude of the spin-wave decreases exponentially across the film thickness, where the maximum amplitude is either at the upper side of the film for spin-waves propagating in the  $+y$  ( $k > 0$ ) direction, or at the lower side for spin-waves propagating in the opposite direction. However in the thin film limit, which already applies to both material systems described here, spin-waves in the Damon-Eshbach configuration essentially propagate in the volume because the amplitude of the spin-wave is almost constant across the thickness despite the exponential fall-off [Pat84; Hur95].

The particularity of the NiFe case is that in the Damon-Eshbach configuration, the dispersion relation has a very steep and positive slope for small  $k$ , which is the opposite of spin-waves in the backward-volume configuration, where the dispersion relation has a very shallow and negative slope. Thus, the spin-waves at small  $k$  have a high group velocity and the behavior of spin-waves is dictated by the dipolar interaction. Indeed, the anisotropic nature of the dipolar interaction is reflected in the anisotropic dispersion relation of the spin-waves at small  $k$ , meaning that the dispersion curve depends heavily on  $\theta_k$ . In contrast, at large  $k$ , where the exchange interaction is dominant, both branches have the same slope and increase with  $k^2$ , due to the isotropic nature of the exchange interaction.

For the Ta/FeCoB/MgO case, the interfacial anisotropy needs to be included into the dispersion relation. An empirical relation is given in [Brä17b]:

$$\omega^2(\mathbf{k}) = (\omega_H + \omega_M \lambda_{ex} k^2) (\omega_H + \omega_M \lambda_{ex} k^2 + (\omega_M - \omega_K) F_{00}) \quad (1.70)$$

where  $\omega_K$  is defined in Eq. (1.37). This is only an approximation validated in a certain window by micromagnetic simulations as shown in the Supporting Information of

[Brä17b]. The PMA competes with the demagnetization energy and renormalizes the last term, reducing the frequency of the spin-waves. In Fig. 1.4(b), the region that is dominated by the dipolar interaction is greatly reduced, the spin-waves are almost immediately influenced by the exchange interaction, due to the extremely small thickness of the ferromagnetic layer and the PMA. As a result, the differences between spin-waves propagating in the backward volume and the Damon-Eshbach configurations are small and mainly restricted to very low wavevectors in the case of ultra thin ferromagnets with PMA, and the group velocity in both configurations quickly increases with  $k$ .

### 1.3.4 Relaxation rate

So far the spin-waves have been described propagating without attenuation. Relaxation processes for spin-waves include magnon-magnon interaction [Gur96], magnon-electron interaction [Kam70] and magnon-phonon interaction [San77]. One can define a spin-wave lifetime  $\tau$  as the time in seconds required for a spin-wave's amplitude to decrease by a factor of  $1/e$  [Sta09]. This can be modeled by describing the spin-wave's frequency by a complex number  $\omega + i\omega_r$ , where the imaginary part represents losses. The relaxation rate, related to the spin-wave lifetime by  $\omega_r = \frac{2\pi}{\tau}$ , is given by [Sta09]:

$$\omega_r = \alpha\omega \frac{\partial\omega(\mathbf{k})}{\partial\omega_H} \quad (1.71)$$

where  $\omega_H = \gamma\mu_0 H$ ,  $\omega$  is the spin-wave angular frequency and  $\omega(\mathbf{k})$  is the dispersion relation. The equation above is valid for  $\omega_r \ll \omega$  and  $\alpha$  is the Gilbert damping parameter [Sta09].

For a ferromagnetic thin film with PMA, the resulting relaxation frequency is derived from Eqs. (1.70) and (1.71):

$$\omega_r = \alpha \left( \omega_H + \omega_M \lambda_{ex} k^2 + \frac{\omega_M - \omega_K}{2} (1 + g_k (\sin^2(\theta_k) - 1)) \right) \quad (1.72)$$

Once again, the PMA competes with the demagnetizing field. Thus, in thin films, the demagnetizing field increases the relaxation rate, while the PMA reduces it. This can be understood by looking at the magnetization as it precesses. Its trajectory can be approximated by an ellipse in the  $(\hat{\mathbf{x}}, \hat{\mathbf{y}})$  plane, with the ellipse flattened in the  $x$  direction due to the demagnetizing field (mitigated by the PMA) in thin films. In the flattened parts of the trajectory, the magnetization is subject to the demagnetizing field and the anisotropy field, thus if the PMA is strong enough it will slow down the magnetization, resulting in a lower local frequency, lower ellipticity and lower relaxation rate.

## 1.4 Spintronics phenomena for controlling and detecting magnetization dynamics

One of the objectives of this thesis is to electrically control and detect magnetization dynamics in a spin-wave waveguide. This can be achieved exploiting spin-orbit

torques that occur in FM/HM bilayer systems when passing a charge current through it. Spin-orbit interactions generate spin currents and local torques that create field-like and damping-like torques, that have to be added to the LLG equation (1.19):

$$\frac{d\mathbf{M}}{dt} = -\gamma\mu_0\mathbf{M} \times \mathbf{H}_{\text{eff}} + \frac{\alpha}{M_s} \left( \mathbf{M} \times \frac{d\mathbf{M}}{dt} \right) + \boldsymbol{\tau}_{fl} + \boldsymbol{\tau}_{dl} \quad (1.73)$$

These torques are described in this section, along with the physical phenomena that are responsible: the Rashba interaction and the spin Hall effect. Since both effects depend on spin-orbit interactions, the search for normal metals, i.e., conductive and non-ferromagnetic, that exhibit these properties has focused on heavy metals such as platinum, tantalum and tungsten, given that a higher atomic number usually means stronger spin-orbit interaction [Tan08].

Additionally, via a phenomenon that can be understood as the opposite effect, a magnetic excitation can be detected electrically through the inverse spin Hall effect. These two reciprocal effects couple charge currents with spin currents.

In the final part of this section, we discuss a further spin-orbit interaction that can be used to detect magnetization dynamics, called anisotropic magnetoresistance. However, for the devices studied in my thesis we will show that the corresponding signal is weak and can be neglected.

### 1.4.1 The Rashba effect

At the interface between two different materials, the local electronic environment is modified, resulting in an electric field perpendicular to the interface. This configuration, called structural inversion asymmetry, was first investigated theoretically for semiconductor surface states [Ohk74] and the theory for 2D electron gases was laid out by Bychkov and Rashba [Byc84]. Through spin-orbit coupling, the electric potential results in the lifting of the spin degeneracy of the 2D electron gas at the interface. The Rashba effect, named after its discoverer, has been observed in other types of materials and interfaces [Che09], including paramagnetic/ferromagnetic metallic systems [Mir10]. A proper derivation of the spin-orbit interaction requires a relativistic treatment of the electron which is beyond the scope of this work. Instead, here we will give a naive semi-classical approach to the spin-orbit interaction that gives rise to the Rashba effect.

In special relativity, electric and magnetic fields are linked through the Lorentz transformation; an electric field  $\mathbf{E}$  is experienced as a magnetic field  $\mathbf{B}$  in the inertial reference frame of an electron moving at a velocity  $\mathbf{v}$ . Thus, the electric field that arises due to symmetry breaking at the interface of two materials transforms into a magnetic field in the moving frame of the electron:

$$\begin{aligned} \mathbf{B} &= \frac{\mathbf{E} \times \mathbf{v}}{c^2 \sqrt{1 - \frac{v^2}{c^2}}} \\ &\approx \frac{\mathbf{E} \times \mathbf{v}}{c^2} \end{aligned} \quad (1.74)$$

where the Fermi velocity  $\mathbf{v}$  is small compared to the speed of light  $c$ . The potential of an electron's spin magnetic moment in a magnetic field is:

$$\begin{aligned} V &= -\boldsymbol{\mu}_S \cdot \mathbf{B} \\ &= \frac{eg}{2m_e^*c^2} \boldsymbol{\sigma} \cdot (\mathbf{E} \times \mathbf{v}) \end{aligned} \quad (1.75)$$

where  $e$  is the electron charge and  $m_e^*$  its effective mass,  $g$  is the Landé g-factor, and  $\boldsymbol{\sigma}$  the Pauli matrices collected into a vector for convenience. The Hamiltonian of a conduction electron at the interface, in the presence of Rashba spin-orbit interaction and the two eigenvalues (the  $\pm$  symbols can be replaced by either  $+$  or  $-$  to yield the two eigenvalues) are [Man08; Man09]:

$$H_{so} = \frac{\hbar}{2m_e^*} \mathbf{k}^2 + \alpha_R (\mathbf{k} \times \boldsymbol{\sigma}) \cdot \hat{\mathbf{n}} \quad E_{\pm} = \frac{\hbar^2 k^2}{2m_e^*} \pm \alpha_R k \quad (1.76)$$

where  $\mathbf{k} = \frac{m_e^*}{\hbar} \mathbf{v}$  is the wavevector of the electron,  $\hbar$  the reduced Planck constant,  $\hat{\mathbf{n}}$  the unit vector normal to the surface, and  $\alpha_R \propto \frac{g\mu_B}{2m_e^*c^2} \|\mathbf{E}\|$  represents the strength of the Rashba interaction. The Rashba term causes a spin and wavevector dependent wavevector shift of the dispersion relation, lifting the two fold spin degeneracy for  $k \neq 0$  as illustrated in Fig. 1.5(b,e). In contrast, applying an external magnetic field will result in a spin dependent but wavevector independent energy shift of the dispersion relation, lifting the spin degeneracy for all  $k$ , shown in Fig. 1.5(d).

Thus, the Rashba effect leads to the polarization of the conduction electrons. On the other hand, in ferromagnets the localized electrons are already polarized. There is thus a competition between the  $s-d$  exchange interaction, which wants to align the spin of the conduction electrons along the local magnetization, and the Rashba effect, which wants to align them in a different direction. The result is a reorientation of the local magnetization. In the absence of a charge current, the  $\mathbf{k}$  and  $-\mathbf{k}$  states are equally populated and there is no net effect on the magnetization. However in the presence of a charge current, the states are no longer equally populated and the average electron wavevector is non-zero, leading to a net torque on the magnetization. In the case where the Rashba interaction is small compared to the  $s-d$  exchange interaction, it can be assimilated to an effective magnetic field, called Rashba field, dependent on the charge current density [Man08]:

$$\mathbf{H}_R = 2 \frac{\alpha_R m_e J_{SD}}{e \hbar M_s \epsilon_F} (\hat{\mathbf{x}} \cdot \mathbf{J}^c) \quad (1.77)$$

where  $J_{SD}$  is a parameter of the  $s-d$  exchange interaction,  $\epsilon_F$  is the Fermi energy,  $\mathbf{J}^c$  is the charge current density and  $\hat{\mathbf{x}}$  is the axis perpendicular to the interface.

Since the Rashba interaction is an interfacial effect, it is expected that its effect on the magnetization will scale with the inverse of the thickness of the ferromagnetic layer [Kim13].

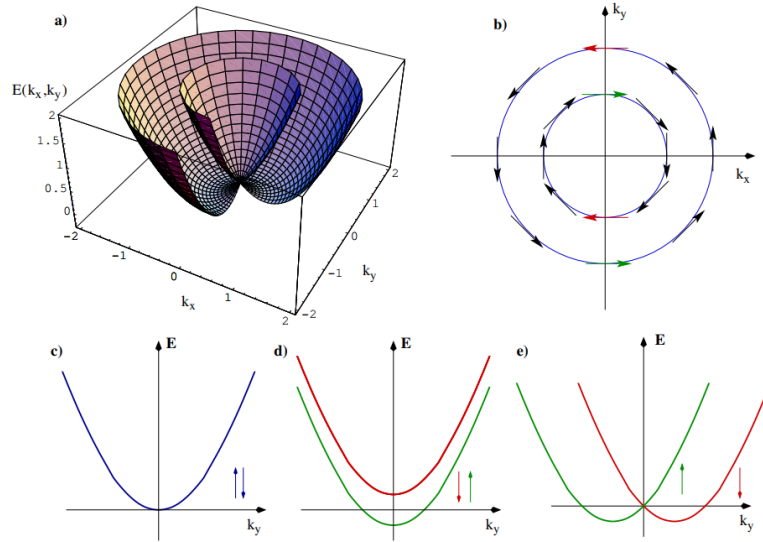


Figure 1.5: Dispersion relation of an electron. a) Section of the 2D dispersion relation with Rashba interaction. b) 2D Fermi contours with Rashba interaction, arrows represent the spin states. c) Dispersion relation of a free electron. d) Dispersion relation of an electron in a magnetic field. e) Dispersion relation of an electron with Rashba interaction. Taken from [Ber04].

### 1.4.2 Spin Hall effects

In 1929, Mott predicted the inelastic scattering of electrons on atomic nuclei, resulting in the spatial separation of electrons with different spins due to spin-orbit coupling [Mot29]. Based on this phenomenon, Dyakonov and Perel proposed in 1971 that a charge current in a semiconductor should result in a perpendicular spin current flowing towards the interfaces [Dya71b; Dya71a] (illustrated in Fig. 1.6(Left)), such that the charge current density vector, the direction of the polarization of the spin current and the interface normal are all orthogonal to each other, as illustrated in Fig. 1.6(Left). This is called the spin Hall effect. They predicted the reciprocal effect as well, called the inverse spin Hall effect (iSHE), shown in Fig. 1.6(Right).

#### Origin of the spin Hall effects

While the SHE was historically predicted by considering the scattering of electrons on nuclei or impurities [Dya71a], several mechanisms have been proposed. They are split into intrinsic [Sin04; Tan08] phenomena, which arise from the band structure of the material, and extrinsic effects such as skew-scattering [Mot29] and side-jumping [Ber70] on impurities. The mechanism that is dominant is material-dependent, a review of the different origins as well as experimental studies of the spin Hall effects can be found in [Sin15].

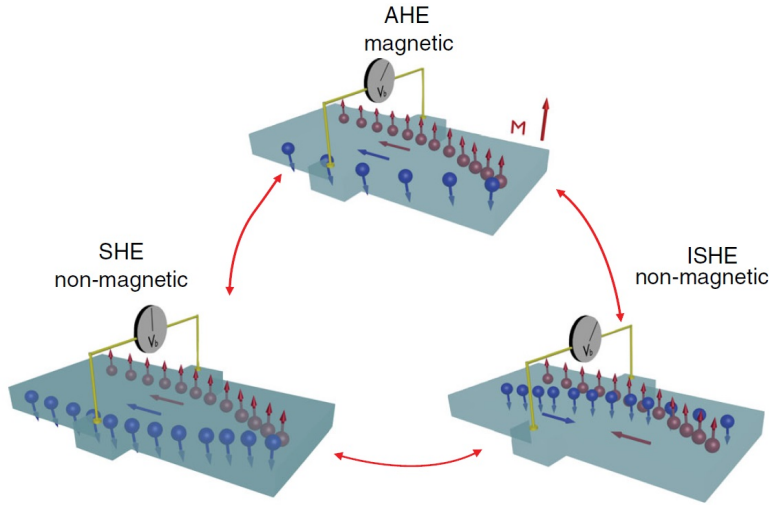


Figure 1.6: Anomalous Hall effect and spin Hall effects. (Top) In the AHE, a spin polarized charge current generates a transverse spin polarized charge current depending on the magnetization. (Left) In the SHE, an unpolarized charge current generates a transverse spin current. (Right) In the iSHE, a spin current generates a transverse charge current. Taken from [Sin15].

### Relationship with the anomalous Hall effect

The SHE, which occurs in semiconductors and paramagnetic metals, is the counterpart of the anomalous Hall effect found in ferromagnetic materials. In a FM, the same spin-orbit processes responsible for SHE lead to the spatial separation of spins, however since there is an asymmetric distribution of spin up and spin down, the spin current is accompanied by a net charge current that is proportional to the spin polarization of the electrons in the FM, as shown in Fig. 1.6(Top). The resulting transverse voltage is then proportional to the magnetization component that is perpendicular to the charge current and the measurement directions. This is called the anomalous Hall effect (AHE).

While the AHE was discovered in 1881 by Hall, it was not until 1984 that the iSHE was observed optically in semiconductors [Bak84], shortly after Dyakanov and Perel's prediction. Moreover, it was only after Hirsch brought back the SHE to attention in 1999 [Hir99] that the first observations of the direct SHE were made using magneto-optical Faraday [Kat04a] and Kerr microscopy [Kat04b] in semiconductors.

### Inverse spin Hall effect

The first electrical measurements of the spin Hall effects [Sai06; Val06] involved the opposite phenomenon, the inverse spin Hall effect (iSHE), where a spin current generates a transverse charge current through the same processes, as illustrated in Fig. 1.6(Right). The two effects are linked by Onsager's reciprocity relations [Jac12], such that the charge-to-spin conversion ratio for the SHE is equal to the spin-to-charge conversion ratio for

the iSHE. This unitless ratio, written  $\theta_{SH}$ , is called the spin Hall angle.

### Interconversion of spin and charge currents

In the following we quantify the SHE and the iSHE by relating charge and spin current densities in the general case. In a normal metal with strong spin-orbit coupling, a charge current density will create an orthogonal spin current density:

$$J_{ij}^s = -\frac{\hbar\theta_{SH}}{2e} J_k^c \quad (1.78)$$

where  $(\hat{\mathbf{i}}, \hat{\mathbf{j}}, \hat{\mathbf{k}})$  form an orthonormal basis,  $J_k^c$  is the charge current density flowing along  $\hat{\mathbf{k}}$  and  $J_{ij}^s$  is the spin current density flowing along  $\hat{\mathbf{i}}$  and polarized along  $\hat{\mathbf{j}}$ .

Conversely, a charge current density can be created by either or both of the following orthogonal spin currents:

$$J_k^c = \frac{2e\theta_{SH}}{\hbar} (J_{ij}^s - J_{ji}^s) \quad (1.79)$$

where  $J_{ji}^s$  is the spin current density flowing along  $\hat{\mathbf{j}}$  and polarized along  $\hat{\mathbf{i}}$ . Thus, by simply injecting a pure charge current in a normal metal, a transverse pure spin current is generated, which can diffuse into an adjacent material. In this work, the adjacent material is a ferromagnetic conductor, such that the spin current will exert a torque on the magnetization. However, since a pure spin current does not rely on a net movement of electronic charges, the spin current can even diffuse into a ferromagnetic insulator such yttrium iron garnet [Kaj10].

We note that further methods exist that generate spin currents. The first is spin pumping, discussed next (in Sec. 1.4.3) and the second is used in magnetic tunnel junctions where the charge current becomes spin polarized and spin and charge current are thus coupled [Slo96; Ra108].

### 1.4.3 Detection of magnetization dynamics via spin pumping and inverse spin Hall effect

The SHE and Rashba effects discussed above can be used to excite or manipulate the magnetization dynamics. In Sec. 1.4.4 we discuss the corresponding torques that have to be added to LLG. Before we come to this, we introduce the effect of spin pumping, which, in conjunction with the ISHE, can be used to detect the magnetization dynamics

Spin-pumping, introduced by Tserkovnyak et al. [Tse02a; Tse02b], can be understood as the reverse process of current-induced magnetization dynamics: a spin current can exert a torque on a magnetization and, vice-versa, a moving magnetization relaxes by emitting a spin current, which accumulates at all the interfaces and can leak into an adjacent layer, as shown in Fig. 1.7. This leads to a dissipation term in the LLG equation which takes a similar form to Gilbert damping. If there is a NM at one of these interfaces, the spin current can flow into it and the injected spins build up near the interface. This creates another spin current that flows back into the FM, until equilibrium is reached and both spin currents cancel out [Tse02b]. In our case, we will consider the simple case

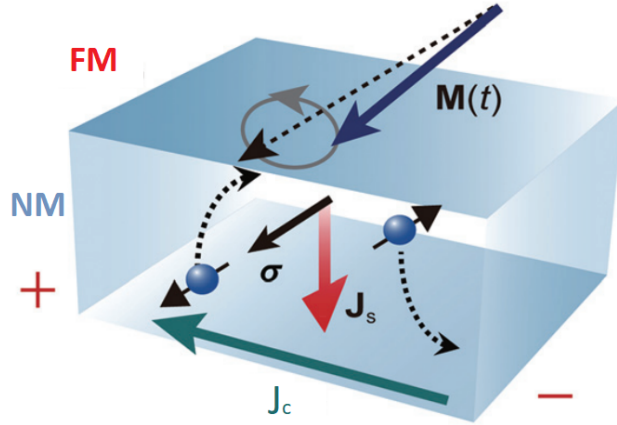


Figure 1.7: A schematic of spin-pumping and the inverse spin Hall effect. Spin-pumping: the precessing magnetization  $\mathbf{M}(t)$  of the ferromagnetic layer (FM) leads to the emission of a spin current  $\mathbf{J}_s$  (also represented by electrons with opposite spin-polarizations  $\sigma$  and  $-\sigma$  moving in opposite directions) which flows in the adjacent normal metal layer (NM). Inverse spin current: the spin current  $\mathbf{J}_s$  is converted into an orthogonal charge current  $\mathbf{J}_c$ . Taken from [And11].

where the NM is an ideal spin sink and there is no spin current backflow. This condition is met if there is sufficient spin diffusion and spin-flip scattering in the NM.

Thus, when the magnetization in a FM/NM bilayer precesses along an in-plane axis  $\hat{\mathbf{z}}$ , a spin current flows from the FM to the NM, ie. along  $\hat{\mathbf{x}}$ . The total spin current density vector created is given by [Har16]:

$$\mathbf{J}_x^{s_0} = \begin{pmatrix} J_{xx}^{s_0} \\ J_{xy}^{s_0} \\ J_{xz}^{s_0} \end{pmatrix} = \frac{\hbar G_r}{4\pi M_s^2} \mathbf{M} \times \frac{d\mathbf{M}}{dt} \quad (1.80)$$

where  $\mathbf{J}_x^{s_0}$  contains all the spin current density vectors flowing along the  $\hat{\mathbf{x}}$  axis, at the interface. The key parameter of spin pumping is the real part of the spin mixing conductance,  $G_r$  in  $\text{m}^{-2}$ , which is related to the reflection and transmission coefficients of spin up and spin down electrons at the FM/NM interface. There is an additional term owing to the imaginary part of the spin mixing conductance, but in most cases [Tse02a], it is up to 3 orders of magnitude smaller than the real part and its contribution can be neglected in the material systems studied in this work. This spin current decays in the NM due to spin relaxation and diffusion, and the spin current density at a distance  $x$  from the interface is [Har16]:

$$J_{xi}^s(x) = J_{xi}^{s_0} \frac{\sinh((x - t_n)/l_{sd})}{\sinh(t_n/l_{sd})} \quad (1.81)$$

where  $i = (x, y, z)$ , and  $t_n$  is the thickness of the NM and  $l_{sd}$  its spin diffusion length. The latter is the average distance over which the electron spin will flip. For a non-polarized

charge current it is the distance where the current becomes polarized in a FM and for a spin-polarized charge current it is the distance where the current depolarizes in a NM.

Thus, magnetization dynamics in a ferromagnetic layer can lead to the creation of a spin current in an adjacent metal. If this metal has strong spin-orbit interaction, the spin current will be converted through the iSHE to a measurable charge current, given by Eq. (1.79), as illustrated in Fig. 1.7. These two combined phenomena, spin-pumping and the inverse spin Hall effect (SP+iSHE), thus provide a means to detect magnetization dynamics. This technique was used to show the presence of SHE in normal metals such as Pt [Sai06].

#### 1.4.4 Modification of the LLG including the field-like torque and the damping-like torque

While it was initially considered that the field-like torque originated from the Rashba effect and that the damping-like torque originated from the SHE [Mir10] [Mir11], the situation is now understood to be more complicated, as some studies suggest that both effects can create both types of torques [Han13; Fre14]. One way to separate the two effects is via a thickness-dependent study of the normal metal [Kim13; Fan13; Zha13], since it is assumed that the Rashba effect is an interfacial effect while the SHE is a volumic effect in the normal metal. However even this methodology has encountered hurdles, due to the fact that varying the normal metal thickness changes the growth of the materials and the interface itself. The experiments presented in this thesis were performed for a fixed thickness of the normal metal Ta, it is thus impossible to distinguish the physical origin of the observed torques. Consequently, their action will be summarized to an effective field-like and an effective damping like torque, which are accessible in the experiment.

##### Field-like torque

When a charge current  $\mathbf{J}^c$  is injected in a normal metal with strong spin-orbit interaction, it generates a field-like torque on the adjacent ferromagnetic layer's magnetization  $\mathbf{M}$  [Gar13]:

$$\boldsymbol{\tau}_{\text{fl}} = -\gamma\beta_{fl}\mathbf{M} \times (\mathbf{J}^c \times \hat{\mathbf{n}}) \quad (1.82)$$

where  $\beta_{fl}$  is a parameter characterizing the strength of the field-like torque (in  $\text{T A}^{-1} \text{m}^2$ ) and  $\hat{\mathbf{n}}$  is the growth axis (with the ferromagnetic layer on top of the normal metal).  $\beta_{fl}$  is defined by the ratio between the effective field of the torque,  $\mathbf{H}_{\text{fl}}$ , and the current density that created it. The effective field of the field-like torque is written:

$$\mathbf{H}_{\text{fl}} = \frac{\beta_{fl}}{\mu_0}(\mathbf{J}^c \times \hat{\mathbf{n}}) \quad (1.83)$$

Since the effective field of the field-like torque does not depend on  $\mathbf{M}$ , the field-like torque is functionally equivalent to one created by a Zeeman field.

### Damping-like torque

In spin-torque oscillators, the damping-like torque is used to completely compensate the damping, such that the oscillations of the magnetization reach a steady state without the use of an RF excitation [Kis03; Hou07], leading to the present name for the torque. Indeed, in the experimental configuration where the polarization of an injected spin current is parallel to the magnetization, the damping-like torque either enhances or reduces the damping on the magnetization dynamics, depending on the polarity of the charge current used to generate the spin current.

The expression of the damping-like torque generated by spin-orbit interaction is given by [Gar13]:

$$\boldsymbol{\tau}_{dl} = -\frac{\gamma\beta_{dl}}{M_s}\mathbf{M} \times (\mathbf{M} \times (\mathbf{J}^c \times \hat{\mathbf{n}})) \quad (1.84)$$

where  $\beta_{dl}$  is a parameter characterizing the strength of the damping-like torque (in  $\text{T A}^{-1} \text{m}^2$ ). In terms of cross products, one can see the similarity between the expression of the damping-like torque and the term due to the damping parameter  $\alpha$  in the LL equation (1.73). The effective field of the damping-like torque is written:

$$\mathbf{H}_{dl} = \frac{\beta_{dl}}{\mu_0 M_s}\mathbf{M} \times (\mathbf{J}^c \times \hat{\mathbf{n}}) \quad (1.85)$$

The effective field of the damping-like torque depends on  $\mathbf{M}$ , thus the damping-like torque is not equivalent to a Zeeman field.

#### 1.4.5 Anisotropic magnetoresistance

Anisotropic magnetoresistance (AMR) was discovered in Fe and Ni in 1857 by Thomson [Tho57]. It also arises from spin-orbit interaction [Ber64; Ash69]. The effect, found in 3d transition ferromagnetic metals and alloys, consists in the change of electrical resistivity as a function of the angle between the magnetization of the material and the direction of the electrical current passing through it. At room temperature, the change in resistivity of bulk NiFe alloys can reach 5% [McG75]. For most materials, the resistivity is minimal when the magnetization is perpendicular to the flow of current and maximal when they are parallel. The anisotropic magnetoresistivity follows the following angular dependence [McG75]:

$$\rho(\theta_M) = \rho(0^\circ) - \Delta\rho_{AMR} \sin^2(\theta_M) \quad (1.86)$$

where  $\theta_M$  is the angle between the current and the magnetization direction, and  $\Delta\rho_{AMR} = \rho(0^\circ) - \rho(90^\circ)$ . When injecting a current in a ferromagnetic layer, the magnetization  $\mathbf{M}$  will affect the resistivity of the layer, and thus the measured voltage across the ferromagnet:

$$V_{AMR} = \int_0^{l_w} \frac{\Delta\rho_{AMR}}{M_s^2} (\mathbf{J} \cdot \mathbf{M}) \mathbf{M} \cdot d\mathbf{l} \quad (1.87)$$

where  $\mathbf{J}$  is the current density vector injected the ferromagnetic layer and  $l_w$  is the length of the ferromagnet between the measurement points. Thus, AMR also provides a way to probe the magnetization dynamics of a ferromagnet.



## Chapter 2

# Device fabrication

In order to characterize the field-like and damping-like spin-orbit torques and to demonstrate the detection of propagating spin-waves using spin pumping and the inverse spin Hall effect for perpendicular magnetic anisotropy materials and their dependence on the ferromagnetic layer thickness we have realized a set of devices that contain a small bar of FM/HM material that serve as spin-wave waveguides with contacts at the ends and with a coplanar waveguide on top. Here we summarize the main steps for the realization of these devices.

### 2.1 Wafer deposition and annealing

The magnetic material chosen for our studies is the Fe rich alloy  $\text{Fe}_{72}\text{Co}_8\text{B}_{20}$  (often referred to as FeCoB in this manuscript) that is used in SPINTEC for developing perpendicular magnetic tunnel junctions for memory applications. FeCoB is characterized by a strong saturation magnetization, low damping and a high perpendicular magnetic anisotropy.

The thin films were deposited by an Actemium sputter deposition machine by Stéphane Auffret (Spintec) on a high resistivity ( $5\text{ k}\Omega\text{ cm}$ ) 2-inch Si wafer, capped with 500 nm  $\text{SiO}_2$ . Materials were sputtered in the following order (thicknesses in nanometers): Ta (5),  $\text{Fe}_{72}\text{Co}_8\text{B}_{20}$  (1.0–1.4), Mg (1.5), Al (2), Ta (1). The Ta (5) layer is used as a seeding layer and is deposited in conditions that allow the formation of  $\beta$ -phase Ta. This phase is recognizable by its high resistivity and demonstrates both spin Hall and Rashba effects [Liu12; All15].

The FeCoB thin film is deposited as a wedge with thicknesses ranging from approximately 1 to 1.4 nm over the 2 inch wafer. An oxidation step under controlled oxygen atmosphere after the deposition of Mg results in a MgO layer. The Al (2) and Ta (1) layers serve as capping layers and are partially oxidized once exposed to the atmosphere. The wafer is then annealed at  $250\text{ }^\circ\text{C}$  for 90 min under vacuum, resulting in the migration of B from the FeCoB to the Ta [Koz10] and the poly-crystallization of bcc (001) FeCo at the MgO interface [Yua05]. The presence of MgO generates PMA at the interface of the ferromagnetic layer which competes with the demagnetizing field (see Sec. 1.1.3), result-

ing in in-plane magnetization for FeCoB thicknesses above  $\approx 1.2$  nm and out-of-plane magnetization for thicknesses below  $\approx 1.2$  nm, as verified by magneto-optic Kerr effect microscopy on a magnetic stack deposited and annealed under the same conditions.

## 2.2 Device fabrication

After annealing, the wafer is processed at the Plateforme Technologique Amont at Minatec and at Nanofab at the Institut Néel (both clean rooms are in Grenoble), using UV and electron-beam lithography. The aim is to obtain a Ta/Fe<sub>72</sub>Co<sub>8</sub>B<sub>20</sub>/MgO/Al<sub>2</sub>O<sub>3</sub>/Ta<sub>2</sub>O<sub>5</sub> wire that will form the spin-wave waveguide, with metallic contacts at each end, and two sets of CPWs above the wire with a Al<sub>2</sub>O<sub>3</sub> insulating layer in between, as shown in Fig. 2.1. The electron-beam lithography was performed by G. Gaudin, the nanofabrication and scanning electron microscopy by T. Brächer and the atomic layer deposition of Al<sub>2</sub>O<sub>3</sub> (described below) by M. Schott at Nanofab.<sup>1</sup> The main steps are summarized:

1. ma-N 2401, an electron-sensitive negative resist with sub 50 nm resolution, is spin-coated on the wafer, resulting in a 100 nm thick layer. Spin-wave waveguides are patterned using electron beam lithography. They are rectangles with a length of 12  $\mu$ m and widths ranging from 500 nm to 5  $\mu$ m.
2. The thin film stack is etched down to the SiO<sub>2</sub> substrate using an Ar ion-beam at 45° angle with respect to the film plane. A secondary ion mass spectrometer is used to monitor the progress of the etching step. The result is a Ta/Fe<sub>72</sub>Co<sub>8</sub>B<sub>20</sub>/MgO/Al<sub>2</sub>O<sub>3</sub>/Ta<sub>2</sub>O<sub>5</sub> wire with ma-N 2401 on top, which is removed in an acetone bath.
3. AZ5214, a negative UV resist, is spin-coated on the wafer. Leads and contact pads are defined using UV lithography for lift-off.
4. Ti (5 nm) and Au (30 nm) are deposited by electron beam evaporation. The UV resist is removed in an ultrasonic acetone bath, resulting in Ti/Au leads and contact pads. These are connected either to the existing SWW or to the coplanar waveguides fabricated in step 8.
5. AZ5214 is spin-coated on the wafer. A rectangle completely covering the SWW is defined by standard UV lithography for lift-off.
6. Al<sub>2</sub>O<sub>3</sub> (30 nm) is deposited on the wafer by atomic layer deposition. The UV resist is then removed in an acetone bath, resulting in an Al<sub>2</sub>O<sub>3</sub> insulating layer covering the SWW.
7. A solution of 4% Poly methyl methacrylate (PMMA) is spin-coated on the wafer, resulting in a 300 to 400 nm thick layer. Shorted coplanar waveguides are defined on top of the SWW using electron beam lithography.

---

<sup>1</sup>While I personally made many samples and devices for the study of magnetization dynamics, these did not result in exploitable results. The specific devices discussed in this thesis were fabricated mainly by T. Brächer.

8. Ti (5) and Au (30) are deposited by electron beam evaporation. The PMMA is then removed in a lift-off process, resulting in Ti/Au CPWs on top of the SWW, separated by a dielectric Al<sub>2</sub>O<sub>3</sub> layer.

## 2.3 Device description

Scanning electron microscopy was used to image the devices. The spin-wave waveguides, shown in Fig. 2.1, have Ti/Au contacts at both ends of the SWW along the long axis. The SWWs have a length of 12  $\mu\text{m}$  and exists in 5 different widths: 5  $\mu\text{m}$ , 2  $\mu\text{m}$ , 1  $\mu\text{m}$ , 500 nm and 250 nm. On top of the SWWs, two identical and separate CPWs are set left and right from the center of the spin-wave waveguide. The distance between the centers of the two CPWs is one of the following: 1.25  $\mu\text{m}$ , 2.5  $\mu\text{m}$  or 5  $\mu\text{m}$ , however this feature was not exploited for the results discussed in this thesis.

There are 3 different CPW designs with varying geometry. Their features are summarized in Tab. 2.1, which gives the width  $2a$  of each conducting wire and the center-to-center separation  $s$  between the signal line and each ground line. All three CPW designs have the same layer composition and thickness: 30 nm of Au on top of 5 nm of Ti, and they are all insulated from the spin-wave waveguide by the 30 nm Al<sub>2</sub>O<sub>3</sub> layer.

Table 2.1: The three coplanar waveguide designs. All three type have the same layer composition and thickness: 30 nm of Au on top of 5 nm of Ti, and are insulated from the spin-wave waveguide by a 30 nm Al<sub>2</sub>O<sub>3</sub> layer. The wire width  $2a$  is the width of a signal line or ground line, and the spacing  $s$  is the center-to-center distance between the signal line and either ground line.

CPW design	$2a$ (nm) wire width	$s$ (nm) spacing
A	120	500
B	70	300
C	70	150

The nanofabrication steps in this process do not pose any particular challenges, except for the CPWs, which are narrow and long. The lift-off step of the CPWs proved to be delicate, causing a number of broken or missing CPWs and resulting in a low yield. The cause was the use of a pipette to start the lift-off in the acetone bath. An alternative that was proven to work on other wafers was to simply put the wafer in a low power ultrasonic bath.

The 30 nm Al<sub>2</sub>O<sub>3</sub> insulating layer, in addition to acting as an electrical insulator, helps to dissipate heat from the SWW and the CPW, given its relatively high thermal conductivity compared to SiO<sub>2</sub> and air.

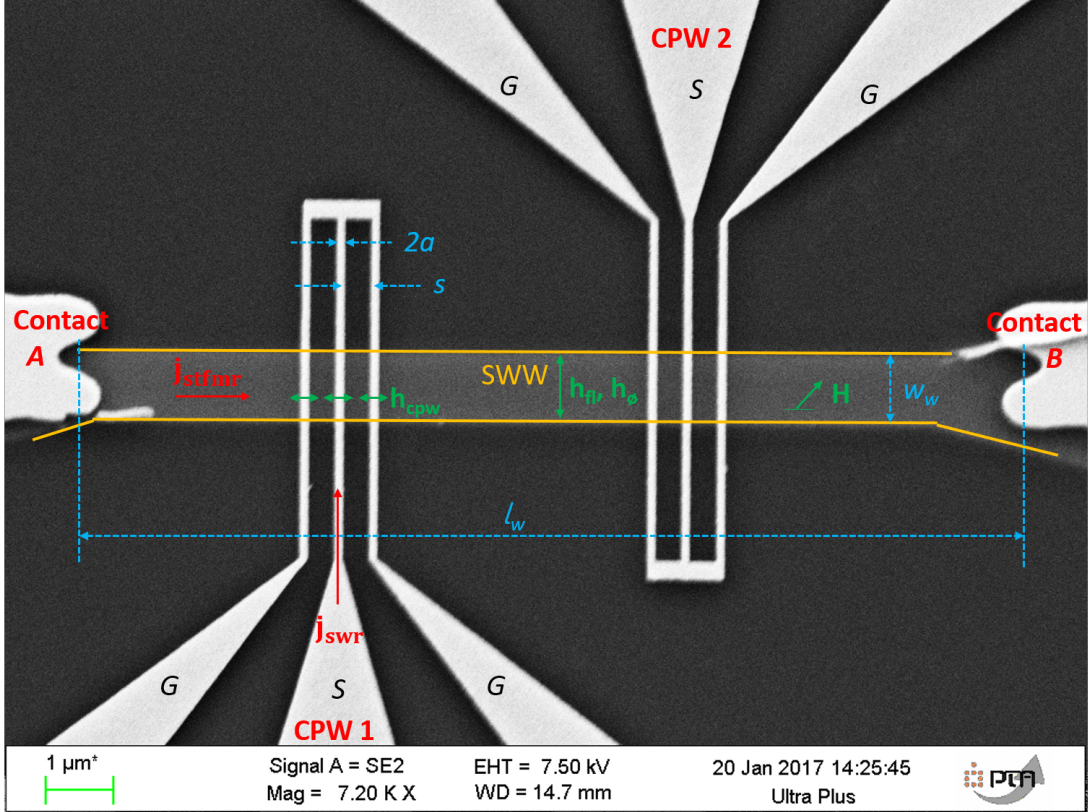


Figure 2.1: Scanning electron microscopy image of a spin-wave waveguide with a length  $l_w = 12 \mu\text{m}$ , width  $w_w = 1 \mu\text{m}$ , and two electrical contacts  $A$  and  $B$ . Two coplanar waveguides (1 and 2) are positioned on top, separated by a  $\text{Al}_2\text{O}_3$  insulator (not visible in this image). The CPWs are of type A, characterized by their wire width  $2a$  and wire spacing  $s$  (see table 2.1). They each have a signal line  $S$  and two ground lines  $G$ . In ST-FMR experiments, an RF current density ( $\mathbf{j}_{\text{stfmr}}$  here) is injected into the SWW, generating the RF fields  $\mathbf{h}_{\text{fl}}$  and  $\mathbf{h}_{\text{p}}$  as well as an RF damping-like torque which is not represented here. In SWR experiments, an RF current density ( $\mathbf{j}_{\text{swr}}$  here) is injected into one of the CPWs, generating an RF field  $\mathbf{h}_{\text{cpw}}$ . An external magnetic field  $\mathbf{H}$  is applied in the plane of the thin film.

## 2.4 Measured samples

Table 2.2 lists the devices that were measured, CPW design, thickness, as well as the type of experiment performed. In this table, ST-FMR stands for spin-torque ferromagnetic resonance, discussed in Chap. 3, SWR stands for spin-wave resonance, described in Sec. 4.4 and BLS stands for Brillouin light scattering, described in Sec. 4.5. Due to the low yield of CPWs, the SWR measurements could not be done on many of the devices that were measured by ST-FMR. Additionally, due to the fragility, some SWR experiments resulted in the destruction of the CPW antennae.

The reported FeCoB thicknesses in the table are based on the Actemium deposition machine's calibration data, extrapolated to each point on the wafer. The wafer is divided into 18 rectangular chips, each containing an identical set of device designs, though the FM thickness varies continuously from one row of chips to another. Each rectangular chip contains 25 SWW devices layed out in a 5 by 5 matrix. From left to right the spin-wave waveguide's width varies, while from top to bottom the CPW design changes and the FM thickness varies. The difference in thickness between two adjacent devices along the wedge direction,  $0.112 \text{ \AA}$ , is smaller than the atomic radius of Fe ( $1.26 \text{ \AA}$ ). However even this minute difference gives rise to a continuous change in effective magnetization, as shown in Sec. 3.4.3. Thus, it is assumed that the difference between two adjacent SWWs lies in the distribution of the local thickness, and the numbers reported are the average of that distribution. While the gradient of thickness is extremely small, the range explored here, near the out-of-plane transition, provides a uniquely rich field of study. The indicated thicknesses have a large number of decimal numbers that does not reflect the real precision, however we left them to distinguish the devices more easily.

Table 2.2: Device repository. The indicated thickness is the nominal thickness, obtained from the deposition machine’s calibration data. The CPW designs A, B and C are summarized in Tab. 2.1. The last two columns indicate which type of experiments were performed on the device (ST-FMR, SWR and BLS).

Device	FeCoB thickness (nm)	CPW design	SWW width ( $\mu\text{m}$ )	Measurements performed ( $\mu\text{m}$ )
2-B3	1.16	none	1	ST-FMR
2-C3	1.171	A	1	ST-FMR
2-D3	1.182	B	1	ST-FMR
2-E3	1.193	C	1	ST-FMR
14-B3	1.233	none	1	ST-FMR
14-C3	1.244	A	1	ST-FMR
14-E3	1.266	C	1	ST-FMR
16-C2	1.244	A	2	SWR
16-C3	1.244	A	1	SWR
16-D3	1.255	B	1	SWR
16-E3	1.266	C	1	SWR
7-B3	1.306	none	1	ST-FMR
7-C1	1.317	A	5	ST-FMR+SWR
7-C2	1.317	A	2	ST-FMR+SWR
7-C3	1.317	A	1	ST-FMR
7-C4	1.317	A	0.5	ST-FMR
7-C5	1.317	A	0.25	ST-FMR
7-D1	1.328	B	5	ST-FMR+SWR
7-D2	1.328	B	2	BLS
7-E1	1.339	C	5	ST-FMR+SWR
8-C1	1.317	A	5	ST-FMR
8-D1	1.328	B	5	ST-FMR
8-D3	1.328	B	1	ST-FMR
5-B3	1.306	none	1	ST-FMR
5-C3	1.317	A	1	ST-FMR
5-D3	1.328	B	1	ST-FMR
5-E3	1.339	C	1	ST-FMR

## Chapter 3

# Spin-orbit torques and damping in Ta/FeCoB/MgO

The aim of this chapter is to characterize the strength of the damping-like and field-like torques (given by  $\beta_{dl}$  and  $\beta_{fl}$  in Eqs. (1.83) and (1.85)) for the PMA SWW of Ta/FeCoB/MgO. For this we use a ferromagnetic resonance (FMR) technique and analyze the resonance peak position and linewidth. The damping-like torque is expected to affect the linewidth and the field-like torque the peak position when a DC current is injected into the SWW. To extract the damping-like torque and field-like torque amplitudes, we first characterize the material parameters such as saturation magnetization, PMA value and damping parameter alpha in absence of a DC current. Indeed, we seek to investigate the behavior of spin-waves in an ultrathin material in which the demagnetizing field is almost compensated by the perpendicular magnetic anisotropy, or even overcompensated, resulting in an out-of-plane magnetization. Once the FMR characterization is done, we can address the spin-orbit torques.

This chapter describes first the FMR technique used in our studies. We then analyze theoretically the dynamic susceptibility (see Chap. 1, Eq. (1.46)) considering different mechanisms that can contribute to the excitation of the dynamics and to the detected electrical signal. This is followed by the description of the experiments in zero DC current to extract the material parameters and finally the experiments under DC current to characterize the damping-like and field-like torque contributions in our SWW with perpendicular magnetic anisotropy.

### 3.1 Spin-torque resonance technique

A standard technique to obtain the material properties of a magnetic system is to use a broadband FMR setup [Kal06; Bil07; Gho12]. It allows for the magnetic probing of continuous thin films by exciting uniform ferromagnetic resonance. In this measurement the sample is placed across a microwave waveguide (such as a stripline or coplanar waveguide) which supplies an RF magnetic field, upon injection of an RF current into the

waveguide. The FMR is detected as an absorption peak of the transmitted RF power. The probed magnetic layer needs to be large enough that it sits across the waveguide and thick enough that the RF power absorbed by the total magnetic moment is detectable. The broadband FMR at our disposal at Spintec, for instance, requires thin film samples that are at least 2 mm wide and, to resolve FMR peaks for FeCoB, needs to have a thickness of at least 2.5 nm due to the small magnetic volume. The thickness range of 1-1.4 nm of the Ta/FeCoB SWW investigated in my thesis is hence below the resolution limit, so that a characterization as a continuous film using our broadband FMR was not possible. Therefore we setup a ferromagnetic resonance technique using electrical excitation and detection to characterize the SWW,<sup>1</sup> called spin-torque ferromagnetic resonance, though in the case of magnetic tunnel junctions it is often called spin-diode resonance [Tul05]. It includes many different excitation schemes and detection mechanisms, though the key difference with standard FMR techniques is that the detection is obtained by measuring a voltage drop across the studied device instead of measuring the absorbed RF power. A high frequency current generates an RF excitation such as an Ørsted field, spin-transfer torque in magnetic tunnel junctions [Tul05; San06] or spin-orbit torques in bilayer systems with strong spin-orbit interaction [Liu11]. Generally, the magnetization is considered to be excited uniformly and the amplitude of the excitation becomes maximum at resonance, i.e. when the excitation frequency is equal to the FMR frequency. Depending on the type of device, the detection relies on one or several rectification effects such as anisotropic magnetoresistance [Mec07; Yam07], tunneling magneto-resistance [Tul05; San06] or the combined effects of spin-pumping and the inverse spin Hall effect [Sai06; Mos10; Aze11]. The rectification creates a detectable DC voltage when the magnetization is precessing at resonance.<sup>2</sup> For the Ta/FeCoB/MgO system, we expect the magnetization to be excited by a combination of an Ørsted field and spin-orbit torques, and the detection to arise from a combination of AMR and iSHE rectification. The analytical expressions for all these excitation schemes and these rectification effects will be investigated in Sec. 3.2 and 3.3. Here we first describe the experimental setup. We will discuss the results on ST-FMR with zero DC current  $I_{dc} = 0$  in Sec. 3.4 and with  $I_{dc} \neq 0$  in Sec. 3.5.

The experimental setup is shown in Fig. 3.1. The device is placed on an electrically isolated platform in the gap of an electromagnet capable of supplying up to 170 mT in the plane of the device, as shown in Fig. 3.2. An RF probe is used to contact the ends of the SWW, represented by the points *A* and *B* in Figs. 2.1 and 3.2. An analog RF signal generator is used to deliver RF power to the device via the high frequency port of a bias-T, while the low frequency port is connected to a Keithley source-meter, for measuring voltage and supplying direct current as needed. Thus, in ST-FMR all currents flow through the length of the Ta/FeCoB/MgO SWW. In our experiments, the frequency of the RF current is kept constant while the external field is swept across the resonance.

In order to improve the signal-to-noise ratio of the rectification signal generated at

---

<sup>1</sup>In collaboration with A. Timopheev, A. Calafora and T. Brächer.

<sup>2</sup>It is relatively easy to detect a DC signal when exciting the system with an RF current, compared to detecting an RF signal when exciting with an RF current at the same frequency.

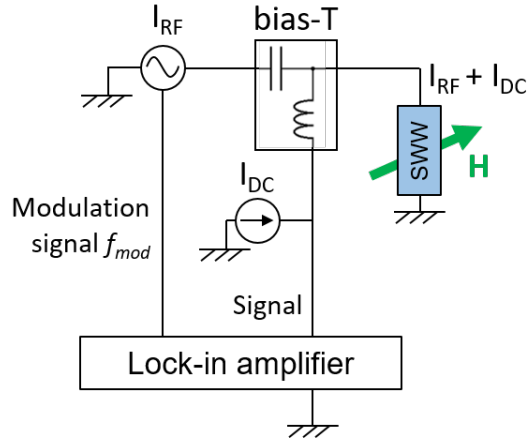


Figure 3.1: ST-FMR setup schematic. An electromagnet generates an in-plane field centered on the spin-wave waveguide, whose terminals are connected via an RF probe to the combined port of a bias tee. The high frequency port is connected to an RF generator, and the low frequency port is connected to a current source and a lock-in amplifier. The lock-in amplifier supplies a low frequency signal to the RF generator that modulates the outputted RF power, allowing the lock-in amplifier to increase the signal-to-noise ratio of the voltage detected at the terminals of the SWW.

resonance, a lock in amplifier (LIA) is used. The LIA provides a sinusoidal reference signal at a frequency of  $f_{mod} = 10.141$  kHz to the RF generator, which is then set to deliver an RF current sinusoidally modulated in power at  $f_{mod}$ . The LIA input is connected to the low frequency port of the bias-T and measures the DC signal at an enhanced signal-to-noise ratio. The modulation frequency and the bias-T were carefully chosen so that  $f_{mod}$  is higher than the cutoff frequency of the high frequency port of the bias-T and at the same time lower than the cutoff frequency of the low frequency port.

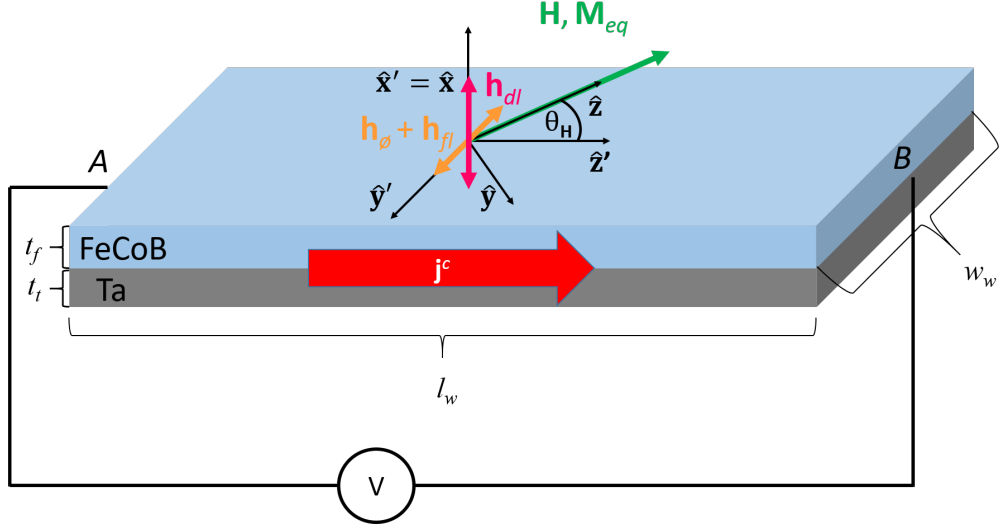


Figure 3.2: Schematic of ST-FMR showing the two coordinate bases used. The magnetization is saturated by an external field  $\mathbf{H} \parallel \hat{\mathbf{z}}$  applied in the plane, at an angle  $\theta_H$  with the long axis of the spin-wave waveguide, and the equilibrium magnetization  $\mathbf{M}_{eq}$  is aligned with  $\mathbf{H}$ . An RF current density  $\mathbf{j}^c \parallel \hat{\mathbf{z}}'$  is driven through the SWW, resulting in dynamic Ørsted  $\mathbf{h}_\phi$ , field-like  $\mathbf{h}_f$  and damping-like  $\mathbf{h}_{dl}$  fields acting on the magnetization. The rectified voltage is measured between  $A$  and  $B$ .

### 3.2 RF Excitation mechanisms

The configuration of the ST-FMR experiment is shown in Fig. 3.2. In an ST-FMR experiment, the charge current density vector  $\mathbf{j}^c$  and the external field vector  $\mathbf{H}$  are not necessarily collinear, and thus they each have their respective coordinate system (see Fig. 3.2): the external field is set parallel to  $\hat{\mathbf{z}}$  while the current density vector is parallel to  $\hat{\mathbf{z}}'$ , and  $\theta_H$  is the angle between the two bases.

In the spin-wave waveguides studied in this work, the current flows through both the FeCoB and Ta layers. For the sake of simplicity, we assume in this section that the whole current only goes through the Ta layer, and that the magnetization is uniform and saturated by the external field. This current then creates at least three effects: an Ørsted field, a field-like torque and a damping-like torque. In ST-FMR experiments, the magnetization is excited by the RF current, a priori via a combination of all three phenomena. The RF current generates an Ørsted field and spin-orbit torques that have a dynamic effect on the magnetization. The effect of each type of RF excitation will be discussed in the following subsections.

Moreover, a DC current can be added to the RF current, giving rise to a DC Ørsted field and DC spin-orbit torques. The effects of these DC terms affect the susceptibility terms directly, which will also be detailed in the following subsections.

### 3.2.1 Excitation by RF Ørsted field or RF field-like torque

Here we address only the RF Ørsted field and the RF field-like torque excitation. We assume that the current flows through the Ta layer and that it creates an Ørsted field that we calculate using the Biot-Savart law. It is assumed to be uniform and totally in the plane. In reality, due to the rectangular cross-section of the SWW, the in-plane Ørsted field component drops off at the lateral edges of the SWW, and an out-of-plane component appears. Numerically, we calculated that the in-plane Ørsted field component is at least at 95% of its maximum strength for more than 95% of the volume of the SWW.

We assume that the effective field of the field-like torque, defined in Eq. (1.83), is uniform across the SWW. Thus it has the same symmetry as the in-plane Ørsted field component, under the assumption described in the paragraph above. The result is that it may be impossible to differentiate the two effects. The effective RF field of the field-like torque  $\mathbf{h}_\mathbf{fl}$  and the Ørsted field  $\mathbf{h}_\phi$  are taken into account by replacing the RF excitation field  $\mathbf{h}$  in Eq. (1.34) by:

$$\mathbf{h} = \mathbf{h}_\mathbf{fl} + \mathbf{h}_\phi \quad (3.1)$$

and the calculations are identical as those performed in Sec. 1.2.4. The resulting susceptibility components are given as a function of applied frequency in Eq. (1.44) and of applied field in Eq. (1.46). Therefore, we expect the field-like torque to create the same excitation as the Ørsted field, and their effects to either add or subtract from each other depending on their relative phase.

In the SWW geometry presented here, where the excitation current flows along the SWW long axis, under the assumptions taken so far, we define the excitation in the basis of  $\mathbf{H}$ :

$$\mathbf{h} = \begin{pmatrix} 0 \\ h_{fl,y} + h_{\phi,y} \end{pmatrix} \quad (3.2)$$

where  $h_{fl,y}$  and  $h_{\phi,y}$  are the projections of  $\mathbf{h}_\mathbf{fl}$  and  $\mathbf{h}_\phi$  onto  $\hat{\mathbf{y}}$ ; there is no out-of-plane component due to this excitation.

### 3.2.2 Excitation by RF damping-like torque

In this subsection, we address a uniform RF damping-like torque as the excitation. The LLG equation including the spin-orbit torques was given in Eq. (1.73). Keeping only the damping-like torque and using Eq. (1.84), the LLG equation becomes:

$$\frac{d\mathbf{M}}{dt} = -\gamma\mu_0(\mathbf{M} \times \mathbf{H}_{\text{eff}}) + \frac{\alpha}{M_s} \left( \mathbf{M} \times \frac{d\mathbf{M}}{dt} \right) - \frac{\gamma\beta_{dl}}{M_s} \mathbf{M} \times (\mathbf{M} \times (\mathbf{j}^c \times \hat{\mathbf{n}})) \quad (3.3)$$

where  $\hat{\mathbf{n}} = \hat{\mathbf{x}}$  and where  $\mathbf{j}^c$  is the RF current density vector, and the effective field is written, using the notations in Sec. 1.2.3:

$$\mathbf{H}_{\text{eff}} = \mathbf{H} + \mathbf{m} \cdot \hat{\mathbf{x}} \left( \frac{2K_i}{\mu_0 M_s^2 t_f} - 1 \right) \hat{\mathbf{x}} \quad (3.4)$$

In contrast to the field-like torque, the damping-like torque cannot be included in the effective field due to the double cross-product with the magnetization. However to keep the same notation as in Eq. (1.28), with  $\mathbf{h}_{\text{dl}}$  as the excitation, we rewrite Eq. (3.3):

$$\frac{d\mathbf{M}}{dt} = -\gamma\mu_0(\mathbf{M} \times \mathbf{H}_{\text{eff}}) + \frac{\alpha}{M_s} \left( \mathbf{M} \times \frac{d\mathbf{M}}{dt} \right) - \gamma\mu_0\mathbf{M} \times \mathbf{h}_{\text{dl}} \quad (3.5)$$

where  $\mathbf{h}_{\text{dl}}$  is the effective field of the RF damping-like torque, defined in Eq. (1.85). Here, with the RF current and the dynamic magnetization, we have:

$$\begin{aligned} \mathbf{h}_{\text{dl}} &= \frac{\beta_{\text{dl}}}{\mu_0 M_s} (\mathbf{M}_{\text{eq}} + \mathbf{m}) \times (\mathbf{j}^{\text{c}} \times \hat{\mathbf{n}}) \\ &= \frac{\beta_{\text{dl}}}{\mu_0 M_s} \mathbf{M}_{\text{eq}} \times (\mathbf{j}^{\text{c}} \times \hat{\mathbf{n}}) \end{aligned} \quad (3.6)$$

where we neglected the cross product of  $\mathbf{m}$  and  $\mathbf{j}^{\text{c}}$  due to the smallness of  $\beta_{\text{dl}}$ .  $\mathbf{h}_{\text{dl}}$  is assumed to be small enough that we are in the small angle approximation. Using the notations in Eqs. (1.26) and (1.37) and eliminating the second order quantities involving products of  $m_x$ ,  $m_y$ ,  $h_{\text{dl},x}$  and  $h_{\text{dl},y}$  (the projections of  $\mathbf{h}_{\text{dl}}$  onto  $\hat{\mathbf{x}}$  and  $\hat{\mathbf{y}}$ ), we obtain:

$$i\omega \begin{pmatrix} m_x \\ m_y \end{pmatrix} = \begin{pmatrix} m_y \\ m_x \end{pmatrix} - \omega_M \begin{pmatrix} -h_{\text{dl},y} \\ h_{\text{dl},x} \end{pmatrix} \begin{pmatrix} \omega_H - i\alpha\omega \\ \omega_H + \omega_M - \omega_K + i\alpha\omega \end{pmatrix}^T \quad (3.7)$$

After rearranging and solving for the magnetization components, we obtain the susceptibility tensor for an RF damping-like torque:

$$\bar{\bar{\chi}} = \frac{\omega_M}{\omega_0^2 - \omega^2 + i\alpha\omega(2\omega_H + \omega_M - \omega_K)} \begin{pmatrix} \omega_H & i\omega \\ -i\omega & \omega_H + \omega_M - \omega_K \end{pmatrix} \quad (3.8)$$

where the resonance frequency  $\omega_0^2 = \omega_H(\omega_H + \omega_M - \omega_K)$  is the same as in Eq. (1.38), after neglecting the term in  $\alpha^2\omega^2$ . The terms  $i\alpha\omega$  in the diagonal elements were also neglected. Thus, we find exactly the same Polder tensor as the case where the excitation is an Ørsted field or the field-like torque. The susceptibility components are given in Eq. (1.44). In the SWW geometry, the excitation field due to the damping-like torque given in Eq. (3.6) does not have a  $y$  component, and only the  $x$  component is relevant:

$$\mathbf{h}_{\text{dl}} = \begin{pmatrix} h_{\text{dl},x} \\ h_{\text{dl},y} \end{pmatrix} = \begin{pmatrix} \frac{-\beta_{\text{dl}} M_s j_z^{\text{c}}}{\mu_0} \\ 0 \end{pmatrix} \quad (3.9)$$

where  $j_z^{\text{c}}$  is the projection of the charge current density vector along the axis of the external field,  $\hat{\mathbf{z}}$ . Thus, the only non-zero component of the excitation field is parallel to  $\hat{\mathbf{x}}$ , whereas for the Ørsted field and the field-like torque, it is parallel to  $\hat{\mathbf{y}}$  (see Eq. (3.2)). This will select different susceptibility components and will therefore lead to different expressions of the detected signal, which also depend on the detection mechanism (AMR, iSHE, etc.).

### 3.2.3 Influence of a DC current on resonance conditions

Next we derive the susceptibility tensor in the presence of DC torques, created via a DC current in the SWW. The DC current creates a DC Ørsted field and a DC field-like torque, as well as a DC damping-like torque. The projection of the Ørsted field and the effective field of the field-like torque onto the axis of the external field do not change the expression of the susceptibilities, beyond a shift of the resonance frequency. The resonance shift can be obtained by substituting  $\omega_H$  in Eq. (1.38) by:

$$\omega'_H = \gamma\mu_0(H + H_s) \quad (3.10)$$

where  $H_s$  is the projection of the DC Ørsted field and the DC field-like torque onto  $\hat{\mathbf{z}}$ , the axis parallel to the external field  $\mathbf{H}$ . A schematic is given in Fig. 3.2. Given that the Ørsted field can be estimated, a study of the resonance field shift vs. current will allow us to extract the field-like torque amplitude  $\beta_{fl}$ .

The components of these fields that are perpendicular to the external field will induce a shift of the equilibrium magnetization, i.e., the direction around which the dynamic magnetization will precess. This may change the expressions of the susceptibilities because it requires writing the LLG equation in a new basis, in which the expression of the effective field  $\mathbf{H}_{\text{eff}}$  is more complicated. In our work, we neglect this shift because the external field applied at resonance is up to 2 orders of magnitude greater than the DC Ørsted field and DC field-like torque, as the experimental results in Sec. 3.5.1 will show. Thus, we consider that the magnetization equilibrium is unmodified by the DC Ørsted field and the DC field-like torque produced by the DC current.

### 3.2.4 Influence of the DC damping-like torque on resonance conditions

Next we calculate the susceptibility under excitation from an RF Ørsted field, in the presence of a DC damping-like torque. Similarly to the previous section, a damping-like torque can shift the equilibrium magnetization slightly though this can also be neglected due to the smallness of the damping-like torque vs. the applied field. For completeness now we provide here the equation that has to be solved to determine the new static equilibrium. First, we take the LLG equation with  $\frac{d\mathbf{M}}{dt} = 0$ :

$$0 = -\gamma\mu_0 (\mathbf{M} \times \mathbf{H}_{\text{eff}}^0) - \frac{\gamma\beta_{dl}}{M_s} \mathbf{M} \times (\mathbf{M} \times \mathbf{P}) \quad (3.11)$$

where  $\mathbf{P} = \mathbf{J}^c \times \hat{\mathbf{n}}$  and  $\mathbf{H}_{\text{eff}}^0$  is the expression of the effective field at equilibrium. By setting  $\mathbf{M} = (0, 0, M_s)$ , we implicitly set the coordinate system to the one in which  $\hat{\mathbf{z}}$  is parallel to the equilibrium magnetization. Thus, we obtain the equilibrium condition from the  $\hat{\mathbf{z}}$  component of the vector equation (3.11):

$$\begin{aligned} 0 &= \mu_0 (m_x H_{eff,y}^0 - m_y H_{eff,x}^0) + \beta_{dl} (m_x P_x + m_y P_y) \\ 0 &= m_x (\mu_0 H_{eff,y}^0 + \beta_{dl} P_x) + m_y (-\mu_0 H_{eff,x}^0 + \beta_{dl} P_y) \end{aligned} \quad (3.12)$$

where  $H_{eff,i}^0$  are the components of the effective field at equilibrium. Excluding trivial solutions such as  $m_x = 0$  and  $m_y = 0$ , the only solution of interest is:

$$\begin{aligned}\beta_{dl}P_x + \mu_0 H_{eff,y}^0 &= 0 \\ \beta_{dl}P_y - \mu_0 H_{eff,x}^0 &= 0\end{aligned}\quad (3.13)$$

These are the equilibrium conditions imposed by the DC damping-like torque, as  $\mathbf{H}_{\text{eff}}^0$  depends on the equilibrium position and thus solving Eq. (3.13) will give the equilibrium position.

The next step is to determine the susceptibility in presence of the DC damping-like torque. The dynamic LLG equation with a damping-like torque is written:

$$\frac{d\mathbf{M}}{dt} = -\gamma\mu_0 (\mathbf{M} \times \mathbf{H}_{\text{eff}}) + \frac{\alpha}{M_s} \left( \mathbf{M} \times \frac{d\mathbf{M}}{dt} \right) - \frac{\gamma\beta_{dl}}{M_s} \mathbf{M} \times (\mathbf{M} \times \mathbf{P}) \quad (3.14)$$

The last term in the equation must be linearized around the equilibrium position defined by Eq. (3.13). This is done similarly to the linearization performed in Sec. 1.2.3. From Eqs. (3.2) and (3.9), the dynamic excitation field due to the Ørsted field, field-like torque and damping-like torque is written:

$$\mathbf{h} = \begin{pmatrix} h_x^\dagger \\ h_y^\dagger \\ 0 \end{pmatrix} = \begin{pmatrix} h_{dl,x} \\ h_{fl,y} + h_{\phi,y} \\ 0 \end{pmatrix} \quad (3.15)$$

where we use the expressions with daggers in the following equations for convenience. Replacing the vectors in Eq. (3.14) by their expressions, we have:

$$\begin{aligned}i\omega \begin{pmatrix} m_x \\ m_y \\ 0 \end{pmatrix} &= -\gamma\mu_0 \begin{pmatrix} m_y \left( H_{eff,z}^0 \right) - M_s \left( H_{eff,y}^0 + h_y^\dagger \right) \\ M_s \left( H_{eff,x}^0 + h_x^\dagger \right) - m_x \left( H_{eff,z}^0 \right) \\ m_x \left( H_{eff,y}^0 + h_y^\dagger \right) - m_y \left( H_{eff,x}^0 + h_x^\dagger \right) \end{pmatrix} \\ &+ i\alpha\omega \begin{pmatrix} -m_y \\ m_x \\ 0 \end{pmatrix} \\ &- \gamma\beta_{dl} \begin{pmatrix} -M_s P_x - m_x P_z \\ -M_s P_y + m_y P_z \\ m_x P_x + m_y P_y \end{pmatrix}\end{aligned}\quad (3.16)$$

Neglecting second order quantities involving products of  $m_i$  and  $h_i^\dagger$ , and using Eq. (3.13) to eliminate terms, we obtain:

$$i\omega \begin{pmatrix} m_x \\ m_y \end{pmatrix} = -\gamma\mu_0 \begin{pmatrix} m_y H_{eff,z}^0 - M_s h_y^\dagger \\ M_s h_x^\dagger - m_x H_{eff,z}^0 \end{pmatrix} + i\alpha\omega \begin{pmatrix} -m_y \\ m_x \end{pmatrix} - \gamma\beta_{dl} \begin{pmatrix} -m_x P_z \\ m_y P_z \end{pmatrix} \quad (3.17)$$

Using the expression of the effective field, given in Eq. (1.34), we have:

$$i\omega \begin{pmatrix} m_x \\ m_y \end{pmatrix} = -\gamma\mu_0 \begin{pmatrix} m_y H_z - M_s h_y^\dagger \\ M_s \left( h_x^\dagger + m_x \left( \frac{2K_i}{\mu_0 M_s^2 t_f} - 1 \right) \right) - m_x H_z \end{pmatrix} + i\alpha\omega \begin{pmatrix} -m_y \\ m_x \end{pmatrix} - \gamma\beta_{dl} \begin{pmatrix} -m_x P_z \\ m_y P_z \end{pmatrix} \quad (3.18)$$

Solving for the excitation fields  $h_x^\dagger$  and  $h_y^\dagger$  and using Eqs. (1.26) and (1.37) yields:

$$\begin{pmatrix} h_x^\dagger \\ h_y^\dagger \end{pmatrix} = \frac{1}{\omega_M} \begin{pmatrix} \omega_H + \omega_M - \omega_K + i\alpha\omega & -i\omega + \gamma\beta_{dl}P_z \\ i\omega - \gamma\beta_{dl}P_z & \omega_H + i\alpha\omega \end{pmatrix} \begin{pmatrix} m_x \\ m_y \end{pmatrix} \quad (3.19)$$

Finally, we obtain the susceptibility tensor in the case of a DC damping-like torque:

$$\begin{aligned} \bar{\chi} &= \frac{\omega_M}{\omega_0^2 - \omega^2 + i\omega(\alpha(2\omega_H + \omega_M - \omega_K) - 2\gamma\beta_{dl}P_z)} \begin{pmatrix} \omega_H & i\omega - \gamma\beta_{dl}P_z \\ -i\omega + \gamma\beta_{dl}P_z & \omega_H + \omega_M - \omega_K \end{pmatrix} \\ \bar{\chi} &= \chi_p \begin{pmatrix} \omega_H & i\omega - \gamma\beta_{dl}P_z \\ -i\omega + \gamma\beta_{dl}P_z & \omega_H + \omega_M - \omega_K \end{pmatrix} \end{aligned} \quad (3.20)$$

where we neglected the  $i\alpha\omega$  terms in the diagonal elements, and the prefactor is called  $\chi_p$ . The resonance frequency, which is given by the real part of the denominator of  $\chi_p$ , is  $\omega_0^2 = \omega_H(\omega_H + \omega_M - \omega_K)$ , after neglecting the second order quantities  $(\alpha\omega)^2$  and  $(\gamma\beta_{dl}P_z)^2$ . It is the same as the one given in Eq. (1.38).

The imaginary part of the denominator of  $\chi_p$  in Eq. (3.20) is responsible for the damping and the linewidth of the resonance peak. Following the same steps that allowed us to transform Eq. (1.44) into Eq. (1.47), we write  $\chi_p$  in Eq. (3.20) as a function of the applied field  $H$  and the resonance field  $H_r$ :

$$\chi_p = \frac{1}{\gamma\mu_0} \frac{M_s}{H + H_r + M_{eff}} \frac{(H - H_r) - i\frac{\omega}{\gamma\mu_0} \frac{\alpha(M_{eff} + 2H) - 2\beta_{dl}P_z/\mu_0}{H + H_r + M_{eff}}}{(H - H_r)^2 + \left( \frac{\omega}{\gamma\mu_0} \frac{\alpha(M_{eff} + 2H) - 2\beta_{dl}P_z/\mu_0}{H + H_r + M_{eff}} \right)^2} \quad (3.21)$$

where we define a generalized expression for the linewidth in the presence of a damping-like torque, as was done in Eq. (1.50):

$$\Delta H_g = \frac{\omega}{2\gamma\mu_0} \frac{\alpha(M_{eff} + 2H) - 2\beta_{dl}P_z/\mu_0}{H + H_r + M_{eff}} \quad (3.22)$$

which at resonance gives:

$$\begin{aligned} \lim_{H \rightarrow H_r} \Delta H_g &= \frac{2\omega}{\gamma\mu_0} \left( \alpha - \frac{2\beta_{dl}P_z/\mu_0}{2H_r + M_{eff}} \right) & \Delta H_{dl} &= -\frac{4\omega}{\gamma\mu_0} \frac{\beta_{dl}P_z/\mu_0}{2H_r + M_{eff}} \\ &= \Delta H_0 + \Delta H_{dl} \end{aligned} \quad (3.23)$$

where  $\Delta H_0$  is given in Eq. (1.50). Thus, the total linewidth is the sum of the Gilbert-type contribution  $\Delta H_0$  and of the linewidth contribution of the damping-like torque  $\Delta H_{dl}$ .

Since the sign of  $P_z$  is dependent on the sign of the DC current, it is straightforward to see that for a given polarity the damping-like torque will reduce the linewidth and for the opposite polarity it will increase it. Thus, a study of the linewidth vs. applied current should allow us to characterize the damping-like torque coefficient  $\beta_{dl}$ .

### 3.3 Electrical detection of magnetization dynamics

In this section we calculate the expression of the DC signals that we can detect in our ST-FMR experiment when the magnetization is resonantly excited by one of the RF fields discussed in Sec. 3.2.1 and 3.2.2. In magnetic stacks where there are two conductive layers, the ferromagnetic and normal metal layers, we have considered two possible sources for detecting a DC voltage in response to magnetization dynamics. The first is a rectification due to anisotropic magnetoresistance, which generates a DC voltage in the FM layer, and the second is due to the combined effects of spin-pumping and inverse spin Hall effect, which generates a DC current in the NM layer. In both cases, the signal is calculated by combining the excitation of the magnetization, represented by the susceptibility tensor and the corresponding excitation field, Eq. (3.15), with the relevant phenomena responsible for the detection of the signal, AMR or the iSHE.

It is noted that depending on the excitation field and mechanisms (see Sec. 3.2), different components of the susceptibility tensor will be responsible for the dynamic response and will lead to different expressions and angular dependencies for the same detection scheme. Therefore, in the next sections we derive the expression for the DC voltage signals combining the different excitation with the different detection schemes.

#### 3.3.1 DC signal via to anisotropic magnetoresistance

In this section we will calculate the voltage resulting from AMR, first with the Ørsted field (or equivalently the field-like torque) as the excitation, with  $\mathbf{h} \parallel \hat{\mathbf{y}}'$ , then with the damping-like torque as the excitation:  $\mathbf{h} \parallel \hat{\mathbf{x}}$ . The DC signal arises from the interplay of the oscillating anisotropic magnetoresistance through the oscillating magnetization, and the injected RF current. The magnetization in previous sections is expressed in the  $(\hat{\mathbf{x}}, \hat{\mathbf{y}}, \hat{\mathbf{z}})$  basis (see Fig. 3.2), where  $\hat{\mathbf{z}}$  is aligned with the static magnetic field  $\mathbf{H}$ , assumed to be in the plane of the thin film, at an angle  $\theta_H$  with respect to the long axis of the SWW. On the other hand, the current density vector  $\mathbf{J}$ , also in the thin film plane, is more easily expressed in its own basis  $(\hat{\mathbf{x}}', \hat{\mathbf{y}}', \hat{\mathbf{z}}')$ , where  $\mathbf{J}$  is parallel to  $\hat{\mathbf{z}}'$  which is the SWW long axis. The two coordinate systems are shown in Fig. 3.2, where the angle between  $\hat{\mathbf{z}}$  and  $\hat{\mathbf{z}}'$  is  $\theta_H$ , and  $\hat{\mathbf{x}} = \hat{\mathbf{x}}'$ . Thus it is necessary to define a rotation matrix  $U$  between the coordinate system defining the equilibrium direction of  $\mathbf{M}$ , called  $b$ , and the primed coordinate system defining the device geometry, called  $b'$ :

$$\begin{pmatrix} 1 & 0 & 0 \\ 0 & \cos \theta_H & -\sin \theta_H \\ 0 & \sin \theta_H & \cos \theta_H \end{pmatrix} \begin{pmatrix} x \\ y \\ z \end{pmatrix}_b = \begin{pmatrix} x' \\ y' \\ z' \end{pmatrix}_{b'} \quad (3.24)$$

Thus, the components of a vector in the basis  $b'$  can be obtained by calculating  $\mathbf{a}' = U\mathbf{a}$ . For clarity, some vectors, matrices, and their components will be written with a prime symbol to indicate that they are written in the primed basis  $b'$ . The static and dynamic magnetizations become, in the primed coordinate system:

$$\mathbf{M}'_{\mathbf{eq}} = \begin{pmatrix} 0 \\ -M_s \sin \theta_H \\ M_s \cos \theta_H \end{pmatrix} \quad \mathbf{m}' = \begin{pmatrix} m_x \\ m_y \cos \theta_H \\ m_y \sin \theta_H \end{pmatrix} \quad (3.25)$$

where  $m_x$  and  $m_y$  are the dynamic components of the magnetization in the  $(\hat{\mathbf{x}}, \hat{\mathbf{y}}, \hat{\mathbf{z}})$  coordinate system. Using the general expression for the voltage that arises from AMR, given in Eq. (1.87), we write:

$$V_{AMR} = \int_0^{l_w} \frac{\Delta \rho_{AMR}}{M_s^2} (\mathbf{j}^c \cdot \mathbf{M}') \mathbf{M}' \cdot d\mathbf{l}' \quad (3.26)$$

where  $\mathbf{j}^c$  is the RF charge current flowing in the SWW and we integrate the electric field due to AMR along  $\hat{\mathbf{z}}'$  across the length  $l_w$  of the SWW (between the two contact points  $A$  and  $B$  shown in Fig. 3.2). Taking the time-averaged value of the AMR voltage, we obtain the DC voltage that arises from AMR, assuming a uniform magnetization and electric field:

$$\begin{aligned} \langle V_{amr} \rangle &= \frac{l_w \Delta \rho_{amr}}{M_s^2} \langle (\mathbf{j}^c \cdot \mathbf{M}') (\mathbf{M}' \cdot \hat{\mathbf{z}}') \rangle \\ &= \frac{l_w \Delta \rho_{amr}}{M_s^2} \langle j_{z'}^c (\mathbf{M}' \cdot \hat{\mathbf{z}}')^2 \rangle \end{aligned} \quad (3.27)$$

where  $\mathbf{j}^c = j_{z'}^c \hat{\mathbf{z}}'$ , and the symbols  $\langle \ \rangle$  indicate time-averaging. Using Eq. (3.25) to express  $\mathbf{M}' = \mathbf{M}'_{\mathbf{eq}} + \mathbf{m}'$ , we have:

$$\langle V_{amr} \rangle = \frac{l_w \Delta \rho_{amr}}{M_s^2} \langle j_{z'}^c (M_s^2 \cos^2 \theta_H + m_y^2 \sin^2 \theta_H + 2M_s m_y \cos \theta_H \sin \theta_H) \rangle \quad (3.28)$$

In the equation above, only  $j_{z'}^c$  and  $m_y$  have a time dependence. Therefore only uneven powers of  $m_y$  inside the parenthesis can give rise to rectification via the product with  $j_{z'}^c$ , which leaves only the last term. Using Eqs. (3.15) and (1.21) and the susceptibility tensor, we can express  $m_y$  as:

$$m_y = -i\chi_{xy} h_x^\dagger + \chi_{yy} h_y^\dagger \quad (3.29)$$

where  $h_x^\dagger$  and  $h_y^\dagger$  are the complex components of the RF fields in the  $(\hat{\mathbf{x}}, \hat{\mathbf{y}}, \hat{\mathbf{z}})$  coordinate system. This equation shows that different components of the susceptibility tensor will contribute to the detected signal, depending on the excitation, as evaluated further.

### Excitation by a field-like torque

Let us first treat the case where the RF field is generated by the field like torque or the Ørsted field. The RF current flows in the SWW in the  $\hat{\mathbf{z}}'$  direction and the components of  $\mathbf{h}$  are more easily written in the primed coordinate system. Setting the damping-like term  $h_{dl,x} = h_x^\dagger = 0$  in Eq. (3.29) and using the inverse of the rotation matrix  $U$  in Eq. (3.24), we have:

$$\begin{aligned} m_y &= \chi_{yy} h_y^\dagger \\ &= \chi_{yy} \cos \theta_H h_{y'}^\dagger \end{aligned} \quad (3.30)$$

where  $h_{y'}^\dagger$  contains the projections on  $\hat{\mathbf{y}}'$  of the RF Ørsted field and the effective field of the field-like torque. They are assumed to be uniform in the volume of the SWW. The voltage in Eq. (3.28) becomes:

$$\begin{aligned} \langle V_{amr}^{fl} \rangle &= \frac{2l_w \Delta \rho_{amr}}{M_s} \cos^2 \theta_H \sin \theta_H \langle j_{z'}^c \chi_{yy} h_{y'}^\dagger \rangle \\ &= \frac{2l_w \Delta \rho_{amr}}{M_s} \cos^2 \theta_H \sin \theta_H \langle j_{z'}^c \chi_{yy} h_{y'}^\dagger \rangle \end{aligned} \quad (3.31)$$

We introduce the lineshape by expressing  $\chi_{yy}$  using its Lorentzian and dispersive components, given by Eq. (1.43):

$$\langle V_{amr}^{fl} \rangle = \frac{2l_w \Delta \rho_{amr}}{M_s} \cos^2 \theta_H \sin \theta_H \langle j_{z'}^c (D + iL) A_{yy} h_{y'}^\dagger \rangle \quad (3.32)$$

We will introduce the complex time dependence, which was ignored up until now, but first we remind that when dealing with complex variables, the real voltage is given by:

$$\mathcal{V}^r = \text{Re}(A) \text{Re}(B) \quad (3.33)$$

where  $A$  and  $B$  are complex numbers. Thus the real DC voltage that arises due to AMR in ST-FMR, between the electrodes of the ferromagnet is given by:

$$\begin{aligned} \langle \mathcal{V}_{amr}^{fl} \rangle &= \frac{2l_w \Delta \rho_{amr}}{M_s} \cos^2 \theta_H \sin \theta_H \left\langle \frac{I_f}{w_w t_f} \text{Re}(e^{i\omega t}) A_{yy} (H_{fl} + H_\phi) \text{Re}((D + iL)e^{i\omega t}) \right\rangle \\ &= \frac{2l_w \Delta \rho_{amr}}{w_w t_f M_s} I_f (H_{fl} + H_\phi) A_{yy} \cos^2 \theta_H \sin \theta_H \langle \cos(\omega t) (D \cos(\omega t) - L \sin(\omega t)) \rangle \\ &= \frac{l_w \Delta \rho_{amr}}{w_w t_f M_s} I_f (H_{fl} + H_\phi) A_{yy} D \cos^2 \theta_H \sin \theta_H \\ &\propto D \end{aligned} \quad (3.34)$$

where  $j_{z'}^c = \frac{I_f}{w_w t_f} e^{i\omega t}$ ,  $I_f$  being the real amplitude of the RF current flowing in the FM layer,  $w_w$  being the width of the SWW and  $t_f$  being the thickness of the ferromagnet;

$h_{y'}^\dagger = (H_{fl} + H_\emptyset)e^{i\omega t}$ , where  $H_\emptyset$  and  $H_{fl}$  are the real amplitude of the RF Ørsted field and of the RF effective field of the field-like torque. Both are proportional to the current flowing in the NM layer.

Since  $I_f$ ,  $H_{fl}$  and  $H_\emptyset$  are all proportional to the total RF current in the SWW, the signal is proportional to the RF power. Moreover, we find that the signal that arises from AMR rectification in the case of field excitation has a purely dispersive lineshape.

### Excitation by a damping-like torque

Now let us treat the same problem with the damping-like torque as the excitation source. We can start from Eq. (3.28). In this case, the excitation field, given in Eq. (3.9), only has one component involved in the magnetization dynamics, and since it aligned with  $\hat{\mathbf{x}}$ , it has the same expression in both coordinate systems. Thus, Eq. (3.29) becomes, with the field-like and Ørsted set to zero ( $h_y^\dagger = 0$ ) :

$$\begin{aligned} m_y &= -i\chi_{xy}h_x^\dagger \\ &= -i\chi_{xy}h_{dl,x'} \end{aligned} \quad (3.35)$$

Following the same steps down to Eq. (3.34), we obtain:

$$\begin{aligned} \langle \mathcal{V}_{amr}^{dl} \rangle &= \frac{2l\Delta\rho_{amr}}{M_s} \cos^2 \theta_H \sin \theta_H \left\langle \frac{I_f}{w_w t_f} \text{Re}(e^{i\omega t}) H_{dl} A_{xy} \text{Re}(-i(D + iL)e^{i\omega t}) \right\rangle \\ &= \frac{2l_w \Delta\rho_{amr}}{w_w t_f M_s} I_f H_{dl} A_{xy} \cos^2 \theta_H \sin \theta_H \langle \cos(\omega t) L \cos(\omega t) + D \sin(\omega t) \rangle \\ &= \frac{l_w \Delta\rho_{amr}}{w_w t_f M_s} I_f H_{dl} A_{xy} L \sin(2\theta_H) \cos \theta_H \\ &\propto L \end{aligned} \quad (3.36)$$

where  $h_{dl,x'} = H_{dl} e^{i\omega t}$  and  $H_{dl}$  is the real amplitude of the effective field of the damping-like torque and is proportional to the current flowing in the NM layer. The voltage here is proportional to the RF power as well.

Thus, we find that the signal that arises from AMR rectification in the case of damping-like torque excitation has a purely Lorentzian lineshape.

### Conclusion for AMR

The voltages for AMR rectification have a similar expression for the field-like excitation and the damping-like torque excitation. The dependence of both signals on the angle of the in-plane external field,  $\theta_H$ , is identical. The difference lies in the shape of the peak, which is dispersive for the field excitation, and Lorentzian for the damping-like torque excitation. Since most material systems with SOTs exhibit both field-like and damping-like torques, AMR rectification leads to a signal that is the sum of a Lorentzian and a dispersive lineshape. By fitting a linear combination of Lorentzian and dispersive functions to the resonance peak, one can determine the amplitudes of both contributions

and thus characterize the damping-like and the field-like torques. This property has been extensively used to determine the ratio between the strength of the damping-like and of the field-like torques, particularly in ferromagnetic materials with high AMR such as Py, which is often coupled with Pt for SOTs [Ski14; Nan15; Pai15]. One can then calculate the current density in the NM layer required to obtain the measured field-like torque, and then obtain the absolute strength of each spin-orbit torque.

### 3.3.2 DC signal via spin pumping and inverse spin Hall rectification

Now let us treat the other major source for generating a DC signal, the combination of spin-pumping and the inverse spin Hall effect. In an ST-FMR experiment, the magnetization is precessing around the effective magnetization which is largely dominated by the externally applied field, set along  $\hat{\mathbf{z}}$ . This magnetization precession generates, via spin-pumping, a spin current that flows in the  $x$  direction to the FM interface. If the device is a FM/NM bilayer system, where the NM is a metal with large spin-orbit coupling, i.e., it has a consequent spin Hall angle, then the spin current is converted into an orthogonal charge current via the iSHE.

The charge current leads to a voltage drop along the  $\hat{\mathbf{z}}'$  direction, measured between the two contacts  $A$  and  $B$  shown in the schematics of Fig. 3.2. Thus, the generated current density vector of interest is parallel to  $\hat{\mathbf{z}}'$ , which is at an angle  $\theta_H$  with respect to the applied field axis  $\hat{\mathbf{z}}$ . According to Eq. (1.80), the precession will create the following spin currents at the interface:

$$\begin{pmatrix} J_{x'x'}^{s0} \\ J_{x'y'}^{s0} \\ J_{x'z'}^{s0} \end{pmatrix}_{b'} = \frac{\hbar G_r}{4\pi M_s^2} \mathbf{M}' \times \frac{d\mathbf{M}'}{dt} \quad (3.37)$$

The charge current of interest is the one along  $\hat{\mathbf{z}}'$  and according to Eq. (1.79), it is created by the following spin currents via the iSHE:

$$J_{z'}^c = \frac{2e\theta_{SH}}{\hbar} (J_{x'y'}^s - J_{y'x'}^s) \quad (3.38)$$

We assume that there are no spin currents flowing in the  $\hat{\mathbf{y}}'$  direction that penetrate the Ta layer, and therefore that only the spin current flowing in the  $\hat{\mathbf{x}}'$  direction through the interface,  $J_{x'y'}^{s0}$ , contributes. In the primed coordinate system, we have:

$$\begin{aligned} J_{x'y'}^{s0} &= \frac{\hbar G_r}{4\pi M_s^2} \hat{\mathbf{y}}' \cdot \left( (\mathbf{M}'_{\text{eq}} + \mathbf{m}') \times \frac{d\mathbf{m}'}{dt} \right) \\ &= \frac{\hbar G_r}{4\pi M_s^2} (M_s \dot{m}_x \cos \theta_H + \sin \theta_H (m_y \dot{m}_x - m_x \dot{m}_y)) \end{aligned} \quad (3.39)$$

Following the same line of thought that led to Eq. (3.33), if we are interested in the real value of the spin current density, we must calculate it using the real values of the magnetization components when multiplying them:

$$J_{x'y'}^{s0} = \frac{\hbar G_r}{4\pi M_s^2} (M_s \text{Re}(\dot{m}_x) \cos \theta_H + \sin \theta_H (\text{Re}(m_y) \text{Re}(\dot{m}_x) - \text{Re}(m_x) \text{Re}(\dot{m}_y))) \quad (3.40)$$

Since only  $m_x$ ,  $m_y$ ,  $\dot{m}_x$  and  $\dot{m}_y$  have time dependence, the first term of the right hand side of the equation above disappears when taking the time average of the spin current, and we only have to calculate the last two terms  $\text{Re}(m_y)\text{Re}(\dot{m}_x) - \text{Re}(m_x)\text{Re}(\dot{m}_y)$ .

### Excitation by a field-like torque

First we will treat the excitation via an RF Ørsted field (or, equivalently, a field-like torque) created by a current flowing through the Ta layer and creating a RF homogeneous field along  $\hat{\mathbf{y}}'$ . The relationship between the magnetization and the excitation field, Eq. (1.21), becomes:

$$\begin{pmatrix} m_x \\ m_y \end{pmatrix} = \begin{pmatrix} \chi_{xx} & i\chi_{xy} \\ -i\chi_{xy} & \chi_{yy} \end{pmatrix} \begin{pmatrix} 0 \\ h_{y'}^\dagger \cos \theta_H \end{pmatrix} \quad (3.41)$$

where we used the rotation matrix  $U$  to write  $h_{y'}^\dagger$  (the sum of the Ørsted field and the effective field of the field-like torque) in the  $b$  basis. To calculate the last two terms of Eq. (3.40), we use Eq. (1.43) and the one above to express the magnetization components and their derivatives:

$$\begin{aligned} m_x &= ih_{y'}^\dagger A_{xy} \cos \theta_H (D + iL) & m_y &= h_{y'}^\dagger A_{yy} \cos \theta_H (D + iL) \\ \dot{m}_x &= -\omega h_{y'}^\dagger A_{xy} \cos \theta_H (D + iL) & \dot{m}_y &= i\omega h_{y'}^\dagger A_{yy} \cos \theta_H (D + iL) \end{aligned} \quad (3.42)$$

where the derivative of the Ørsted field is  $\dot{h}_{y'}^\dagger = i\omega h_{y'}^\dagger$ . Taking the real parts yields:

$$\begin{aligned} \text{Re}(m_x) &= (H_{fl} + H_\phi) A_{xy} \cos \theta_H (-D \sin(\omega t) - L \cos(\omega t)) \\ \text{Re}(\dot{m}_x) &= \omega (H_{fl} + H_\phi) A_{xy} \cos \theta_H (-D \cos(\omega t) + L \sin(\omega t)) \\ \text{Re}(m_y) &= (H_{fl} + H_\phi) A_{yy} \cos \theta_H (D \cos(\omega t) - L \sin(\omega t)) \\ \text{Re}(\dot{m}_y) &= \omega (H_{fl} + H_\phi) A_{yy} \cos \theta_H (-D \sin(\omega t) - L \cos(\omega t)) \end{aligned} \quad (3.43)$$

where  $h_{y'}^\dagger = (H_\phi + H_{fl})e^{i\omega t}$ , the real amplitudes of the Ørsted field and of the effective field of the field-like torque. The last two terms in the last line of Eq. (3.40) then become:

$$\begin{aligned} \text{Re}(m_y)\text{Re}(\dot{m}_x) - \text{Re}(m_x)\text{Re}(\dot{m}_y) &= -\omega (H_{fl} + H_\phi)^2 \cos^2 \theta_H \sin \theta_H A_{xy} A_{yy} (D^2 + L^2) \\ &= -\omega (H_{fl} + H_\phi)^2 \cos^2 \theta_H \sin \theta_H A_{xy} A_{yy} L \end{aligned} \quad (3.44)$$

where we used the equality<sup>3</sup>  $D^2 + L^2 = L$ . The spin current at the interface in Eq. (3.40) becomes:

$$\begin{aligned} \mathcal{J}_{x'y'}^{s_0} &= -\frac{\hbar\omega G_r}{4\pi M_s^2} (H_{fl} + H_\phi)^2 \cos^2 \theta_H \sin \theta_H A_{xy} A_{yy} L \\ &= \langle \mathcal{J}_{x'y'}^{s_0} \rangle \end{aligned} \quad (3.45)$$

<sup>3</sup>The result of  $D^2 + L^2$  depends on how  $D$  and  $L$  are defined. They are given in Eq. (1.48). However the result is always proportional to  $L$ .

The time dependence has disappeared, therefore the equation already gives the DC spin current at the interface. Combining Eq. (3.45) with Eq. (1.81), we have the expression of the spin current as a function of depth as it decays in the NM:

$$\langle \mathcal{J}_{x'y'}^s \rangle = \langle \mathcal{J}_{x'y'}^{s_0} \rangle \frac{\sinh((x - t_n)/l_{sd})}{\sinh(t_n/l_{sd})} \quad (3.46)$$

Then, by combining the equation above with Eq. (3.38) and integrating along the thickness and the width of the NM, we have an expression for the real charge current generated by the iSHE in the NM that flows along the  $\hat{z}'$  axis:

$$\begin{aligned} \langle \mathcal{I}_{z'}^c \rangle &= \frac{2e\theta_{SH}}{\hbar} \langle \mathcal{J}_{x'y'}^{s_0} \rangle \int_{-\frac{w_w}{2}}^{\frac{w_w}{2}} \int_0^{t_n} \frac{\sinh((x - t_n)/l_{sd})}{\sinh(t_n/l_{sd})} dx' dy' \\ &= -\frac{2w_w l_{sd} e \theta_{SH}}{\hbar} \langle \mathcal{J}_{x'y'}^{s_0} \rangle \tanh\left(\frac{t_n}{2l_{sd}}\right) \end{aligned} \quad (3.47)$$

where  $t_n$  is the thickness of the NM and  $l_{sd}$  its spin diffusion length, and  $w_w$  is the width of the SWW. Replacing  $\mathcal{J}_{x'y'}^{s_0}$  by its expression in Eq. (3.45) we obtain:

$$\langle \mathcal{I}_{z'}^c \rangle = \frac{w_w e G_r l_{sd} \theta_{sh}}{2\pi M_s^2} \omega (H_{fl} + H_\phi)^2 \cos^2 \theta_H \sin \theta_H A_{xy} A_{yy} L \tanh\left(\frac{t_n}{2l_{sd}}\right) \quad (3.48)$$

Finally, we can write the DC voltage that arises due to the combined effects of spin-pumping and the inverse spin Hall effect, under an  $\text{\AA}$ rsted field (or equivalently, a field-like torque) excitation:

$$\langle \mathcal{V}_{ishe}^{fl} \rangle = \frac{\rho_n l_w e G_r l_{sd} \theta_{sh}}{2\pi t_n M_s^2} \omega (H_{fl} + H_\phi)^2 \cos^2 \theta_H \sin \theta_H A_{xy} A_{yy} L \tanh\left(\frac{t_n}{2l_{sd}}\right) \quad (3.49)$$

where  $\rho_n$  is the resistivity of the NM and  $l_w$  the length of the SWW. Thus, we find that the signal that is generated by the iSHE in the case of field excitation has a purely Lorentzian lineshape.

### Excitation by damping-like excitation

Now we shall calculate the voltage that arises from a damping-like torque excitation. Starting from Eq. (3.40), we must calculate the last two terms. The relationship between the magnetization and the equivalent field of the damping-like torque is given by:

$$\begin{pmatrix} m_x \\ m_y \end{pmatrix} = \begin{pmatrix} \chi_{xx} & i\chi_{xy} \\ -i\chi_{xy} & \chi_{yy} \end{pmatrix} \begin{pmatrix} h_{dl,x'} \cos \theta_H \\ 0 \end{pmatrix} \quad (3.50)$$

where we used the rotation matrix defined in Eq. (3.24). The components of the magnetization and their derivatives are:

$$\begin{aligned} m_x &= h_{dl,x'} A_{xx} \cos \theta_H (D + iL) & m_y &= -i h_{dl,x'} A_{xy} \cos \theta_H (D + iL) \\ \dot{m}_x &= i\omega h_{dl,x'} A_{xx} \cos \theta_H (D + iL) & \dot{m}_y &= \omega h_{dl,x'} A_{xy} \cos \theta_H (D + iL) \end{aligned} \quad (3.51)$$

Taking the real parts yields:

$$\begin{aligned}
\text{Re}(m_x) &= H_{dl} A_{xx} \cos \theta_H (D \cos(\omega t) - L \sin(\omega t)) \\
\text{Re}(\dot{m}_x) &= \omega H_{dl} A_{xx} \cos \theta_H (-D \sin(\omega t) - L \cos(\omega t)) \\
\text{Re}(m_y) &= H_{dl} A_{xy} \cos \theta_H (D \sin(\omega t) + L \cos(\omega t)) \\
\text{Re}(\dot{m}_y) &= \omega H_{dl} A_{xy} \cos \theta_H (D \cos(\omega t) - L \sin(\omega t))
\end{aligned} \tag{3.52}$$

where  $h_{dl,x'} = H_{dl} e^{i\omega t}$ ,  $H_{dl}$  being the real amplitude of the effective field of the damping-like torque along the  $\hat{\mathbf{x}}'$  axis. The last two terms in the last line of Eq. (3.40) then become:

$$\text{Re}(m_y)\text{Re}(\dot{m}_x) - \text{Re}(m_x)\text{Re}(\dot{m}_y) = -\omega H_{dl}^2 \cos^2 \theta_H \sin \theta_H A_{xy} A_{xx} L \tag{3.53}$$

which, apart from the field amplitude and the term  $A_{xx}$  replacing  $A_{yy}$ , is the same as Eq. (3.44), where the excitation source is an Ørsted field. Following the same steps as for Eq. (3.49), we obtain:

$$\langle \mathcal{V}_{ishe}^{dl} \rangle = \frac{\rho_n l_w e G_r l_{sd} \theta_{sh}}{2\pi t_n M_s^2} \omega H_{dl}^2 \cos^2 \theta_H \sin \theta_H A_{xy} A_{xx} L \tanh\left(\frac{t_n}{2l_{sd}}\right) \tag{3.54}$$

Thus, we find that the signal that is generated by the iSHE in the case of damping-like torque excitation has a purely Lorentzian lineshape as well.

### 3.3.3 Conclusion: AMR vs iSHE

To conclude, we have calculated all the voltages that we expect to contribute to the signals detected along the SWWs, under an in-plane saturating magnetic field at an angle  $\theta_H$ , and injecting an RF current in the SWW at a frequency  $\omega$ . There are three possible RF excitation sources in our Ta/FeCoB/MgO system: the damping-like torque, the field-like torque and the Ørsted field; the latter two being indiscernible. These excitations can each combine with anisotropic magnetoresistance rectification or the combined spin-pumping and inverse spin Hall effect, resulting in a DC signal. This results in a linear combination of up to 4 voltages, the lineshapes of which are summarized in Table 3.1. We recall the calculated voltages here for convenience:

$$\begin{aligned}
\langle \mathcal{V}_{amr}^{fl} \rangle &= \frac{l_w \Delta \rho_{amr}}{w_w t_f M_s} \cos^2 \theta_H \sin \theta_H I_f (H_{fl} + H_\phi) A_{yy} D \\
\langle \mathcal{V}_{amr}^{dl} \rangle &= \frac{l_w \Delta \rho_{amr}}{w_w t_f M_s} \sin(2\theta_H) \cos \theta_H I_f H_{dl} A_{xy} L \\
\langle \mathcal{V}_{ishe}^{fl} \rangle &= \frac{l_w \rho_n e G_r l_{sd} \theta_{sh}}{2\pi t_n M_s^2} \tanh\left(\frac{t_n}{2l_{sd}}\right) \cos^2 \theta_H \sin \theta_H \omega (H_{fl} + H_\phi)^2 A_{xy} A_{yy} L \\
\langle \mathcal{V}_{ishe}^{dl} \rangle &= \frac{l_w \rho_n e G_r l_{sd} \theta_{sh}}{2\pi t_n M_s^2} \tanh\left(\frac{t_n}{2l_{sd}}\right) \cos^2 \theta_H \sin \theta_H \omega H_{dl}^2 A_{xy} A_{xx} L
\end{aligned} \tag{3.55}$$

where the terms  $A_{ij}$  are defined in Eq. (1.48)<sup>4</sup>. The amplitudes  $I_f$ ,  $(H_{fl} + H_\theta)$  and  $H_{dl}$  are all proportional to the amplitude of the current applied to the whole SWW, therefore all 4 voltages scale with the RF power. Additionally, in this configuration all of the voltages have the same dependence on the in-plane angle  $\theta_H$  of the applied field, despite the different expressions of AMR and spin-pumping and the iSHE. However, AMR and the iSHE have a different out-of-plane angle dependence. The AMR and iSHE voltages have been calculated for numerous configurations by Harder *et al.* in [Har16], including different RF excitation directions, detection axes, and applied field directions. Unfortunately we could not perform out-of-plane field measurements with the electromagnet at our disposal.

FeCoB alloys are known to have weak  $\rho_{amr}$  compared to NiFe alloys, and the proportion of current flowing in the FeCoB layer is expected to be small given that the Ta layer is 4 times thicker than the FeCoB, at comparable resistivities. Another difference lies in the frequency dependence of the signals, given by the direct dependence on  $\omega$  as well as via the  $A_{ij}$  terms (see Eq. (1.48)). However such a study would require impedance matched devices so that signals at different frequencies can be easily compared. As can be seen in Fig. 3.3 in Sec. 3.4, the variability of the amplitudes of the resonance peaks for different frequencies indicates that the devices are not fit for a frequency-dependent study.

This conclusion is supported when analyzing the lineshape. We give an example in Fig. 3.4 in Sec. 3.4.1, which shows that the lineshape of the peak is Lorentzian, indicating that  $\mathcal{V}_{amr}^{fl}$ , which is the only signal with a dispersive lineshape, is negligible. This implies that the studied system either does not exhibit field-like torque or does not give a strong AMR signal. However, the field-like torque has been measured in Ta/Fe<sub>72</sub>Co<sub>8</sub>B<sub>20</sub>/MgO samples fabricated using the same deposition machine as our devices, by other measurement techniques [Gar13]. The field-like torque has also been measured in similar Fe-rich systems such as Ta/Fe<sub>60</sub>Co<sub>20</sub>B<sub>20</sub>/MgO [Kim13]. Thus it is reasonable to expect similar dependencies for the materials studied here, and the absence of a dispersive lineshape in our measurements indicates that the AMR signal is weak. With this, we conclude that the iSHE is the dominant source of the signal in our SWWs.

Moreover, the results of Chap. 4 are obtained in a configuration where the AMR contribution is expected to be minimum and the iSHE contribution maximum, indicating that the signals detected are purely the result of spin-pumping and the iSHE (see Sec. 4.4.3). This is due to the different geometry of the excitation field used for the experiments in Chap. 4 (as compared to Chap. 3), resulting in a different angle-dependence for the AMR and the iSHE signals. In any case, the exact origin of the signal does not influence the interpretation of the results shown in this chapter.

With the iSHE as the dominant source of the detected DC signal, it will not be possible to distinguish between the contribution of the damping-like torque and of the field-like torque excitation by comparing the relative amplitudes of the Lorentzian contri-

---

<sup>4</sup>In the case of a DC damping-like torque, the off-diagonal elements  $A_{xy}$  are modified as seen in Eq. (3.20)

bution vs the dispersive contribution.<sup>5</sup> Thus, the method used in [Ski14; Nan15; Pai15] cannot be used here to determine the relative strength of each spin-orbit torque.

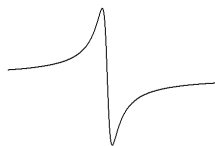
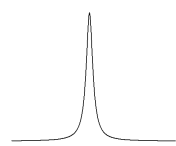
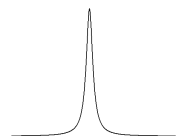
Excitation Rectification	Ørsted field or field-like torque	Damping-like torque
AMR		
iSHE		

Table 3.1: Summary of the FMR lineshapes created by the possible excitation sources and the possible rectification methods.

### 3.4 ST-FMR characterization of Ta/FeCoB/MgO at zero DC current

In this section, ST-FMR will be used to characterize materials properties of the SWW, using an RF current for the excitation of the ferromagnetic resonance, but without a DC current.

By characterizing the resonance field  $H_r$  and the resonance linewidth  $\Delta H$  as a function of frequency and FeCoB layer thickness, magnetic properties such as the saturation magnetization, interfacial anisotropy and the damping can be obtained in principle. All the devices measured in this chapter have a width of  $w_w = 1 \mu\text{m}$ . First we will describe the measurement protocol and verify the angle dependence that was calculated in Eq. (3.55). Thereafter we will present the dynamic ST-FMR characterization of the SWW at zero DC current.

#### 3.4.1 Measurement protocol

A sinusoidal RF current, set at constant frequency throughout the measurement, is sent through the SWW. The electromagnet is set such that the field will be in the plane of the device at an angle  $\theta_H = 68^\circ$  with respect to the long axis of the SWW, as shown in Fig. 3.2. The magnetic field is initially at  $\mu_0 H = 0 \text{ mT}$  and is then slowly decreased to  $\mu_0 H = -170 \text{ mT}$  and then increased to  $\mu_0 H = 170 \text{ mT}$ , and finally decreased back

<sup>5</sup>In ST-FMR experiments performed on magnetic tunnel junctions, it is possible to differentiate them due to the fact that the damping-like torque is antisymmetric with respect to the current, whereas the field-like torque is symmetric with respect to the current [Kub08].

to  $\mu_0 H = 0$  mT. The field step, for all segments, is 1 mT. The field is swept across the resonance a total of 4 times: twice for negative fields and twice for positive fields. The DC voltage is measured along the SWW, with the signal-to-noise ratio enhanced via the modulation of the RF power and the lock-in amplifier.

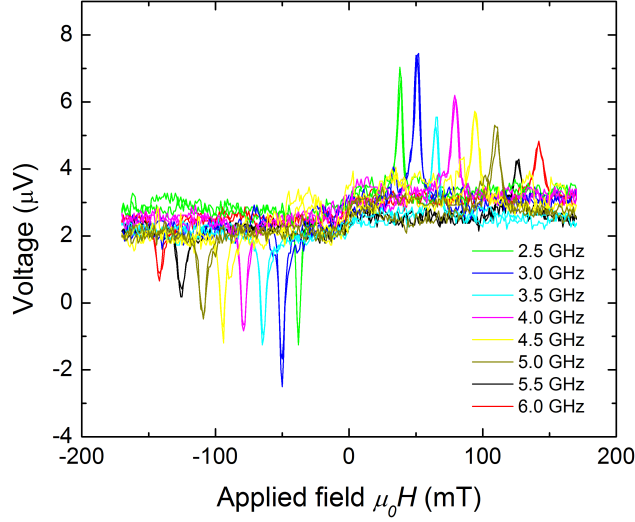


Figure 3.3: ST-FMR resonances without DC current for an in-plane magnetized SWW, with a 1.33 nm thick FeCoB layer. The applied frequency ranges from 2.5 to 6.0 GHz. The uneven decrease of the resonance peak as the frequency increases is likely due to impedance mismatch.

The result is a Lorentzian peak centered around the resonance field  $H_r$ , with a non-zero linewidth  $\Delta H$ , which in this work corresponds to the full width at half maximum (FWHM). Examples of field sweep measurements are shown in Fig. 3.3 for different frequencies of the RF current. The resonance peaks are then individually fitted using a Lorentzian function:

$$V = V_m \frac{\frac{\Delta H^2}{4}}{(H_r - H)^2 + \frac{\Delta H^2}{4}} + V_0 \quad (3.56)$$

where  $H$  is the applied field,  $V_0$  is an offset voltage,  $H_r$  is the resonance field,  $V_m$  is the maximum voltage of the resonance peak and  $\Delta H$  its full width at half maximum. An example of a Lorentzian function fitted to a resonance peak is given in Fig 3.4. The non-zero offset voltage  $V_0$  will be discussed in Sec. 3.5 as it has a dependence on the DC current used in the experiments described in that section.

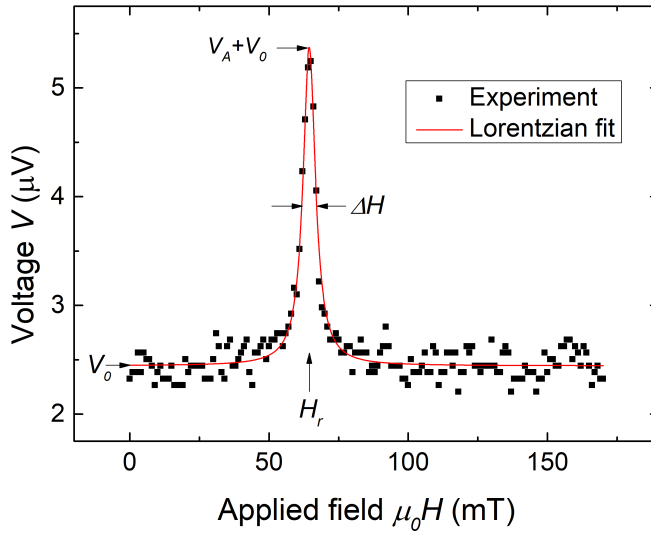


Figure 3.4: ST-FMR resonance peak at 3.5 GHz without DC for an in-plane magnetized SWW. A Lorentzian function, defined in Eq. (3.56), is fitted to the curve, yielding  $V_0 = 2.45 \mu\text{V}$ ,  $V_A = 2.92 \mu\text{V}$ ,  $H_r = 64.45 \text{ mT}$  and  $\Delta H = 5.4 \text{ mT}$ .

#### Linearity with respect to RF power

The models and equations provided in Sec. 3.2 and 3.3 have been developed in the linear approximation of the Landau-Lifshitz equation, which is inherently nonlinear. Thus, we must make sure that the magnetization dynamics we study are in the linear response regime. In the nonlinear regime, effects take place such as two magnon scattering can take place [Hei85; Hur98; Kri10]. The two-magnon scattering process involves the coupling between the uniform FMR mode and degenerate spin-waves which have the same resonance frequency, leading to increased relaxation of the uniform mode. In practice, the linear regime is characterized by the FMR linewidth being proportional to the frequency, or the square of the resonance peak voltage being proportional to the absorbed RF power.

We attempted to reach the non-linearity by increasing the RF power up to the limit of our signal generator. When plotting the logarithm of the resonance peak voltage as a function of the power in dBm (resulting in a log-log plot), the peak voltage is still linear with respect to RF power even at +10 dBm. This is due to the fact that the SWW is not impedance-matched to the signal generator which has a source impedance of  $50 \Omega$ . Indeed, the  $1 \mu\text{m}$ -wide SWWs have a resistance between 2 and  $3 \text{ k}\Omega$ , resulting in a reflection coefficient of:

$$\begin{aligned} \Gamma &= \frac{Z_l - Z_s}{Z_l + Z_s} \\ &= \frac{2000 - 50}{2000 + 50} \approx 95\% \end{aligned} \quad (3.57)$$

where  $Z_l$  is the SWW load impedance and where  $Z_s$  is the source impedance of the signal generator, and we considered only purely resistive behavior. This means that less than 5% of the RF power is transmitted to the SWW. For an RF power of +10 dBm at the signal generator output, only -3 dBm is transmitted to the SWW.<sup>6</sup>

In fact, the linearity limit can be observed in the data presented in Fig. 3.24 in Sec. 3.5, where a DC current is added to the RF power in the SWW. The combined RF+DC power in this case leads to non-linear behavior visible in the linewidth of the resonance.

### 3.4.2 Angle dependence

Since both AMR and the iSHE have the same angle dependence for an in-plane field in ST-FMR, the two rectification effects cannot be decoupled this way. We nevertheless performed an angle-dependent measurement to verify that the signal has at least the expected symmetry calculated in Eq. (3.55). The resonance peak amplitude as a function of field angle is shown in Fig. 3.5 and is fitted by  $\sin\theta_H \cos^2\theta_H$ , which carries the expected symmetry for in-plane AMR and the iSHE, calculated in Sec. 3.3.1 and 3.3.2. To completely ascertain the source of the signal, an out-of-plane angle-dependent measurement is necessary but such an electromagnet was not at our disposal.

The angular dependence in Fig. 3.5 shows that the signal has a maximum at  $45^\circ$  and minima at  $0^\circ$  and  $90^\circ$ , which are repeated periodically. Therefore it would make sense to set the external field at  $45^\circ$ . This angle takes into account the angular dependence of the detection mechanism (iSHE in our case) and the angular dependence of the excitation mechanism (a greater excitation would result in a larger precession cone and thus a greater signal). However, for the experiments in Sec. 3.5.1 and 3.5.2, where the DC field-like and damping-like torques are studied, it is favorable to use an angle where their amplitudes are maximized, which is  $90^\circ$ . Thus,  $\theta_H = 68^\circ$  was chosen as a compromise between signal strength and DC torque efficiency.

The contribution at resonance of the anomalous Nernst effect, which has a  $\cos\theta_H$  dependence on the applied field angle [Sch12], can also be dismissed. This is due to the extremely small thickness of the FM layer, which likely has a negligible temperature gradient.

Another possible rectification is the spin Hall magnetoresistance,

### 3.4.3 Saturation magnetization and interfacial anisotropy

ST-FMR can be used to extract basic material parameters such as the saturation magnetization and the interfacial anisotropy. By sweeping the field while applying an RF current at constant frequency, we extract the resonance field from the Lorentzian fit, defined in Eq. (3.56). This measurement is repeated for a number of frequencies in the GHz range, at zero DC current for devices of different FM layer thickness, listed in Table

---

<sup>6</sup>In reality the transmission cables, contact probes, contact pads and the SWW itself all have complex impedance. Since the SWW is much smaller than the wavelength in free space of the applied RF current, the impedances can be approximated by their real resistances. The other components have much smaller resistances than the SWW.

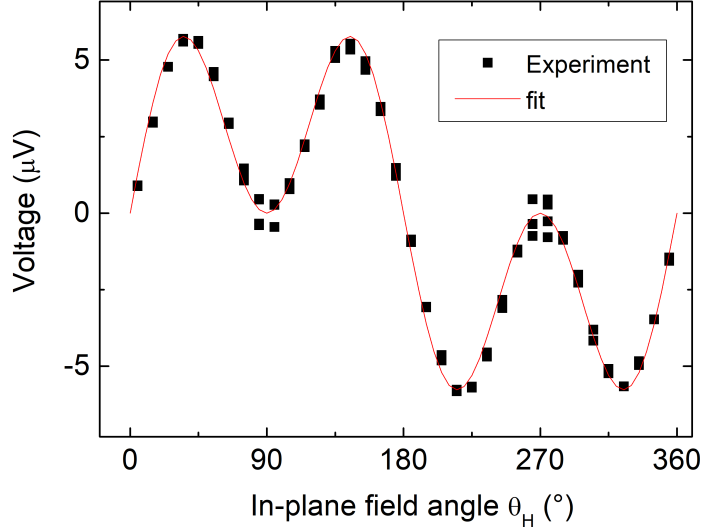


Figure 3.5: ST-FMR resonance peak amplitude at 3.5 GHz as a function of field angle  $\theta_H$ .  $\theta_H = 0$  corresponds to the external field being parallel to the long axis of the SWW. The fitting function is proportional to  $\sin\theta_H \cos^2\theta_H$ . The large dispersion around  $90^\circ$  and  $180^\circ$  is due to the fact that the device is not perfectly positioned in the center of the gap of the electromagnet.

2.2. For the Ta/FeCoB/MgO system, the interfacial anisotropy due to the FeCoB/MgO interface and the demagnetizing field have to be taken into account. The resonance frequency is given by Eq. (1.38), which can be written in units of GHz and as a function of the effective magnetization  $M_{eff}$  (given in Eq. (1.14)):

$$f_r = \gamma' \mu_0 \sqrt{H(H + M_{eff})} \quad (3.58)$$

where  $\gamma' = \frac{\gamma}{2\pi} = 29.25 \text{ GHz T}^{-1}$  is the gyromagnetic ratio,  $f_r$  is the resonance frequency in GHz,  $H$  is the applied field and  $M_{eff}$  is the effective magnetization which includes the demagnetizing field and the interfacial anisotropy field. Rearranging the equation above and solving for  $H > 0$  gives the resonance field  $H_r$  as a function of the applied frequency  $f$ :

$$H_r = \frac{1}{2} \left( -M_{eff} + \sqrt{M_{eff}^2 + \left( \frac{2f}{\gamma' \mu_0} \right)^2} \right) \quad (3.59)$$

In Fig. 3.6 we show the resonance fields as a function of frequency for a set of devices with FeCoB thickness ranging from 1.16 to 1.34 nm. We use Eq. (3.59) to fit the experimental data. For devices with an out-of-plane magnetization (described by  $Q > 1$  in Fig.3.6, and defined in Eq. (3.61)), the resonance field given in Eq. (3.59) is an approximation

under the assumption that the field saturates the magnetization (this is further discussed at the end of this subsection). We extract  $M_{eff}$  from the fits, and plot it as a function of thickness in Fig. 3.7. The effective magnetization is related to the thickness by Eq. (1.14):

$$M_{eff} = M_s - \frac{2K_i}{\mu_0 M_s t_f} \quad (3.60)$$

which allows us to linearly fit the effective magnetization as a function of the inverse FeCoB thickness. The equation fits the data very well for devices with  $M_{eff} > 0$ , but not as much for devices with  $M_{eff} < 0$ .

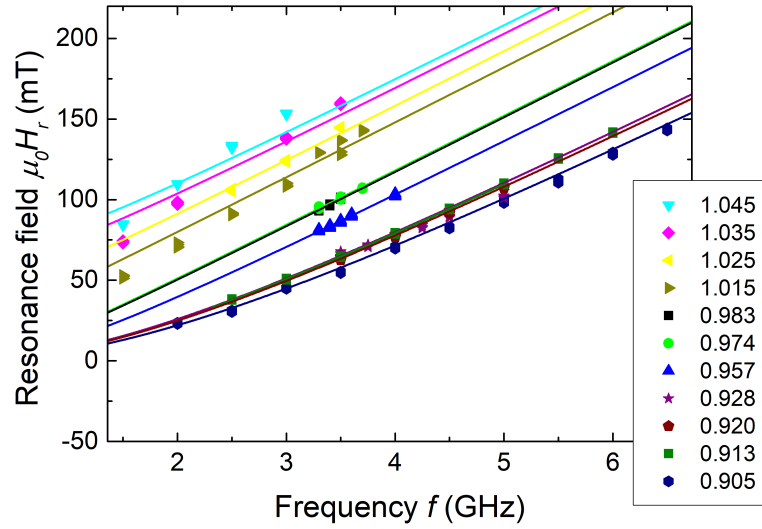


Figure 3.6: Resonance field for devices with different ferromagnetic layer thickness. Each data set, identified by its color, corresponds to a device of a certain thickness and the corresponding value indicated in the legend is the device’s Q-factor, defined in Eq. (3.61). In-plane samples are characterized by  $Q < 1$  and out-of-plane samples by  $Q > 1$ . Continuous lines are fitted to the data using Eq. (3.59).

The fit yields  $M_s = (1.48 \pm 0.04) \text{ MA m}^{-1}$  for the saturation magnetization<sup>7</sup> and an interfacial anisotropy constant of  $K_i = (1.67 \pm 0.07) \text{ mJ m}^{-2}$ , which results from both interfaces. The critical thickness where the magnetization switches from in-plane to out-of-plane magnetized, extracted from the condition  $M_{eff} = 0$ , is  $t_c = (1.21 \pm 0.05) \text{ nm}$  as shown in Fig. 3.7.

It is convenient to characterize the thickness dependence via the Q-factor<sup>8</sup> which is the ratio between the anisotropy field and the demagnetizing field, or equivalently the

<sup>7</sup>  $\mu_0 M_s = (1.87 \pm 0.05) \text{ T}$ .

<sup>8</sup>Not to be confused with the quality factor used to describe how underdamped a harmonic oscillator is, or how sharp a resonance peak is relative to its base.

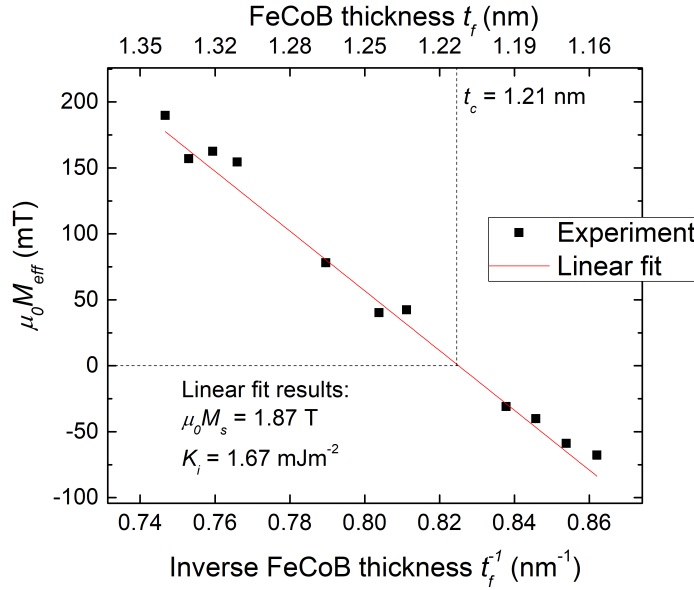


Figure 3.7: Effective magnetization as a function of the inverse of the ferromagnetic layer's thickness. The linear fit yields a saturation magnetization of  $M_s = (1.48 \pm 0.04) \text{ MA m}^{-1}$  and an interfacial anisotropy constant of  $K_i = (1.67 \pm 0.07) \text{ mJ m}^{-2}$ . The top scale for  $t_f$  is non-linear.

ratio between the anisotropy energy and the demagnetizing energy [Bea07]:

$$\begin{aligned}
 Q &= \frac{2K_i}{\mu_0 M_s^2 t_f} \\
 &= \frac{t_c}{t_f}
 \end{aligned}
 \tag{3.61}$$

where the condition  $t_f = t_c$  is equivalent to  $Q = 1$  and  $M_{eff} = 0$ . Thus, in zero field, an in-plane magnetized SWW is characterized by  $Q < 1$  and an out-of-plane SWW by  $Q > 1$ . The devices measured in this chapter vary from  $Q = 0.90$  ( $t_f = 1.34 \text{ nm}$ ) to  $Q = 1.05$  ( $t_f = 1.16 \text{ nm}$ ). The relation between  $Q$  and  $t_f$  is shown in Fig. 3.8. From now on, data and devices will be referred to by their Q-factor, instead of their thickness.

We did not take into account a possible dead layer for the thickness of the ferromagnet and for the Q-factors described in this work. When a ferromagnetic layer is sputtered onto Ta (or vice-versa), part of the ferromagnetic material intermixes with the Ta. The resulting non-magnetic layer is called the dead layer. It has been shown by Cuchet in her thesis [Cuc15], using the same deposition machine and the same FeCoB alloy, that the FeCoB/Ta interface results in a magnetic dead layer. The thickness of the dead layer depends on the Ta thickness and on the order of deposition: for Ta deposited on top of FeCoB, it can be up to 0.6 nm thick, whereas for FeCoB deposited on top of Ta, it is only 0.3 nm. The thicker dead-layer resulting from the deposition of Ta on top of

FeCoB can be explained by the bombardment of the latter by heavy Ta ions, increasing the intermixing between the materials. In our case, since the Ta is deposited first, we expect a moderate dead layer thickness, but we have not measured it precisely. To give an idea of the  $Q$ -factor that would result from taking into a possible account dead layer, we provide in Fig. 3.8 the  $Q$ -factor for the devices (blue stars) calculated using:

$$Q = \frac{t_c - t_d}{t_f - t_d} \quad (3.62)$$

where the dead layer thickness estimate is  $t_d = 0.3$  nm. The transition from out-of-plane to in-plane magnetization is defined by  $Q = 1$  in both models. The values of  $Q$  for the devices do not change significantly because they are near  $Q = 1$ , which is where the difference between the models with and without dead layers is smallest. If we assume 0.3 nm of dead layer, we obtain  $M_s = (1.15 \pm 0.04)$  MA m<sup>-1</sup> for the saturation magnetization<sup>9</sup> and  $K_i = (0.75 \pm 0.07)$  mJ m<sup>-1</sup> for the anisotropy constant.<sup>10</sup> For comparison, in [Cuc15], Cuchet found  $M_s = 1.03$  MA m<sup>-1</sup> with 0.24 nm of dead layer in Ta(0.3)/Fe<sub>72</sub>Co<sub>8</sub>B<sub>20</sub>(1.2-2.2)/MgO (thicknesses in nm).<sup>11</sup>

While the possible errors for  $M_s$  and  $K_i$  are potentially significant, most of the data represented in this chapter depend on either  $Q$ , which changes by up to 2.5% when accounting a dead layer of 0.3 nm, or on  $M_{eff}$ , which is unaffected. Due to the fact that we did not measure the dead layer thickness, in this chapter we simply used the uncorrected values of  $Q$  that do not take into account the dead layer thickness (black squares in Fig. 3.8). The thicknesses we indicate for each device are the nominal thicknesses at each position on the wafer that we expect from the calibration of the deposition machine. Thus, any drift from the calibration introduces errors that we cannot easily account for. Therefore, in any thickness-dependent graph, the error bars do not take into account the possible error in the thickness or the  $Q$ -factor of the device.

To demonstrate the self-consistency of the fits, we calculate the expected resonance field for  $f_r = 3.5$  GHz, which is the frequency used for the DC SOT characterization in Sec. 3.5.1 and 3.5.2, using Eq. (3.59) as a function of the  $Q$ -factor, and compare it to the experimental results. The results are shown in Fig. 3.9, and we find that the calculated values fit the variation in thickness adequately.

In order to extract material parameters from FMR it is preferable to be in the condition where the equilibrium magnetization is aligned with the external field's direction, i.e., the magnetization is saturated. The formulas for the FMR resonance field and the linewidth in Sec. 1.2.5 were derived under this condition. For SWWs with  $Q < 1$  this is always the case since the in-plane shape anisotropy is negligible. However for devices with  $Q > 1$ , we must verify that the magnetization is saturated by our electromagnet, which can apply a maximum field of  $\mu_0 H = 170$  mT in the plane. Using the saturation

<sup>9</sup> $\mu_0 M_s = (1.44 \pm 0.05)$  T.

<sup>10</sup>This result is obtained by plotting  $\mu_0 M_{eff}$  as a function of  $(t_f - 0.3$  nm), where  $t_f$  is the nominal FeCoB thickness, and performing a linear fit similarly to the one done in Fig. 3.7.

<sup>11</sup>The composition is abbreviated. The full stack composition is: substrate/Ta(3)/Pt(5)/(Co(0.5)/Pt(0.25))<sub>5</sub>/Co(0.5)/Ru(0.9)/(Co(0.5)/Pt(0.25))<sub>3</sub>/Co(0.5)/Ta(0.3)/Fe<sub>72</sub>Co<sub>8</sub>B<sub>20</sub>(1.2-2.2)/MgO/Fe<sub>72</sub>Co<sub>8</sub>B<sub>20</sub>(0.8-1.8)/Ta(1)/Pt(2) (thicknesses in nm).

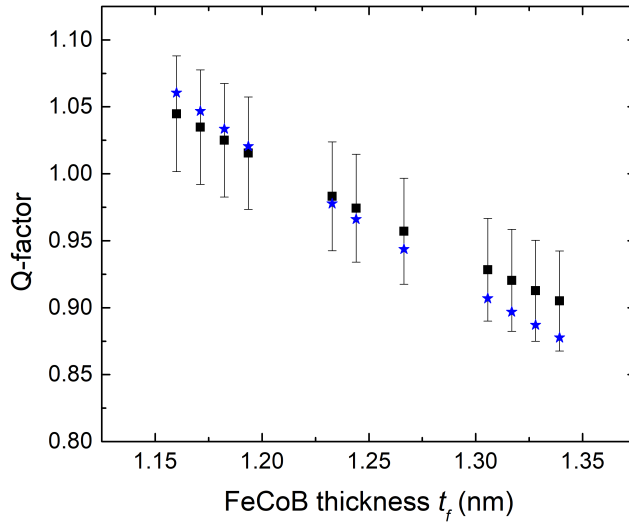


Figure 3.8: Q-factor as a function of FeCoB thickness. Black squares are calculated without consideration of a possible dead layer, using Eq. (3.61). Blue stars are calculated by taking into account a dead layer 0.3 nm thick, using Eq. (3.62). However the abscissa used for the blue stars is the nominal FeCoB thickness  $t_f$ .

magnetization and anisotropy constants obtained from the experiments, we calculate the resonance frequency for the saturated and unsaturated state as a function of the applied field for various Q-factors. The results are shown in Fig. 3.10. For a given Q-factor such that  $Q > 1$ , the resonance curve is described by two monotonic parts with the saturation field  $H_{sat}$  marking a clear divide between the parts. For  $H < H_{sat}$ , the resonance frequency  $f_r$  decreases with the applied field  $H$  while for  $H > H_{sat}$ ,  $f_r$  increases with  $H$ . Comparing Fig. 3.10 to Fig. 3.6, we see that the experimentally extracted resonance fields for all thicknesses always increases with  $f$ , thus for all  $Q$ , the devices have been saturated.<sup>12</sup> With this, Eq. (3.59) gives a good approximation of the resonance field for devices with  $Q > 1$ . For SWWs with a Q-factor up to 1.08, the magnetization should be saturated by the maximum available field. However, in practice we could not adequately measure resonances for a SWW with a Q-factor higher than 1.05, therefore, devices with  $Q > 1.05$  are not included in the discussions here.

#### 3.4.4 Linewidth and damping in the absence of DC current

The field linewidth  $\Delta H$  can be used to extract information on the damping constant  $\alpha$  of the material as well as inhomogeneous contributions to the linewidth. Using the

<sup>12</sup>Fig. 3.10 is a plot of resonance frequency as a function of applied field, while Fig. 3.6 is a plot of resonance field as a function of applied frequency.

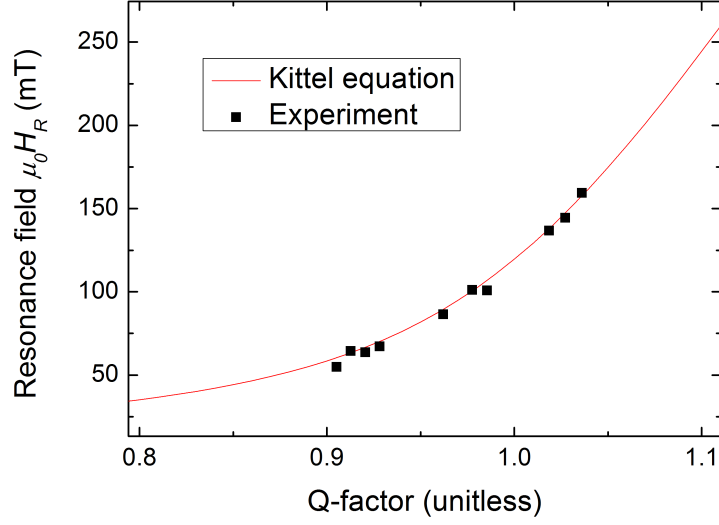


Figure 3.9: Resonance field as a function of Q-factor at 3.5 GHz. Eq. (3.59) and Eq. (3.61) are used to fit the data as a function of  $Q$ .

expression of the Gilbert-type linewidth in Eq. (1.50) when  $H$  is near the resonance field  $H_r$ , the field linewidth is related to the damping parameter:

$$\Delta H_0 = \frac{2\alpha f_r}{\gamma' \mu_0} \quad (3.63)$$

where  $\gamma'$  is the gyromagnetic ratio in  $\text{GHz T}^{-1}$  and  $\Delta H_0$  is the Gilbert-type contribution to the linewidth. However the linewidth can have other contributions, therefore instead of calculating  $\alpha$  from only one data point, the usual method is to measure the linewidth at several frequencies and to fit the curve with a linear function. The slope is equal to  $\frac{2\alpha}{\gamma' \mu_0}$  according to Eq. (3.63). As an example, we show the linear fitting of the linewidth in Fig. 3.11 for a device with  $Q = 0.91$ , obtaining  $\alpha = 0.016$ . Unfortunately, not all devices were investigated with the same range of frequencies,<sup>13</sup> resulting in an incomplete picture in terms of linewidth vs. frequency, and thus  $\alpha$ . Furthermore, while we were able to measure the damping for devices with  $Q < 0.95$ , obtaining values in the 0.015 – 0.020 range, in other devices, especially those with  $Q > 1$  and  $Q \approx 1$ , the linewidth does not increase linearly with the frequency. Instead, it decreases or is non-linear, as shown in Fig. 3.12, and it is not possible to extract  $\alpha$  for these SWWs in the small range of frequencies that we used, using Eq. (3.63). Additionally, we treated the devices as thin

<sup>13</sup>This is due to several factors. For high frequencies, the resonance field exceeds the maximum field the electromagnet can generate. For lower frequencies, the resonance field approaches zero, where the measurement setup produces an unexplained large noisy peak, which can overlap with the resonance peak. Additionally, the bias-T imposed its own limit on low frequencies for  $f < 1$  GHz.

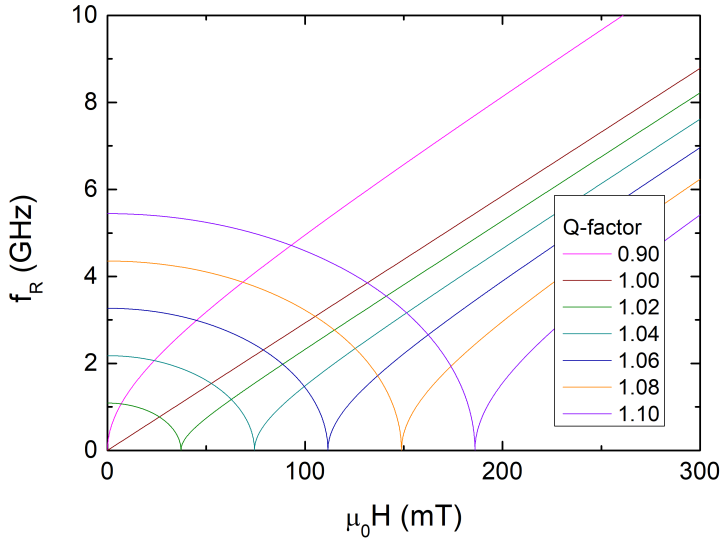


Figure 3.10: Calculated resonance frequency as a function of applied field for out-of-plane SWWs ( $Q > 1$ ). For comparison, calculations for  $Q = 0.9$  and  $Q = 1$  are included.

films whereas the lateral dimension is  $1 \mu\text{m}$  for the devices studied in this chapter. In FMR experiments, there is often a frequency-independent inhomogeneous contribution to the linewidth that leads to a constant offset at  $f_r = 0$ . However in the devices studied here there is evidence of a non-Gilbert damping process that is frequency-dependent.

### Origin of the non-Gilbert damping

In order to explain such an unusual dependence, we examine how the quality of the FeCoB film and a distribution of  $Q$  affects the linewidth. We expect that variations in the growth and thicknesses of the FeCoB and MgO layers at the thin film limit as well as roughness at the interfaces can result in fluctuations in the anisotropy constant and the saturation magnetization, creating regions with slightly different magnetic properties, including the effective magnetization.<sup>14</sup> Thus each region has a slightly shifted resonance frequency, which, when the spectra are summed, results in an overall linewidth broadening of the resonance peak of the device.<sup>15</sup> If we assume that the regions interact weakly, we can then simply sum the different linewidth contributions. This hypothesis requires that the average size of regions with different properties is greater than the exchange length  $l_{ex}$  defined in Eq. (1.60), which, for FeCoB, is estimated to be approximately 3

<sup>14</sup>Not to be confused with the concept of magnetic domains, which are regions of a magnetic material with the same properties but different magnetic orientation, separated by domain walls.

<sup>15</sup>The resulting spectrum can be approximated by a single peak equal to the sum of the individual spectra if the variation in resonance frequency is smaller than the individual linewidths.

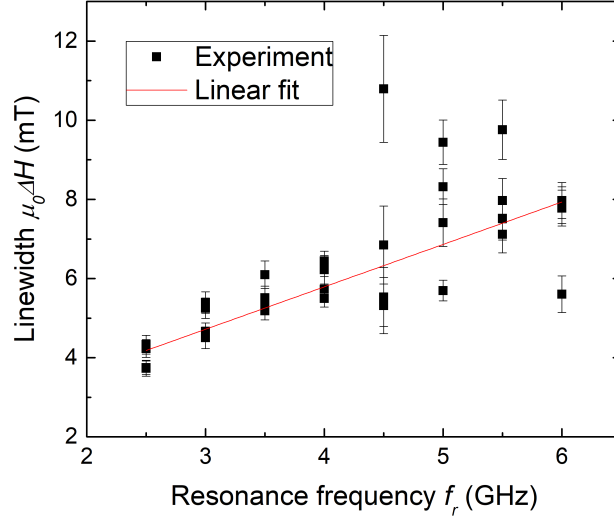


Figure 3.11: Linewidth as a function of inverse thickness for a SWW with  $Q = 0.91$ . The fit yields a damping parameter  $\alpha = 0.016$ .

nm depending on the value of  $M_s$ .<sup>16</sup> We were not able to quantify that the average size of such regions is greater than  $l_{ex}$ , though with the Brillouin light scattering microscope described in Sec. 4.5, which has a spatial resolution of 250 nm, we were able to observe variations in the local effective magnetization. Thus we assume that the sizes of the regions described above are large enough. We write the total linewidth:

$$\Delta H = \Delta H_0 + \Delta H_{in} \quad (3.64)$$

where  $\Delta H_0$  is the Gilbert-type linewidth given in Eq. (3.63) and  $\Delta H_{in}$  represents the frequency-dependent non-linear linewidth contribution due to the inhomogeneity of the magnetic properties of the SWW.

The linewidth broadening arises from the fluctuations of the resonance field over the volume. As written in Eq. (3.59), the resonance field is a function of the FeCoB thickness, the anisotropy constant and the saturation magnetization. Thus, for a fixed frequency, we can estimate a finite variation of the resonance field using its partial derivatives, following McMichael's example [McM04]:

$$\Delta H_r = 2 \sqrt{\left(\frac{\partial H_r}{\partial M_s}\right)^2 \Delta M_s^2 + \left(\frac{\partial H_r}{\partial K_i}\right)^2 \Delta K_i^2 + \left(\frac{\partial H_r}{\partial t_f}\right)^2 \Delta t_f^2} \quad (3.65)$$

$$\Delta H_r = \Delta H_{in}$$

where  $\Delta t$ ,  $\Delta K_i$  and  $\Delta M_s$  represent the dispersion of the values of the FeCoB thickness, the anisotropy constant and the saturation magnetization, assuming that the magnetic

<sup>16</sup>Assuming  $A_{ex} = 10 \text{ pJ m}^{-1}$  from [Bel17] and  $M_s = 1.48 \text{ MA m}^{-1}$ , we obtained  $l_{ex} = 2.7 \mu\text{m}$ .

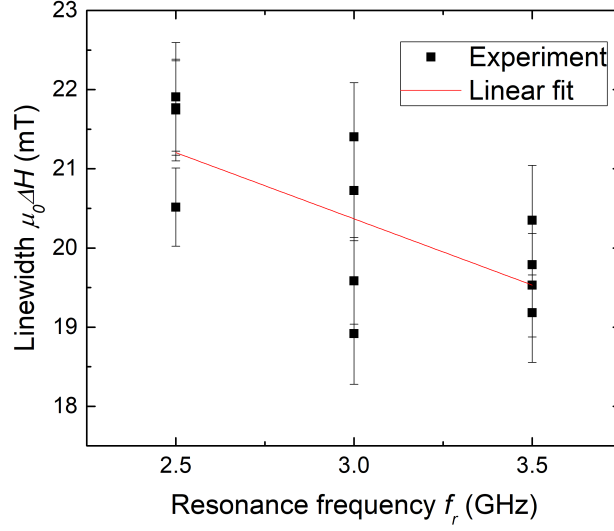


Figure 3.12: Linewidth as a function of inverse thickness for a SWW with  $Q = 1.02$ .

properties of the different regions have Gaussian distributions. The Q-factor is a function of the same variables, therefore the dispersion of the values of  $Q$  (defined in Eq. (3.61)) can be written as:

$$\Delta Q = 2\sqrt{\left(\frac{\partial Q}{\partial M_s}\right)^2 \Delta M_s^2 + \left(\frac{\partial Q}{\partial K_i}\right)^2 \Delta K_i^2 + \left(\frac{\partial Q}{\partial t_f}\right)^2 \Delta t_f^2} \quad (3.66)$$

We can use this result to write  $\Delta H_{in}$  as a function of  $\Delta Q$  only:

$$\begin{aligned} \Delta H_{in} &= 2\sqrt{\left(\frac{\partial H_r}{\partial Q} \frac{\partial Q}{\partial M_s}\right)^2 \Delta M_s^2 + \left(\frac{\partial H_r}{\partial Q} \frac{\partial Q}{\partial K_i}\right)^2 \Delta K_i^2 + \left(\frac{\partial H_r}{\partial Q} \frac{\partial Q}{\partial t_f}\right)^2 \Delta t_f^2} \\ &= 2\left|\frac{\partial H_r}{\partial Q}\right| \sqrt{\left(\frac{\partial Q}{\partial M_s}\right)^2 \Delta M_s^2 + \left(\frac{\partial Q}{\partial K_i}\right)^2 \Delta K_i^2 + \left(\frac{\partial Q}{\partial t_f}\right)^2 \Delta t_f^2} \\ &= \left|\frac{\partial H_r}{\partial Q}\right| \Delta Q \end{aligned} \quad (3.67)$$

Thus, we can study the effect of the variations of all these quantities on the linewidth using a single fluctuating parameter  $\Delta Q$ . Before calculating the derivative in the equation above, we rewrite the resonance field in Eq. (3.59) as a function of the Q-factor:

$$H_r = \frac{1}{2} \left( -M_s(1 - Q) + \sqrt{M_s^2(1 - Q)^2 + \left(\frac{2\omega}{\gamma}\right)^2} \right) \quad (3.68)$$

We then calculate the derivative of Eq. (3.68):

$$\frac{\partial H_r}{\partial Q} = \frac{1}{2} \left( M_s + \frac{M_s^2(Q-1)}{\sqrt{M_s^2(Q-1)^2 + \left(\frac{2\omega}{\gamma}\right)^2}} \right) \quad (3.69)$$

Inserting into Eq. (3.67) yields the frequency-dependent inhomogeneous linewidth broadening contribution:

$$\Delta H_{in} = M_s \Delta Q \left( \frac{1}{2} + \frac{M_s(Q-1)}{2\sqrt{M_s^2(Q-1)^2 + \left(\frac{2\omega}{\gamma}\right)^2}} \right) \quad (3.70)$$

Finally, combining the equation above with Eqs. (3.63) and (3.64), we have the total linewidth:

$$\Delta H = \frac{2\alpha f_R}{\gamma' \mu_0} + M_s \Delta Q \left( \frac{1}{2} + \frac{M_s(Q-1)}{2\sqrt{M_s^2(Q-1)^2 + \left(\frac{2\omega}{\gamma}\right)^2}} \right) \quad (3.71)$$

Thus, the inhomogeneities give rise to a non-linear and frequency-dependent contribution to the linewidth, with two distinct behaviors based on whether the device has  $Q > 1$  or  $Q < 1$ . Calculations of the total linewidth as a function of frequency for several values of  $Q$  and for  $\mu_0 M_s \Delta Q = 30$  mT are presented in Fig. 3.13. At high frequencies and for all values of  $Q$ ,  $\Delta H_{in}$  reduces to a frequency-independent contribution  $\Delta H_{in} = \frac{1}{2} M_s \Delta Q$  and we have  $\Delta H \propto \alpha f_r$  with positive slope. However, at low frequencies the contribution of the inhomogeneous linewidth can be very large, such that the linewidth is no longer linear, and in fact the initial slope can even be negative for  $Q > 1$  as seen in the experiment, Fig. 3.12. In particular, for  $Q > 1$ : there is first a decrease at low frequency followed by an increase of the linewidth at higher frequency. The range of frequencies where this occurs corresponds to the one used in the experiment. For  $Q < 1$ , there is an increase of the linewidth at low frequencies before it turns over in an almost linear dependence.

Before trying to fit the linewidths using this model for the inhomogeneous broadening for different devices as a function of frequency, we first show the measured linewidth as a function of  $Q$  for  $f = 3.5$  GHz in Fig. 3.14, along with the total linewidth calculated according to Eq. (3.71) for different values of inhomogeneities  $\mu_0 M_s \Delta Q$  ranging from 0 to 50 mT and  $\alpha = 0.02$ . As can be seen the linewidth is not constant as a function of  $Q$ , or equivalently  $\frac{1}{t_f}$ , but increases strongly with  $Q$ . Interestingly, independent of  $M_s \Delta Q$ , the values of  $\Delta H$  level off to the same linewidth value of 5 mT for low  $Q$ , but differ strongly for large values of  $Q$  given by  $\Delta H_0 + M_s \Delta Q$ . The comparison in Fig. 3.14 of the experimental data (black stars) vs. these calculated linewidths suggests that for  $Q > 0.95$  the distribution  $\Delta Q$  increases with  $Q$ . This suggests that the source of the fluctuations of the magnetic properties, for example the ferromagnetic layer thickness  $t_f$ , are constant as a function of  $t_f$ , however their effect decreases as  $t_f$  increases.

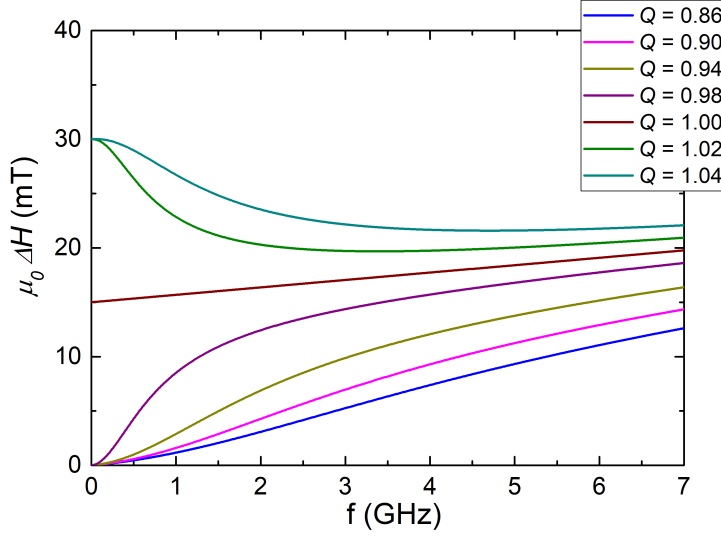


Figure 3.13: Calculated total linewidth  $\mu_0\Delta H$  as a function of frequency for values of  $Q$  ranging from 0.86 to 1.04. The linewidth is calculated using (3.71) with  $\alpha = 0.02$  and  $\mu_0 M_s \Delta Q = 30$  mT for all curves. The inhomogeneous linewidth contribution is responsible for the non-linear behavior at low frequency (approximately  $< 3$  GHz) of the total linewidth for  $Q \neq 0$ , as well as the initial value at  $f = 0$  for  $Q \geq 0$ .

Due to this dependence, we fitted the total linewidth  $\Delta H$  vs. the frequency  $f$  for each SWW of different thickness, where  $M_s \Delta Q$  was the fitting parameter. In principle there is also a thickness-dependent contribution to the damping arising from spin-pumping  $\alpha_{sp}$  [Tse02a; Tse05], but it would be difficult to fit the experimental data keeping both  $M_s \Delta Q$  and  $\alpha + \alpha_{sp}$  as fit parameters for devices of different  $Q$ . Therefore, for the qualitative study we present here, we assumed  $\alpha$  to be constant using a value of 0.02 based on the relatively constant linewidth at  $f = 3.5$  GHz found for 3 devices with  $0.91 < Q < 0.93$  (see fits shown in Fig. 3.14).<sup>17</sup> These devices also present the smallest linewidths. This is under the assumption that for these values of  $Q$ , the inhomogeneous contribution is small compared to the Gilbert-type damping and spin-pumping.

We present in Fig. 3.15 the linewidths plotted as a function of frequency for SWWs with different  $Q$ -factors. Eq. (3.71) is fitted to each curve, using  $M_s \Delta Q$  as fitting variable. The accuracy of the fitted total linewidth varies greatly from device to device and the range of frequencies used for some SWWs is insufficient for a satisfying fit. Thus we are far

<sup>17</sup>For these 3 devices, we assume the damping to be constant because the contribution of spin-pumping to the effective damping is small due to the small variation in thickness between the devices. We extracted the real part of the spin mixing conductance  $G_r$  by plotting  $\alpha_{eff}$  vs.  $1/t_f$  and using  $\alpha_{eff} = \alpha + \hbar\gamma G_r / (4\pi M_s t_f)$  (see Eq. (60) in [Tse05]) from 4 separately prepared samples with FeCoB thicknesses of 2.5, 5, 20 and 40 nm, obtaining  $G_r \approx 12$  nm<sup>-2</sup>. This results in variations of 2% due to spin-pumping for the effective damping for the very small thickness range covered by the three devices.

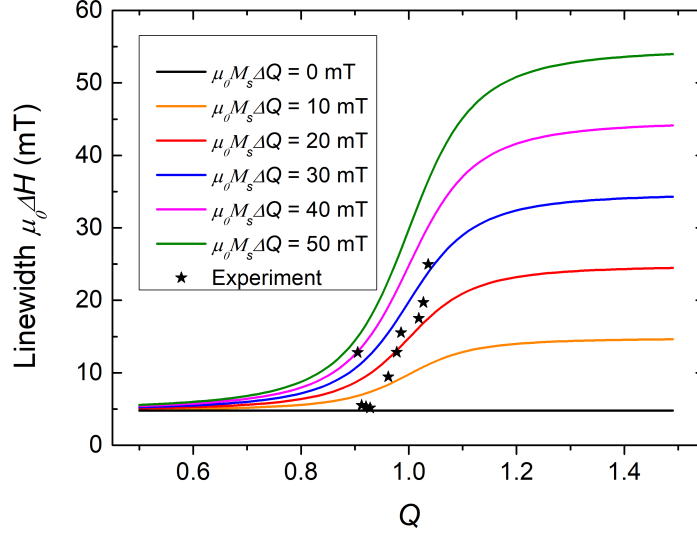


Figure 3.14: Linewidth as a function of  $Q$  for  $f_r = 3.5$  GHz. Lines represent calculated linewidths for values of  $\mu_0 M_s \Delta Q$  ranging from 0 to 50 mT, with  $\alpha = 0.02$ . Stars represent experimental data.

from a quantitative agreement. However the inhomogeneous linewidth broadening model is capable of qualitatively predicting the non-linear behavior: for  $Q < 1$ , it accounts for the increase of the linewidth with respect to intrinsic linewidth, and for  $Q > 1$ , it explains the initial decrease of the linewidth at low frequencies. We summarize the fit results in Fig 3.16. The inhomogeneity distribution  $\Delta Q$  linearly increases as  $Q$  increases, indicating that the thinner the FeCoB layer, the greater the effect of the inhomogeneities on the linewidth, confirming the interfacial nature of its origin.

In this section we neglected an important contribution to the linewidth, which is spin-pumping (see Sec. 1.4.3). Spin-pumping is a relaxation channel that increases the effective damping, and its role increases as the FeCoB thickness decreases, due to being an interfacial effect. While we neglected spin-pumping in this subsection, it cannot account for the decrease of linewidth for devices with  $Q > 1$  at low frequencies since the contribution of spin-pumping to the effective damping is positive. Thus, a thickness-dependent effective damping parameter does not call into question our model. However, a quantitative validation of our model would require accurately measuring the effective damping at high frequencies such that  $\Delta H \propto \alpha_{eff} f_r$ , as well as taking into account spin-pumping, whose contribution can be obtained by performing a thickness-dependent study.

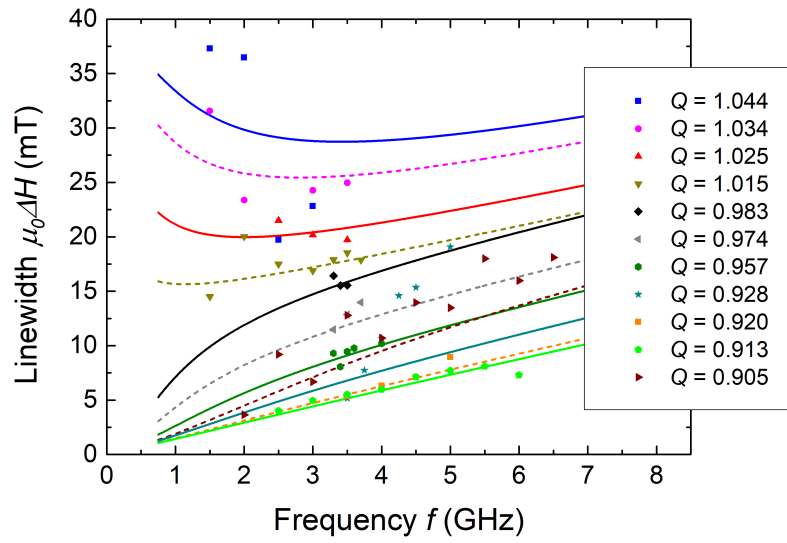


Figure 3.15: Linewidths as a function of frequency for devices with  $Q$  ranging from 1.044 to 0.905. Symbols represent experimental data. Each data set is fitted by Eq. (3.71), with  $\alpha = 0.02$ , and represented by either full or dashed lines. Some curves cross due to the fact that different values of  $M_s\Delta Q$  were used for each device.

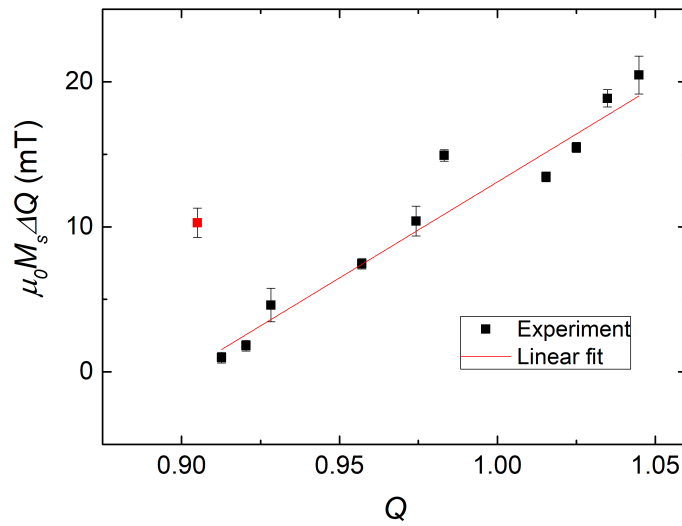


Figure 3.16: Summary of the fitted parameter  $\mu_0 M_s \Delta Q$  (squares) as a function of  $Q$ , obtained from fitting Eq. (3.71) to the experimental data. The linear fit (red line) does not take into account the red square data point.

### 3.5 ST-FMR characterization of Ta/FeCoB/MgO with DC current

We now seek to characterize how the spin-orbit torques generated by a DC current within the Ta layer as well as at the Ta/ FeCoB interface affect the magnetization dynamics. In Sec. 3.3 it was shown that the RF excitation, whether by the Ørsted field or by the SOTs, results in Lorentzian resonance peaks in the case where the rectification phenomenon is the iSHE. Thus, it is impossible to characterize the SOTs with RF currents in these devices. However, if in addition a DC current is injected, each torque changes the susceptibility components, as shown in Sec. 3.2.3 and 3.2.4: the field-like torque is expected to shift the resonance field, and the damping-like torque is expected to enhance or reduce the resonance linewidth. This technique was used for bilayers in [Liu11; Kas14; Nan15] as well as for the characterization of spin Hall nanoscillators [Zah18] and magnetic tunnel junctions [Tar18].

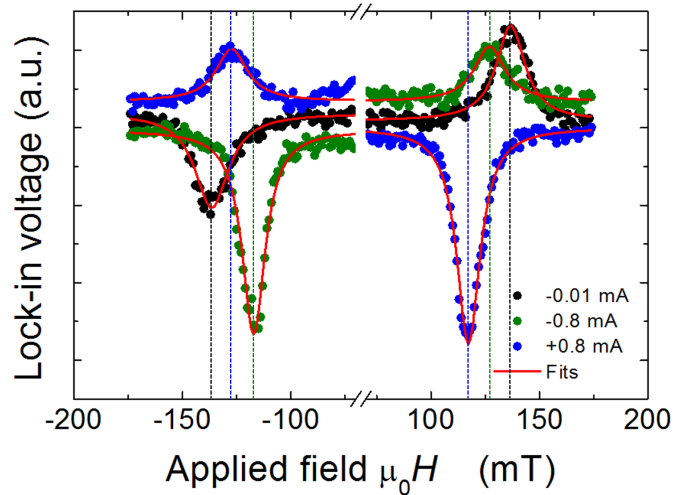


Figure 3.17: Example of ST-FMR resonances for a device with  $Q = 0.974$ . The symbols represent experimental data, the red curves are Lorentzian functions fitted to the data, and the vertical dashed lines are guides for the eye to indicate resonance fields. With near zero DC current injected (black symbols), the resonances are antisymmetric with respect to the field. With  $-0.8$  mA DC (green symbols), the resonance at negative field has reduced linewidth while the resonance at positive field has increased linewidth. With  $+0.8$  mA DC (blue symbols), this behavior is reversed with respect to the field. For both  $-0.8$  and  $+0.8$  mA DC, the resonance field is shifted toward zero.

In Fig. 3.17, we give an example of resonance peaks measured for the same device, at 3.5 GHz, for 3 different currents. The black symbols represent data taken at  $I_{dc} = -0.01$  mA, which for this paragraph serves as the zero DC current example. For this current, the resonance field and the linewidth of the peaks at negative field and positive field are equal in magnitude. The blue symbols represent data taken at  $I_{dc} = 0.8$  mA.

For both field polarities the resonance peak is shifted toward smaller absolute field values, however the shift is more pronounced for  $H > 0$ . Additionally, the peak at  $H > 0$  has a smaller linewidth than the peak at  $H < 0$ . For data taken at  $I_{dc} = -0.8$  mA, symbolized by green circles, there is also a shift of the resonance field toward smaller values for both polarities, but this time the shift is greater for  $H < 0$ . Likewise, the linewidth is smaller at  $H < 0$  than for  $H > 0$  for the data represented by the green circles. It is this field and current dependent behavior that we will study to characterize the field-like torque and the damping-like torque in the next two subsections, for devices of different Q-factor.

The measurement protocol is similar as in the previous section: the field is swept at a  $68^\circ$  angle, starting at 0 and down to  $\mu_0 H = -170$  mT, then back to 0. The measurement is then immediately repeated for positive fields. In addition, measurements are made at different DC currents, from -1 to +1 mA, in steps of 0.1 or 0.2 mA. Thus, each pair of field polarity and current polarity is measured twice. Due to the limited magnetic field range available, we could not vary the frequency to a reasonable range on all devices (due to the resonance moving outside the field range. Thus we limit the frequency used in this section to 3.5 GHz. We remind that all of the devices measured in this chapter have a width of  $w_w = 1$   $\mu\text{m}$ .

### Offset voltage dependence on $I_{dc}$

As mentioned in Sec. 3.4.1, the detected signal has an offset voltage, shown by  $V_0$  in Fig. 3.4, which is dependent of the DC current (in Fig. 3.17, the offset voltages have been removed to compare the resonance peaks).

Though a contribution of the anomalous Nernst effect (ANE) to the peak resonance signal was dismissed in Sec. 3.4.2, it be responsible for the offset voltage. It has been measured in a system similar to ours, Ta/Fe<sub>60</sub>Co<sub>20</sub>B<sub>20</sub>/MgO [Tu17]. The ANE is observed when a ferromagnet is has a thermal gradient, resulting in an electric field that is perpendicular to both the thermal gradient and the FM's magnetization. In the SWWs, it is likely that there is a heat gradient perpendicular to the layers, due to uniform Joule heating by the RF current and asymmetric heat dissipation between the top and bottom interfaces of the SWW. The RF power is modulated by the lock-in amplifier, therefore the heat gradient also varies at the modulation frequency. Thus, a Nernst voltage can be detected by the lock-in amplifier. In the experiments described in this section, an additional DC current is injected in the SWW, and the offset voltage increases considerably with the current. Fig. 3.18 shows the offset voltage vs. the applied DC current  $I_{dc}$  for several frequencies. The following function fits the experimental data adequately:

$$V_0 = a + b \operatorname{sgn}(I_{dc}) I_{dc} + c I_{dc}^2 \quad (3.72)$$

where  $\operatorname{sgn}(I_{dc})$  gives the sign of  $I_{dc}$ , and  $a, b > 0$  and  $c < 0$ . The Nernst effect contributes to  $a$ . We expect the dynamic resistance of the SWW (due to Joule heating via the modulated RF current) to contribute to  $b$ . However we did not identify a possible cause for  $c$  which is negative nor for the dependence on  $\operatorname{sgn}(I_{dc})$  of the linear term.

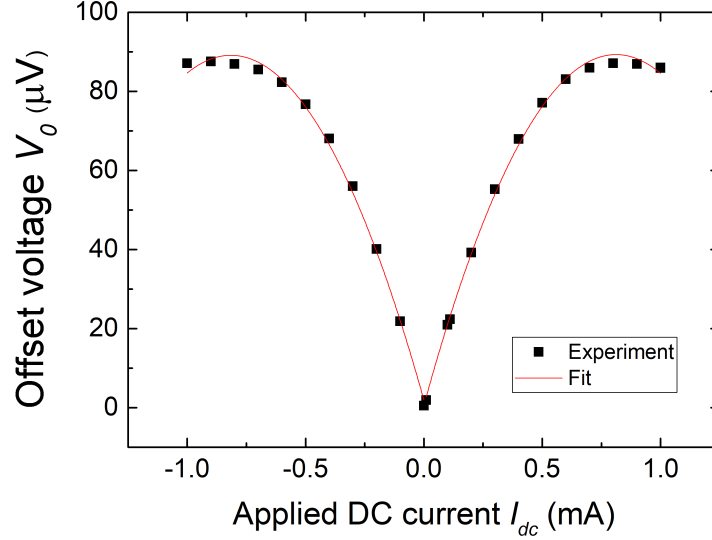


Figure 3.18: Offset voltage vs. applied DC current at  $f = 3.5$  GHz for a device with  $Q = 0.921$ . Eq. (3.72) is fitted to the experimental data (solid lines).

### 3.5.1 Shifting of the resonance field via DC current

The Ørsted field and the field-like torque both manifest as in-plane fields for the experimental conditions studied here. Therefore their effect is expected to simply shift the resonance field by an amount proportional to their projection onto the external field axis. Thus, we will be looking at the resonance field shift  $H_s$  as a function of DC current injected, which will generate a static Ørsted field and a static field-like torque. We will refer to them as current-mediated fields.<sup>18</sup> The current will also generate a static damping-like torque, that will be characterized in the next subsection. Additionally, we expect the field-like torque to have a dependence on the thickness of the ferromagnet [Fan13; Kim13], that we will investigate through a thickness-dependent study.

The resonance field, for a given excitation frequency, is a function of the effective magnetization  $M_{eff}$  and the applied field  $H$ , according to Eq. (3.59). In Sec. 3.2.3, we gave the modified resonance frequency due to an additional DC field in Eq. (3.10). Equivalently, we express the new resonance field in the presence of current-mediated fields by modifying Eq. (1.50):

$$H_r = \frac{1}{2} \left( -M_{eff} + \sqrt{M_{eff}^2 + \left( \frac{2\omega}{\gamma\mu_0} \right)^2} \right) - H_s \quad (3.73)$$

where  $H_s$  is the sum of the projections of the Ørsted field  $H_\emptyset$  and the effective field of

<sup>18</sup>In this chapter we consider the following DC fields: the external field  $H$ , the Ørsted field  $H_\emptyset$ , the effective field of the field-like torque  $H_{fl}$  and the effective field of the damping-like torque  $H_{dl}$ .

the field-like torque  $H_{fl}$ , onto the axis of the external field,  $\hat{\mathbf{z}}$ . Both of these fields are proportional to the DC current. The general measurement scheme is shown in Fig. 3.2.

Repeating the measurement shown in Fig. 3.17 for currents ranging from -1 to +1 mA and for devices of different thickness, we extract the resonance field. We show the result for 3 devices of different Q-factor in Fig. 3.19 at 3.5 GHz. The data are divided between positive (up-pointing triangles) and negative (down-pointing triangles) fields.

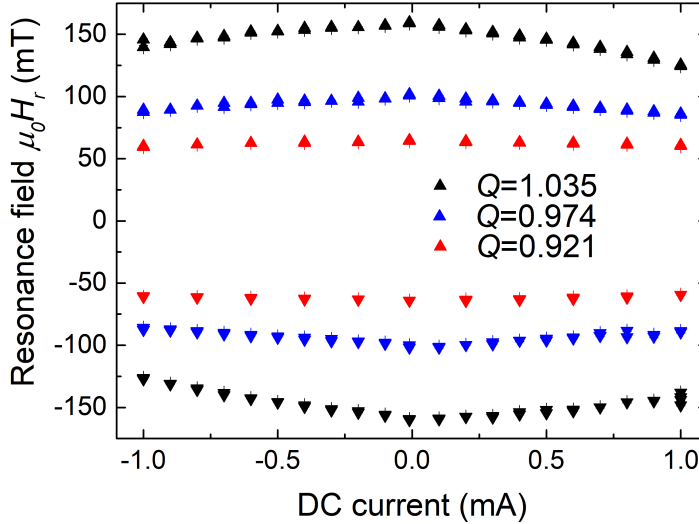


Figure 3.19: Resonance field at 3.5 GHz as a function of DC current for devices with  $Q = 1.035$  (black),  $Q = 0.974$  (blue) and  $Q = 0.921$  (red). Up-pointing triangles represent data points under a positive field and down-pointing triangles under a negative field.

The first noticeable behavior is the decrease of the magnitude of the resonance field with current, for both current polarities and both field polarities. Such a symmetric behavior cannot be attributed to the Ørsted field or the field-like torque, which are linear functions of the current. According to Eq. (1.38), for a fixed frequency, if the resonance field decreases, then the effective magnetization, proportional to  $\omega_M - \omega_K$  in the aforementioned equation, must increase. Thus, according to this equation, the effective magnetization should increase with the magnitude of the DC current.

When injecting a current into a conductor, due to Joule heating, the temperature increases with the square of the current amplitude. This increasing temperature is related to a decrease of the saturation magnetization [Du 19]. In our case, the situation is more complicated as the interfacial anisotropy decreases as well with the temperature [Lee17]. Thus, we attribute the decrease of the resonant field to Joule heating inducing a faster decrease of the interfacial anisotropy compared to the decrease of the saturation magnetization and, in consequence, an overall increase of the effective magnetization.

This phenomenon is well known and is exploited to more easily control the magnetization of a storage layer in MRAM via heating in a thermally assisted switching scheme [Pre13; Str18].

Since the saturation magnetization and the interfacial anisotropy vary with temperature, which itself varies with the square of the current, they are both even functions of the current. There are other temperature effects that may give rise to a voltage in our experiment, such as the Nernst effect [Tu17], but none are expected to shift the resonance field. A simple method of eliminating the even component of a function and keeping only the odd component is to calculate:

$$H_{r,odd}(I) = \frac{H_r(I) - H_r(-I)}{2} \quad (3.74)$$

Thus, we eliminate all temperature-dependent effects from the resonance field. The only odd functions of the current, that we know of, that can change the resonance field are the Ørsted field and the field-like torque, which are linear with current.<sup>19</sup> Garello *et al.* [Gar13] have shown evidence of higher order SOTs, relative to the angle of the magnetization, though they are still odd functions of the current. We did not consider them here because their effects on the magnetization dynamics are weaker than the two SOT terms we consider in this work.<sup>20</sup>

In Fig. 3.20, we show the odd part of the resonance field, extracted using Eq. (3.74), for a device with  $Q < 1$  and for a device with  $Q > 1$ .<sup>21</sup> The graph shows a linear trend for both samples, though the slope is positive and small for  $Q = 0.913$ , while it is negative and large for  $Q = 1.035$ . We linearly fit the data only for  $H > 0$  since the other half of the graph contains the same information. The slope of the linear fit, which is the resonance field shift per unit current, is attributed to the field-like torque and the Ørsted field. Thus, we have:

$$\frac{\partial H_{r,odd}}{\partial I_{dc}} = \frac{\partial H_s}{\partial I_{dc}} \quad (3.75)$$

This treatment of the extracted resonance field is repeated for devices of different  $Q$ -factor. In Fig. 3.21, we plot  $\frac{\partial H_s}{\partial I_{dc}}$  as a function of  $Q$ , extracted from linear fits and averaged for results from positive and negative fields. The graph shows that  $\frac{\partial H_s}{\partial I_{dc}}$  increases in magnitude with  $Q$ , with a change of sign around  $Q = 0.93$ . Such a change of sign is indicative of two opposing effects: the field-like torque and the Ørsted field.

<sup>19</sup>Large values of the damping-like and field-like torque can also change the resonance field by changing the equilibrium position of the magnetization, and thus the expression of the resonance field, however we neglect this in our calculations. Indeed, the external field, when reaching the value of resonance, is two orders of magnitude larger than the effective fields of the field-like and damping-like torques we measure in this chapter.

<sup>20</sup>This conclusion was reached after performing simulations on a uniform magnetization, adding the SOT terms one by one, using the values for Ta/FeCoB in [Gar13].

<sup>21</sup>For some devices, there is an unidentified offset that is dependent on the sign of the current, resulting in two parallel curves that do not meet at the origin. We were not able to explain this discrepancy. Since we are interested in the slope of the linear fit, an offset does not change the treatment of the data.

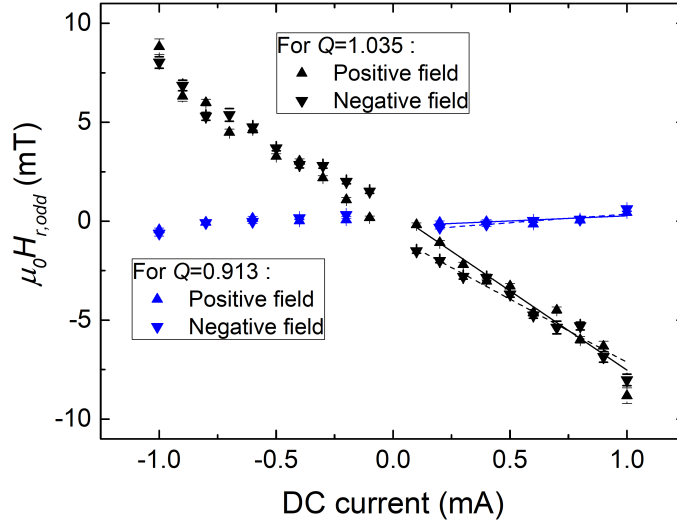


Figure 3.20: Odd component of the resonance field with respect to the applied current, calculated according to Eq. (3.74). Only the Ørsted field and the field-like torque contributions, which are odd functions of the DC current, are kept. Blue triangles represent resonance fields for positive (up-pointing) and negative (down-pointing) fields for  $Q = 0.913$ . Black triangle represent resonance fields for positive (up-pointing) and negative (down-pointing) fields for  $Q = 1.035$ . For  $I_{dc} > 0$ , full lines are linear fits of the positive field data points, while dashed lines are linear fits of the negative field data points.

We estimate the Ørsted field under the following considerations: only part of the DC current goes into the Ta layer and the magnetic field is applied at a  $68^\circ$  angle with respect to the SWW long axis.

Let us make an estimation of the Ørsted field by only considering the one generated by the DC current in the Ta layer,  $I_t$ . We will not calculate the Ørsted field generated by the current in the FeCoB layer, as its net effect on itself is negligible compared to the field generated by the Ta layer. Using Ørsted's law, we calculate the field in the FeCoB layer, far from the lateral and longitudinal edges, where it is assumed to be the strongest and parallel to the interface. The Ørsted field is approximated for very thin wires, i.e., their thickness is much smaller than their width, by:

$$H_\phi = \frac{I_t}{2d} \quad (3.76)$$

where  $d$  is the width of the wire and  $I_t$  is the current that flows in the Ta layer. At this stage, we do not know whether  $H_\phi$  and  $H_{fl}$  have the same sign or not,<sup>22</sup> thus we

<sup>22</sup>The absolute direction of the Ørsted field could have been determined from the direction of the current, however this information was lost to entropy.

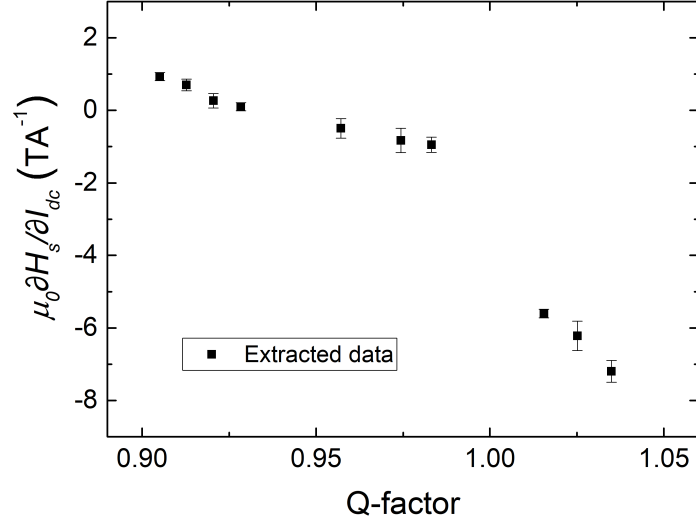


Figure 3.21: Shift of the resonance field per unit of current as a function of  $Q$ . Each data point is the average of the slopes of the linear fit of the odd part of the resonance field, for positive and negative fields, as a function of applied current.

can write the contribution of the Ørsted field as  $\delta_\phi \frac{\partial H_\phi}{\partial I_t}$ , where  $\delta_\phi = +1$  if the fields are parallel, and  $\delta_\phi = -1$  if not.

Additionally, the external field is at a  $68^\circ$  angle with respect to the SWW. The change in resonance field is due to the projection of the current-mediated fields onto the axis of the external field. Therefore the fields are overestimated by a factor of  $\cos 22^\circ$ . Thus, we have:

$$\mu_0 \frac{\partial H_s}{\partial I_{dc}} = \mu_0 \left( \frac{\partial H_{fl}}{\partial I_{dc}} + \delta_\phi \frac{\partial H_\phi}{\partial I_{dc}} \right) \cos 22^\circ \quad (3.77)$$

Next, the SWW contains two conductive layers, Ta and FeCoB. Let us make a rough estimation of the fraction of the current that goes through the Ta layer, under the assumption that the two layers can be assimilated to two parallel resistances:

$$\frac{I_t}{I_{dc}} = \frac{\frac{\rho_f}{t_f}}{\frac{\rho_f}{t_f} + \frac{\rho_n}{t_n}} \quad (3.78)$$

where  $I_t$  is the current that goes through the Ta layer,  $\rho_f$  and  $t_f$  are the resistivity and the thickness of the FeCoB layer, and  $\rho_n$  and  $t_n$  are the resistivity and the thickness of the Ta layer. The resistivity of Ta was measured to be  $\rho_n = 196 \mu\Omega \text{ cm}$  for a 5 nm thick Ta film<sup>23</sup> and the resistivity of FeCoB was measured to be  $\rho_f = 275 \mu\Omega \text{ cm}$  for a 1.5 nm

<sup>23</sup>The Ta test sample was not capped, thus we may expect a lower resistivity for the 5 nm Ta in the SWW.

thick film capped by 2 nm of naturally oxidized aluminum.<sup>24</sup> Finally the ratio of current that goes through the Ta layer is 85%, when using an average thickness of FeCoB, 1.2 nm, according to Eq. (3.78). This ratio varies by  $\pm 1\%$  for the two extreme thicknesses involved, thus we use this average value for all devices.

For each slope that we extract from the odd part of the resonance field shift we make the following correction :

$$\begin{aligned}\mu_0 \frac{\partial H_{fl}}{\partial I_t} &= \mu_0 \left( \frac{1}{\cos 22^\circ} \frac{I_{dc}}{I_t} \frac{\partial H_s}{\partial I_{dc}} - \delta_\phi \frac{\partial H_\phi}{\partial I_t} \right) \\ &= \mu_0 \left( \frac{1}{\cos 22^\circ} \frac{I_{dc}}{I_t} \frac{\partial H_s}{\partial I_{dc}} - \delta_\phi \frac{1}{2d} \right)\end{aligned}\quad (3.79)$$

where  $\frac{\partial I_{dc}}{\partial I_t} = \frac{I_{dc}}{I_t}$ .

Finally, we report the strength of the field-like torque  $\beta_{fl}$  as a function of  $Q$  in units of  $\text{T m}^2 \text{A}^{-1}$  in Fig. 3.22 by multiplying by the cross section of the Ta layer,  $w_w \times t_n = 1 \mu\text{m} \times 5 \text{nm}$ :

$$\beta_{fl} = w_w t_n \mu_0 \frac{\partial H_{fl}}{\partial I_t} \quad (3.80)$$

In Fig. 3.22, we show  $\beta_{fl}$  in the case where  $H_{fl}$  is parallel to the  $H_\phi$  (black squares) and in the case where they are anti-parallel (blue circles). Under the assumption that the Ørsted field varies little with  $Q$  (see Eq. (3.76)), and that  $\beta_{fl}$  can vary with  $Q$ , we infer that the change of sign of  $\frac{\partial H_s}{\partial I_{dc}}$  in Fig. 3.21 signifies that  $H_{fl}$  and  $H_\phi$  have the same sign for  $Q < 0.94$  and opposite sign for  $Q > 0.94$ . Thus, we conclude that the blue circles in Fig. 3.22 represent  $\beta_{fl}$  correctly.

In Fig. 3.22, we drew a line suggesting that  $\beta_{fl}$  follows a linear trend with  $Q$ , i.e.,  $\beta_{fl}$  is inversely proportional to the ferromagnetic layer thickness  $t_f$ . This behavior would be consistent with the fact that as the ferromagnetic volume decreases, the field-like torque has a greater influence. Although, our measurements do not allow an adequate fit we nevertheless conclude that globally  $|\beta_{fl}|$  increases with  $1/t_f$ . A similar result was found by Kim *et al.* who studied Ta(1)/Co<sub>20</sub>Fe<sub>60</sub>B<sub>20</sub>(0.9-1.4)/MgO (thicknesses in nm), they reported values of the field-like torque strength that increase with  $1/t_f$  [Kim13].

Since we did not vary the thickness of the Ta, we cannot conclude on the interfacial or volumic origin of the torque, and much less contribute to the Rashba vs. spin Hall effect debate [Han13]. It is also difficult to directly compare results with the literature as our Fe<sub>72</sub>Co<sub>8</sub>B<sub>20</sub> alloy is less common and therefore less studied, and the Ta (5 nm) used here is thicker than most studies, which has been shown to have a large impact on the spin-orbit torques [Kim13; Zha13]. Garello *et al.* [Gar13] studied an out-of-plane system consisting of Ta(3)/Co<sub>60</sub>Fe<sub>20</sub>B<sub>20</sub>(0.9)/MgO (thicknesses in nm) and obtained  $|\beta_{fl}| = 4.5 \times 10^{14} \text{T A}^{-1} \text{m}^2$ , a result within the same order of magnitude as ours for a system that is not too dissimilar.

---

<sup>24</sup>The capped FeCoB test sample was deposited directly onto a Si wafer, which can affect its growth and its resistivity compared to the FeCoB in our devices, which is grown on Ta.

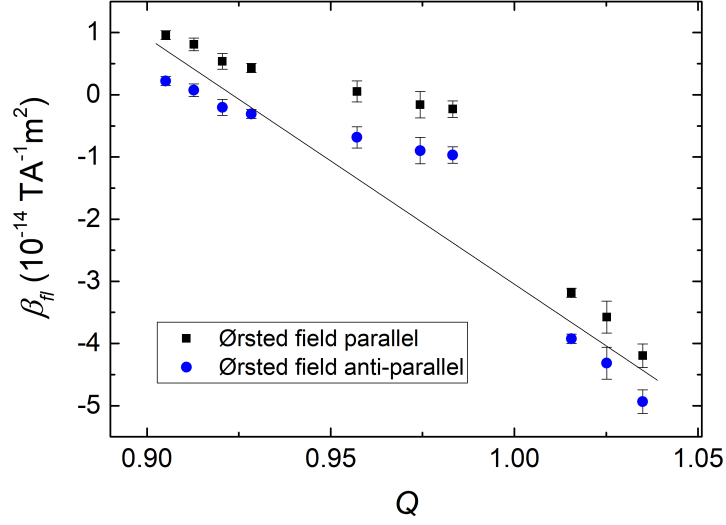


Figure 3.22: Strength of the field-like torque  $\beta_{fl}$  as a function of  $Q$ . The  $h_\phi$  field is considered to be either parallel (black squares) or anti-parallel (blue circles) to  $h_{fl}$ . The line is a guide for the eye.

### 3.5.2 Control of the damping via DC current

We now seek to characterize the damping-like torque, which, depending on the current polarity, either enhances the damping or reduces it. Thus, we will characterize the linewidth, which is modified proportionally to the current and the damping-like torque, see Eq. (3.20). In Fig. 3.17, we see the effect of the DC current on the linewidth, either broadening or diminishing the linewidth depending on the polarities of  $I_{dc}$  and  $H$ . Thus a study of the linewidth as a function of the injected current should allow us to characterize the damping-like torque. However due to the low field resolution (due to the relatively large field step of 1 mT during field sweeps) and the high increase of the offset voltage when increasing  $|I_{dc}|$  (see Fig. 3.18) leading to a lower sensitivity setting on the lock-in amplifier, the linewidth of the resonance peaks is difficult to characterize for  $|I_{dc}| > 0.1$  mA.

A property of the Lorentzian function defined in Eq. (3.56) is that the linewidth (defined as the full width at half maximum)  $\Delta H$  and the peak amplitude  $V_A$  are inversely proportional. However we must verify that this is true for the linewidth under the influence of a DC damping-like torque. The DC damping-like term  $\beta_{dl}P_z$  is present in the imaginary part of the denominator of the prefactor  $\chi_p$  of Eq. (3.20), where it affects the linewidth and therefore the inverse peak voltage proportionally for all iSHE lineshapes. The DC damping-like term is also present in the off-diagonal terms of Eq. (3.20), however we show in Appendix A that this effect is negligible.

To verify that the signal shares this property we measured a device with good signal-

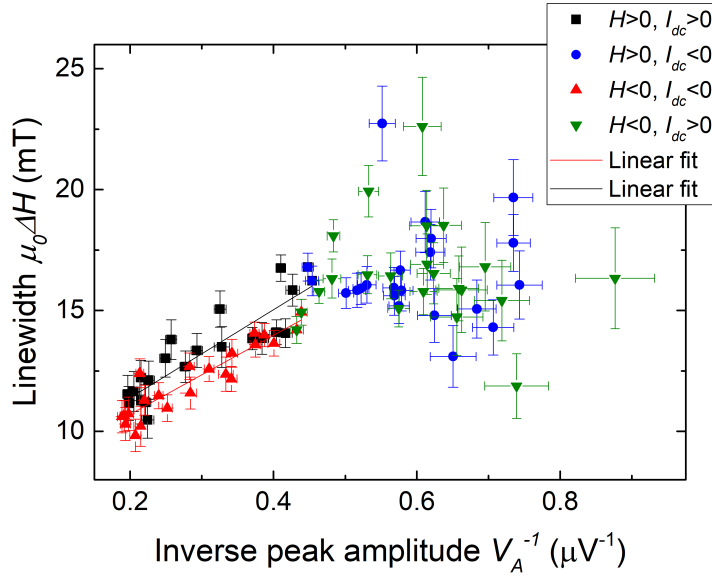


Figure 3.23: Field linewidth vs. inverse peak voltage for a device with  $Q = 0.98$ , obtained for different  $H$  field sweep polarity and  $I_{dc}$  current polarity. For  $H < 0, I_{dc} < 0$  (red triangles) and  $H > 0, I_{dc} > 0$  (black squares), the linewidth is more or less proportional to the inverse peak voltage (linear fits are in solid lines). For  $H > 0, I_{dc} < 0$  (blue circles) and  $H < 0, I_{dc} > 0$  (green triangles), the linewidth and the inverse peak voltage are completely uncorrelated and the error bars are larger. For most data points, the linewidth error bars are smaller or equal to the inverse peak amplitude error bars.

to-noise ratio and found that in the case where the DC current reduces the linewidth, the fitted linewidth  $\Delta H$  is proportional to the inverse of the inverse peak amplitude, as shown in Fig. 3.23, though the error bar in the linear fit is considerable. However in the case where the current increases the linewidth, the linewidth and the inverse peak amplitude are, in the worst cases, completely uncorrelated. This is due to the fact that when the damping-like torque increases the linewidth, the peak broadens and decreases in amplitude, approaching the noise level. In these conditions, the fitting of the linewidth is often ineffective, while the fitting of the peak height yielded coherent values, even if the error bars is still large. Thus, we used the inverse peak height to characterize the linewidth, under the assumption they are always proportional.

The analysis presented in this section is based on the same data as the previous section, thus the experimental protocol is identical. In terms of data treatment, the Lorentzian function defined in Eq. (3.56) is fitted to the peak, and the peak height,  $V_a$ , is extracted.

We show the result of the Lorentzian fits for a device with  $Q = 0.983$  at  $f_r = 3.5$  GHz, in Fig. 3.24. The inverse of the resonance peak height is plotted as a function of DC current, for both field polarities, and are fitted linearly. The dependence on the signs of

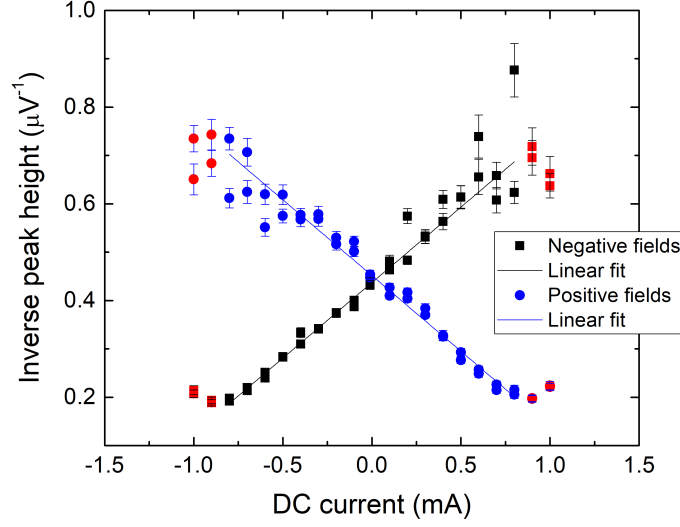


Figure 3.24: Inverse resonance peak height as a function of current for negative (black squares) and positive (blue circles) fields, for  $Q = 0.983$ . The peak height of the fitted Lorentzian curve is inversely proportional to its linewidth. The effect of the current saturates at high magnitudes, therefore the red squares are not taken into account for the linear fits, represented by full lines.

$I_{dc}$  and  $H$  is made clear here: for  $I_{dc}H > 0$  (lower left and lower right quadrants), the inverse peak heights, which are proportional to linewidth, are reduced, while they are increased for  $I_{dc}H < 0$  (upper left and upper right quadrants). However the reduction in linewidth saturates, as shown by the red points, for  $|I_{dc}| \geq 0.8$  mA for both current polarities. This is assumed to be due to effects arising at high current densities such as temperature effects and non-linear magnetization dynamics. Therefore, for the purpose of data extraction, we ignore some data points corresponding to the highest current values.<sup>25</sup> This is done independently for each device. At the end of this subsection, we give additional details on the non-linearity encountered here.

Moreover, the fitting algorithm takes uncertainties into account by lowering the weight of data points associated with large error bars.<sup>26</sup> In our case, it means that the data in the upper quadrants, which have large error bars due to low signal-to-noise ratio in the Lorentzian peak fitting, is automatically and impartially neglected as dictated by the fitting algorithm. Instead the linear fits are mostly dependent on data in the lower quadrants, where the uncertainties of the peak fitting are lowest. We show in Fig. 3.25

<sup>25</sup>For symmetry, when doing so we also remove the data points corresponding to the opposite current and opposite field.

<sup>26</sup>The fitting algorithm described here is the default algorithm of the software Origin®, <https://www.originlab.com/>.

the results for two additional devices, one in-plane with  $Q = 0.921$  and one out-of-plane with  $Q = 1.035$ .

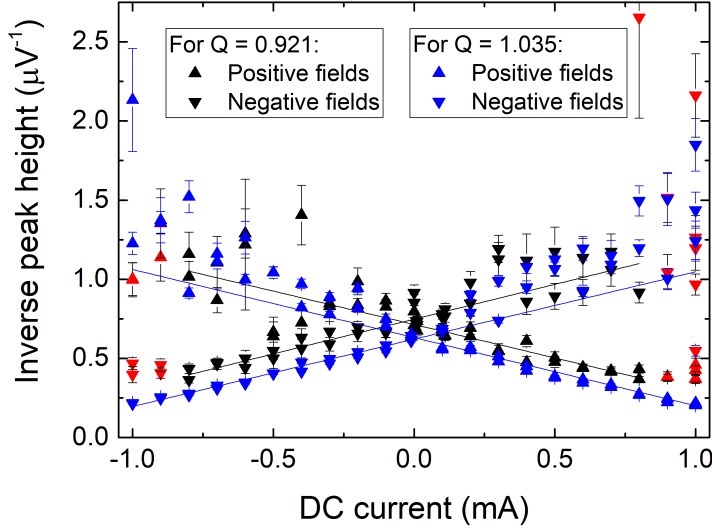


Figure 3.25: Inverse resonance peak height as a function of current for negative (down-pointing triangles) and positive (up-pointing triangles) fields, for  $Q = 0.921$  (black) and for  $Q = 1.035$  (blue). Red symbols are not taken into account for the linear fits, represented by full lines.

We are interested in the slope of the linear fit of the inverse resonance peak height vs. current, as it is proportional to the linewidth reduction per unit of current. Unfortunately, this proportionality factor is a priori unknown, and is dependent on experimental parameters such as SWW impedance, contact resistance, RF power used, etc. Therefore, we cannot use the slope directly. However this same proportionality factor links the intercept of the linear fit, which is equal to the inverse resonance peak height at zero current, to the linewidth at zero current, which we are capable of measuring accurately, as shown in Sec. 3.4.4. Thus we have the proportionality factor linking inverse peak height and linewidth, and we can calculate the linewidth reduction per unit of current,  $\epsilon$  (in  $\text{T A}^{-1}$ ):

$$\epsilon = \mu_0 \text{slope} \frac{\Delta H_{i=0}}{\text{intercept}} \quad (3.81)$$

where *slope* and *intercept* are obtained from the linear fitting of the inverse peak height vs. current. The linewidth at zero current,  $\Delta H_{i=0}$ , is measured directly via the full width at half maximum. Indeed, the FWHM at zero current can be reliably measured to obtain the correct and absolute value of the FWHM that serves to determine the proportionality factor. The linewidth reduction per unit of current (in  $\text{T A}^{-1}$ ) extracted in this way as a function of  $Q$  is shown in Fig. 3.26.

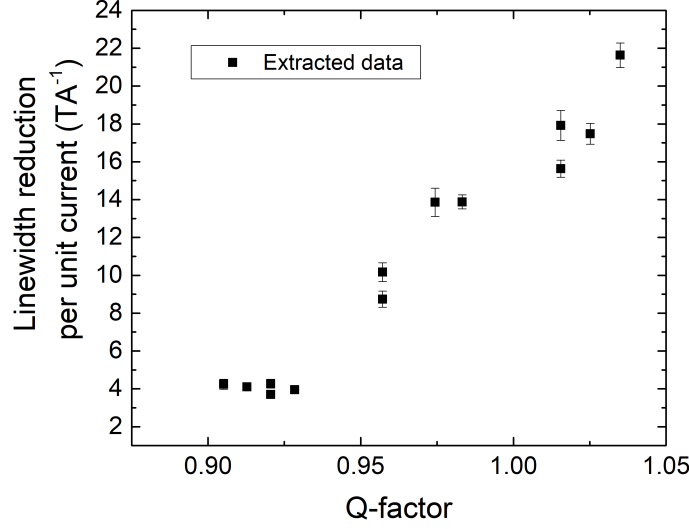


Figure 3.26: Reduction of the linewidth per unit of current as a function of  $Q$ .

Similar corrections as in Sec. 3.5.1 need to be made: the damping-like torque is underestimated due to the  $68^\circ$  angle between the external field and the SWW long axis, and the current has to be corrected to obtain the fraction going through the Ta layer, see Eq. (3.78). The corrections amount to:

$$\epsilon' = \epsilon \frac{I_{dc}}{I_t} \frac{1}{\cos 22^\circ} \quad (3.82)$$

We then calculate the strength of the damping-like torque in  $\text{T m}^2 \text{A}^{-1}$  by multiplying by the cross section of the Ta layer  $w_w \times t_n = 1 \mu\text{m} \times 5 \text{nm}$ :

$$\beta_{dl} = w_w t_n \epsilon' \quad (3.83)$$

The results are shown in Fig. 3.27. The damping-like torque is constant and weak for  $Q < 0.95$ , i.e., for large thicknesses. For  $Q > 0.95$ ,  $\beta_{dl}$  increases with  $Q$ . Regardless of the interfacial or volumic origin of the damping-like torque, for a fixed Ta layer and a varying FeCoB layer thickness, we can expect the effects of the damping-like torque to decrease as the magnetic volume increases. However Kim *et al.*, who studied a Ta(1)/Ta/Fe<sub>60</sub>Co<sub>20</sub>B<sub>20</sub>(0.9-1.4)/MgO system (thicknesses in nm) did not find such a clear trend [Kim13]. Once again, it is difficult to compare with results from the literature due to our specific FeCoB alloy and the thicknesses used. Garello *et al.* measured  $|\beta_{dl}| = 2.4 \times 10^{14} \text{T A}^{-1} \text{m}^2$  in an out-of-plane Ta(3)/Co<sub>60</sub>Fe<sub>20</sub>B<sub>20</sub>(0.9)/MgO (thicknesses in nm).

Interestingly, we found that for all  $t_f$ , the damping-like torque is twice as strong as the field-like torque, which is in contrast to most studies where the field-like torque is

greater: [Kim13; Gar13; Avc14]. This is perhaps due to the thicker Ta layer (5nm) as compared to the aforementioned studies (1, 3 and 3 nm respectively). This could indicate that the damping-like torque's origin lies in the bulk of the Ta, via the SHE, instead of the Ta/FeCoB interface. On the other hand, Zhang *et al.* performed a Ta thickness-dependent study on Ta (1-5)/CoFeB(1)/MgO(1.3)/Ta(1), and found that while both the damping-like and the field-like torques increased with the Ta thickness, the damping-like torque is never stronger than the field-like torque, even for 5 nm of Ta [Zha13]. Since SOTs in Ta/CoFeB have shown to be sensitive to growth conditions [Avc14], another explanation for our finding might come from the different deposition techniques and annealing protocols used for our devices.

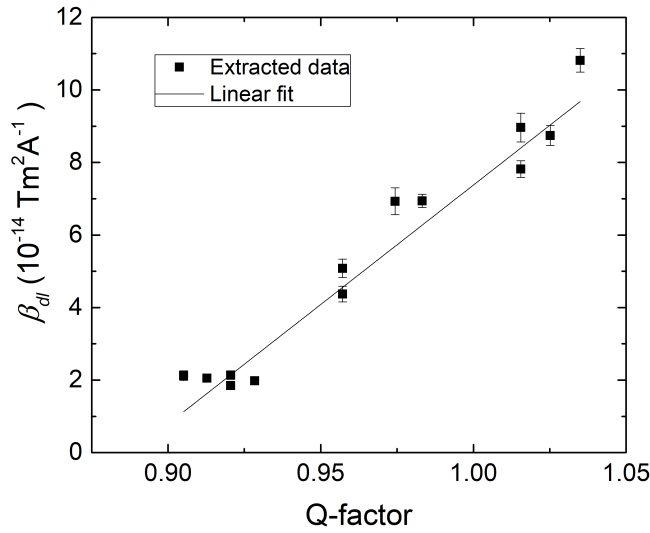


Figure 3.27: Strength of the damping-like torque  $\beta_{dl}$  as a function of  $Q$ .  $\beta_{dl}$  relates the effective field in T to the current density that created it in  $\text{A m}^{-2}$ . The current density used is the estimated current density in the Ta layer. The solid line is a linear fit of the latter.

### Non-linearity of the linewidth at high DC current

In Figs. 3.24, the inverse peak height for data points in the lower half of the graph at high DC currents (approximately  $|I_{dc}| > 0.8 \text{ mA}$ ) no longer follow the linear decreasing trend: the linewidth increases instead. It has been shown by Demidov *et al.* in [Dem11] that when the damping-like torque approaches the critical value required to fully compensate the damping over an oscillation period (i.e., the current for which the linewidth is equal to 0), strong non-linear effects appear. This is due to the fact that the damping-like torque acts on all oscillation modes, including FMR and spin-waves, as well as relaxation processes arising between the modes such as two-magnon scattering

[Hei85; Hur98; Len06], all of which lead to the increase of the linewidth. For the experiment shown in Fig. 3.24, we can extrapolate the DC current required to obtain a zero linewidth, obtaining a critical current  $I_{crit} = 1.4 \text{ mA}$ .

### 3.6 Conclusion

In this chapter we used ST-FMR spectroscopy to study Ta/FeCoB/MgO spin-wave waveguides as a function of thickness to characterize the magnetic properties in absence of DC current and the damping-like and field-like torques in presence of DC current. To analyze the experimental results, in the first part of this chapter we derived the susceptibility equations using the concepts established in Sec. 1.2.5, considering different excitation schemes by dynamic Ørsted field  $\mathbf{h}_\phi$ , field-like  $\mathbf{h}_\mathbf{fl}$  and damping-like  $\mathbf{h}_\mathbf{dl}$ , generated by an RF current in the SWW. We then calculated the expected DC voltages generated by AMR and iSHE rectification to determine which components of the Polder susceptibility tensor contribute to the signal for different excitation schemes, as well as the lineshape (symmetric Lorentzian or anti-symmetric dispersive) of each possible signal. Based on this and the purely Lorentzian nature of the measured signals, we concluded that the dominant source of DC signal in our SWWs is the combined action of spin-pumping and the inverse Hall effect. Finally, we derived the shift of the resonance field by a static Ørsted  $\mathbf{H}_\phi$  and static field-like  $\mathbf{H}_\mathbf{fl}$  fields, as well as the reduction of the linewidth via a static damping-like  $\mathbf{H}_\mathbf{dl}$  due to a DC current in the SWW.

In the second part of this chapter, we describe the FMR experiments using our ST-FMR setup. For  $I_{dc} = 0$  we extracted the effective magnetization  $M_{eff}$  as a function of thickness, allowing us to extract the saturation magnetization and the interfacial anisotropy constant, as well as the ferromagnetic layer critical thickness where the magnetization reorients from in-plane to out-of-plane. We analyzed the field linewidth  $\Delta H$  and qualitatively explained its unexpected variation as a function of thickness, in particular, negative slopes of  $\Delta H$  vs. the excitation frequency. This was accounted for by the inhomogeneous distribution of the saturation magnetization, the FeCoB thickness and the anisotropy constant, which can be taken into account by only considering an inhomogeneous distribution of the Q-factor that leads to a frequency-dependent contribution to the field linewidth.

By performing ST-FMR experiments with the addition of a DC current, we carried out a careful and systematic characterization of the field-like and damping-like torques of Ta/Fe<sub>72</sub>Co<sub>8</sub>B<sub>20</sub>/MgO vs. the ferromagnetic layer thickness, at the transition of the magnetization from in-plane to out-of-plane orientation, i.e., for Q-factors between approximately 0.9 and 1.1. Firstly, we analyzed the shift in resonance field and removed the Joule heating contribution, and, taking the current distribution in the SWW and the Ørsted field into account, we extracted  $\beta_{fl}$ , the ratio between the effective field of the field-like torque and the current density. The data shows that  $\beta_{fl}$  and  $Q$ , i.e., the inverse of the FeCoB thickness, are linear, with some deviations around  $Q \approx 1$ . Secondly, we analyzed the voltage peak height, which is inversely proportional to the linewidth, and extracted  $\beta_{dl}$ , the ratio between the effective field of the damping-like torque and

the current density, which was found to be proportional to the inverse of the FeCoB thickness. The absolute values of the field-like torque  $\beta_{fl}$  are comprised between 0 and  $5 \times 10^{14} \text{ T A}^{-1} \text{ m}^2$  depending on the ferromagnetic layer thickness, and values of the damping-like torque  $\beta_{dl}$  between 2 and  $10 \times 10^{14} \text{ T A}^{-1} \text{ m}^2$ . Surprisingly, the damping-like torque is twice as strong as the field-like torque in our devices for all FeCoB layer thicknesses, which is in contrast to most studies on similar systems. This might be explained by the thicker Ta layer we used, which may enhance the SHE contribution of the bulk Ta to the damping-like torque.

Now that we have demonstrated that SOTs can affect the  $k = 0$  uniform mode precession (resonance field and linewidth) in Ta/FeCoB/MgO layers, and that the iSHE can be used to detect the dynamic response, it will be of interest to see whether SOTs can also affect propagating  $k \neq 0$  spin-waves and whether the iSHE can be used to detect them. The second aspect (detection via iSHE) will be the subject of the next chapter, while preliminary results on the first aspect will be summarized in the Conclusion and Perspectives.



## Chapter 4

# Spin-wave excitation and detection in Ta/FeCoB/MgO

In this chapter we present the detection of spin-waves in a Ta/FeCoB/MgO spin-wave waveguide using the combined effect of spin-pumping and the inverse spin Hall effect. The spin-wave waveguides are the same as those studied in Chap. 3. We use a nanometric coplanar waveguide (CPW) antenna to excite spin-waves within a large range of wavevectors. A first task is therefore to calculate the expected spin-wave spectrum for perpendicular magnetic anisotropy materials characterized by non-zero linewidth by taking the geometry of the CPW antenna into account that will define the spatial periodicity of the excitation. The excitation is a convolution of the excitation field and the dynamic spin-wave susceptibility. We summarize the approach to obtain an expression for the wavevector dependent excitation efficiency of spin-waves and calculate the expected spin-wave spectrum including also finite linewidth. The calculated spectrum is then compared to the experiments where the spin-waves are electrically detected via rectification due to the inverse spin Hall effect.

The results obtained using this detection technique, which we call spin-wave rectification spectroscopy (SWR), are also compared to Brillouin light scattering (BLS) experiments that were carried out at the university of Kaiserslautern by T. Brächer and myself. The BLS experiments furthermore allow us to determine the spin-wave decay length, and to extract the spin-wave lifetime. Finally, we discuss the merits of the spin-wave rectification technique with regards to device integration compared to other detection schemes.

The main findings of this chapter were published in [Brä17b]. Thus, some text and figures have been adopted from the publication.

### 4.1 Material and device characterization

The spin-wave waveguides investigated in this chapter are described in Chap. 2, along with the details of their fabrication. A schematic of the device and the electrical contacts

is shown in Fig. 4.1.

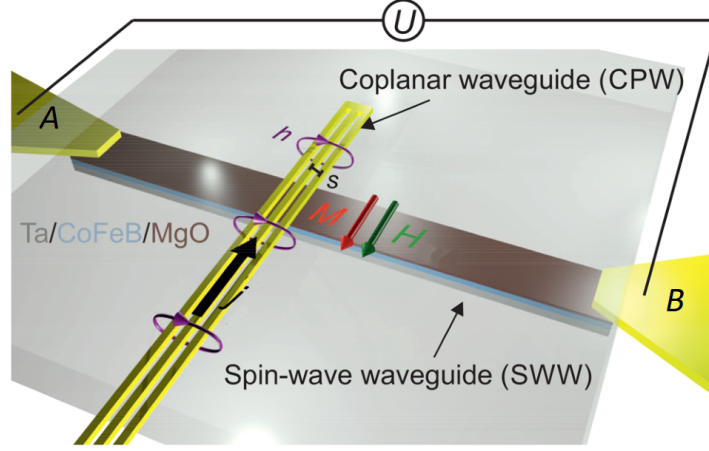


Figure 4.1: Schematic of the spin-wave waveguide. A Ta/Fe<sub>72</sub>Co<sub>8</sub>B<sub>20</sub>/MgO trilayer is patterned into a wire with leads to measure the voltage drop between A and B. An Al<sub>2</sub>O<sub>3</sub> layer insulates the SWW from the shorted coplanar waveguide on top that acts as a spin-wave excitation source. Taken from [Brä17b].

The SWWs are from the same wafer as those used for the ST-FMR experiments in Chap. 3 that provided the materials properties and the strength of the damping-like and field-like torques. However the calculations and numerical simulations described in this chapter were performed before the thickness-dependent material characterization described in Sec. 3.4 was completed, therefore there are some differences in the material parameters used to analyze the results here. This does however not affect the main results and conclusions presented.

The devices measured in this chapter are in-plane magnetized and have  $0.85 < Q < 0.90$  (for the Q-factor see Eq. (3.61)). Due to the low Q-factor, in these devices the inhomogeneous contribution to the linewidth described in Sec. 3.4.4 is less important and thus we are able to estimate the damping constant  $\alpha$ , neglecting the inhomogeneous broadening the damping via ST-FMR measurements (see Sec. 3.4.4). The values of the damping were averaged for all devices in this chapter, obtaining  $\alpha = 0.019$ . The value of the saturation magnetization used here,  $M_s = 1.25 \text{ MA m}^{-1}$ ,<sup>1</sup> is assumed based on the study of Fe<sub>60</sub>Co<sub>20</sub>B<sub>20</sub> in [Ver14]. Using this value, the interfacial anisotropy constant is extracted from the measured effective magnetization  $M_{eff}$  via the method described in Sec. 3.4.3, obtaining  $K_i = 1.18 \text{ mJ m}^{-1}$ . The exchange stiffness constant  $A_{ex} = 10 \text{ pJ m}^{-1}$  is assumed based on the study of Fe<sub>60</sub>Co<sub>20</sub>B<sub>20</sub> in [Bel17]. These three constants,  $M_s$ ,  $K_i$  and  $A_{ex}$ , are parameters that govern the dispersion relation given in Eq. (1.70), which is the basis of most of the calculations in this chapter. As such, slightly different values of  $M_s$  and  $K_i$  (which are linked by  $M_{eff}$ , and is the most easily measured parameter) would result in a different value of  $A_{ex}$  and not greatly affect the calculations

<sup>1</sup> $\mu_0 M_s = 1.57 \text{ T}$ .

and results of this chapter.

In contrast to Chap. 3, in which devices are referred to by their Q-factor, in this chapter the devices are mainly referred to by the CPW antenna design used to excite spin-waves (see Chap. 2). Moreover, it was shown in Chap. 3 that there is a non Gilbert-type damping present arising from the local inhomogeneities of the magnetic properties of the SWW, resulting in us being unable to properly determine the Gilbert damping parameter. We carried out a separate ST-FMR analysis on the linewidth of the devices measured in this chapter and obtained  $\alpha = 0.019$ , assuming the entire damping is Gilbert-type. This value was used for all calculations and simulations in this chapter.

## 4.2 Verification of the frequency-wavevector dispersion relation

In order to compare the spin-wave rectification experiments of Sec. 4.4 to the spin-wave efficiency calculated in the subsections below, we need the frequency-wavevector dispersion relation. We gave an empirically obtained expression in Eq. (1.70) for a continuous film with PMA. To verify that the expression is also correct for the wires studied here, micromagnetic simulation were performed by T. Brächer using Mumax3.<sup>2</sup> The details of the simulations can be found in the supporting information of [Brä17b]. A discretized ferromagnetic wire is modeled by  $2048 \times 256 \times 1$  cells (length  $\times$  width  $\times$  thickness), and the magnetization is excited by a localized Gaussian magnetic field pulse. Two successive FFTs of the local magnetization as a function of time and space (i.e., cell position) yields data in the frequency-wavevector domain, from which the dispersion relation is extracted. The results are presented in Fig. 4.2 for several values of anisotropy constants<sup>3</sup> Eq. (1.70) was fitted to the results. The good agreement of the fit shows that the dispersion relation given in Eq. (1.70) accurately predicts the numerical results given by the simulations. Hence we can use the dispersion relation given in Eq. (1.70) to calculate the spin-wave efficiency later in this chapter, as well as the group velocity and the relaxation rate.

---

<sup>2</sup>**mumax<sup>3</sup>** is an open-source GPU-accelerated micromagnetic simulation program developed at the DyNaMat group of Prof. Van Waeyenberge at Ghent University. For more information, see [Van14] or visit <http://mumax.github.io/>.

<sup>3</sup>In reality, all simulations were performed with the same number of cells and geometry. Instead of varying the anisotropy field by varying the thickness, the anisotropy constant was varied for a fixed thickness (i.e., the wire always has a thickness of 1 cell).

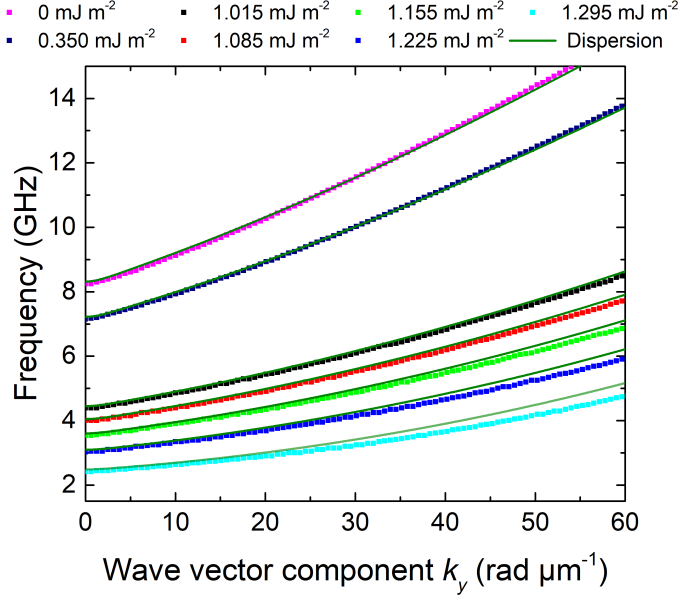


Figure 4.2: Squares: numerically simulated dispersion relation in a FeCoB SWW for different PMA constants  $K_i$ . Solid lines: dispersion relations calculated from Eq. (1.70) with the corresponding anisotropy constants. Taken from [Brä17b].

### 4.3 Excitation of spin-waves via coplanar waveguides

The aim of this section is to derive an expression of the spin-wave excitation in SWW using a CPW in order to predict the expected spin-wave spectrum, that is experimentally measured in Sec. 4.4. In FMR and ST-FMR experiments, a spatially uniform excitation (magnetic field or effective field due to damping-like torque or field-like torque, see Sec. 3.2) is used to excite ferromagnetic resonance, which are non-propagative oscillations characterized by a wavevector  $\mathbf{k} = 0$ . On the other hand, spin-waves are propagating oscillations, with finite wavevector  $\mathbf{k} \neq 0$ . Accordingly they are excited by spatially non-uniform magnetic fields, which one can characterize by their Fourier transform in  $\mathbf{k}$ -space. A coplanar waveguide, through which an RF current flows, is an example of an antenna generating a non-uniform magnetic field.

In this section, we calculate how efficiently a CPW antenna at a given frequency and field excites spin-waves in a certain wavevector range. The derivation of this efficiency involves obtaining an expression for the dynamic magnetization  $\mathbf{m}$  of spin-waves under excitation from the combination of (i) the CPW field and (ii) the non-local dipolar field generated by the spin-waves themselves. Since these calculations depend on having a correct frequency-wavevector dispersion relation, we first present in the subsection below micromagnetic simulations that allow us to verify that the dispersion relation given in Eq. (1.70) is adequate. We then address in Sec. 4.3.1 the calculation of point (i) to determine the spatial profile of the CPW field. In Sec. 4.3.3 and 4.3.4 we address the

calculation of  $\mathbf{m}$  considering both contributions as well as the finite linewidth. We then numerically evaluate the derived expressions to predict the expected spin-wave spectrum for the three coplanar waveguides (for details on the CPW designs, see Tab. 2.1).

### 4.3.1 Magnetic field generated by a coplanar waveguide

The coplanar waveguides used in this work are composed of three parallel, thin wires with a rectangular cross-section, as shown in Fig. 4.1. The CPWs are shorted at one end, and have contact pads at the other end for a ground-signal-ground RF probe; both the short and the contacts are far away from the spin-wave waveguide. The CPW is on top of the SWW and perpendicular to the SWW axis so that the RF field is oriented along the SWW long axis, see Fig. 4.1. A cross section of the CPW is shown in Fig. 4.3 along with the coordinate system. In this chapter, we will use only one coordinate system:  $\hat{\mathbf{x}}$  is the out-of-plane axis,  $\hat{\mathbf{y}}$  is the long axis of the SWW and also the direction of propagation of the spin-waves, and  $\hat{\mathbf{z}}$  is the in-plane axis transverse to the SWW and parallel to the long axis of the CPW. It is also the direction of equilibrium of the magnetization since a magnetic DC field is applied in this direction to saturate the magnetization.

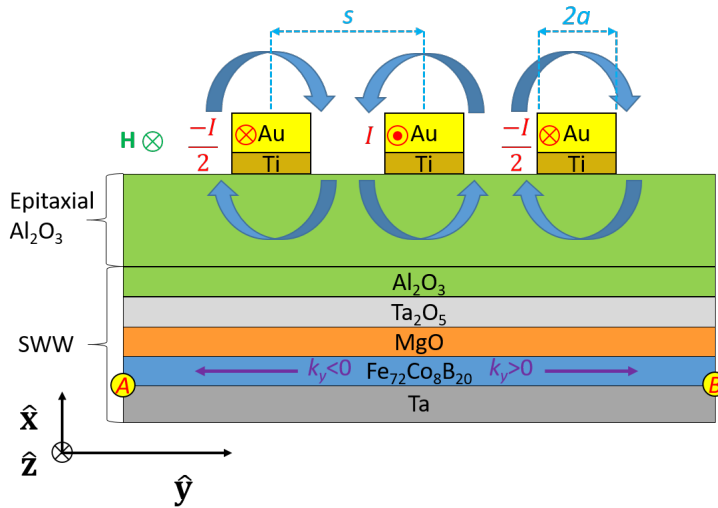


Figure 4.3: Cross section of the coplanar waveguide antenna. The epitaxial  $\text{Al}_2\text{O}_3$  layer covers the whole SWW and insulates it from the CPW. None of the thicknesses or widths are to scale. The curved arrows represent the Ørsted field created by the current  $I$  in the CPW wires. The field  $\mathbf{H}$  is applied parallel to the long axis of the CPW and perpendicular to the long axis of the SWW. When an RF current is injected in the CPW, the RF Ørsted field excites spin-waves that propagate away from the CPW in either direction (purple arrows), and they can be detected via the iSHE by measuring the voltage between  $A$  and  $B$ .

When a current  $I$  is driven through the CPW, one can consider that the resulting magnetic field is the sum of the magnetic field of each conducting wire. The expression

of the magnetic field created by a current in a conductor with a rectangular cross section can be calculated using the Biot-Savart law.<sup>4</sup> Such a derivation can be found in [Chu06]. We give the expressions of the magnetic field components generated by the central wire, called the signal line, at a point  $(x, y)$  in space outside of the wires:

$$\begin{aligned}
H_x^{wire} = -\frac{I}{8\pi ab} & \left[ + (b-x) \left[ \frac{1}{2} \ln \left( \frac{(b-x)^2 + (a-y)^2}{(b-x)^2 + (-a-y)^2} \right) \right. \right. \\
& \left. \left. + \frac{a-y}{b-x} \arctan \left( \frac{b-x}{a-y} \right) - \frac{-a-y}{b-x} \arctan \left( \frac{b-x}{-a-y} \right) \right] \right. \\
& \left. + (b+x) \left[ \frac{1}{2} \ln \left( \frac{(-b-x)^2 + (a-y)^2}{(-b-x)^2 + (-a-y)^2} \right) \right. \right. \\
& \left. \left. + \frac{a-y}{-b-x} \arctan \left( \frac{-b-x}{a-y} \right) - \frac{-a-y}{-b-x} \arctan \left( \frac{-b-x}{-a-y} \right) \right] \right] \quad (4.1)
\end{aligned}$$

$$\begin{aligned}
H_y^{wire} = -\frac{I}{8\pi ab} & \left[ + (a-y) \left[ \frac{1}{2} \ln \left( \frac{(b-x)^2 + (a-y)^2}{(-b-x)^2 + (a-y)^2} \right) \right. \right. \\
& \left. \left. + \frac{b-x}{a-y} \arctan \left( \frac{a-y}{b-x} \right) - \frac{-b-x}{a-y} \arctan \left( \frac{a-y}{-b-x} \right) \right] \right. \\
& \left. + (a+y) \left[ \frac{1}{2} \ln \left( \frac{(b-x)^2 + (-a-y)^2}{(-b-x)^2 + (-a-y)^2} \right) \right. \right. \\
& \left. \left. + \frac{b-x}{-a-y} \arctan \left( \frac{-a-y}{b-x} \right) - \frac{-b-x}{-a-y} \arctan \left( \frac{-a-y}{-b-x} \right) \right] \right] \quad (4.2)
\end{aligned}$$

where  $x$  is the position along the out-of-plane axis and  $y$  is the position along the SWW's long axis;  $2a$  and  $2b$  are the width and the thickness of the signal line and  $I$  is the current flowing through it. Since the current flows from the central signal line to the two adjacent wires, called ground lines (see Figs. 4.1 and 4.3), the currents in the latter have the opposite sign. Thus, the field generated by each ground line can be found by taking Eqs. (4.1) and (4.2) and replacing  $a$  and  $b$  by  $a'$  and  $b'$ ,  $I$  by  $\frac{-I}{2}$ , and performing the variable change:  $y' = y \pm s$ , where  $s$  is the center-to-center spacing between the signal line and the ground lines, and the plus or minus sign indicates which ground line is being calculated: the one to the left or the one to the right of the signal line. Then, the total magnetic field created by the CPW at a given position in the SWW is simply the sum of these 3 terms.

We present in Fig. 4.4 the components of the total magnetic field, calculated as a function of the distance  $y$  along the SWW, at a fixed position  $x$  below the center of the CPW,  $x = 54.5$  nm, which corresponds to the surface of the ferromagnetic layer in

---

<sup>4</sup>We assume that the wire is infinitely long.

our experiments.<sup>5</sup> The CPW design used in the example of Fig.4.4 is type C, which has  $2a = 70$  nm wide wires with  $s = 150$  nm center-to-center spacing, and thickness  $2b = 30$  nm.

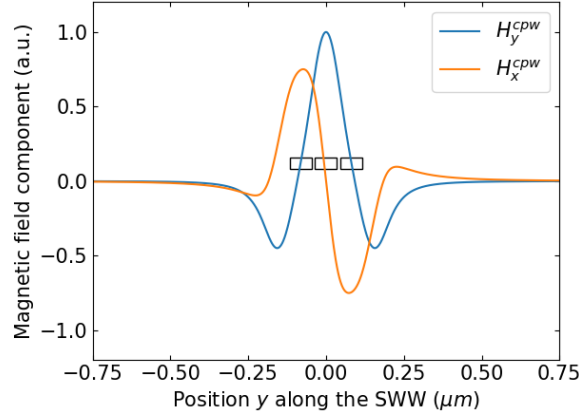


Figure 4.4: In-plane field component  $\mu_0 H_y^{cpw}$  (blue) and out-of-plane field component  $\mu_0 H_x^{cpw}$  (orange) created by a CPW, 54.5 nm below the center of the CPW. The field components are calculated according to Eqs. (4.1) and (4.2), for lines with width  $2a = 70$  nm, thickness  $2b = 30$  nm and center-to-center spacing  $s = 150$  nm. The rectangles drawn in black represent the cross section of the CPW. Each curve is normalized to the maximum of the blue curve.

Let us make several remarks. Firstly, all CPWs are composed of 30 nm Au and 5 nm Ti. Additionally, bulk Ti is 20 times more resistive than bulk Au and the true resistivity of the Ti layer is expected to be even larger given its thickness and the interface with the underlying alumina layer. Thus, we treat the Ti as non-conductive in the calculation of the magnetic field due to its lower thickness and its higher resistivity.

Secondly, the Biot-Savart equation is valid for magnetostatics, but here the aim is to inject an RF current in the GHz range and thus one would expect the Biot-Savart equation to be inadequate for this purpose. However, it has been shown in [Heu15] via numerical calculations that the Biot-Savart equation gives a good approximation of the strength of the magnetic field even at frequencies in the GHz range.

Finally, at high frequencies in thick enough conductors, the electric current flows mainly within the skin depth of the conductor. This is due to eddy currents induced by the changing magnetic field caused by the alternating current. The skin depth is given by:

$$\delta = \sqrt{\frac{\rho}{\pi f \mu_r \mu_0}} \quad (4.3)$$

where  $\rho = 22.2$  n $\Omega$  m and  $\mu_r = 1$  are the bulk resistivity and relative permeability of Au,

<sup>5</sup>The calculated depth corresponds to: 15 nm of Au (half of the total Au), 5 nm of Ti, 30 nm epitaxial Al<sub>2</sub>O<sub>3</sub>, 2 nm Al<sub>2</sub>O<sub>3</sub>, 1 nm Ta<sub>2</sub>O<sub>5</sub>, and 1.5 nm MgO.

and  $f = 6$  GHz is the upper bound of the frequency used in the experiments described in this chapter. The resulting skin depth is  $\delta = 0.97 \mu\text{m}$ , which is much larger than the thickness and width of the conducting lines of the CPWs.

Thus, we take the magnetostatic fields calculated via Eqs. (4.1) and (4.2) to be valid for RF currents up to the GHz range. As shown in Fig. 4.4, the CPW gives rise to a symmetrical in-plane field, parallel to the long axis of the SWW, which reaches its maximum amplitude under the center of the CPW. On the other hand, the out-of-plane field is anti-symmetrical, vanishes under the center of the CPW and then changes sign, reaches its maximum amplitude under each ground line.

From the spatial profile in Fig. 4.4 we obtain the Fourier spectrum of an antenna's magnetic field, shown in Fig. 4.5. Since we are performing numerical calculations, the data is non-continuous and we use a fast Fourier transform (FFT) algorithm to calculate the Fourier spectrum of the magnetic field for all three CPW designs. An interesting property of the magnetic field of a given CPW is that the absolute value of the FFT of the in-plane and of the out-of-plane components are equal. The fields are calculated as per Fig. 4.4: at a depth 54.5 nm below the center of the wires, which corresponds to the surface of the ferromagnetic layer; and as a function of  $y$ . Therefore the Fourier coefficients, written  $b_{k_y}$  for either field component, are expressed as a function of  $k_y$ , the wavevector component parallel to the direction of propagation  $\hat{y}$ , and they constitute the Fourier spectrum of the CPW, written  $(b_{k_y})$ .<sup>6</sup>

Moreover, the Fourier spectra of all the CPW designs (A, B, C) show a similar profile: the first maximum is the highest, each following maximum is notably smaller than the previous one, and the amplitude is zero between maxima. More importantly, the minima are situated at integer multiples of  $\frac{2\pi}{s}$ , where  $s$  is the center-to-center spacing. Consequently, the smaller  $s$  is, the larger is the range of wavevectors between two minima. In fact, if one uses a single wire, a design called stripe antenna, there is only one maximum, at  $k_y = 0$ , and the amplitude decreases to 0 for increasing wavevectors [Ciu16]. On the other hand, the width  $2a$  only has an influence on the maximum amplitudes of the curve between the minima.

Thus we have designed nanometric CPW antennae for the purpose of exciting a large range of non-zero wavevectors. These antennae are scalable not only because one can reduce their size and spacing and still obtain fields capable of exciting spin-waves, but also because this reduction leads to shorter wavelengths, which is a basic requirement for scaling down any magnonic device to the nanometer scale. Moreover, the wavevector dependent spin-wave excitation of the CPWs will allow us to characterize the iSHE detection scheme by comparing the expected spectrum vs. the measured signal, and determine whether the iSHE detection is wavevector independent or not.

---

<sup>6</sup> $(b_{k_y})$  refers to the Fourier spectrum, while  $b_{k_y}$  refers to a specific Fourier coefficient of this spectrum.

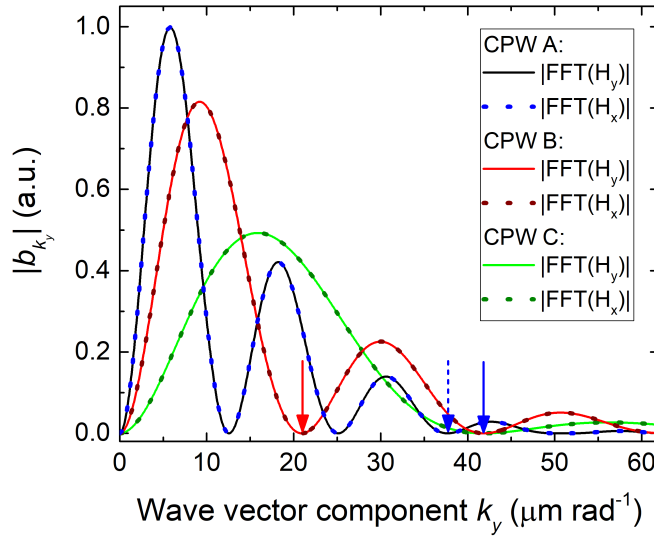


Figure 4.5: Absolute value of the FFT of the magnetic field components created by three different CPW designs, assuming a fixed current. CPW type A: in-plane (black line) and out-of-plane component (blue dots). CPW type B: in-plane (red line) and out-of-plane component (dark red dots). CPW type C : in-plane (green line) and out-of-plane component (dark green dots). Each curve is normalized to the maximum of the black line curve. For details about the CPW designs, see Tab. 2.1. The blue arrows show the minima detected in the spin-wave rectification experiments for CPW A (dashed blue) and CPW B and C (solid blue). The red arrow shows the minimum of the spectrum close to the minimum detected in the Brillouin light scattering microscopy experiment for CPW B.

### 4.3.2 Spatial profile of spin-waves in a spin-wave waveguide in the Damon-Eshbach configuration

We remind the two main configurations for spin-wave excitation that were described in Sec. 1.3.3: the backward volume configuration, where the saturating external field is applied parallel to the direction of propagation, and the Damon-Eshbach configuration, where the field is applied in-plane but transversely to the direction of propagation. In this chapter, we will mainly deal with the Damon-Eshbach configuration, thus the calculations will be done in that geometry.

We consider the Damon-Eshbach configuration, with a propagation of spin-waves in the  $y$  direction and the magnetization saturated through a magnetic field along the  $z$  direction. Here we summarize the expressions for the components  $k_x$ ,  $k_y$ ,  $k_z$  of the corresponding wavevector  $\mathbf{k}$ . Different waveguide modes can be excited, each with a different spatial configuration in the  $(x, z)$  plane due to the finite size, analogous to the vibration modes of a drum membrane.

In the  $x$  direction, perpendicular to the film, according to Sec. 1.3.3, the ferromagnetic layer is thin enough that the spin-waves present an homogeneous profile across the thickness of the film, with  $k_x = 0$  as higher modes require much higher excitation frequencies.

The SWW is half a  $\mu\text{m}$  to several  $\mu\text{m}$  wide, which is small enough to induce quantization of the width mode, described by the width or waveguide mode number  $n$ . Thus, spin-wave modes of different profiles can exist along the  $z$  direction, described here by the mode number  $n$  and  $k_z = \frac{(n+1)\pi}{w_w}$ . In the Damon-Eshbach configuration, the magnetization at the lateral edges of the SWW can be aligned with the external field (the edges are unpinned) or aligned with the long axis of the SWW (the edges are pinned) as well as anywhere in between. This is due to the competition between the Zeeman energy and the dipolar energy, and it can lead to an inhomogeneous effective field, which is reduced near the edges. In such a case, one can define an effective width  $w_{eff}$  as the width of the SWW where the effective field is greater than half the external field. For more details on the calculation see [Brä15]. In our case, we determined using Eq. (2.56) in [Brä15]:

$$H_{eff}(z) = H - \frac{M_s}{\pi} \left( \arctan\left(\frac{t_f}{2z + w_w}\right) - \arctan\left(\frac{t_f}{2z - w_w}\right) \right) \quad (4.4)$$

that  $w_{eff} \approx w_w$  for the  $5\ \mu\text{m}$  wide SWW. This means that the magnetization at the lateral edges of the SWW are pinned and parallel to the edges.

Finally,  $k_y$ , the wavevector component parallel to the propagation direction, is continuous.

### 4.3.3 Excitation efficiency

Now that we have calculated the magnetic field created by the three CPW designs, we can look at the spin-waves they can excite. Interestingly, the amplitude of the FFT for all three CPWs for  $k_y = 0$  is zero, a characteristic of CPWs. This means that an RF field generated by the CPWs is incapable of exciting ferromagnetic resonance, which has  $\mathbf{k} = 0$ .

As mentioned before, the aim is to have an expression for the excitation efficiency, where the excitation field has two contributions. In the previous section we considered the field from the CPW, but one also has to consider the dynamic dipolar field generated by the SWs themselves that is obtained from the spatial profile of the spin-waves. This involves solving the equation of motion for the spin-wave magnetization as was done in [Sch08] for the Damon-Eshbach and the backward volume configurations.<sup>7</sup> Here we will summarize the main steps for the Damon-Eshbach configuration.

The propagation of spin-waves is affected by the dipolar field created by the spin-waves themselves. Therefore, the relation in Eq. (1.21) becomes, for spin-waves:

$$\mathbf{m} = \bar{\bar{\chi}} (\mathbf{h} + \mathbf{h}_d) \quad (4.5)$$

<sup>7</sup>Further reading may include [Kal80; Gus02; Kos07; Dem09].

where  $\mathbf{h}$  is the excitation field generated by the CPW,  $\mathbf{h}_d$  is the spin-wave dipole field and  $\bar{\chi}$  is the susceptibility tensor for the uniform mode excitation (see Eq. (1.29) in Sec. 1.2.4). The dipolar field can be written as [Sch08]:

$$\mathbf{h}_d(\mathbf{y}) = \int_{-\infty}^{+\infty} \bar{\bar{G}}(\mathbf{y} - \mathbf{y}') \mathbf{m}(\mathbf{y}') d\mathbf{y}' \quad (4.6)$$

where  $\bar{\bar{G}}$  is a 2D tensorial Green's function. The Green's function for magnetostatics is detailed in [Gus02]. It describes the dipolar field at a point  $\mathbf{y}$  created by the magnetization at a point  $\mathbf{y}'$ , and the integration over the ferromagnet gives the total dipolar field at the position  $\mathbf{y}$ . The elements of the tensorial Green's function are related to the components of the susceptibility tensor for uniform magnetization dynamics using Eq. (4.6). One can rewrite Eq. (4.5) as an expression relating the magnetization to the uniform mode susceptibility components. In the Damon-Eshbach configuration, this is given by [Sch08; Dem09]:

$$m_x(\mathbf{y}, t) = \frac{4\pi}{t_f} |b_{k_y}| \frac{\chi_{\perp} - \text{sign}(k_y)}{\chi_{\perp}^2 - \chi_{\parallel}^2} e^{ik_y y} e^{i\omega t} \quad (4.7)$$

where  $m_x$  is the out-of-plane component of the magnetization,  $t_f$  is the thickness of the ferromagnetic layer,  $y$  is the position of the spin-wave along the direction of propagation,  $k_y$  the component of the wavevector parallel to the direction of propagation,  $\chi_{\parallel}$  and  $\chi_{\perp}$  are the diagonal and off-diagonal components of the susceptibility tensor in Eq. (1.29),  $|b_{k_y}|$  is the amplitude of the Fourier transform of the CPW field for the wavevector  $k_y$ , presented in Sec. 4.3.1, and  $\omega$  is the angular frequency of the excitation field.

In Eq. (4.7), both the in-plane and the out-of-plane components of the CPW's field are taken into account, though their combined effect on the spin-wave depends on its direction of propagation, given by  $\text{sign}(k_y)$ .<sup>8</sup> Indeed, as seen in Fig. 4.4, the magnetic field components have the same sign under the left ground line while they have opposite sign under the right ground line. Due to the well-defined direction of rotation of the magnetization, the torques of the two components of the RF field on the magnetization are in phase on one side of the antenna, and out of phase on the other side of it. The result is an asymmetry of the amplitude of the spin-waves depending on the propagation direction. Thus, spin-waves with  $k_y > 0$  have greater amplitude than spin-waves with  $k_y < 0$ .

The amplitude of dynamic magnetization oscillation  $|\mathbf{m}|$  at a given wavevector  $k_y$  is a measure of how efficiently a spin-wave at  $k_y$  is excited and provides the wavevector resolved spin-wave spectrum as it can be measured in an experiment. We therefore define the excitation efficiency here  $\eta \propto |m|$ . For a thin film system with perpendicular anisotropy, the excitation efficiency is written [Brä17b]:

$$\eta_n^{\pm}(k_y) = |b_{z,n}| |b_{k_y}| \left| \frac{f_n(k_y)}{\mu_0 \gamma'} \pm \frac{1}{\mu_0 M_{eff}} \left( \frac{f_n(k_y)^2}{\gamma'^2} - \mu_0^2 H_{eff}^2 \right) \right| \quad (4.8)$$

<sup>8</sup>If  $b_{k_y, h_x}$  is the Fourier transform of the out-of-plane field as a function of  $y$ , and  $b_{k_y, h_y}$  is the Fourier transform of the in-plane field as a function of  $y$ , then through symmetry arguments and using Maxwell's equations, Schneider *et al.* found that  $b_{k_y, h_x} = i \text{sign}(y) b_{k_y, h_y}$  [Sch08].

where  $\pm$  indicates whether  $k_y > 0$  or  $k_y < 0$ ,  $f_n(k_y)$  is the frequency of the spin-wave with  $k_y$  and  $n$  indicates the waveguide mode  $n$  due to the quantification of  $k_z$  across the width of the SWW, see Sec. 4.3.2.<sup>9</sup>  $\gamma'$  is the gyromagnetic ratio in  $\text{GHz T}^{-1}$ ,  $M_{eff}$  is the effective magnetization defined in Eq. (1.14),  $H_{eff}$  is the effective field in the ferromagnetic layer as defined in Eq. (1.12). The  $b_{z,n}$  factor is proportional to the net torque that the RF fields can exert on the magnetization for a given waveguide mode  $n$ . Therefore,  $b_{z,n}$  is proportional to the net integrated magnetic moment across the effective width:

$$b_{z,n} \propto \frac{1}{n+1} \cos \left[ \pi(n+1) \left( z + \frac{d_{eff}}{2} \right) \right] \frac{d_{eff}}{2} = \begin{cases} \frac{1}{n+1} & \text{for } n \text{ even} \\ 0 & \text{for } n \text{ uneven} \end{cases} \quad (4.9)$$

As a result, uneven-numbered modes cannot be excited in the Damon-Eshbach geometry, and waveguide modes of increasing number  $n$  have an excitation efficiency that decreases with  $\frac{1}{n+1}$ .<sup>10</sup>

In the model described thus far, if one excites a SWW with a CPW, a certain range of wavevectors can be excited, depending on the spatial features of the CPW. However, due to the dispersion relation, the choice of applied frequency and external static field will select only one wavevector. Additionally, only uneven waveguide modes can be excited, and one direction of propagation will be favored. The asymmetry of the spin-wave's amplitude as a function of propagation direction can be a desired property for some applications, for example spin-wave logic gates in which information must pass only in one direction.

#### 4.3.4 Non-zero linewidth model

The effect of relaxation processes on spin-waves was not discussed in the derivation of the excitation efficiency Eq. (4.8). In this subsection, we include the non-zero linewidth in the excitation efficiency as derived by T. Brächer and P. Pirro in [Brä17b]. Phenomenological losses in magnetization dynamics lead to a non-zero frequency linewidth, which can be linked to the relaxation rate given in Eq. (1.71), via:

$$\Delta f_n(k_y) = \frac{\omega_r}{\pi} \quad (4.10)$$

where  $\Delta f_n(k_y)$  is the linewidth in units of frequency for the spin-wave frequency  $f_n(k_y)$ . A consequence of the non-zero frequency linewidth is that the spin-waves with  $k_y$  can be excited not only at frequencies  $f_n(k_y)$  but also at frequencies close by  $f' \neq f_n(k_y)$ . The

<sup>9</sup>The frequency and the wavenumber are related by the dispersion equation (1.70) for a FeCoB thin film system with perpendicular anisotropy. It is therefore a function of  $k_x$ ,  $k_y$  and  $k_z$ ; however since  $k_x = 0$  and  $k_z$  has discrete values depending on  $n$ , we write the spin-wave frequency as  $f_n(k_y)$  for ease of reading.

<sup>10</sup>In other works in the literature, such as [Dem09; Brä17a; Brä17b], the mode index starts at  $n = 1$  for the fundamental mode, and thus in that numbering scheme only uneven modes can be excited and their efficiency decreases with  $\frac{1}{n}$ . We started the index at  $n = 0$  for the fundamental mode due to the lack of nodes in its profile, similarly to [Wan].

distribution of the frequencies  $f'$  of the spin-waves with a given wavevector  $k_y$  excited at  $f_n(k_y)$  is given by a Lorentzian function [Hei94]:

$$L_{k_y}(f') = \frac{2}{\pi} \frac{\Delta f_n^2(k_y)}{4[f' - f_n(k_y)]^2 + \Delta f_n(k_y)^2} \quad (4.11)$$

This Lorentzian function is defined such that  $\int_{-\infty}^{+\infty} L_{k_y}(f') df' = 1$  to reflect its property as a probability density. To account for all of the spin-waves with wavevector component  $k_y$  and waveguide mode  $n$ , excited by a source generating a magnetic field at a frequency  $f = f_n(k_y)$ , we calculate the excitation efficiency of Eq. (4.8) by the frequency distribution due to the non-zero linewidth:

$$c_n^\pm(f', k_y) = \eta_n^\pm(k_y) \times L_{k_y}(f') \quad (4.12)$$

In the following we will numerically evaluate the expression in Eq. (4.12) to predict the excitation spectrum that we expect to measure in a wavevector independent experiment such as the spin-wave rectification for which only the frequency of the excitation source is swept continuously. For this we have to integrate Eq. (4.12) over all wavevectors to obtain an expression of the excitation efficiency  $C_n^\pm(f')$  as a function of the excitation frequency  $f'$ . In the numerical evaluations, due to discretization this will be a sum over  $k_y$ :

$$C_n^\pm(f') = \sum_{k_y} c_n^\pm(f', k_y) \quad (4.13)$$

Next we describe the procedure for the evaluation of  $C_n^\pm(f')$ . Using the dispersion relation given in Eq. (1.70), we substitute the variable  $k_y$  by  $f_n(k_y)$  and calculate  $c_n^\pm(f', f_n(k_y))$  for  $f'$  and  $f_n(k_y)$ , with both variables ranging from 0 to 10 GHz in steps of 1 MHz. In the resulting 2D matrix, where the values of  $c_n^\pm(f', f_n(k_y))$  as a function of  $f'$  (and fixed  $f_n(k_y)$ ) are stored in the columns, a summation over the rows gives the total excitation efficiency  $C_n^\pm(f')$  in the presence of non-zero linewidth, for a given waveguide mode  $n$  and for a fixed external field  $H$ .

We present in Fig. 4.6 the normalized excitation efficiency  $C_n^\pm(f')$ , calculated for all three CPW designs, under a DC field  $\mu_0 H = 55$  mT. The unnormalized data show a large difference in amplitude. To better compare, in Fig. 4.6 we normalized each excitation efficiency to its respective maximum. We compare the excitation efficiency  $C_n^\pm(f')$  taking into account only the waveguide mode  $n = 0$  (solid lines) and when taking into account the modes with  $n$  up to  $n = 4$  (dotted lines). As can be seen, the influence of the  $n = 2$  and  $n = 4$  modes is negligible for all three CPW designs, and for all frequencies in the explored range. This is due to the fact that while the width of the SWW is small enough for quantization of the waveguide modes, it is large enough that the mode separation in terms of frequency is small, and therefore the excitation profile changes little between modes. Additionally, the amplitude of each higher mode decreases with  $1/(n+1)$ . Thus, for all further calculations, we ignore the effects of the higher order waveguide modes  $n > 0$ .

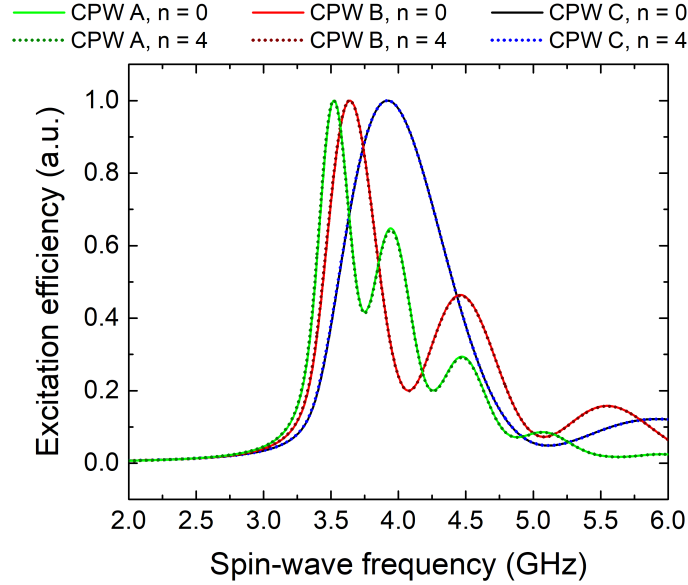


Figure 4.6: Normalized excitation efficiency of the three CPW designs for a fixed magnetic field  $\mu_0 H_{eff} = 55$  mT and for an effective magnetization  $\mu_0 M_{eff} = 194$  mT. The solid lines are the calculations including only the fundamental mode  $n = 0$ , the dotted lines include all modes up to  $n = 4$ . Each curve is normalized to its respective maximum.

Additionally, it is clear that we are far from exciting a single spin-wave with a given wavevector component and its associated frequency. The combination of the large range of wavevectors that the CPW antenna can excite, and the non-zero linewidth leads to a complex excitation efficiency with several peaks of varying amplitude, as shown in Fig. 4.6.

## 4.4 Spin-wave rectification experiments

### 4.4.1 Experimental setup

The experimental setup for spin-wave rectification spectroscopy (SWR) is somewhat similar to the one used for the ST-FMR experiments in Chap. 3: an electromagnet supplies a uniform magnetic field that is slowly varied. The setup, shown in Fig. 4.7 (see also Figs. 4.1 and 4.3) for SWR measurements uses a similar principle than ST-FMR but with the important difference that the RF current is not applied to the SWW but to the CPW antenna fabricated on top. As described in Sec. 4.3 this will excite spin-waves of non-zero wavevector (see Fig. 4.6), and the experiment can thus provide information on the propagating spin-waves. For their excitation, high-frequency probes are connected to nanometric shorted CPWs on top of the SWWs. A signal generator supplies a high frequency current in the GHz range, which is modulated in power at a

frequency in the 10 kHz range via a lock-in amplifier (LIA). The LIA is connected to the leads of the SWWs. It is used to detect the voltage rectified via iSHE which arises from the resulting spin-wave dynamics in the FeCoB. In the SWR experimental geometry, the magnetization is oriented along the short axis of the SWW by the external field. This maximizes the iSHE signal, as will be discussed in Sec. 4.4.3.

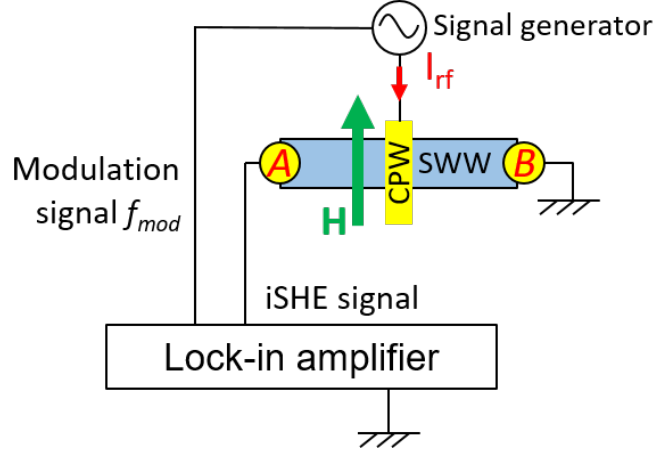


Figure 4.7: Schematic of the spin-wave rectification setup. An electromagnet generates a magnetic field  $\mathbf{H}$  perpendicularly to the long axis of the SWW. A signal generator supplies the CPW antenna with an RF current which is modulated at  $f_{mod}$  by the lock-in amplifier. The lock-in amplifier measures the iSHE voltage between  $A$  and  $B$ .

Like in the ST-FMR measurements, the rectified voltage is detected as a function of the applied field for a given excitation frequency. The applied power of -1 dBm corresponds to the regime of linear excitation, whereas an increase of the power by about 2-3 dB leads to a deviation of the linear scaling of the measured voltage with the applied microwave power.

#### 4.4.2 Measurement protocol

A sinusoidal RF current, set at constant frequency throughout the measurement, is sent through the CPW antenna. The electromagnet is set such that the field will be in the plane of the device at an angle  $\theta_H = 90^\circ$  with respect to the long axis of the SWW, as shown in Fig. 4.1. The magnetic field is then decreased down to a minimum of  $\mu_0 H = -170$  mT, sweeping across the resonance and then decreased back to 0. The measurement is then immediately repeated for positive fields. The DC voltage is measured across the SWW Au contacts, with the signal-to-noise ratio enhanced via the modulation of the RF power and the lock-in amplifier.

Unlike ST-FMR experiments, the result of SWR is not a Lorentzian peak. When the field is swept, it excites a continuous range of spin-waves, resulting in one or more non-Lorentzian peaks, depending on the CPW design used. Thus, the linewidth cannot be

characterized. The results are then compared to the expected excitation profiles obtained via the calculations derived in Sec. 4.3.

### Linearity with respect to RF power

As with the ST-FMR experiments (see Sec. 3.4.1), we seek to study spin waves in the linear excitation regime, which we characterize by the proportionality between the square of the resonance peak voltage and the RF power injected in the CPW. Of course, we are simultaneously exciting a continuum of spin-waves with a certain range of wavevectors, and thus cannot compare two spin-wave resonance peaks individually. Thus, we plot the logarithm of the maximum voltage of the measured spin-wave spectrum as function of the RF power injected in the CPW, shown in Fig. 4.8. In the resulting log-log plot, the linear fit is adequate until a power threshold of about  $-1$  dBm. Thus the SWR experiments are performed at this power or below. Unfortunately, the BLS experiments described in Sec. 4.5 were carried out before we could determine the linearity power threshold.

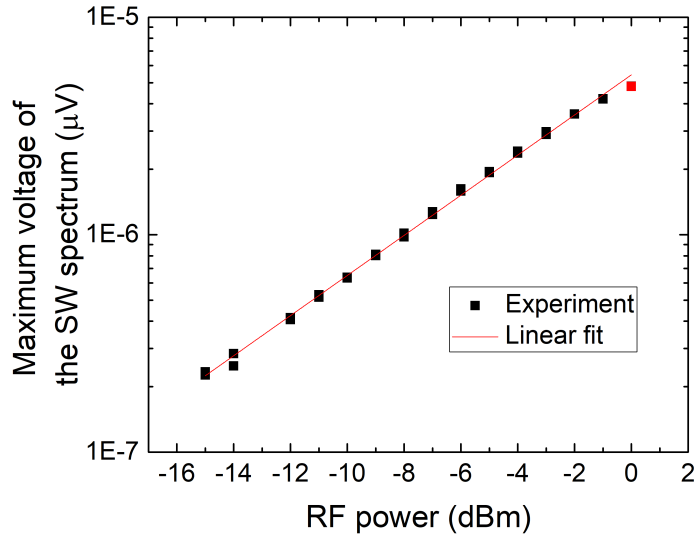


Figure 4.8: Maximum voltage of the spin-wave spectrum as a function of the RF power injected in the CPW antenna. The linear fit on the log-log scale shows the linearity threshold at approximately  $-1$  dBm.

#### 4.4.3 Angle dependence of spin-wave rectification

We performed an angle-dependent measurement of the spin-wave rectification, similarly to the ST-FMR measurements by varying the in-plane field angle  $\theta_H$  similarly to the experiment described in Sec. 3.4.2 for ST-FMR. From the spin-wave spectra we extract

the maximum amplitude and plot the results as a function of the in-plane angle of the field in Fig. 4.9.

There are some key differences with ST-FMR. Firstly, the spin-wave excitation is the result of two field components, an in-plane one and an out-of-plane one (see Fig. 4.4). In the case of uniform FMR, the angle dependences for AMR and iSHE for these field configurations have been calculated in [Har16].<sup>11</sup> We summarize their findings here:

$$\begin{aligned} V_{ishe}^x &\propto \sin \theta_H & V_{amr}^x &\propto \sin(2\theta_H) \\ V_{ishe}^y &\propto \sin \theta_H^3 & V_{amr}^y &\propto \sin(2\theta_H) \sin \theta_H \end{aligned} \quad (4.14)$$

where  $V_{ishe}^x$  is the signal generated by the out-of-plane CPW field excitation via the iSHE,  $V_{amr}^y$  is the signal generated by the longitudinal CPW field excitation via AMR, and  $\theta_H$  is the in-plane angle of the external field.

In the experiments described in this chapter we deal with spin-waves, therefore the signals obtained may deviate from these results. As one rotates the electromagnet in the plane of the thin film, the geometry changes from the Damon-Eshbach configuration to the backward-volume configuration periodically meaning that, as shown in Fig. 1.4(b), the dispersion relation continuously shifts from one curve to the other.<sup>12</sup> As seen in Eq. (4.8), the excitation efficiency of a CPW antenna depends on the frequency and therefore on the dispersion relation. Hence the spectrum of the excited spin-waves is expected change as a function of the angle as well. In Fig. 4.9, we only plot the maximum amplitude of the spectra as a function of the angle, and we are not able to take into account the change in dispersion relation due to the angle.

As seen in Fig. 4.9, the angular dependence of the maximum voltage of the excited spin-wave spectrum is well fitted by a linear combination of  $V_{ishe}^x$  and  $V_{ishe}^y$  from Eq. (4.14), and cannot be fitted adequately by  $V_{amr}^x$  or  $V_{amr}^y$ . This allows us to conclude that the SWR signal in the SWW due to AMR is negligible, and that the combined effects of spin-pumping and the iSHE are the dominant source of the signal. Furthermore, the experiments presented in this chapter are performed at  $90^\circ$ , an angle for which the AMR signal is minimum, while the iSHE is maximum.

As mentioned for the ST-FMR case in Sec. 3.4.2, the Nernst effect, which has a  $\cos \theta_H$  dependence on the applied field angle [Sch12], can also be dismissed. This is likely due to the extremely small thickness of the FM layer, which likely has a negligible temperature gradient.

#### 4.4.4 Experimental results

In the following, we address the excitation and detection of propagating spin-waves with non-zero wavevectors in spin-wave rectification (SWR) experiments and we show that this technique allows for the wavevector independent detection of the locally excited spin-wave dynamics in a large wavevector range. In the SWR experiment, the CPWs

<sup>11</sup>In [Har16], the rectification voltages for AMR can be found in Tab. 4 and the voltages for the iSHE in Tab. 6.

<sup>12</sup>Here,  $\theta_k = \theta_H$ .

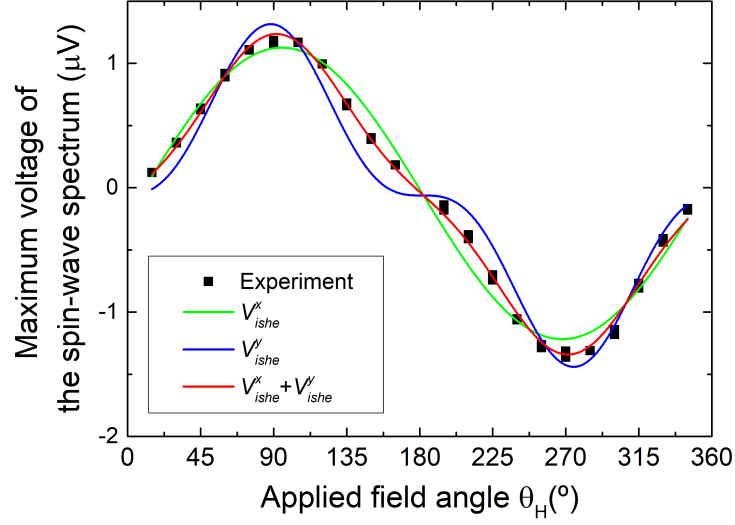


Figure 4.9: Angle dependence of the spin-wave rectification signal. The maximum voltage of the detected spin-wave spectrum is plotted vs. the applied field angle  $\theta_H$  (black squares). The solid curves are the calculated angle-dependence of the iSHE voltages, given in Eq. (4.14), fitted to the experimental data.

are used to excite propagating spin-waves and the rectified DC voltage arising from the driven spin-wave dynamics is measured by the leads at the edges of the SWW. Therefore the excitation as a function of the spin-wave wavevector is determined by the spatial extent of the excitation source, which is shown in reciprocal space in Fig. 4.5. The SWWs are magnetized along their short axis to maximize the torque from the in-plane Oersted field created by the CPWs, in the Damon-Eshbach configuration.

Experimental results of the spin-wave rectification (SWR) measurements are shown in Fig. 4.10 for all three CPW designs A, B and C (see Tab. 4.1). Each device has a different CPW design and a different FM layer thickness and therefore a different effective magnetization. The characteristics of the 3 devices are resumed in Tab. 4.1.<sup>13</sup>

The three CPW designs gives access to different wavevector ranges (see Fig. 4.5). The SWR voltage due to spin-pumping and the iSHE is proportional to the square of the dynamic magnetization  $\mathbf{m}^2$  (see Eq. (1.80)), and thus to the square of the spin-wave excitation efficiency calculated in Sec. 4.3.3. The measurements have been performed with an applied RF power of  $P = 800 \mu\text{W} = -1 \text{ dBm}$  at a frequency of 4.8 GHz. The voltages have been normalized to their individual maximum, which is on the order of  $\mu\text{V}$ . Further details on the absolute values of the measured voltages are given in a subsection below.

As can be seen in Fig. 4.10 the spin-wave rectification spectra vs field for  $f = 4.8 \text{ GHz}$

<sup>13</sup>The devices investigated in this section are 7-C1, 7-D1 and 7-E1 in Tab. 2.2.

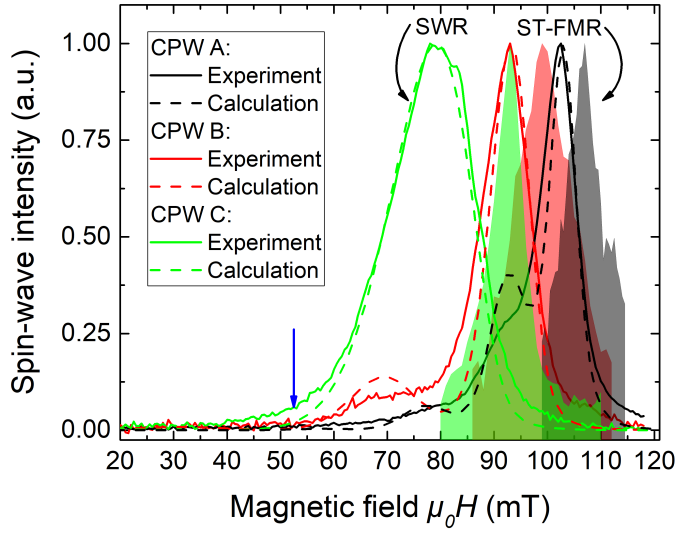


Figure 4.10: Measured spin-wave intensity spectra (solid lines) and analytical calculations of the expected excitation spectra (dashed lines), at a fixed frequency of 4.8 GHz, for 3 different CPW designs and effective magnetizations. Black lines: CPW type A and  $\mu_0 M_{eff} = 168$  mT. Red lines: CPW type B and  $\mu_0 M_{eff} = 194$  mT. Green lines: CPW type C and  $\mu_0 M_{eff} = 221$  mT (See Tab. 4.1 for details on the CPWs). The shaded peaks show the ST-FMR peaks of each spin-wave waveguide, colored correspondingly. All measured voltages and calculated spectra have been normalized to their respective maximums for comparison. The blue arrow shows the approximate field value where the calculated spectra fall below the noise level of the measurement.

(full lines) show one large peak, with a subsidiary peak in some cases. The dashed lines represent the square of the spin-wave excitation efficiency calculated via Eq. (4.13). For comparison, the ST-FMR peaks of the same devices are shown (shaded peaks). The width of the SWR peaks as well as the field separation between the SWR peaks and the FMR peak increase as the distance  $s$  between the signal line and ground lines of the CPWs decrease. This is because the smaller CPWs excite a wider range of wavevectors, centered around a higher wavevector component  $k_y$ , as predicted by Fig. 4.5.

Using the analytical formalism presented in Sec. 4.3, we determine the spin-wave spectrum in the SWWs. Taking into account the perpendicular magnetic anisotropy, the non-zero linewidth, an effective width of the SWW of  $w_{eff} = 5 \mu\text{m}$ , we calculate the expected spin-wave intensity spectrum excited by the CPWs, which is proportional to the square of the excitation efficiency calculated in Eq. (4.13) and shown in Fig. 4.6. They are represented by the dashed lines in Fig. 4.10, plotted as a function of applied field instead of applied frequency.

We average over the two emission directions along the wire, which are not equal due to

Table 4.1: Characteristics of the SWW used for the spin-wave rectification experiments. Each device has a different CPW design and a different FM layer thickness. The devices are referred to by their CPW design.

CPW design	$2a$ (nm) wire width	$s$ (nm) wire spacing	$\mu_0 M_{eff}$ (mT)
A	120	500	168
B	70	300	195
C	70	150	221

the interplay of the in-plane and out-of-plane component of the CPW field, as described by the  $\pm$  symbol in Eq. (4.8). Furthermore, we only consider the fundamental waveguide mode  $n = 0$ <sup>14</sup> in the calculations since the influence of higher modes is negligible as shown in Fig. 4.11. The analytical calculations assuming a wavevector independent detection efficiency by the iSHE are in good agreement with the experimentally obtained spectra. The small visible deviations are likely caused by a too simple description of the material's damping, which is assumed to be entirely Gilbert-type,<sup>15</sup> and by an idealization of the CPWs which neglects their edge roughness.

The calculated intensity drops close to the noise level of our experimental setup for  $\mu_0 H \approx 52$  mT. We convert this field value into a wavevector for each device via Eq. (4.13),<sup>16</sup> obtaining a different value for each CPW design. Thus, the calculated intensity drops to the noise level of the setup for wavevectors beyond the third minimum of the CPWs of type A, beyond the second minimum for type B and beyond the first minimum for type C (see the blue vertical arrow in Figs. 4.5 and 4.10). This field value corresponds to approximately  $40 \text{ rad } \mu\text{m}^{-1}$  for all three types of CPWs and is equivalent to a wavelength of  $\lambda = 166$  nm for type A and of  $\lambda = 150$  nm for type B and C, because the minima are situated at integer multiples of  $\frac{2\pi}{s}$ , where  $s$  is the center-to-center spacing of the CPWs. The experimentally accessible wavevector range and the envelopes of the measured spectra are predominantly determined by the features of the excitation source and no systematic discrepancy with increasing wavevector is observed. Thus, the detection efficiency via iSHE is independent of the spin-wave wavevector in the experimentally accessible wavevector range.

To demonstrate the feasibility of the iSHE detection for a broader range of frequencies, Fig. 4.11 compares the measured excitation spectra of the three different CPW types to the corresponding expected excitation spectra for frequencies between 2 and 5.5 GHz, determined by the available field range of our experiments. The measured voltage and the expected spin-wave intensity are displayed color-coded as a function of the applied

<sup>14</sup>We remind that in other works, the fundamental width mode can be referred to as  $n = 1$ .

<sup>15</sup>In Sec. 3.4.4, we qualitatively characterize a non-Gilbert-type damping in ST-FMR experiments, caused by a inhomogeneous effective magnetization of the ferromagnetic layer. This non-Gilbert-type damping is also present in the devices used in this section but has not been characterized.

<sup>16</sup>For each device, we calculate Eq. (4.13) for  $\mu_0 H = 52$  mT and  $f = 4.8$  GHz and using the device's  $M_{eff}$  and its CPW design. We sum over the rows to account for the non-zero linewidth, and look up the corresponding wavevector.

field and frequency. The white lines correspond to the Kittel fits obtained from the ST-FMR measurements. The spectra have been normalized individually to their maximum at each frequency to account for the changes of the input impedance. All color maps use an identical, logarithmic scale. As can be seen from Fig. 4.11, the measured spectra are in good qualitative agreement in the probed field and frequency range. In the entire range, the noise-limited maximum detectable wavevector is about  $40 \text{ rad } \mu\text{m}^{-1}$  and is determined by the Fourier spectrum of the excitation source. The visible small peak at fields larger than the FMR, which corresponds to a spin-wave mode below the spin-wave band, is associated with an edge mode, [Gub04] which is weakly excited by the CPW.

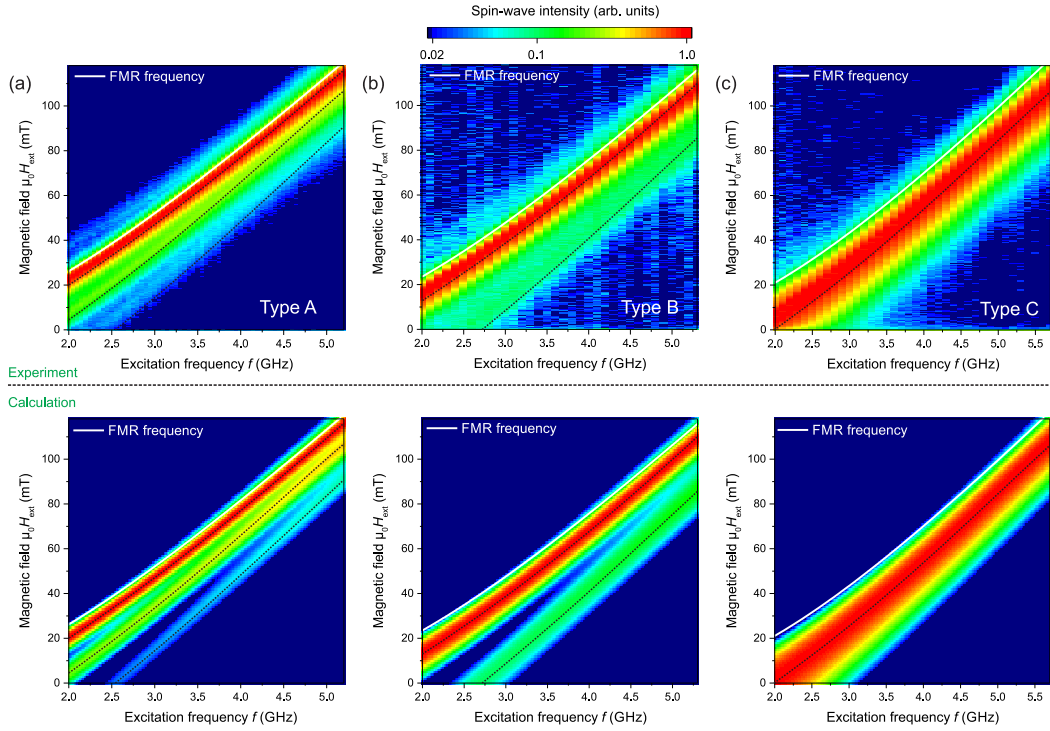


Figure 4.11: Color-coded measured and calculated spin-wave intensities as a function of the applied frequency and applied magnetic field. Both have been normalized to their respective maximum for a given frequency. The upper panel shows the measurement and the lower panel the analytical calculations. (a): CPW type A and  $\mu_0 M_{eff} = 168 \text{ mT}$ . (b): CPW type B and  $\mu_0 M_{eff} = 194 \text{ mT}$ . (c): CPW type C and  $\mu_0 M_{eff} = 221 \text{ mT}$ . The white lines represent the Kittel fits obtained from the ST-FMR measurements. In both panels, the dashed lines are guides to the eye indicating the position of the maxima of the spectra expected from the calculations. Taken from [Brä17b].

### Comparison of measured voltages

In the following paragraphs, we provide a more quantitative analysis of the amplitude of the iSHE signals. In order to check whether there is a dependence of the iSHE voltage level on the excited wavevector itself we compare the voltage levels for the different types of CPW that have their first maximum at different wavevectors. The peak voltages for the different CPW antennae obtained in the experiments are: CPW type A:  $V_{max} = (13.2 \pm 1.3) \mu\text{V}$ , CPW type B:  $V_{max} = (2.5 \pm 0.3) \mu\text{V}$ , and CPW type C:  $V_{max} = (1.1 \pm 0.1) \mu\text{V}$ . The ratio between the voltages for each CPW, [C:B:A], is thus [(1) : (2 ± 1) : (12 ± 2)]; the error following from assuming a 10% uncertainty in the voltages arising from the variations in the contacting and the device resistance. These experimental values are compared to calculations from Sec. 4.3. These are determined by three factors:

In the following we will try to estimate the expected voltage ratios between the different CPWs, which are determined by three factors:

1. The Fourier spectrum of the CPWs: Fig. 4.12 shows the square of the Fourier spectrum of the three CPWs normalized to CPW type C. This corresponds to the relative excitation amplitude which is expected if the current sent into the CPWs is kept fixed. It corresponds to a different voltage ratio [C:B:A] of [1:2.7:4.1] between the different CPWs.
2. The different transmission characteristics of the CPWs: for a fixed microwave current, the peak values of the microwave fields created by all three CPWs are the same within  $\pm 10\%$ , so we assume them to be equal for simplicity. The CPWs of type B and C feature identical resistances, typically around  $550 \Omega$ ; devices of type A feature a twice larger track width and, thus, a twice smaller resistance, typically around  $275 \Omega$ . Assuming that due to the very small size of the structures in comparison to the microwave wavelength the impedance is essentially determined by the resistance, this results in a larger reflection from CPW B and C than from CPW A. The transmission coefficient of the antennae is related to the reflexion coefficient given in Eq. (3.57):

$$T = 1 - \Gamma = \frac{2 \times 50}{R_{cpw} + 50} \quad (4.15)$$

where  $R_{cpw}$  is the resistance of the considered CPW design and the source impedance of the signal generator is  $50 \Omega$ . The ratio of the transmission coefficient for CPW A over the transmission coefficient for CPW B and C is 1.85, thus we have a contribution of [1:1:1.85].

3. The excitation volume of the CPWs: given that the FM layer is ultra-thin and that all of the antennae designs feature CPWs that extend over the whole width of the SWW, we can consider that the excited SWW thickness  $t_f$  and width  $w_w$  (see Fig. 4.3) is equal for all CPW designs. However the width of the signal and ground lines are not equal among the CPW designs: type B and C feature three 70

nm wide lines whereas type A features 120 nm wide lines and, hence, the excited SWW length is  $120/70 \approx 1.71$  times larger. The iSHE voltage is proportional to the excited volume, therefore this leads to an increase of the expected iSHE voltage for CPW type A by a factor of 1.71, leading to [1:1:1.71].

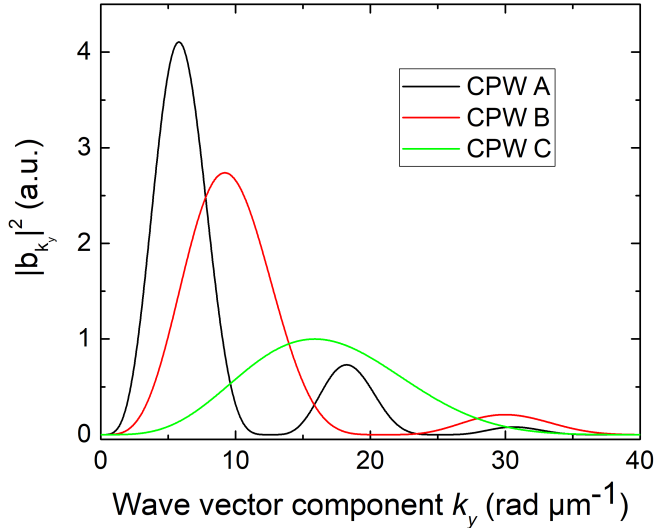


Figure 4.12: Square of the absolute value of the FFT of the field created by the CPW antennae. Black line: CPW type A. Red line: CPW type B. Green line: CPW type C.

Multiplying these 3 contributions together, the expected voltage ratio is [1:2.7:13], which is in very good agreement with the experimentally obtained ratio [(1) : (2 ± 1) : (12 ± 2)]. We can conclude that the ratio is determined by the experimental setup and that the iSHE voltage level does not depend on the excited wavevector, within the experimentally accessible wavevector range, and within the range of frequencies explored in Fig. 4.11.

## 4.5 Brillouin light scattering experiments

In the previous section, we successfully detected magnetization dynamics via the iSHE rectification effect. To prove that we are measuring propagating spin-waves, we performed micro-focused Brillouin light scattering (BLS) experiments. Additionally, we are interested in characterizing the propagation of the spin-waves, which is possible with spatially resolved BLS microscopy, for two reasons. Firstly, to characterize the decay length of the spin-waves and thus their lifetime. Secondly, to verify that the spin-waves detected via the iSHE are far away from the contacts, to show that the iSHE detection scheme is sensitive to localized spin-waves dynamics.

Micro-focused Brillouin light scattering is an optical technique that allows the detection of local magnetization dynamics. We<sup>17</sup> were given the opportunity to perform measurements on our devices using a Brillouin light scattering microscope in the group of B. Hillebrands at the State Research Center OPTIMAS at the Technical University of Kaiserslautern. Measurements were performed with the help of T. Meyer, T. Fischer and P. Pirro. The working principles of BLS, as well as a detailed description of the microscope itself and of the measurement technique can be found in the dissertation of T. Brächer [Brä15]. Alternatively, reviews on BLS microscopy can be found here [Seb15; Dem15]. In the following, we will only give a very brief overview.

### 4.5.1 Working principle

Brillouin light scattering is based on the interaction of light (photons) with oscillations in a material. The nature of these oscillations can be acoustic (phonons), dielectric (polarons) or magnetic (magnons).<sup>18</sup> The scattering of photons with magnons is inelastic, meaning that the energy of the photon is not conserved following the interaction with the ferromagnetic material. However, the total energy of all particles involved in the interaction is conserved:

$$h\nu' = h\nu \pm hf(k) \quad (4.16)$$

where  $h$  is Planck's constant,  $\nu$  and  $\nu'$  are the photon's frequency before and after the scattering process respectively and  $f(k)$  is the frequency of the interacting magnon with wavenumber  $k$ . During the scattering process, the photon can either create or annihilate a magnon (the creation of a magnon is illustrated in Fig. 4.13), which is represented by the  $\pm$  sign. Thus, the interaction of photons with magnons results in a frequency-shift of the photons that is equal to the frequency of the detected spin-wave.

### 4.5.2 Description of the microscope

A schematic of the microscope is given in Fig. 4.14. A solid-state laser provides a monochromatic light source at a wavelength of 532 nm. The light is guided onto the sample by a microscope objective and focused down to a spot size of about 400 nm, with an effective spatial resolution of about 250 nm. Micro-step motors and an auxiliary optical microscope allow precise positioning of the spot on the sample's surface. The inelastically scattered light is recollectd by the objective and guided into a 3+3-pass JRS Tandem Fabry-Pérot interferometer [Moc87] where it is analyzed with respect to frequency and intensity. The obtained BLS intensity at a given frequency is proportional to the number of inelastic scattering events of the light with magnons of this frequency in the probing spot. Thus, it is directly proportional to the local spin-wave intensity under the laser spot.

In addition to the change in energy described in Eq. (4.16), the photon also experiences a change in momentum. In the simplified case where the magnon's wavenumber is

---

<sup>17</sup>T. Brächer and I.

<sup>18</sup>Following the concept of wave-particle duality, magnons are quantized spin-waves.

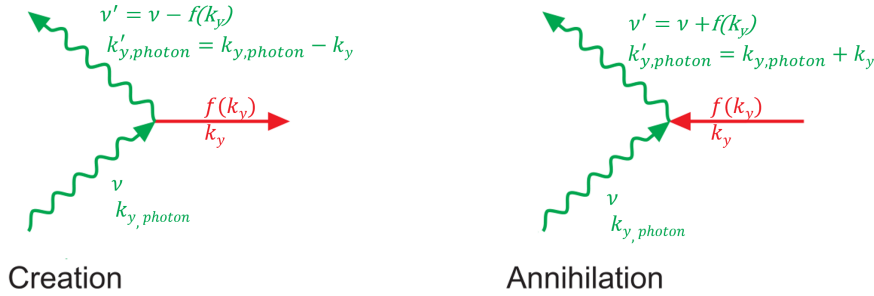


Figure 4.13: Sketch of magnon-photon scattering processes. The incident photon with frequency  $\nu$  and wavevector  $k_{y,photon}$  creates a magnon in the ferromagnetic layer with frequency  $f(k_y)$  and wavevector  $k_y$ . The scattered photon has a reduced frequency  $\nu'$  and reduced wavevector  $k'_{y,photon}$  due to energy and momentum conservation. In the opposite process, a magnon is annihilated by the incident photon, and the scattered photon has an increased frequency and increased wavevector. Taken from [Brä15].

simply  $k = k_y$ ,  $y$  being the direction of propagation and along the axis of the SWW, we have:

$$k'_{y,photon} = k_{y,photon} \pm k_y \quad (4.17)$$

where  $k_{y,photon}$  and  $k'_{y,photon}$  are the photon's wavevector component parallel to  $y$  before and after the scattering, respectively. Since the reflected light is collected by the same microscope objective that focuses the incident light, this change of wavevector has an important consequence. The direction of propagation of a photon is given by its wavevector, which means that the interaction with a magnon changes the reflected photon's direction. Since the objective has a limited aperture, a reflected photon with too great a change in wavevector cannot be captured by the objective. In other words, such BLS microscopes are inherently limited by their optics and cannot detect spin-waves beyond a certain wavevector. The resolution limit of the microscope used in this work is  $19 \text{ rad } \mu\text{m}^{-1}$ .

Unlike the ST-FMR experiments of Chap. 3 and the SWR experiments of Sec. 4, in the BLS experiments presented in this section the applied field is set to a fixed value. There is no RF current or field. The analysis of the scattered photons gives the spin-wave spectrum in the frequency domain.

### 4.5.3 BLS measurements

The BLS measurements are performed on a  $2 \mu\text{m}$  wide SWW with a type B CPW,  $\mu_0 M_{eff} = 195 \text{ mT}$ ,<sup>19</sup> in the Damon-Eshbach configuration: the SWW is magnetized along the short axis by a fixed external magnetic field. The microwave frequency is swept at an applied power of  $1.26 \text{ mW} = +1 \text{ dBm}$ . This is above the non-linearity threshold

<sup>19</sup>Device 8-D2 in Tab. 2.2.

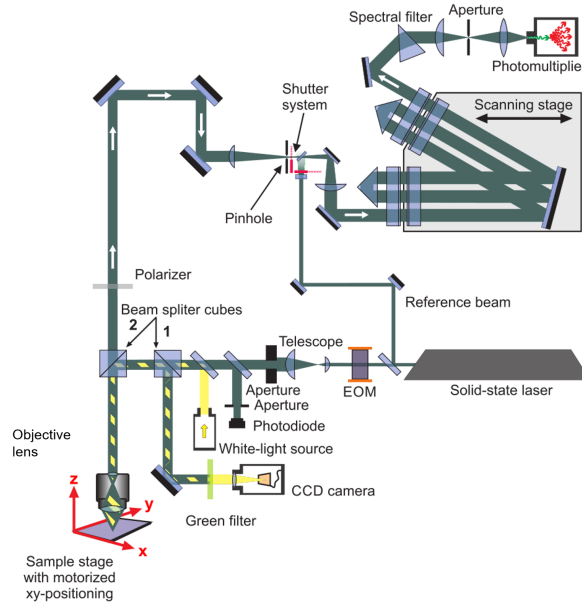


Figure 4.14: Schematic of a Brillouin light scattering micro-focused microscope. For more information, see the source [Brä15], Sec. 3.2.

identified in Fig. 4.8 for the ST-FMR experiment, which may not be accurate for the BLS experiments presented here. Non-linearities appear as kinks in the exponential decay length (see Sec. 4.5.4), which were not observed. Thus we assume that we are in the linear excitation regime. Fig. 4.15 shows the BLS intensity spectra measured at a distance of about 200 nm to the right edge of the CPW for  $\mu_0 H = \pm 55$  mT. The measured spectrum in the vicinity of the CPW is compared to the analytically expected spin-wave excitation spectrum (dashed lines) calculated in Sec. 4.3, Fig. 4.6,<sup>20</sup> and to the spin-wave dispersion relation of the fundamental mode (dotted green line). Both measurement and calculations have been normalized to the maximum intensity in the efficient emission direction (in this case for positive magnetic fields). As can be seen from Fig. 4.15, the two field polarities exhibit a strong asymmetry in terms of the overall intensity, the ratio is approximately 10 to 1. The strong asymmetry is mediated by the PMA together with the excitation characteristics of the CPW described by Eq. (4.8), owing to the dependence on the wavevector sign  $\pm k_y$ . The PMA decreases the ellipticity of precession and this way increases the relative spin-wave excitation efficiency of the dynamic out-of-plane fields created by the CPWs [Sch08; Kos13]. Consequently, the interplay of the dynamic out-of-plane and the dynamic in-plane field components becomes more pronounced, which is responsible for the asymmetric emission of antennae in this geometry (see Sec. 4.3.3). Thus, the use of CPWs or similar excitation sources for the spin-wave excitation in ultra-thin films with large PMA results intrinsically in

<sup>20</sup>The BLS measurement gives access to the spin-wave intensity, which is proportional to the square of the excitation efficiency calculated in Fig. 4.6.

a pronounced unidirectional emission. Therefore, this excitation non-reciprocity is a feature of the CPW excitation and not directly connected to the intrinsic non-reciprocity of the classical Damon-Eshbach waves [Gur96] (see Sec. 4.3.3).

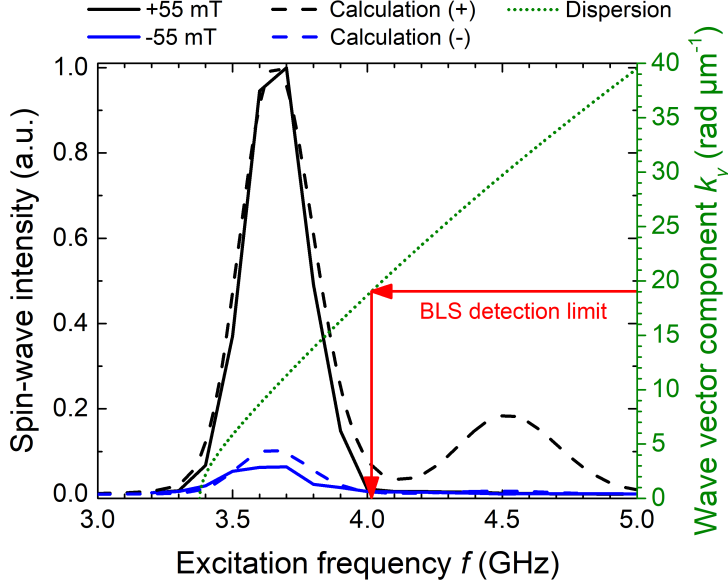


Figure 4.15: Measured (solid line) and calculated (dashed line) spin-wave intensity spectra detected at a distance of about 200 nm to the right edge of the CPW for  $\mu_0 H = \pm 55$  mT. The dotted green line shows the dispersion relation of the fundamental mode (right y-axis). The red arrows mark the BLS detection limit in terms of spin-wave wavevector ( $k_y \approx 19$  rad  $\mu\text{m}^{-1}$ ) as well as spin-wave frequency.

The calculation and experiments agree up to the first minimum of the CPW excitation at  $k_y \approx 21$  rad  $\mu\text{m}^{-1}$  (compare the red arrow in Fig. 4.15 and in Fig. 4.5). This is expected because this minimum incidentally almost corresponds to the maximum wavevector which can be detected by the micro-focused BLS setup  $k_y \approx 19$  rad  $\mu\text{m}^{-1}$ . In contrast, the detection via the iSHE can efficiently detect spin-waves with larger wavevectors. Moreover, the position of the first minimum and the cutoff appear at the same frequency for both emission directions, indicating the absence of a sizable Dzyaloshinskii-Moriya interaction (DMI) in our Ta/FeCoB/MgO. For systems consisting of layers of Ta and FeCoB-based alloys, the presence [Tet15; Gro16] or absence [Sou16; Kha16; Sou16] of DMI is still debated.

#### 4.5.4 Spin-wave decay length

We now seek to characterize the propagation length of the spin-waves in the SWW. Due to relaxation processes, the amplitude of the spin-wave decays exponentially as the wave propagates in the ferromagnetic material. We previously described the spin-wave relaxation rate  $\omega_r$  in Eq. (1.72), which is related to the spin-wave lifetime  $\tau$  via  $\omega_r = \frac{2\pi}{\tau}$ .

It represents the time in seconds it takes for a spin-wave's amplitude to drop by  $1/e$ . The group velocity  $v_g$ , obtained in Eq. (1.51) from the dispersion relation, can be understood as the velocity at which the spin-wave's energy is transported along the direction of propagation. Thus, the spin-wave decay length  $\delta$  is related to the spin-wave lifetime and the group velocity by:

$$\delta = v_g \tau \quad (4.18)$$

where  $\delta$  is the distance over which a spin-wave's amplitude drops by  $1/e$ . Thus, if the dispersion relation is known, the spin-wave decay length  $\delta$  gives us access to the spin-wave lifetime  $\tau$ .

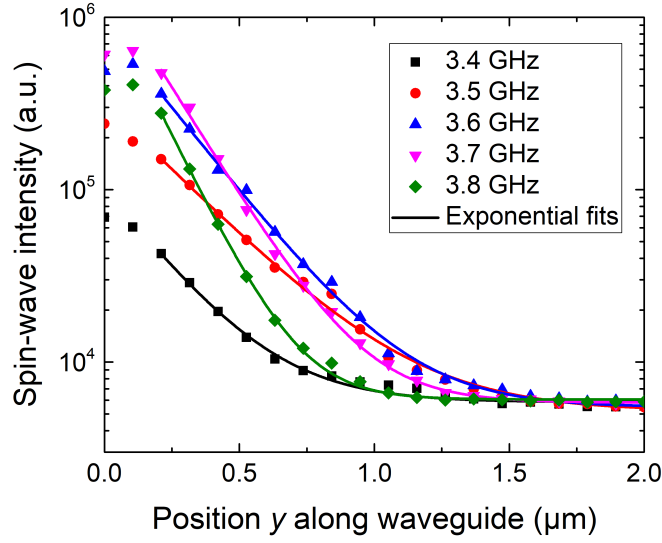


Figure 4.16: Spin-wave intensity as a function of the position along the long axis SWW for different excitation frequencies. Solid lines are exponential fits of the data.

The spin-wave intensity  $I$  was measured at different positions  $y$  along the length of the SWW. As seen in Fig. 4.15, the intensity of the spin-waves is not equal for both directions, and for the experiment described in this subsection we naturally chose the direction with the higher intensity, using an applied field  $|\mu_0 H| = 55$  mT. For each  $y$ , we measured the spin-wave intensity for certain frequencies at different positions  $z$  across the width of the SWW, and averaged these measurements for a given  $y$ . The results are shown in Fig. 4.16 with symbols, which give the spin-wave intensity as a function of  $y$  for a few frequencies between 3.4 GHz and 3.8 GHz, within the detection range of the BLS microscope. We fitted the following exponential function to the experimental data:

$$I(y) = I_0 + \left( A e^{-\frac{y-y_0}{\delta}} \right)^2 \quad (4.19)$$

where  $I_0$  is the offset due to the experimental noise, and  $A$  is the spin-wave amplitude at the point  $y_0$ . The squaring of the last term is due to the fact that the spin-wave intensity

is the square of the spin-wave amplitude. The exponential fits are performed only for  $y > 200$  nm, sufficiently far from the CPW so that the laser spot is not partially on the CPW, which would distort the detected spin-wave intensity.

As can be seen in Fig. 4.16, the spin-wave intensity is highest near the CPW and it decays exponentially along the SWW, indicating that the spin-waves are excited locally by the CPW and propagate with losses. Because of the exponential decay of the spin-waves, the iSHE voltage is dominated by the dynamics of the spin-waves in the vicinity of the CPW.

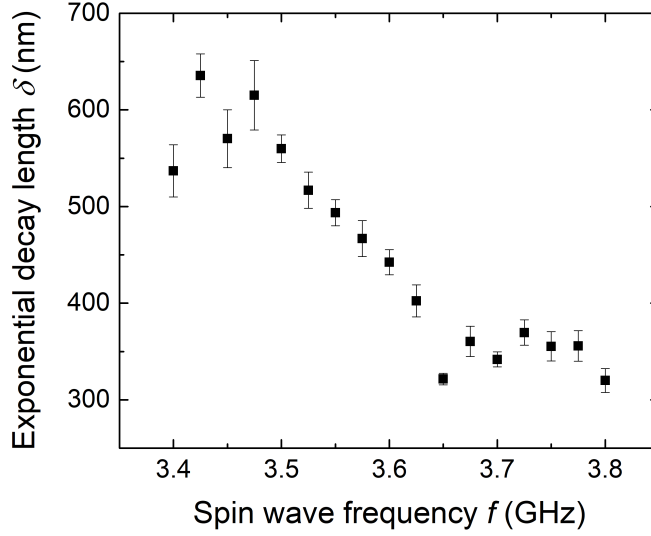


Figure 4.17: Exponential spin-wave decay length as a function of applied frequency, extracted from spatially resolved BLS measurements at  $|\mu_0 H| = 55$  mT using Eq. (4.19).

In Fig. 4.17, we plot the spin-wave exponential decay length  $\delta$  as a function of frequency. It initially increases with increasing frequencies up until approximately 3.45 GHz and then the decay decreases with increasing frequencies. Around a frequency of 3.45 GHz,  $\delta$  reaches its largest value of about  $\delta \approx 600$  nm. We compare this to the decay length calculated from the dispersion relation in Eq. (1.70), by using the expressions of the relaxation rate in Eq. (1.71), the group velocity in Eq. (1.51), the decay length in Eq. (4.18) as well as  $\omega_r = \frac{2\pi}{\tau}$ :

$$\begin{aligned} \delta &= v_g \frac{2\pi}{\omega_r} \\ &= 2\pi \left| \frac{\partial \omega(\mathbf{k})}{\partial \mathbf{k}} \right| \left( \alpha \omega \frac{\partial \omega(\mathbf{k})}{\partial \omega_H} \right)^{-1} \end{aligned} \quad (4.20)$$

Assuming the aforementioned values of  $\alpha = 0.019$  and  $\mu_0 M_{eff} = 195$  mT for the device with CPW type B (see Tab. 4.1), the exponential decay length obtained is  $\delta = 400$  nm

at 3.45 GHz, which is in reasonable agreement with the experimentally measured value above.

Using Eq. (4.18), we calculate the spin-wave lifetime corresponding to the spin-wave decay lengths in Fig. 4.17. The spin-wave lifetimes presented in Fig. 4.18 show a maximum value of around 3 ns close to 3.45 GHz. These values are comparable to the

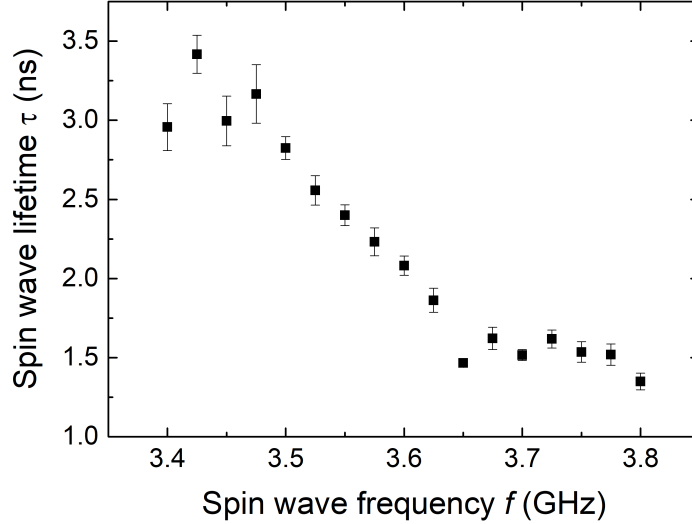


Figure 4.18: Spin-wave lifetimes obtained from the experimentally measured spin-wave decay lengths in Fig. 4.17 via Eq. (4.18).

ones obtained by micromagnetic simulations carried out by T. Brächer, presented in the Supporting Information of [Brä17b]. Based on the same Mumax3 model presented in Sec. 4.2, the spin-wave lifetime is extracted from the same simulations. The lifetimes obtained from the simulations are presented in Fig. 4.19 for different values of the anisotropy constant. For comparison, the spin-wave lifetime calculated according to Eq. (1.72) is also shown for the same anisotropy constants.

The spin-wave lifetimes obtained by experiments, the analytical calculations and the micromagnetic simulations are all large in comparison to the values expected from a material system with similar values of  $M_s$  and  $\alpha$  but no PMA. This can be understood from the ellipticity contribution to the lifetime for the ferromagnetic resonance. The FMR lifetime  $\tau_{fmr}$ , in seconds, is given by [Hei94]:

$$\frac{1}{\tau_{fmr}} = \alpha\gamma'\mu_0 \left( H + \frac{M_{eff}}{2} \right) \quad (4.21)$$

A reduction of  $M_{eff}$  due to the PMA significantly increases the lifetime at low magnetic fields where  $H \approx M_{eff}$ . The experimentally obtained value of 3 ns is comparable to the lifetime in thicker ferromagnetic films on the order of tens of nanometers from metallic

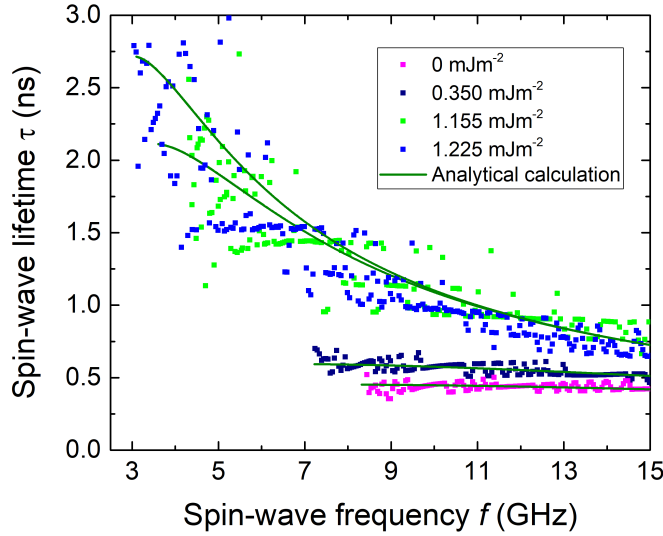


Figure 4.19: Spin-wave lifetimes obtained via Eq. (1.72) (green lines) and by micromagnetic simulations (squares) for different values of interfacial anisotropy. The interfacial anisotropy measured in devices for this chapter is  $K_i = 1.18 \text{ mJ m}^{-1}$ . The important spread of the results is due to the finite resolution in space (the number of cells that compose the simulated magnetic volume) and in time of the simulation model. Taken from [Brä17b].

materials such as NiFe [Bau15] or the half-metallic Heusler compound  $\text{Co}_2\text{Mn}_{0.6}\text{Fe}_{0.4}\text{Si}$  in the absence of pronounced interfacial damping [Seb12].<sup>21</sup>

For slightly larger frequencies, above 3.45 GHz, the spin-wave lifetimes obtained experimentally in Fig. 4.18 shows an unexpectedly strong decrease in the short range of frequencies measured as compared to the numerically obtained lifetimes in Fig. 4.19. This potentially indicates the presence of a wavevector-dependent relaxation process in the measured devices. This is not incorporated into the analytical formalism, which might also explain why the maxima/minima in the measured spectra are not as well resolved as predicted. We recall that in the ST-FMR experiments described in Sec. 3.4.4, we found a frequency-dependent and thickness-dependent contribution to the linewidth, though it manifests itself at lower frequencies and smaller FeCoB thicknesses than the ones used here.

<sup>21</sup>Heusler compounds are alloys which can present a unique mix of properties such as semi- or half-metallicity, ferro- or antiferromagnetism, low magnetic damping, etc. [Tru10].

## 4.6 Comparison of spin-wave detection methods

Ultimately, we would like to compare the iSHE detection to other detection methods: BLS detection (and other magneto-optical techniques like Kerr magnetometry) is local and the measured intensity depends on the local spin-wave density, which makes it a very powerful tool that does not require a large magnetic volume [Seb15; Dem15]. In principle, it is possible to measure the phase-evolution of propagating spin-waves directly by BLS, meaning that this method can give information on the wave amplitude and phase simultaneously. In contrast, the maximum resolvable wavevector is quite low (around  $k = 19 \text{ rad } \mu\text{m}^{-1}$  for the microscope used in this chapter), which does not suffice to study the short-waved spin-waves of interest for future magnonic applications. In addition, the limitations by optical diffraction also limit the usefulness of BLS for nanoscopic structures. The optical setup makes it a good tool for laboratory work but will be difficult to implement in actual magnonic devices integrated on chips. For this electrical excitation and detection schemes are required.

For the detection of spin waves, we can also use antennae (CPWs and other designs) in a reciprocal effect as discussed here for excitation of spin-waves. Such inductive techniques are used in many laboratories and can be integrated on a chip. However they can only give information about the spin-wave phase if costly microwave equipment like vector network analyzers or ultrafast oscilloscopes are used [Bai03]. In addition, inductive antennae exhibit a strong wavevector selectivity given by their Fourier spectrum.<sup>22</sup> Furthermore, the weak inductive coupling between the antenna and the dynamic magnetization limits the applicability of inductive detection to microscopic devices; their sensitivity is insufficient for nanoscopic structures. Because it scales with the magnetic volume, inductive detection are less suited for miniaturized structures made from ultra-thin films or films with low magnetization.

In contrast, the iSHE detection excels in such layer systems as shown here: iSHE detectors can be easily integrated on a chip and show enough sensitivity and signal-to-noise ratio. The iSHE scales with the length over which spin-waves propagate, whereas inductive detection scale with the size of the antenna used. If only thin metallic layers are involved, the iSHE voltage is not shunted and is straightforward to detect. In contrast, in thick ferromagnetic layers, the iSHE voltage is reduced due to shunting effects and other phenomena, such as thermal effects arising from an inhomogeneous heating of the magnetic layer that can dominate the electric signal. As shown in the experiments described here, the iSHE detection limit is at least  $k = 40 \text{ rad } \mu\text{m}^{-1}$  (determined by the excitation antenna used), though there is nothing in the detection mechanisms leading to the DC voltage that suggests that there is an intrinsic limit to the range of wavevectors detectable by the iSHE. The same holds true for the wavevector-independence of this technique. Thus, it is an ideal detection method for the development of scalable magnonic devices which calls for the reduction of the spin-wave wavelengths used. However, the

---

<sup>22</sup>The Fourier spectrum that gives an antenna's spin-wave excitation profile (see Sec. 4.3.1) also gives its spin-wave detection profile, making antennae an intrinsically wavevector-dependent detection technique.

iSHE detection can, by itself, always only provide amplitude and no phase information. Thus, the phase must be converted into another type of information, for instance, by translating it into an amplitude information [Brä16].

The studied spin-wave rectification experiment is similar to the thermoelectric detection in [Sch12], in which spin-waves propagate in a 100 nm thick NiFe SWW. Instead of the iSHE, spin-waves are detected via the anomalous Nernst effect (ANE). The decay of magnons create a temperature gradient which is detected as a voltage drop via the ANE. Such a detection technique is also expected to have no limit in wavelength and to be wavevector-independent. However, as shown in Sec. 4.4.3, we did not detect any significant ANE signal, which is likely due to the fact that the FM layer in our devices is so thin that a thermal gradient is negligible. Thus, ANE detection is not suited for ultrathin SWWs.

## 4.7 Conclusion

Using the model derived by T. Brächer and P. Pirro, we have calculated the complete spectrum of the spin-wave excitation efficiency of the coplanar waveguides, taking into account the perpendicular anisotropy of the Ta/FeCoB/MgO system and the non-zero linewidth of the spin-waves.

We detected propagating spin-waves presenting a large range of wavevectors up to  $\approx 40 \text{ rad } \mu\text{m}^{-1}$  via the inverse spin Hall effect for several devices and CPW designs. Furthermore, the wavevector dependence that can be observed (the maxima and minima of the spectra) as well as the upper limit of detectable wavevector can be exclusively attributed to the excitation scheme using CPW antennae. Hence it is concluded that iSHE is wavevector independent and can be used for detecting spin-waves in a much larger range of wavevectors.

By performing Brillouin light scattering experiments on the same spin-wave waveguides, we confirmed that the voltage generated by iSHE is due to propagating spin-waves, and that the iSHE is capable of detecting spin-waves localized far away from the where the DC signal is measured. A strong asymmetry was measured between the spin-waves propagating in either direction away from the CPW, which was predicted by the spin-wave excitation efficiency. This is due to the interplay between the in-plane and out-of-plane RF field of the CPW and is not related to the non-reciprocity of the classical Damon-Eshbach waves or to the Dzyaloshinskii-Moriya interaction, which is shown to be absent in the Ta/FeCoB/MgO material system.

Using BLS, we measured the spin-wave decay length in Ta/FeCoB/MgO, allowing us to calculate the spin-wave lifetime. We obtained a lifetime that is comparable to systems with relatively low intrinsic damping, due to the role of the perpendicular magnetic anisotropy in the Ta/FeCoB/MgO system, in which the demagnetizing field is almost compensated by the PMA field.

To conclude, the Ta/Fe/MgO system with strong PMA investigated here, together with the iSHE detection technique, are compatible with the integration into conventional microelectronics, owing to the compatibility of the material deposition and fabrication

techniques, and the fact that the iSHE voltage naturally arises in any bilayer system where a FM and a NM with a significant spin Hall angle share a large interface. Additionally, the iSHE detection scheme is an ideal candidate for scalable magnonic devices, as its wavevector sensitivity shows no indication of an upper limit nor any wavevector dependence, allowing the reduction of the device size and the wavelength used. Moreover, the chosen material system allows the manipulation of spin-waves with a simple electric current via the spin-orbit torques demonstrated in Chap. 3. Finally, the Ta/FeCoB/MgO stack is also compatible with other spintronic technologies such as MRAM, which are already commercialized. This paves the way for the development of scalable wave-based logic devices integrated onto CMOS electronics, with the possibility of including STT-MRAM or newer generation SOT-MRAM for fast, non-volatile memory.

# Conclusion and perspectives

This thesis addresses the applicability of a Ta/FeCoB/MgO slab with an ultrathin ferromagnetic layer and characterized by a strong PMA, as a spin-wave waveguide. In particular, we focused on the characterization of the spin-orbit torques with the aim of using them to manipulate spin-waves as well as the capacity of the inverse spin Hall effect to provide a wavevector independent method of detecting spin-waves.

The first experimental chapter is dedicated to the characterization of the magnetic properties of Ta/FeCoB/MgO spin-wave waveguides via spin-torque ferromagnetic resonance. The expected voltages arising from this technique were calculated, taking into account the different RF excitation sources as well as the two possible rectification mechanisms. It was concluded that in our spin-wave waveguides the main source of the DC signal is the combined effects of spin-pumping and the inverse spin Hall effect, and that anisotropic magnetoresistance rectification is negligible. Due to the lineshapes of the signals generated by the inverse spin Hall effect, it was impossible for us to differentiate between Ørsted field, field-like torque or damping-like torque excitations. However, this does not mean that measuring the spin-orbit torques via ST-FMR is impossible. Indeed, we derived the modifications to the susceptibilities induced by a DC field-like torque and a DC damping-like torque, both produced by a DC current injected in the SWW. Following an analysis of the linewidth of the resonance peak as well as its resonance field as a function of the injected DC current, we characterized  $\beta_{fl}$  (respectively  $\beta_{dl}$ ), the ratio between the effective field of the field-like (respectively damping-like) torque and the current density in the Ta layer. From the characterization as a function of ferromagnetic layer thickness, we concluded that both  $\beta_{fl}$  and  $\beta_{dl}$  increase as the ferromagnetic layer thickness decreases, which is consistent with the fact that  $\beta_{fl}$  and  $\beta_{dl}$  are inversely proportional to the volume, i.e. the thickness.

Before analyzing the DL and FL torque as a function of current and ferromagnetic layer thickness, we performed an analysis at  $I_{dc} = 0$  and extracted the effective magnetization as a function of ferromagnetic layer thickness, which governs the balance between the demagnetization energy and the perpendicular magnetic anisotropy energy, determining the orientation of the magnetization. We identified the critical thickness of reorientation and studied devices around and at the transition. The extraction of the damping proved to be more complicated than expected, as an unexpected variation of the field linewidth  $\Delta H$  vs. the excitation frequency appeared for many devices. We qualitatively explained this result, particularly the negative slope of the linewidth vs. the

excitation frequency by taking into account an inhomogeneous distribution of the magnetic properties of the ferromagnetic layer, resulting in a non-linear frequency-dependent contribution to the field linewidth.

The second experimental chapter is devoted to the excitation, propagation and detection of spin-waves in the same Ta/FeCoB/MgO spin-wave waveguides. The excitation spectrum of the nanometric coplanar waveguides was calculated, taking into account the perpendicular magnetic anisotropy as well as the non-zero linewidth of the spin-waves. Taking advantage of the same detection mechanism that was demonstrated in Ta/FeCoB/MgO for uniform ( $k = 0$ ) modes in the previous chapter, we performed spin-wave rectification experiments. By comparing the measured spin-wave spectrum to the calculated excitation spectrum, we concluded that the detection mechanism is wavevector independent up to a wavevector of at least  $40 \text{ rad } \mu\text{m}^{-1}$ , at which value the signal drops below the noise level. This value corresponds to minima for the excitation by the coplanar waveguides, hinting that the iSHE-based detection method is effective and wavevector independent even for higher wavevectors.

The spin-wave rectification experiments were complemented by Brillouin light scattering microscopy, confirming that the detected signal arises from propagating spin-waves. We then measured the spin-wave intensity as a function of distance from the coplanar waveguide and extracted the spin-wave decay length, which allowed us to calculate the spin-wave lifetime. We found a spin-wave decay length of 600 nm and a spin-wave lifetime of approximately 3 ns, which is comparable to the lifetime of thicker NiFe systems which lack a pronounced interfacial damping. The large lifetime is attributed to the perpendicular anisotropy of the Ta/FeCoB/MgO, which reduces the effective magnetization and its contribution to the ellipticity, leading to a reduced lifetime.

In comparison to other spin-wave detection methods such as BLS and inductive coupling, the main advantage of the iSHE method used in this work is its wavevector-independence. More importantly it can be directly integrated with the device and the measurement requires no extensive laboratory equipment: the spin-wave dynamics is converted to a charge current, which can be detected by a transistor for example. Additionally, it shows no limit in terms of scalability, in terms of nanofabrication or wavelength limit. Of course, it lacks an important feature, namely that it cannot measure the phase of a spin-wave.

The next logical step is therefore combining the two main concepts studied in this work: spin-orbit torques and spin-waves. By injecting a DC current in the waveguide with the correct polarity, the damping-like torque can reduce the effective damping of the system, enhancing the lifetime of the spin-waves. We present in Fig. 4.20 preliminary results in which the voltage of the highest peak of the measured spin-wave spectrum is plotted as a function of the DC current injected longitudinally in the SWW. An RF current with  $f = 4.8 \text{ GHz}$  is supplied to the CPW antenna for several values between 0 and -12 dBm, while the applied field is swept across the resonance. In this configuration, a negative DC current is expected to enhance the effective damping, while a positive one is expected to reduce it. Surprisingly, for both current polarities, the peak height increases as the current magnitude increases. In fact the effect is more pronounced for

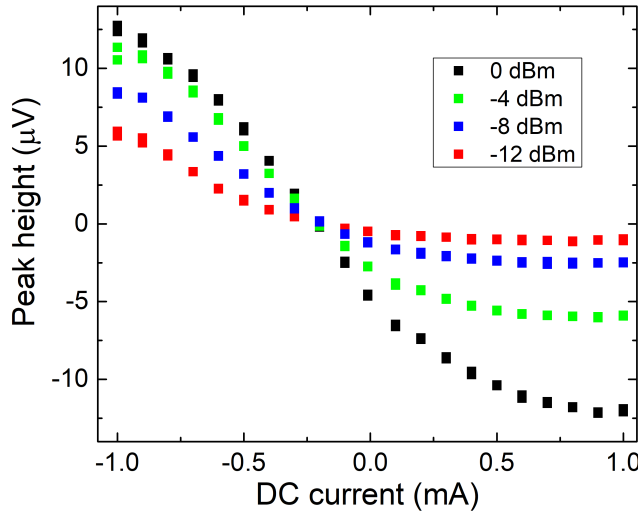


Figure 4.20: Spin-wave rectification experiment with DC current injected in a  $1\ \mu\text{m}$  wide SWW, at  $f = 4.8\ \text{GHz}$ . The voltage of the highest peak is plotted as a function of applied DC current. Each curve corresponds to a different RF power injected in the CPW antenna.

negative currents, which is contrary to our expectations. In Fig. 4.21, we plot the peak voltage as a function of the power applied to the CPW antenna, for  $\pm 0.5\ \text{mA}$  and  $\pm 1\ \text{mA}$ . Since the power is in dBm, and the voltage scale is in logarithm, this is a log-log plot. Thus, the linearity between the measured voltage (which is related to the square of the dynamic magnetization) and the applied power is straightforward to verify. We see that for positive currents, the voltage is linear up to at least  $-2\ \text{dBm}$ , while for negative currents, the voltage is non-linear for values starting at  $-8\ \text{dBm}$ . Additionally, we see that doubling the positive current does not result in significant changes, while doubling the negative current changes the non-linearity threshold and changes the slope of the linear fit.

We were unable to explain both the very high increase of the peak for currents expected to increase the effective damping (negative currents), nor the lack of effect on the peak for currents expected to decrease the effective damping (positive currents). In any case, the decrease of the nonlinear threshold for negative currents shows that for one polarity, there is a clear increase in nonlinear relaxation processes. It would be interesting for future work to address these questions, as the enhancement of spin-waves via spin-orbit torques was achieved in different material and geometric configurations [Dem14; Che16], including nanowires [Dua14] similar to our SWWs. In these studies, the excited magnetic volume is much reduced, resulting in the separation of the spin-wave modes such that at a given excitation frequency, only one mode may exist, and therefore,

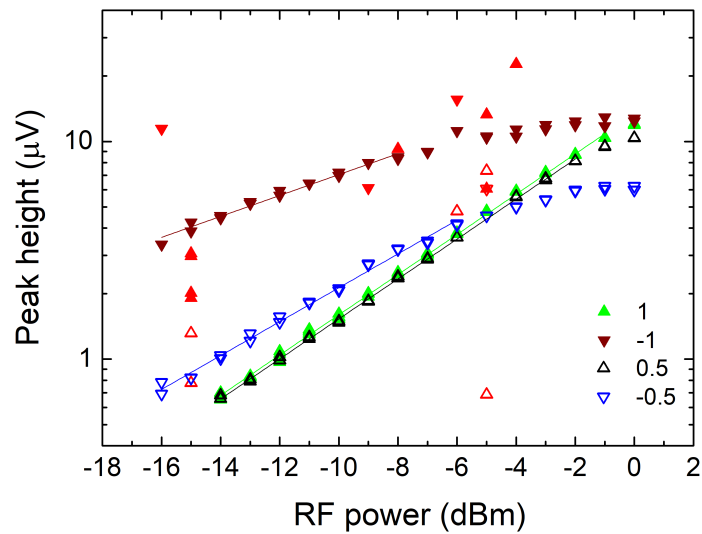


Figure 4.21: Spin-wave rectification experiment with DC current injected in a  $1\ \mu\text{m}$  wide SWW, at  $f = 4.8\ \text{GHz}$ . The voltage of the highest peak is plotted as a function of power applied to the CPW antenna. Up-pointing triangles correspond to positive currents, and down-pointing triangles correspond to negative currents. The solid lines are partial linear fits of the data.

only one mode can be excited by the spin-orbit torques. Thus, one can expect that in sufficiently narrow Ta/FeCoB/MgO, spin-waves enhanced by spin-orbit torques might reach propagation lengths of several  $\mu\text{m}$ , paving the way for the development of metallic magnonic devices that were previously only demonstrated in YIG, as well as their scaling down to nanometric sizes to contend with CMOS logic.

## Appendix A

# Linewidth and peak height under a DC damping-like torque

In this section we verify that for the iSHE signal, the inverse peak height of the resonance is proportional to the field linewidth. Using the expression of the susceptibility under a DC damping-like torque derived in Eq. (3.20) in Sec. 3.2.4, we calculate  $\Delta H \times \textit{Peak height}$ , where  $\Delta H$  is the linewidth and *Peak height* is the amplitude at resonance of the real and imaginary parts of each susceptibility components.<sup>1</sup> They are plotted as function of normalized current density in Fig. A.1. The current density is normalized by the critical current, which is defined as the current density for which the linewidth is reduced to zero. For  $\text{Re}(\chi_{xy})$ , the product of peak height and linewidth increases with  $J$  due to the DC damping-like torque (see Eq. (3.20)). However compared to the amplitudes of the other terms, which are constant as a function of  $J$ , this increase is small. Thus, when we consider the iSHE voltages in Eq. (3.55), we expect that the mixing of the off-diagonal and diagonal components of the susceptibility results in Lorentzian peaks in which the linewidth and the inverse peak height can be approximated as proportional.

---

<sup>1</sup>We used  $M_s = 1.25 \text{ MA m}^{-1}$ ,  $K_i = 1.18 \text{ mJ m}^{-1}$ ,  $t_f = 1.35 \text{ nm}$ ,  $\alpha = 0.02$ ,  $\beta_{dl} P_z = 5 \times 10^{14} \text{ T A}^{-1} \text{ m}^2$ .

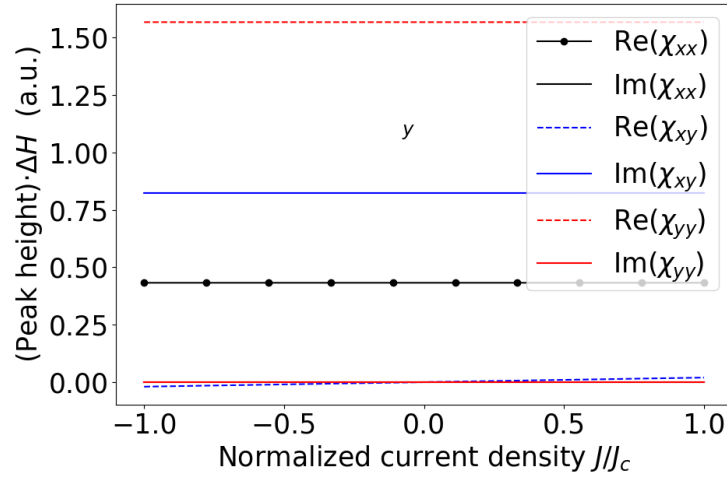


Figure A.1: Product of the peak height and the linewidth, where the *Peak height* and  $\Delta H$  are calculated for each susceptibility component's real and imaginary part:  $\Delta H(\chi_{kl}) \times \text{Re}(\chi_{kl})$  and  $\Delta H(\chi_{kl}) \times \text{Im}(\chi_{kl})$ , for  $kl = \{xx, xy, yy\}$ . For the imaginary parts of  $\chi_{xx}$  and  $\chi_{yy}$ , the lines are superimposed because they have dispersive lineshapes and thus their amplitude at resonance is zero. The current density  $J$  is normalized to the critical current density  $J_c$ .

# Bibliography

- [All15] G. Allen, S. Manipatruni, D. E. Nikonov, M. Doczy, and I. A. Young. Experimental Demonstration of the Coexistence of Spin Hall and Rashba Effects in  $\beta$ -tantalum/ferromagnet bilayers. *Physical Review B* **91**, 14 (2015).  
DOI: [10.1103/PhysRevB.91.144412](https://doi.org/10.1103/PhysRevB.91.144412).
- [And09] K. Ando, J. Ieda, K. Sasage, S. Takahashi, S. Maekawa, and E. Saitoh. Electric Detection of Spin Wave Resonance Using Inverse Spin-Hall Effect. *Applied Physics Letters* **94**, 26 (2009).  
DOI: [10.1063/1.3167826](https://doi.org/10.1063/1.3167826).
- [And08] K. Ando, Y. Kajiwara, S. Takahashi, S. Maekawa, K. Takemoto, M. Takatsu, and E. Saitoh. Angular Dependence of Inverse Spin-Hall Effect Induced by Spin Pumping Investigated in a Ni<sub>81</sub>Fe<sub>19</sub>/Pt Thin Film. *Physical Review B* **78**, 1 (2008).  
DOI: [10.1103/PhysRevB.78.014413](https://doi.org/10.1103/PhysRevB.78.014413).
- [And11] K. Ando, S. Takahashi, J. Ieda, Y. Kajiwara, H. Nakayama, T. Yoshino, K. Harii, Y. Fujikawa, M. Matsuo, S. Maekawa, and E. Saitoh. Inverse Spin-Hall Effect Induced by Spin Pumping in Metallic System. *Journal of Applied Physics* **109**, 10 (2011).  
DOI: [10.1063/1.3587173](https://doi.org/10.1063/1.3587173).
- [Ash69] H. Ashworth, D. Sengupta, G. Schnakenberg, L. Shapiro, and L. Berger. Galvanomagnetic Effects, Magnetostriction, and Spin-Orbit Interaction in Cu-Ni-Fe and Other Ferromagnetic Nickel Alloys. *Physical Review* **185**, 2 (1969).  
DOI: [10.1103/PhysRev.185.792](https://doi.org/10.1103/PhysRev.185.792).
- [Avc14] C. O. Avcı, K. Garello, C. Nistor, S. Godey, B. Ballesteros, A. Mugarza, A. Barla, M. Valvidares, E. Pellegrin, A. Ghosh, I. M. Miron, O. Boulle, S. Auffret, G. Gaudin, and P. Gambardella. Fieldlike and Antidamping Spin-Orbit Torques in as-Grown and Annealed Ta/CoFeB/MgO Layers. *Physical Review B* **89**, 21 (2014).  
DOI: [10.1103/PhysRevB.89.214419](https://doi.org/10.1103/PhysRevB.89.214419).
- [Aze11] A. Azevedo, L. H. Vilela-Leão, R. L. Rodríguez-Suárez, A. F. Lacerda Santos, and S. M. Rezende. Spin Pumping and Anisotropic Magnetoresistance Voltages in Magnetic Bilayers: Theory and Experiment. *Physical Review B* **83**, 14

- (2011).  
DOI: [10.1103/PhysRevB.83.144402](https://doi.org/10.1103/PhysRevB.83.144402).
- [Bai88] M. N. Baibich, J. M. Broto, A. Fert, F. N. Van Dau, F. Petroff, P. Etienne, G. Creuzet, A. Friederich, and J. Chazelas. Giant Magnetoresistance of (001)Fe/(001)Cr Magnetic Superlattices. *Physical Review Letters* **61**, 21 (1988).  
DOI: [10.1103/PhysRevLett.61.2472](https://doi.org/10.1103/PhysRevLett.61.2472).
- [Bai03] M. Bailleul, D. Olligs, and C. Fermon. Propagating Spin Wave Spectroscopy in a Permalloy Film: A Quantitative Analysis. *Applied Physics Letters* **83**, 5 (2003).  
DOI: [10.1063/1.1597745](https://doi.org/10.1063/1.1597745).
- [Bak84] A. Bakun, B. Zakharchenya, A. Rogachev, M. Tkachuk, and V. Fleisher. Observation of a Surface Photocurrent Caused by Optical Orientation of Electrons in a Semiconductor. *JETP Lett* **40**, 11 (1984).  
URL: [http://www.jetpletters.ac.ru/ps/1262/article\\_19087.shtml](http://www.jetpletters.ac.ru/ps/1262/article_19087.shtml).
- [Bau15] H. G. Bauer, P. Majchrak, T. Kachel, C. H. Back, and G. Woltersdorf. Non-linear Spin-Wave Excitations at Low Magnetic Bias Fields. *Nature Communications* **6** (2015).  
DOI: [10.1038/ncomms9274](https://doi.org/10.1038/ncomms9274).
- [Bea07] J.-M. Beaujour, W. Chen, K. Krycka, C.-C. Kao, J. Z. Sun, and A. D. Kent. Ferromagnetic Resonance Study of Sputtered Co|Ni Multilayers. *The European Physical Journal B* **59**, 4 (2007).  
DOI: [10.1140/epjb/e2007-00071-1](https://doi.org/10.1140/epjb/e2007-00071-1).
- [Bel17] M. Belmeguenai, D. Apalkov, Y. Roussigné, M. Chérif, A. Stashkevich, G. Feng, and X. Tang. Exchange Stiffness and Damping Constants in Diluted  $\text{Co}_x\text{Fe}_y\text{B}_{1-x-y}$  Thin Films. *Journal of Physics D: Applied Physics* **50**, 41 (2017).  
DOI: [10.1088/1361-6463/aa81a5](https://doi.org/10.1088/1361-6463/aa81a5).
- [Ber04] D. Bercioux. “Spin-Dependent Transport in Nanostructures,” PhD thesis. Università degli studi di Napoli Federico II, 2004.  
URL: <http://www.fedoa.unina.it/136/1/masterthesis.pdf>.
- [Ber64] L. Berger. Influence of Spin-Orbit Interaction on the Transport Processes in Ferromagnetic Nickel Alloys, in the Presence of a Degeneracy of the 3d Band. *Physica* **30**, 6 (1964).  
DOI: [10.1016/0031-8914\(64\)90105-3](https://doi.org/10.1016/0031-8914(64)90105-3).
- [Ber70] L. Berger. Side-Jump Mechanism for the Hall Effect of Ferromagnets. *Physical Review B* **2**, 11 (1970).  
DOI: [10.1103/PhysRevB.2.4559](https://doi.org/10.1103/PhysRevB.2.4559).
- [Ber96] L. Berger. Emission of Spin Waves by a Magnetic Multilayer Traversed by a Current. *Physical Review B* **54**, 13 (1996).  
DOI: [10.1103/PhysRevB.54.9353](https://doi.org/10.1103/PhysRevB.54.9353).

- [Bil07] C. Bilzer, T. Devolder, P. Crozat, C. Chappert, S. Cardoso, and P. P. Freitas. Vector Network Analyzer Ferromagnetic Resonance of Thin Films on Coplanar Waveguides: Comparison of Different Evaluation Methods. *Journal of Applied Physics* **101**, 7 (2007).  
DOI: [10.1063/1.2716995](https://doi.org/10.1063/1.2716995).
- [Bin89] G. Binasch, P. Grünberg, F. Saurenbach, and W. Zinn. Enhanced Magnetoresistance in Layered Magnetic Structures with Antiferromagnetic Interlayer Exchange. *Physical Review B* **39**, 7 (1989).  
DOI: [10.1103/PhysRevB.39.4828](https://doi.org/10.1103/PhysRevB.39.4828).
- [Boz42] R. M. Bozorth and D. M. Chapin. Demagnetizing Factors of Rods. *Journal of Applied Physics* **13**, 5 (1942).  
DOI: [10.1063/1.1714873](https://doi.org/10.1063/1.1714873).
- [Brä17a] T. Brächer, O. Boulle, G. Gaudin, and P. Pirro. Creation of Unidirectional Spin-Wave Emitters by Utilizing Interfacial Dzyaloshinskii-Moriya Interaction. *Physical Review B* **95**, 6 (2017).  
DOI: [10.1103/PhysRevB.95.064429](https://doi.org/10.1103/PhysRevB.95.064429).
- [Brä17b] T. Brächer, M. Fabre, T. Meyer, T. Fischer, S. Auffret, O. Boulle, U. Ebels, P. Pirro, and G. Gaudin. Detection of Short-Waved Spin Waves in Individual Microscopic Spin-Wave Waveguides Using the Inverse Spin Hall Effect. *Nano Letters* **17**, 12 (2017).  
DOI: [10.1021/acs.nanolett.7b02458](https://doi.org/10.1021/acs.nanolett.7b02458).
- [Brä16] T. Brächer, F. Heussner, P. Pirro, T. Meyer, T. Fischer, M. Geilen, B. Heinz, B. Lägel, A. A. Serga, and B. Hillebrands. Phase-to-Intensity Conversion of Magnonic Spin Currents and Application to the Design of a Majority Gate. *Scientific Reports* **6** (2016).  
DOI: [10.1038/srep38235](https://doi.org/10.1038/srep38235).
- [Brä15] T. Brächer. “Parallel Parametric Amplification of Spin Waves in Micro-Structures”. PhD Thesis. Technischen Universität Kaiserslautern, 2015.  
URL: [https://www.physik.uni-kl.de/fileadmin/hillebrands/Diplom-\\_und\\_Doktorarbeiten/PhD\\_Braecher.pdf](https://www.physik.uni-kl.de/fileadmin/hillebrands/Diplom-_und_Doktorarbeiten/PhD_Braecher.pdf).
- [Byc84] Y. A. Bychkov and É. I. Rashba. Properties of a 2D Electron Gas with Lifted Spectral Degeneracy. *Journal of Experimental and Theoretical Physics* **39**, 2 (1984).  
URL: [http://www.jetpletters.ac.ru/ps/1264/article\\_19121.pdf](http://www.jetpletters.ac.ru/ps/1264/article_19121.pdf).
- [Che16] T. Chen, R. K. Dumas, A. Eklund, P. K. Muduli, A. Houshang, A. A. Awad, P. Dürrenfeld, B. G. Malm, A. Rusu, and J. Åkerman. Spin-Torque and Spin-Hall Nano-Oscillators. *Proceedings of the IEEE* **104**, 10 (2016).  
DOI: [10.1109/JPROC.2016.2554518](https://doi.org/10.1109/JPROC.2016.2554518).

- [Che93] V. Cherepanov, I. Kolokolov, and V. L'vov. The Saga of YIG: Spectra, Thermodynamics, Interaction and Relaxation of Magnons in a Complex Magnet. *Physics Reports* **229**, 3 (1993).  
DOI: [10.1016/0370-1573\(93\)90107-0](https://doi.org/10.1016/0370-1573(93)90107-0).
- [Che09] A. Chernyshov, M. Overby, X. Liu, J. K. Furdyna, Y. Lyanda-Geller, and L. P. Rokhinson. Evidence for Reversible Control of Magnetization in a Ferromagnetic Material by Means of Spin–Orbit Magnetic Field. *Nature Physics* **5**, 9 (2009).  
DOI: [10.1038/nphys1362](https://doi.org/10.1038/nphys1362).
- [Chu17] A. V. Chumak, A. A. Serga, and B. Hillebrands. Magnonic Crystals for Data Processing. *Journal of Physics D: Applied Physics* **50**, 24 (2017).  
DOI: [10.1088/1361-6463/aa6a65](https://doi.org/10.1088/1361-6463/aa6a65).
- [Chu14] A. V. Chumak, A. A. Serga, and B. Hillebrands. Magnon Transistor for All-Magnon Data Processing. *Nature Communications* **5** (2014).  
DOI: [10.1038/ncomms5700](https://doi.org/10.1038/ncomms5700).
- [Chu06] D. Chumakov. “High Frequency Behaviour of Magnetic Thin Film Elements for Microelectronics”. Leibniz-Institut für Festkörper- und Werkstoffforschung Dresden, 2006.  
URL: [https://www.ifw-dresden.de/userfiles/groups/imw\\_folder/publications/theses/Dr\\_Chumakov.pdf](https://www.ifw-dresden.de/userfiles/groups/imw_folder/publications/theses/Dr_Chumakov.pdf).
- [Ciu16] F. Ciubotaru, T. Devolder, M. Manfrini, C. Adelman, and I. P. Radu. All Electrical Propagating Spin Wave Spectroscopy with Broadband Wavevector Capability. *Applied Physics Letters* **109**, 1 (2016).  
DOI: [10.1063/1.4955030](https://doi.org/10.1063/1.4955030).
- [Con13] A. Conca, J. Greser, T. Sebastian, S. Klingler, B. Obry, B. Leven, and B. Hillebrands. Low Spin-Wave Damping in Amorphous Co<sub>40</sub>Fe<sub>40</sub>B<sub>20</sub> Thin Films. *Journal of Applied Physics* **113**, 21 (2013).  
DOI: [10.1063/1.4808462](https://doi.org/10.1063/1.4808462).
- [Cub18] M. Cubukcu, O. Boule, N. Mikuszeit, C. Hamelin, T. Bracher, N. Lamard, M.-C. Cyrille, L. Buda-Prejbeanu, K. Garello, I. M. Miron, O. Klein, G. de Loubens, V. V. Naletov, J. Langer, B. Ocker, P. Gambardella, and G. Gaudin. Ultra-Fast Perpendicular Spin–Orbit Torque MRAM. *IEEE Transactions on Magnetism* **54**, 4 (2018).  
DOI: [10.1109/TMAG.2017.2772185](https://doi.org/10.1109/TMAG.2017.2772185).
- [Cuc15] L. Cuchet. “Magnetic and transport properties of single and double perpendicular magnetic tunnel junctions”. Université Grenoble Alpes, 2015.  
URL: <https://tel.archives-ouvertes.fr/tel-01312194/document>.
- [Dam61] R. Damon and J. Eshbach. Magnetostatic Modes of a Ferromagnet Slab. *Journal of Physics and Chemistry of Solids* **19**, 3-4 (1961).  
DOI: [10.1016/0022-3697\(61\)90041-5](https://doi.org/10.1016/0022-3697(61)90041-5).

- [Dem15] V. E. Demidov and S. O. Demokritov. Magnonic Waveguides Studied by Microfocus Brillouin Light Scattering. *IEEE Transactions on Magnetics* **51**, 4 (2015).  
DOI: [10.1109/TMAG.2014.2388196](https://doi.org/10.1109/TMAG.2014.2388196).
- [Dem11] V. E. Demidov, S. Urazhdin, E. R. J. Edwards, M. D. Stiles, R. D. McMichael, and S. O. Demokritov. Control of Magnetic Fluctuations by Spin Current. *Physical Review Letters* **107**, 10 (2011).  
DOI: [10.1103/PhysRevLett.107.107204](https://doi.org/10.1103/PhysRevLett.107.107204).
- [Dem14] V. E. Demidov, S. Urazhdin, A. Zholud, A. V. Sadovnikov, and S. O. Demokritov. Nanoconstriction-Based Spin-Hall Nano-Oscillator. *Applied Physics Letters* **105**, 17 (2014).  
DOI: [10.1063/1.4901027](https://doi.org/10.1063/1.4901027).
- [Dem09] V. E. Demidov, M. P. Kostylev, K. Rott, P. Krzysteczko, G. Reiss, and S. O. Demokritov. Excitation of Microwaveguide Modes by a Stripe Antenna. *Applied Physics Letters* **95**, 11 (2009).  
DOI: [10.1063/1.3231875](https://doi.org/10.1063/1.3231875).
- [Dev13] T. Devolder, P.-H. Ducrot, J.-P. Adam, I. Barisic, N. Vernier, J.-V. Kim, B. Ockert, and D. Ravelosona. Damping of CoFe80-xB20 Ultrathin Films with Perpendicular Magnetic Anisotropy. *Applied Physics Letters* **102**, 2 (2013).  
DOI: [10.1063/1.4775684](https://doi.org/10.1063/1.4775684).
- [Die19] G. Dieterle, J. Förster, H. Stoll, A. S. Semisalova, S. Finizio, A. Gangwar, M. Weigand, M. Noske, M. Fähnle, I. Bykova, J. Gräfe, D. A. Bozhko, H. Y. Musiienko-Shmarova, V. Tiberkevich, A. N. Slavin, C. H. Back, J. Raabe, G. Schütz, and S. Wintz. Coherent Excitation of Heterosymmetric Spin Waves with Ultrashort Wavelengths. *Physical Review Letters* **122**, 11 (2019).  
DOI: [10.1103/PhysRevLett.122.117202](https://doi.org/10.1103/PhysRevLett.122.117202).
- [Dor93] P. C. Dorsey, S. E. Bushnell, R. G. Seed, and C. Vittoria. Epitaxial Yttrium Iron Garnet Films Grown by Pulsed Laser Deposition. *Journal of Applied Physics* **74**, 2 (1993).  
DOI: [10.1063/1.354927](https://doi.org/10.1063/1.354927).
- [Du 19] E. Du Trémolet de Lacheisserie. *Magnétisme - Tome I*. 2019.  
URL: [/en/product/201/9782759801312/Magnetisme%20-%20Tome%20I](https://www.editions-eyrolles.com/en/product/201/9782759801312/Magnetisme%20-%20Tome%20I).
- [Dua14] Z. Duan, A. Smith, L. Yang, B. Youngblood, J. Lindner, V. E. Demidov, S. O. Demokritov, and I. N. Krivorotov. Nanowire Spin Torque Oscillator Driven by Spin Orbit Torques. *Nature Communications* **5** (2014).  
DOI: [10.1038/ncomms6616](https://doi.org/10.1038/ncomms6616).
- [Dya71a] M. I. Dyakonov and V. I. Perel. Current-Induced Spin Orientation of Electrons in Semiconductors. *Physics Letters A* **35**, 6 (1971).  
DOI: [10.1016/0375-9601\(71\)90196-4](https://doi.org/10.1016/0375-9601(71)90196-4).

- [Dya71b] M. I. Dyakonov and V. I. Perel. Possibility of Orienting Electron Spins with Current. *Soviet Journal of Experimental and Theoretical Physics Letters* **13**, 11 (1971).  
URL: [http://www.jetpletters.ac.ru/ps/1587/article\\_24366.pdf](http://www.jetpletters.ac.ru/ps/1587/article_24366.pdf).
- [Esh60] J. R. Eshbach and R. W. Damon. Surface Magnetostatic Modes and Surface Spin Waves. *Physical Review* **118**, 5 (1960).  
DOI: [10.1103/PhysRev.118.1208](https://doi.org/10.1103/PhysRev.118.1208).
- [Fan13] X. Fan, J. Wu, Y. Chen, M. J. Jerry, H. Zhang, and J. Q. Xiao. Observation of the Nonlocal Spin-Orbital Effective Field. *Nature Communications* **4** (2013).  
DOI: [10.1038/ncomms2709](https://doi.org/10.1038/ncomms2709).
- [Fre14] F. Freimuth, S. Blügel, and Y. Mokrousov. Spin-Orbit Torques in Co/Pt(111) and Mn/W(001) Magnetic Bilayers from First Principles. *Physical Review B* **90**, 17 (2014).  
DOI: [10.1103/PhysRevB.90.174423](https://doi.org/10.1103/PhysRevB.90.174423).
- [Gal06] W. J. Gallagher and S. S. P. Parkin. Development of the Magnetic Tunnel Junction MRAM at IBM: From First Junctions to a 16-Mb MRAM Demonstrator Chip. *IBM Journal of Research and Development* **50**, 1 (2006).  
DOI: [10.1147/rd.501.0005](https://doi.org/10.1147/rd.501.0005).
- [Gan75] A. Ganguly and D. Webb. Microstrip Excitation of Magnetostatic Surface Waves: Theory and Experiment. *IEEE Transactions on Microwave Theory and Techniques* **23**, 12 (1975).  
DOI: [10.1109/TMTT.1975.1128733](https://doi.org/10.1109/TMTT.1975.1128733).
- [Gar18] K. Garello, F. Yasin, S. Couet, L. Souriau, J. Swerts, S. Rao, S. Van Beek, W. Kim, E. Liu, S. Kundu, D. Tsvetanova, K. Croes, N. Jossart, E. Grimaldi, M. Baumgartner, D. Crotti, A. Fumemont, P. Gambardella, and G. Kar. “SOT-MRAM 300MM Integration for Low Power and Ultrafast Embedded Memories”. IEEE, 2018.  
DOI: [10.1109/VLSIC.2018.8502269](https://doi.org/10.1109/VLSIC.2018.8502269).
- [Gar13] K. Garello, I. M. Miron, C. O. Avci, F. Freimuth, Y. Mokrousov, S. Blügel, S. Auffret, O. Boulle, G. Gaudin, and P. Gambardella. Symmetry and Magnitude of Spin–Orbit Torques in Ferromagnetic Heterostructures. *Nature Nanotechnology* **8**, 8 (2013).  
DOI: [10.1038/nnano.2013.145](https://doi.org/10.1038/nnano.2013.145).
- [Gho12] A. Ghosh. “Spin Pumping and Spin Absorption in Magnetic Heterostructures”. Theses. Université de Grenoble, 2012.  
URL: <https://tel.archives-ouvertes.fr/tel-00846031>.
- [Gil55] T. L. Gilbert and J. M. Kelly. “Anomalous Rotational Damping in Ferromagnetic Sheets”. *Anomalous Rotational Damping in Ferromagnetic Sheets*. Magnetism and Magnetic Materials Conference. Pittsburgh, USA, 1955.  
URL: [http://people.physics.tamu.edu/saslow/MMMConf55\\_253GilbertKelly.pdf](http://people.physics.tamu.edu/saslow/MMMConf55_253GilbertKelly.pdf).

- [Gla76] H. L. Glass and M. T. Elliot. Attainment of the Intrinsic FMR Linewidth in Yttrium Iron Garnet Films Grown by Liquid Phase Epitaxy. *Journal of Crystal Growth* **34**, 2 (1976).  
DOI: [10.1016/0022-0248\(76\)90141-X](https://doi.org/10.1016/0022-0248(76)90141-X).
- [Gro16] I. Gross, L. J. Martínez, J.-P. Tetienne, T. Hingant, J.-F. Roch, K. Garcia, R. Soucaille, J. P. Adam, J.-V. Kim, S. Rohart, A. Thiaville, J. Torrejon, M. Hayashi, and V. Jacques. Direct Measurement of Interfacial Dzyaloshinskii-Moriya Interaction in X|CoFeB|MgO Heterostructures with a Scanning NV Magnetometer (X = Ta, TaN, and W). *Physical Review B* **94**, 6 (2016).  
DOI: [10.1103/PhysRevB.94.064413](https://doi.org/10.1103/PhysRevB.94.064413).
- [Gub04] G. Gubbiotti, M. Conti, G. Carlotti, P. Candeloro, E. D. Fabrizio, K. Y. Guslienko, A. Andre, C. Bayer, and A. N. Slavin. Magnetic Field Dependence of Quantized and Localized Spin Wave Modes in Thin Rectangular Magnetic Dots. *Journal of Physics: Condensed Matter* **16**, 43 (2004).  
DOI: [10.1088/0953-8984/16/43/011](https://doi.org/10.1088/0953-8984/16/43/011).
- [Gur96] A. G. Gurevich and G. A. Melkov. *Magnetization Oscillations and Waves*. CRC Press, 1996.
- [Gus02] K. Y. Guslienko, S. O. Demokritov, B. Hillebrands, and A. N. Slavin. Effective Dipolar Boundary Conditions for Dynamic Magnetization in Thin Magnetic Stripes. *Physical Review B* **66**, 13 (2002).  
DOI: [10.1103/PhysRevB.66.132402](https://doi.org/10.1103/PhysRevB.66.132402).
- [Hah13] C. Hahn, G. de Loubens, O. Klein, M. Viret, V. V. Naletov, and J. Ben Youssef. Comparative Measurements of Inverse Spin Hall Effects and Magnetoresistance in YIG/Pt and YIG/Ta. *Physical Review B* **87**, 17 (2013).  
DOI: [10.1103/PhysRevB.87.174417](https://doi.org/10.1103/PhysRevB.87.174417).
- [Ham14] A. Hamadeh, O. d'Allivy Kelly, C. Hahn, H. Meley, R. Bernard, A. H. Molpeceres, V. V. Naletov, M. Viret, A. Anane, V. Cros, S. O. Demokritov, J. L. Prieto, M. Muñoz, G. de Loubens, and O. Klein. Full Control of the Spin-Wave Damping in a Magnetic Insulator Using Spin-Orbit Torque. *Physical Review Letters* **113**, 19 (2014).  
DOI: [10.1103/PhysRevLett.113.197203](https://doi.org/10.1103/PhysRevLett.113.197203).
- [Han13] P. M. Haney, H.-W. Lee, K.-J. Lee, A. Manchon, and M. D. Stiles. Current Induced Torques and Interfacial Spin-Orbit Coupling: Semiclassical Modeling. *Physical Review B* **87**, 17 (2013).  
DOI: [10.1103/PhysRevB.87.174411](https://doi.org/10.1103/PhysRevB.87.174411).
- [Har16] M. Harder, Y. Gui, and C.-M. Hu. Electrical Detection of Magnetization Dynamics via Spin Rectification Effects. *Physics Reports* **661** (2016).  
DOI: [10.1016/j.physrep.2016.10.002](https://doi.org/10.1016/j.physrep.2016.10.002).

- [Har68] K. J. Harte. Theory of Magnetization Ripple in Ferromagnetic Films. *Journal of Applied Physics* **39**, 3 (1968).  
DOI: [10.1063/1.1656388](https://doi.org/10.1063/1.1656388).
- [Heh96] M. Hehn, S. Padovani, K. Ounadjela, and J. P. Bucher. Nanoscale Magnetic Domain Structures in Epitaxial Cobalt Films. *Physical Review B* **54**, 5 (1996).  
DOI: [10.1103/PhysRevB.54.3428](https://doi.org/10.1103/PhysRevB.54.3428).
- [Hei85] B. Heinrich, J. F. Cochran, and R. Hasegawa. FMR Linebroadening in Metals Due to Two-magnon Scattering. *Journal of Applied Physics* **57**, 8 (1985).  
DOI: [10.1063/1.334991](https://doi.org/10.1063/1.334991).
- [Hei94] B. Heinrich and J. A. C. Bland, eds. *Ultrathin Magnetic Structures II: Measurement Techniques and Novel Magnetic Properties*. Berlin Heidelberg: Springer-Verlag, 1994.  
URL: <https://www.springer.com/fr/book/9783540219569>.
- [Hei28] W. Heisenberg. Zur Theorie des Ferromagnetismus. *Zeitschrift für Physik* **49**, 9-10 (1928).  
DOI: [10.1007/BF01328601](https://doi.org/10.1007/BF01328601).
- [Her51] C. Herring and C. Kittel. On the Theory of Spin Waves in Ferromagnetic Media. *Physical Review* **81**, 5 (1951).  
DOI: [10.1103/PhysRev.81.869](https://doi.org/10.1103/PhysRev.81.869).
- [Heu15] T. Heussner. “Lokalisierte Parallele Parametrische Verstärkung von Kohärent Angeregten Spinwellen in Ni81Fe19-Mikrostreifen”. Technischen Universität Kaiserslautern, 2015.
- [Hic09] M. C. Hickey and J. S. Moodera. Origin of Intrinsic Gilbert Damping. *Physical Review Letters* **102**, 13 (2009).  
DOI: [10.1103/PhysRevLett.102.137601](https://doi.org/10.1103/PhysRevLett.102.137601).
- [Hir99] J. E. Hirsch. Spin Hall Effect. *Physical Review Letters* **83**, 9 (1999).  
DOI: <https://doi.org/10.1103/PhysRevLett.83.1834>.
- [Hol40] T. Holstein and H. Primakoff. Field Dependence of the Intrinsic Domain Magnetization of a Ferromagnet. *Physical Review* **58**, 12 (1940).  
DOI: [10.1103/PhysRev.58.1098](https://doi.org/10.1103/PhysRev.58.1098).
- [Hou07] D. Houssameddine, U. Ebels, B. Delaët, B. Rodmacq, I. Firastrau, F. Pontehner, M. Brunet, C. Thirion, J.-P. Michel, L. Prejbeanu-Buda, M.-C. Cyrille, O. Redon, and B. Dieny. Spin-Torque Oscillator Using a Perpendicular Polarizer and a Planar Free Layer. *Nature Materials* **6**, 6 (2007).  
DOI: [10.1038/nmat1905](https://doi.org/10.1038/nmat1905).
- [Hur95] M. J. Hurben and C. E. Patton. Theory of Magnetostatic Waves for In-Plane Magnetized Isotropic Films. *Journal of Magnetism and Magnetic Materials* **139**, 3 (1995).  
DOI: [10.1016/0304-8853\(95\)90006-3](https://doi.org/10.1016/0304-8853(95)90006-3).

- [Hur98] M. J. Hurben and C. E. Patton. Theory of Two Magnon Scattering Microwave Relaxation and Ferromagnetic Resonance Linewidth in Magnetic Thin Films. *Journal of Applied Physics* **83**, 8 (1998).  
DOI: [10.1063/1.367194](https://doi.org/10.1063/1.367194).
- [Iih16] S. Iihama, Y. Sasaki, A. Sugihara, A. Kamimaki, Y. Ando, and S. Mizukami. Quantification of a Propagating Spin-Wave Packet Created by an Ultrashort Laser Pulse in a Thin Film of a Magnetic Metal. *Physical Review B* **94**, 2 (2016).  
DOI: [10.1103/PhysRevB.94.020401](https://doi.org/10.1103/PhysRevB.94.020401).
- [Jac12] P. Jacquod, R. S. Whitney, J. Meair, and M. Büttiker. Onsager Relations in Coupled Electric, Thermoelectric, and Spin Transport: The Tenfold Way. *Physical Review B* **86**, 15 (2012).  
DOI: [10.1103/PhysRevB.86.155118](https://doi.org/10.1103/PhysRevB.86.155118).
- [Jeo10] H. Jeon, Y.-B. Kim, and M. Choi. Standby Leakage Power Reduction Technique for Nanoscale CMOS VLSI Systems. *IEEE Transactions on Instrumentation and Measurement* **59**, 5 (2010).  
DOI: [10.1109/TIM.2010.2044710](https://doi.org/10.1109/TIM.2010.2044710).
- [Ji03] Y. Ji, C. L. Chien, and M. D. Stiles. Current-Induced Spin-Wave Excitations in a Single Ferromagnetic Layer. *Physical Review Letters* **90**, 10 (2003).  
DOI: [10.1103/PhysRevLett.90.106601](https://doi.org/10.1103/PhysRevLett.90.106601).
- [Jos65] R. I. Joseph and E. Schlömann. Demagnetizing Field in Nonellipsoidal Bodies. *Journal of Applied Physics* **36**, 5 (1965).  
DOI: [10.1063/1.1703091](https://doi.org/10.1063/1.1703091).
- [Jul75] M. Julliere. Tunneling between Ferromagnetic Films. *Physics Letters A* **54**, 3 (1975).  
DOI: [10.1016/0375-9601\(75\)90174-7](https://doi.org/10.1016/0375-9601(75)90174-7).
- [Jur60] H. J. Juretschke. Electromagnetic Theory of Dc Effects in Ferromagnetic Resonance. *Journal of Applied Physics* **31**, 8 (1960).  
DOI: [10.1063/1.1735851](https://doi.org/10.1063/1.1735851).
- [Kaj10] Y. Kajiwara, K. Harii, S. Takahashi, J. Ohe, K. Uchida, M. Mizuguchi, H. Umezawa, H. Kawai, K. Ando, K. Takanashi, S. Maekawa, and E. Saitoh. Transmission of Electrical Signals by Spin-Wave Interconversion in a Magnetic Insulator. *Nature* **464**, 7286 (2010).  
DOI: [10.1038/nature08876](https://doi.org/10.1038/nature08876).
- [Kal06] S. S. Kalarickal, P. Krivosik, M. Wu, C. E. Patton, M. L. Schneider, P. Kabos, T. J. Silva, and J. P. Nibarger. Ferromagnetic Resonance Linewidth in Metallic Thin Films: Comparison of Measurement Methods. *Journal of Applied Physics* **99**, 9 (2006).  
DOI: [10.1063/1.2197087](https://doi.org/10.1063/1.2197087).

- [Kal81] B. A. Kalinikos. Spectrum and Linear Excitation of Spin Waves in Ferromagnetic Films. *Soviet Physics Journal* **24**, 8 (1981).  
DOI: [10.1007/BF00941342](https://doi.org/10.1007/BF00941342).
- [Kal86] B. A. Kalinikos and A. N. Slavin. Theory of Dipole-Exchange Spin Wave Spectrum for Ferromagnetic Films with Mixed Exchange Boundary Conditions. *Journal of Physics C: Solid State Physics* **19**, 35 (1986).  
DOI: [10.1088/0022-3719/19/35/014](https://doi.org/10.1088/0022-3719/19/35/014).
- [Kal80] B. Kalinikos. Excitation of Propagating Spin Waves in Ferromagnetic Films. *IEE Proceedings H Microwaves, Optics and Antennas* **127**, 1 (1980).  
DOI: [10.1049/ip-h-1.1980.0002](https://doi.org/10.1049/ip-h-1.1980.0002).
- [Kam70] V. Kamberský. On the Landau–Lifshitz Relaxation in Ferromagnetic Metals. *Canadian Journal of Physics* **48**, 24 (1970).  
DOI: [10.1139/p70-361](https://doi.org/10.1139/p70-361).
- [Kas14] S. Kasai, K. Kondou, H. Sukegawa, S. Mitani, K. Tsukagoshi, and Y. Otani. Modulation of Effective Damping Constant Using Spin Hall Effect. *Applied Physics Letters* **104**, 9 (2014).  
DOI: [10.1063/1.4867649](https://doi.org/10.1063/1.4867649).
- [Kat04a] Y. K. Kato, R. C. Myers, A. C. Gossard, and D. D. Awschalom. Current-Induced Spin Polarization in Strained Semiconductors. *Physical Review Letters* **93**, 17 (2004).  
DOI: [10.1103/PhysRevLett.93.176601](https://doi.org/10.1103/PhysRevLett.93.176601).
- [Kat04b] Y. K. Kato, R. C. Myers, A. C. Gossard, and D. D. Awschalom. Observation of the Spin Hall Effect in Semiconductors. *Science* **306**, 5703 (2004).  
DOI: [10.1126/science.1105514](https://doi.org/10.1126/science.1105514).
- [Kha16] R. A. Khan, P. M. Shepley, A. Hrabec, A. W. J. Wells, B. Ocker, C. H. Marrows, and T. A. Moore. Effect of Annealing on the Interfacial Dzyaloshinskii-Moriya Interaction in Ta/CoFeB/MgO Trilayers. *Applied Physics Letters* **109**, 13 (2016).  
DOI: [10.1063/1.4963731](https://doi.org/10.1063/1.4963731).
- [Khi11] A. Khitun and K. L. Wang. Non-Volatile Magnonic Logic Circuits Engineering. *Journal of Applied Physics* **110**, 3 (2011).  
DOI: [10.1063/1.3609062](https://doi.org/10.1063/1.3609062).
- [Kim13] J. Kim, J. Sinha, M. Hayashi, M. Yamanouchi, S. Fukami, T. Suzuki, S. Mitani, and H. Ohno. Layer Thickness Dependence of the Current-Induced Effective Field Vector in Ta|CoFeB|MgO. *Nature Materials* **12**, 3 (2013).  
DOI: [10.1038/nmat3522](https://doi.org/10.1038/nmat3522).
- [Kis03] S. I. Kiselev, J. C. Sankey, I. N. Krivorotov, N. C. Emley, R. J. Schoelkopf, R. A. Buhrman, and D. C. Ralph. Microwave Oscillations of a Nanomagnet Driven by a Spin-Polarized Current. *Nature* **425**, 6956 (2003).  
DOI: [10.1038/nature01967](https://doi.org/10.1038/nature01967).

- [Kit48] C. Kittel. On the Theory of Ferromagnetic Resonance Absorption. *Physical Review* **73**, 2 (1948).
- [Kli14] S. Klingler, P. Pirro, T. Brächer, B. Leven, B. Hillebrands, and A. V. Chumak. Design of a Spin-Wave Majority Gate Employing Mode Selection. *Applied Physics Letters* **105**, 15 (2014).  
DOI: [10.1063/1.4898042](https://doi.org/10.1063/1.4898042).
- [Kos13] M. Kostylev. Non-Reciprocity of Dipole-Exchange Spin Waves in Thin Ferromagnetic Films. *Journal of Applied Physics* **113**, 5 (2013).  
DOI: [10.1063/1.4789962](https://doi.org/10.1063/1.4789962).
- [Kos07] M. P. Kostylev, A. A. Serga, T. Schneider, T. Neumann, B. Leven, B. Hillebrands, and R. L. Stamps. Resonant and Nonresonant Scattering of Dipole-Dominated Spin Waves from a Region of Inhomogeneous Magnetic Field in a Ferromagnetic Film. *Physical Review B* **76**, 18 (2007).  
DOI: [10.1103/PhysRevB.76.184419](https://doi.org/10.1103/PhysRevB.76.184419).
- [Koz10] X. Kozina, S. Ouardi, B. Balke, G. Stryganyuk, G. H. Fecher, C. Felser, S. Ikeda, H. Ohno, and E. Ikenaga. A Nondestructive Analysis of the B Diffusion in Ta-CoFeBMgO-CoFeB-Ta Magnetic Tunnel Junctions by Hard x-Ray Photoemission. *Applied Physics Letters* **96**, 7 (2010).  
DOI: [10.1063/1.3309702](https://doi.org/10.1063/1.3309702).
- [Kri10] P. Krivosik and C. E. Patton. Hamiltonian Formulation of Nonlinear Spin-Wave Dynamics: Theory and Applications. *Physical Review B* **82**, 18 (2010).  
DOI: [10.1103/PhysRevB.82.184428](https://doi.org/10.1103/PhysRevB.82.184428).
- [Kub08] H. Kubota, A. Fukushima, K. Yakushiji, T. Nagahama, S. Yuasa, K. Ando, H. Maehara, Y. Nagamine, K. Tsunekawa, D. D. Djayaprawira, N. Watanabe, and Y. Suzuki. Quantitative Measurement of Voltage Dependence of Spin-Transfer Torque in MgO-Based Magnetic Tunnel Junctions. *Nature Physics* **4**, 1 (2008).  
DOI: [10.1038/nphys784](https://doi.org/10.1038/nphys784).
- [Lan35] L. Landau and E. Lifshits. On the Theory of the Dispersion of Magnetic Permeability in Ferromagnetic Bodies. Pdf. *Phys. Zeitsch. der Sow.* **8** (1935).  
URL: <https://pdfs.semanticscholar.org/0c90/4c5ff5fff97bced606a5dc4d98cf9ebc4ed6.pdf>.
- [Lee17] K.-M. Lee, J. W. Choi, J. Sok, and B.-C. Min. Temperature Dependence of the Interfacial Magnetic Anisotropy in W/CoFeB/MgO. *AIP Advances* **7**, 6 (2017).  
DOI: [10.1063/1.4985720](https://doi.org/10.1063/1.4985720).
- [Len06] K. Lenz, H. Wende, W. Kuch, K. Baberschke, K. Nagy, and A. Jánossy. Two-Magnon Scattering and Viscous Gilbert Damping in Ultrathin Ferromagnets. *Physical Review B* **73**, 14 (2006).  
DOI: [10.1103/PhysRevB.73.144424](https://doi.org/10.1103/PhysRevB.73.144424).

- [Lin09] C. J. Lin, S. H. Kang, Y. J. Wang, K. Lee, X. Zhu, W. C. Chen, X. Li, W. N. Hsu, Y. C. Kao, M. T. Liu, W. C. Chen, YiChing Lin, M. Nowak, N. Yu, and Luan Tran. “45nm Low Power CMOS Logic Compatible Embedded STT MRAM Utilizing a Reverse-Connection 1T/1MTJ Cell”. *2009 IEEE International Electron Devices Meeting (IEDM)*. 2009 IEEE International Electron Devices Meeting (IEDM). 2009.  
DOI: [10.1109/IEDM.2009.5424368](https://doi.org/10.1109/IEDM.2009.5424368).
- [Lin03] J. Lindner, K. Lenz, E. Kosubek, K. Baberschke, D. Spoddig, R. Meckenstock, J. Pelzl, Z. Frait, and D. L. Mills. Non-Gilbert-Type Damping of the Magnetic Relaxation in Ultrathin Ferromagnets: Importance of Magnon-Magnon Scattering. *Physical Review B* **68**, 6 (2003).  
DOI: [10.1103/PhysRevB.68.060102](https://doi.org/10.1103/PhysRevB.68.060102).
- [Liu11] L. Liu, T. Moriyama, D. C. Ralph, and R. A. Buhrman. Spin-Torque Ferromagnetic Resonance Induced by the Spin Hall Effect. *Physical Review Letters* **106**, 3 (2011).  
DOI: [10.1103/PhysRevLett.106.036601](https://doi.org/10.1103/PhysRevLett.106.036601).
- [Liu12] L. Liu, C.-F. Pai, Y. Li, H. W. Tseng, D. C. Ralph, and R. A. Buhrman. Spin-Torque Switching with the Giant Spin Hall Effect of Tantalum. *Science* **336**, 6081 (2012).
- [Mad11] M. Madami, S. Bonetti, G. Consolo, S. Tacchi, G. Carlotti, G. Gubbiotti, F. B. Mancoff, M. A. Yar, and J. Åkerman. Direct Observation of a Propagating Spin Wave Induced by Spin-Transfer Torque. *Nature Nanotechnology* **6**, 10 (2011).  
DOI: [10.1038/nnano.2011.140](https://doi.org/10.1038/nnano.2011.140).
- [Man08] A. Manchon and S. Zhang. Theory of Nonequilibrium Intrinsic Spin Torque in a Single Nanomagnet. *Physical Review B* **78**, 21 (2008).  
DOI: [10.1103/PhysRevB.78.212405](https://doi.org/10.1103/PhysRevB.78.212405).
- [Man09] A. Manchon and S. Zhang. Theory of Spin Torque Due to Spin-Orbit Coupling. *Physical Review B* **79**, 9 (2009).  
DOI: [10.1103/PhysRevB.79.094422](https://doi.org/10.1103/PhysRevB.79.094422).
- [McG75] T. McGuire and R. Potter. Anisotropic Magnetoresistance in Ferromagnetic 3d Alloys. *IEEE Transactions on Magnetics* **11**, 4 (1975).  
DOI: [10.1109/TMAG.1975.1058782](https://doi.org/10.1109/TMAG.1975.1058782).
- [McM04] R. D. McMichael. Ferromagnetic Resonance Linewidth Models for Perpendicular Media. *Journal of Applied Physics* **95**, 11 (2004).  
DOI: [10.1063/1.1667446](https://doi.org/10.1063/1.1667446).
- [Mec07] N. Mecking, Y. S. Gui, and C.-M. Hu. Microwave Photovoltage and Photoresistance Effects in Ferromagnetic Microstrips. *Physical Review B* **76**, 22 (2007).  
DOI: [10.1103/PhysRevB.76.224430](https://doi.org/10.1103/PhysRevB.76.224430).

- [Mer19] R. Mertens. *Everspin Starts to Ship Customer Samples of Its 28nm 1Gb STT-MRAM Chips | MRAM-Info*. 2019. URL: <https://www.mram-info.com/everspin-starts-ship-customer-samples-its-28nm-1gb-stt-mram-chips>.
- [Mir11] I. M. Miron, K. Garello, G. Gaudin, P.-J. Zermatten, M. V. Costache, S. Auffret, S. Bandiera, B. Rodmacq, A. Schuhl, and P. Gambardella. Perpendicular Switching of a Single Ferromagnetic Layer Induced by In-Plane Current Injection. *Nature* **476**, 7359 (2011).  
DOI: [10.1038/nature10309](https://doi.org/10.1038/nature10309).
- [Mir10] I. M. Miron, G. Gaudin, S. Auffret, B. Rodmacq, A. Schuhl, S. Pizzini, J. Vogel, and P. Gambardella. Current-Driven Spin Torque Induced by the Rashba Effect in a Ferromagnetic Metal Layer. *Nature Materials* **9**, 3 (2010).  
DOI: [10.1038/nmat2613](https://doi.org/10.1038/nmat2613).
- [Moc87] R. Mock, B. Hillebrands, and R. Sandercock. Construction and Performance of a Brillouin Scattering Set-up Using a Triple-Pass Tandem Fabry-Perot Interferometer. *Journal of Physics E: Scientific Instruments* **20**, 6 (1987).  
DOI: [10.1088/0022-3735/20/6/017](https://doi.org/10.1088/0022-3735/20/6/017).
- [Mon02] S. Monso, B. Rodmacq, S. Auffret, G. Casali, F. Fettar, B. Gilles, B. Dieny, and P. Boyer. Crossover from In-Plane to Perpendicular Anisotropy in Pt/CoFe/AlOx Sandwiches as a Function of Al Oxidation: A Very Accurate Control of the Oxidation of Tunnel Barriers. *Applied Physics Letters* **80**, 22 (2002).  
DOI: [10.1063/1.1483122](https://doi.org/10.1063/1.1483122).
- [Mor01] A. H. Morrish. *The Physical Principles of Magnetism*. John Wiley & Sons, Inc., 2001.
- [Mos10] O. Mosendz, J. E. Pearson, F. Y. Fradin, G. E. W. Bauer, S. D. Bader, and A. Hoffmann. Quantifying Spin Hall Angles from Spin Pumping: Experiments and Theory. *Physical Review Letters* **104**, 4 (2010).  
DOI: [10.1103/PhysRevLett.104.046601](https://doi.org/10.1103/PhysRevLett.104.046601).
- [Mot29] N. F. Mott and B. A. The Scattering of Fast Electrons by Atomic Nuclei. *Proc. R. Soc. Lond. A* **124**, 794 (1929).  
DOI: [10.1098/rspa.1929.0127](https://doi.org/10.1098/rspa.1929.0127).
- [Nan15] T. Nan, S. Emori, C. T. Boone, X. Wang, T. M. Oxholm, J. G. Jones, B. M. Howe, G. J. Brown, and N. X. Sun. Comparison of Spin-Orbit Torques and Spin Pumping across NiFe/Pt and NiFe/Cu/Pt Interfaces. *Physical Review B* **91**, 21 (2015).  
DOI: [10.1103/PhysRevB.91.214416](https://doi.org/10.1103/PhysRevB.91.214416).

- [Nem11] H. T. Nembach, T. J. Silva, J. M. Shaw, M. L. Schneider, M. J. Carey, S. Maat, and J. R. Childress. Perpendicular Ferromagnetic Resonance Measurements of Damping and Lande G-Factor in Sputtered (Co<sub>2</sub>Mn)<sub>1-x</sub>Gex Thin Films. *Physical Review B* **84**, 5 (2011).  
DOI: [10.1103/PhysRevB.84.054424](https://doi.org/10.1103/PhysRevB.84.054424).
- [New93] A. J. Newell, W. Williams, and D. J. Dunlop. A Generalization of the Demagnetizing Tensor for Nonuniform Magnetization. *Journal of Geophysical Research* **98**, B6 (1993).  
DOI: [10.1029/93JB00694](https://doi.org/10.1029/93JB00694).
- [Nik15] A. A. Nikitin, A. B. Ustinov, A. A. Semenov, A. V. Chumak, A. A. Serga, V. I. Vasyuchka, E. Lähderanta, B. A. Kalinikos, and B. Hillebrands. A Spin-Wave Logic Gate Based on a Width-Modulated Dynamic Magnonic Crystal. *Applied Physics Letters* **106**, 10 (2015).  
DOI: [10.1063/1.4914506](https://doi.org/10.1063/1.4914506).
- [OHa99] R. C. O'Handley. *Modern Magnetic Materials: Principles and Applications*. Wiley, 1999.
- [Ohk74] F. J. Ohkawa and Y. Uemura. Quantized Surface States of a Narrow Gap Semiconductor. *Japanese Journal of Applied Physics* **13**, S2 (1974).  
DOI: [10.7567/JJAPS.2S2.355](https://doi.org/10.7567/JJAPS.2S2.355).
- [Ols67] F. A. Olson, E. K. Kirchner, K. B. Mehta, F. J. Peternell, and B. C. Morley. Propagation of Magnetostatic Surface Waves in YIG Rods. *Journal of Applied Physics* **38**, 3 (1967).  
DOI: [10.1063/1.1709546](https://doi.org/10.1063/1.1709546).
- [Osb45] J. A. Osborn. Demagnetizing Factors of the General Ellipsoid. *Physical Review* **67**, 11-12 (1945).  
DOI: [10.1103/PhysRev.67.351](https://doi.org/10.1103/PhysRev.67.351).
- [Pai15] C.-F. Pai, Y. Ou, L. H. Vilela-Leão, D. C. Ralph, and R. A. Buhrman. Dependence of the Efficiency of Spin Hall Torque on the Transparency of Pt/Ferromagnetic Layer Interfaces. *Physical Review B* **92**, 6 (2015).  
DOI: [10.1103/PhysRevB.92.064426](https://doi.org/10.1103/PhysRevB.92.064426).
- [Par02] J. P. Park, P. Eames, D. M. Engebretson, J. Berezovsky, and P. A. Crowell. Spatially Resolved Dynamics of Localized Spin-Wave Modes in Ferromagnetic Wires. *Physical Review Letters* **89**, 27 (2002).  
DOI: [10.1103/PhysRevLett.89.277201](https://doi.org/10.1103/PhysRevLett.89.277201).
- [Pat84] C. E. Patton. Magnetic Excitations in Solids. *Physics Reports* **103**, 5 (1984).  
DOI: [10.1016/0370-1573\(84\)90023-1](https://doi.org/10.1016/0370-1573(84)90023-1).

- [Pir14] P. Pirro, T. Sebastian, T. Brächer, A. A. Serga, T. Kubota, H. Naganuma, M. Oogane, Y. Ando, and B. Hillebrands. Non-Gilbert-Damping Mechanism in a Ferromagnetic Heusler Compound Probed by Nonlinear Spin Dynamics. *Physical Review Letters* **113**, 22 (2014).  
DOI: [10.1103/PhysRevLett.113.227601](https://doi.org/10.1103/PhysRevLett.113.227601).
- [Pre13] I. L. Prejbeanu, S. Bandiera, J. Alvarez-Hérault, R. C. Sousa, B. Dieny, and J.-P. Nozières. Thermally Assisted MRAMs: Ultimate Scalability and Logic Functionalities. *Journal of Physics D: Applied Physics* **46**, 7 (2013).  
DOI: [10.1088/0022-3727/46/7/074002](https://doi.org/10.1088/0022-3727/46/7/074002).
- [Pre09] G. Prenat, B. Dieny, W. Guo, M. E. Baraji, V. Javerliac, and J. Nozieres. Beyond MRAM, CMOS/MTJ Integration for Logic Components. *IEEE Transactions on Magnetics* **45**, 10 (2009).  
DOI: [10.1109/TMAG.2009.2025257](https://doi.org/10.1109/TMAG.2009.2025257).
- [Pre16] G. Prenat, K. Jabeur, P. Vanhauwaert, G. D. Pendina, F. Oboril, R. Bishnoi, M. Ebrahimi, N. Lamard, O. Boule, K. Garello, J. Langer, B. Ocker, M.-C. Cyrille, P. Gambardella, M. Tahoori, and G. Gaudin. Ultra-Fast and High-Reliability SOT-MRAM: From Cache Replacement to Normally-Off Computing. *IEEE Transactions on Multi-Scale Computing Systems* **2**, 1 (2016).  
DOI: [10.1109/TMSCS.2015.2509963](https://doi.org/10.1109/TMSCS.2015.2509963).
- [Ral08] D. C. Ralph and M. D. Stiles. Spin Transfer Torques. *Journal of Magnetism and Magnetic Materials* **320**, 7 (2008).  
DOI: [10.1016/j.jmmm.2007.12.019](https://doi.org/10.1016/j.jmmm.2007.12.019).
- [Ran17] B. Rana, Y. Fukuma, K. Miura, H. Takahashi, and Y. Otani. Excitation of Coherent Propagating Spin Waves in Ultrathin CoFeB Film by Voltage-Controlled Magnetic Anisotropy. *Applied Physics Letters* **111**, 5 (2017).  
DOI: [10.1063/1.4990724](https://doi.org/10.1063/1.4990724).
- [Rod09] B. Rodmacq, A. Manchon, C. Ducruet, S. Auffret, and B. Dieny. Influence of Thermal Annealing on the Perpendicular Magnetic Anisotropy of Pt/Co/AlOx Trilayers. *Physical Review B* **79**, 2 (2009).  
DOI: [10.1103/PhysRevB.79.024423](https://doi.org/10.1103/PhysRevB.79.024423).
- [Sad15a] A. V. Sadovnikov, E. N. Beginin, S. E. Sheshukova, D. V. Romanenko, Y. P. Sharaevskii, and S. A. Nikitov. Directional Multimode Coupler for Planar Magnonics: Side-Coupled Magnetic Stripes. *Applied Physics Letters* **107**, 20 (2015).  
DOI: [10.1063/1.4936207](https://doi.org/10.1063/1.4936207).
- [Sad15b] A. V. Sadovnikov, C. S. Davies, S. V. Grishin, V. V. Kruglyak, D. V. Romanenko, Y. P. Sharaevskii, and S. A. Nikitov. Magnonic Beam Splitter: The Building Block of Parallel Magnonic Circuitry. *Applied Physics Letters* **106**, 19 (2015).  
DOI: [10.1063/1.4921206](https://doi.org/10.1063/1.4921206).

- [Sai17] D. Saida, S. Kashiwada, M. Yakabe, T. Daibou, M. Fukumoto, S. Miwa, Y. Suzuki, K. Abe, H. Noguchi, J. Ito, and S. Fujita.  $1\times$  to  $2\times$  -Nm Perpendicular MTJ Switching at Sub-3-Ns Pulses Below  $100\mu A$  for High-Performance Embedded STT-MRAM for Sub-20-Nm CMOS. *IEEE Transactions on Electron Devices* **64**, 2 (2017).  
DOI: [10.1109/TED.2016.2636326](https://doi.org/10.1109/TED.2016.2636326).
- [Sai06] E. Saitoh, M. Ueda, H. Miyajima, and G. Tatara. Conversion of Spin Current into Charge Current at Room Temperature: Inverse Spin-Hall Effect. *Applied Physics Letters* **88**, 18 (2006).  
DOI: [10.1063/1.2199473](https://doi.org/10.1063/1.2199473).
- [San77] D. J. Sanders and D. Walton. Effect of Magnon-Phonon Thermal Relaxation on Heat Transport by Magnons. *Physical Review B* **15**, 3 (1977).  
DOI: [10.1103/PhysRevB.15.1489](https://doi.org/10.1103/PhysRevB.15.1489).
- [San06] J. C. Sankey, P. M. Braganca, A. G. F. Garcia, I. N. Krivorotov, R. A. Buhrman, and D. C. Ralph. Spin-Transfer-Driven Ferromagnetic Resonance of Individual Nanomagnets. *Physical Review Letters* **96**, 22 (2006).  
DOI: [10.1103/PhysRevLett.96.227601](https://doi.org/10.1103/PhysRevLett.96.227601).
- [Sch08] T. Schneider, A. A. Serga, T. Neumann, B. Hillebrands, and M. P. Kostylev. Phase Reciprocity of Spin-Wave Excitation by a Microstrip Antenna. *Physical Review B* **77**, 21 (2008).  
DOI: [10.1103/PhysRevB.77.214411](https://doi.org/10.1103/PhysRevB.77.214411).
- [Sch12] H. Schultheiss, J. E. Pearson, S. D. Bader, and A. Hoffmann. Thermoelectric Detection of Spin Waves. *Physical Review Letters* **109**, 23 (2012).  
DOI: [10.1103/PhysRevLett.109.237204](https://doi.org/10.1103/PhysRevLett.109.237204).
- [Seb12] T. Sebastian, Y. Ohdaira, T. Kubota, P. Pirro, T. Brächer, K. Vogt, A. A. Serga, H. Naganuma, M. Oogane, Y. Ando, and B. Hillebrands. Low-Damping Spin-Wave Propagation in a Micro-Structured  $\text{Co}_2\text{Mn}_{0.6}\text{Fe}_{0.4}\text{Si}$  Heusler Waveguide. *Applied Physics Letters* **100**, 11 (2012).  
DOI: [10.1063/1.3693391](https://doi.org/10.1063/1.3693391).
- [Seb15] T. Sebastian, K. Schultheiss, B. Obry, B. Hillebrands, and H. Schultheiss. Micro-Focused Brillouin Light Scattering: Imaging Spin Waves at the Nanoscale. *Frontiers in Physics* **3** (2015).  
DOI: [10.3389/fphy.2015.00035](https://doi.org/10.3389/fphy.2015.00035).
- [Sho85] M. Shone. The Technology of YIG Film Growth. *Circuits, Systems and Signal Processing* **4**, 1 (1985).  
DOI: [10.1007/BF01600074](https://doi.org/10.1007/BF01600074).
- [Sin04] J. Sinova, D. Culcer, Q. Niu, N. A. Sinitsyn, T. Jungwirth, and A. H. MacDonald. Universal Intrinsic Spin Hall Effect. *Physical Review Letters* **92**, 12 (2004).  
DOI: [10.1103/PhysRevLett.92.126603](https://doi.org/10.1103/PhysRevLett.92.126603).

- [Sin15] J. Sinova, S. O. Valenzuela, J. Wunderlich, C. H. Back, and T. Jungwirth. Spin Hall Effects. *Reviews of Modern Physics* **87**, 4 (2015).  
DOI: [10.1103/RevModPhys.87.1213](https://doi.org/10.1103/RevModPhys.87.1213).
- [Ski14] T. D. Skinner, M. Wang, A. T. Hindmarch, A. W. Rushforth, A. C. Irvine, D. Heiss, H. Kurebayashi, and A. J. Ferguson. Spin-Orbit Torque Opposing the Oersted Torque in Ultrathin Co/Pt Bilayers. *Applied Physics Letters* **104**, 6 (2014).  
DOI: [10.1063/1.4864399](https://doi.org/10.1063/1.4864399).
- [Sla05] A. Slavin and V. Tiberkevich. Spin Wave Mode Excited by Spin-Polarized Current in a Magnetic Nanocontact Is a Standing Self-Localized Wave Bullet. *Physical Review Letters* **95**, 23 (2005).  
DOI: [10.1103/PhysRevLett.95.237201](https://doi.org/10.1103/PhysRevLett.95.237201).
- [Slo96] J. C. Slonczewski. Current-Driven Excitation of Magnetic Multilayers. *Journal of Magnetism and Magnetic Materials* **159**, 1 (1996).  
DOI: [10.1016/0304-8853\(96\)00062-5](https://doi.org/10.1016/0304-8853(96)00062-5).
- [Sou16] R. Soucaille, M. Belmeguenai, J. Torrejon, J.-V. Kim, T. Devolder, Y. Rousigné, S.-M. Chérif, A. A. Stashkevich, M. Hayashi, and J.-P. Adam. Probing the Dzyaloshinskii-Moriya Interaction in CoFeB Ultrathin Films Using Domain Wall Creep and Brillouin Light Spectroscopy. *Physical Review B* **94**, 10 (2016).  
DOI: [10.1103/PhysRevB.94.104431](https://doi.org/10.1103/PhysRevB.94.104431).
- [Sta09] D. D. Stancil and A. Prabhakar. *Spin Waves: Theory and Applications*. Springer US, 2009.
- [Stö06] J. Stöhr and H. C. Siegmann. *Magnetism: From Fundamentals to Nanoscale Dynamics*. Springer-Verlag, 2006.
- [Str18] N. Strelkov, A. Chavent, A. Timopheev, R. C. Sousa, I. L. Prejbeanu, L. D. Buda-Prejbeanu, and B. Dieny. Impact of Joule Heating on the Stability Phase Diagrams of Perpendicular Magnetic Tunnel Junctions. *Physical Review B* **98**, 21 (2018).  
DOI: [10.1103/PhysRevB.98.214410](https://doi.org/10.1103/PhysRevB.98.214410).
- [Sun12] Y. Sun, Y.-Y. Song, H. Chang, M. Kabatek, M. Jantz, W. Schneider, M. Wu, H. Schultheiss, and A. Hoffmann. Growth and Ferromagnetic Resonance Properties of Nanometer-Thick Yttrium Iron Garnet Films. *Applied Physics Letters* **101**, 15 (2012).  
DOI: [10.1063/1.4759039](https://doi.org/10.1063/1.4759039).

- [Tak07] T. Takeuchi, K. Tsunekawa, Y.-s. Choi, Y. Nagamine, D. D. Djayaprawira, A. Genseki, Y. Hoshi, and Y. Kitamoto. Crystallization of Amorphous CoFeB Ferromagnetic Layers in CoFeB/MgO/CoFeB Magnetic Tunnel Junctions. *Japanese Journal of Applied Physics* **46** (No. 25 2007).  
DOI: [10.1143/JJAP.46.L623](https://doi.org/10.1143/JJAP.46.L623).
- [Tan08] T. Tanaka, H. Kontani, M. Naito, T. Naito, D. S. Hirashima, K. Yamada, and J. Inoue. Intrinsic Spin Hall Effect and Orbital Hall Effect in 4d and 5d Transition Metals. *Physical Review B* **77**, 16 (2008).  
DOI: [10.1103/PhysRevB.77.165117](https://doi.org/10.1103/PhysRevB.77.165117).
- [Tar18] M. Tarequzzaman, T. Bohnert, A. S. Jenkins, J. Borme, E. Paz, R. Ferreira, and P. P. Freitas. Influence of MgO Tunnel Barrier Thickness on the Output Power of Three-Terminal Spin Hall Nano-Oscillators. *IEEE Transactions on Magnetics* **54**, 11 (2018).  
DOI: [10.1109/TMAG.2018.2831242](https://doi.org/10.1109/TMAG.2018.2831242).
- [Teh99] S. Tehrani, J. M. Slaughter, E. Chen, M. Durlam, J. Shi, and M. DeHerren. Progress and Outlook for MRAM Technology. *IEEE Transactions on Magnetics* **35**, 5 (1999).  
DOI: [10.1109/20.800991](https://doi.org/10.1109/20.800991).
- [Tet15] J.-P. Tetienne, T. Hingant, L. J. Martínez, S. Rohart, A. Thiaville, L. H. Diez, K. Garcia, J.-P. Adam, J.-V. Kim, J.-F. Roch, I. M. Miron, G. Gaudin, L. Vila, B. Ocker, D. Ravelosona, and V. Jacques. The Nature of Domain Walls in Ultrathin Ferromagnets Revealed by Scanning Nanomagnetometry. *Nature Communications* **6** (2015).  
DOI: [10.1038/ncomms7733](https://doi.org/10.1038/ncomms7733).
- [Tho57] W. Thomson. On the Electro-Dynamic Qualities of Metals:—Effects of Magnetization on the Electric Conductivity of Nickel and of Iron. *Proceedings of the Royal Society of London* **8** (1857).  
DOI: [10.1098/rspl.1856.0144](https://doi.org/10.1098/rspl.1856.0144).
- [Tru10] S. Trudel, O. Gaier, J. Hamrle, and B. Hillebrands. Magnetic Anisotropy, Exchange and Damping in Cobalt-Based Full-Heusler Compounds: An Experimental Review. *Journal of Physics D: Applied Physics* **43**, 19 (2010).  
DOI: [10.1088/0022-3727/43/19/193001](https://doi.org/10.1088/0022-3727/43/19/193001).
- [Tse05] Y. Tserkovnyak, A. Brataas, G. E. W. Bauer, and B. I. Halperin. Nonlocal Magnetization Dynamics in Ferromagnetic Heterostructures. *Rev. Mod. Phys.* **77**, 4 (2005).
- [Tse02a] Y. Tserkovnyak, A. Brataas, and G. E. W. Bauer. Enhanced Gilbert Damping in Thin Ferromagnetic Films. *Physical Review Letters* **88**, 11 (2002).  
DOI: [10.1103/PhysRevLett.88.117601](https://doi.org/10.1103/PhysRevLett.88.117601).

- [Tse02b] Y. Tserkovnyak, A. Brataas, and G. E. W. Bauer. Spin Pumping and Magnetization Dynamics in Metallic Multilayers. *Physical Review B* **66**, 22 (2002). DOI: [10.1103/PhysRevB.66.224403](https://doi.org/10.1103/PhysRevB.66.224403).
- [Tso98] M. Tsoi, A. G. M. Jansen, J. Bass, W.-C. Chiang, M. Seck, V. Tsoi, and P. Wyder. Excitation of a Magnetic Multilayer by an Electric Current. *Physical Review Letters* **80**, 19 (1998). DOI: [10.1103/PhysRevLett.80.4281](https://doi.org/10.1103/PhysRevLett.80.4281).
- [Tu17] S. Tu, J. Hu, G. Yu, H. Yu, C. Liu, F. Heimbach, X. Wang, J. Zhang, Y. Zhang, A. Hamzić, K. L. Wang, W. Zhao, and J.-P. Ansermet. Anomalous Nernst Effect in Ir<sub>22</sub>Mn<sub>78</sub>/Co<sub>20</sub>Fe<sub>60</sub>B<sub>20</sub>/MgO Layers with Perpendicular Magnetic Anisotropy. *Applied Physics Letters* **111**, 22 (2017). DOI: [10.1063/1.4996399](https://doi.org/10.1063/1.4996399).
- [Tul05] A. A. Tulapurkar, Y. Suzuki, A. Fukushima, H. Kubota, H. Maehara, K. Tsunekawa, D. D. Djayaprawira, N. Watanabe, and S. Yuasa. Spin-Torque Diode Effect in Magnetic Tunnel Junctions. *Nature* **438**, 7066 (2005). DOI: [10.1038/nature04207](https://doi.org/10.1038/nature04207).
- [Val06] S. O. Valenzuela and M. Tinkham. Direct Electronic Measurement of the Spin Hall Effect. *Nature* **442**, 7099 (2006). DOI: [10.1038/nature04937](https://doi.org/10.1038/nature04937).
- [Van14] A. Vansteenkiste, J. Leliaert, M. Dvornik, M. Helsen, F. Garcia-Sanchez, and B. Van Waeyenberge. The Design and Verification of MuMax3. *AIP Advances* **4**, 10 (2014). DOI: [10.1063/1.4899186](https://doi.org/10.1063/1.4899186).
- [Ver14] N. Vernier, J.-P. Adam, S. Eimer, G. Agnus, T. Devolder, T. Hauet, B. Ocker, F. Garcia, and D. Ravelosona. Measurement of Magnetization Using Domain Compressibility in CoFeB Films with Perpendicular Anisotropy. *Applied Physics Letters* **104**, 12 (2014). DOI: [10.1063/1.4869482](https://doi.org/10.1063/1.4869482).
- [Vog14] K. Vogt, F. Y. Fradin, J. E. Pearson, T. Sebastian, S. D. Bader, B. Hillebrands, A. Hoffmann, and H. Schultheiss. Realization of a Spin-Wave Multiplexer. *Nature Communications* **5** (2014). DOI: [10.1038/ncomms4727](https://doi.org/10.1038/ncomms4727).
- [Wal58] L. R. Walker. Resonant Modes of Ferromagnetic Spheroids. *Journal of Applied Physics* **29**, 3 (1958). DOI: [10.1063/1.1723117](https://doi.org/10.1063/1.1723117).
- [Wan] Q. Wang, B. Heinz, R. Verba, M. Kewenig, P. Pirro, M. Schneider, T. Meyer, B. Lägél, C. Dubs, T. Brächer, and A. V. Chumak. Spin Pinning and Spin-Wave Dispersion in Nanoscopic Ferromagnetic Waveguides (). URL: <https://arxiv.org/pdf/1807.01358>.

- [Yam07] A. Yamaguchi, H. Miyajima, T. Ono, Y. Suzuki, S. Yuasa, A. Tulapurkar, and Y. Nakatani. Rectification of Radio Frequency Current in Ferromagnetic Nanowire. *Applied Physics Letters* **90**, 18 (2007).  
DOI: [10.1063/1.2737134](https://doi.org/10.1063/1.2737134).
- [Yam09] A. Yamaguchi, K. Motoi, A. Hirohata, and H. Miyajima. Anomalous Hall Voltage Rectification and Quantized Spin-Wave Excitation Induced by Simultaneous Application of Dc and Rf Currents in a Single-Layered Ni<sub>81</sub>Fe<sub>19</sub> Nanoscale Wire. *Physical Review B* **79**, 22 (2009).  
DOI: [10.1103/PhysRevB.79.224409](https://doi.org/10.1103/PhysRevB.79.224409).
- [Yan11] H. X. Yang, M. Chshiev, B. Dieny, J. H. Lee, A. Manchon, and K. H. Shin. First-Principles Investigation of the Very Large Perpendicular Magnetic Anisotropy at Fe | MgO and Co | MgO Interfaces. *Physical Review B* **84**, 5 (2011).  
DOI: [10.1103/PhysRevB.84.054401](https://doi.org/10.1103/PhysRevB.84.054401).
- [Yua05] S. Yuasa, Y. Suzuki, T. Katayama, and K. Ando. Characterization of Growth and Crystallization Processes in CoFeB/MgO/CoFeB Magnetic Tunnel Junction Structure by Reflective High-Energy Electron Diffraction. *Applied Physics Letters* **87**, 24 (2005).  
DOI: [10.1063/1.2140612](https://doi.org/10.1063/1.2140612).
- [Zah18] M. Zahedinejad, H. Mazraati, H. Fulara, J. Yue, S. Jiang, A. A. Awad, and J. Åkerman. CMOS Compatible W/CoFeB/MgO Spin Hall Nano-Oscillators with Wide Frequency Tunability. *Applied Physics Letters* **112**, 13 (2018).  
DOI: [10.1063/1.5022049](https://doi.org/10.1063/1.5022049).
- [Zha13] C. Zhang, M. Yamanouchi, H. Sato, S. Fukami, S. Ikeda, F. Matsukura, and H. Ohno. Magnetotransport Measurements of Current Induced Effective Fields in Ta/CoFeB/MgO. *Applied Physics Letters* **103**, 26 (2013).  
DOI: [10.1063/1.4859656](https://doi.org/10.1063/1.4859656).
- [Zha11] H. Zhao, A. Lyle, Y. Zhang, P. K. Amiri, G. Rowlands, Z. Zeng, J. Katine, H. Jiang, K. Galatsis, K. L. Wang, I. N. Krivorotov, and J.-P. Wang. Low Writing Energy and Sub Nanosecond Spin Torque Transfer Switching of In-Plane Magnetic Tunnel Junction for Spin Torque Transfer Random Access Memory. *Journal of Applied Physics* **109**, 7 (2011).  
DOI: [10.1063/1.3556784](https://doi.org/10.1063/1.3556784).

## Abstract

Spin-waves have been proposed as a possible technological path to overcome the hurdles encountered by the miniaturization of complementary metal-oxide-semiconductor (CMOS) into the nanometer range, demonstrated by recent developments in spin-wave-based logic devices. However the industrial appeal of these proofs-of-concept is conditional upon their scalable integration with CMOS technology. Here, we report on ultrathin Ta/CoFeB/MgO wires used as spin-wave waveguides. This system is chosen for its compatibility with CMOS processes, its perpendicular magnetic anisotropy and strong spin-orbit interactions. The latter are of interest for manipulating spin waves and are characterized via spin-torque ferromagnetic resonance where it is shown that the inverse spin Hall effect is responsible for the detection of magnetization dynamics. Following this, we use integrated nanometric coplanar waveguides to locally excite spin-waves in a broad range of wavevectors. Comparison of the measured spin-wave spectrum with analytical calculations show that the inverse spin Hall effect allows the wavevector-independent detection of spin-waves with wavelengths down to 150 nm. Complementary Brillouin light scattering experiments reveal that spin-waves in the ultrathin spin-wave waveguide with perpendicular magnetic anisotropy have unexpectedly high propagation lengths considering the relatively high damping in Ta/CoFeB/MgO systems. These findings pave the way for ultrathin CMOS-compatible spin-wave devices with excitation and detection techniques that are scalable into the nanometer range, with the prospect of controlling spin-waves via spin-orbit torques.

## Résumé

Les ondes de spin sont une des voies technologiques proposées pour surmonter les obstacles que rencontre la miniaturisation des *complementary metal-oxide-semiconductor* (CMOS) dans la gamme du nanomètre, comme en témoignent les derniers développements en matière de dispositifs logiques à ondes de spin. Cependant, l'attrait industriel de ces preuves de concept est conditionné par leur intégration évolutive à la technologie CMOS. Ici, nous présentons des pistes ultrafines de Ta/CoFeB/MgO utilisées comme guides d'ondes de spin. Ce système a été choisi pour sa compatibilité avec les procédés CMOS, son anisotropie magnétique perpendiculaire et sa fortes interactions spin-orbite. Ces derniers sont intéressants pour manipuler les ondes de spin et ont été caractérisés par résonance ferromagnétique à couple de spin où il est démontré que l'effet Hall de spin inverse est responsable de la détection de la dynamique de magnétisation. Ensuite, nous utilisons des guides d'ondes coplanaires nanométriques intégrés pour exciter localement des ondes de spin dans une large gamme de vecteurs d'onde. La comparaison du spectre d'ondes de spin mesuré avec les calculs analytiques montre que l'effet Hall de spin inverse permet la détection des ondes de spin indépendamment de leur vecteur d'onde avec des longueurs d'onde allant jusqu'à 150 nm. Des expériences complémentaires de diffusion de la lumière de Brillouin révèlent que les ondes de spin dans le guide d'ondes de spin ultra-mince à anisotropie magnétique perpendiculaire ont des longueurs de propagation étonnamment élevées compte tenu de l'amortissement relativement élevé des systèmes Ta/CoFeB/MgO. Ces résultats ouvrent la voie à des dispositifs à ondes de spin ultra-minces compatibles CMOS avec des techniques d'excitation et de détection évolutives jusqu'à l'ordre du nanomètre, avec la perspective de contrôler les ondes de spin via des couples de spin-orbite.